



**HAL**  
open science

# Cardiac MR thermometry for the monitoring of radiofrequency ablation

Solenn Toupin

► **To cite this version:**

Solenn Toupin. Cardiac MR thermometry for the monitoring of radiofrequency ablation. Human health and pathology. Université de Bordeaux, 2016. English. NNT : 2016BORD0346 . tel-01511066

**HAL Id: tel-01511066**

**<https://theses.hal.science/tel-01511066>**

Submitted on 20 Apr 2017

**HAL** is a multi-disciplinary open access archive for the deposit and dissemination of scientific research documents, whether they are published or not. The documents may come from teaching and research institutions in France or abroad, or from public or private research centers.

L'archive ouverte pluridisciplinaire **HAL**, est destinée au dépôt et à la diffusion de documents scientifiques de niveau recherche, publiés ou non, émanant des établissements d'enseignement et de recherche français ou étrangers, des laboratoires publics ou privés.

THÈSE PRÉSENTÉE  
POUR OBTENIR LE GRADE DE  
**DOCTEUR DE**  
**L'UNIVERSITÉ de BORDEAUX**

ÉCOLE DOCTORALE SCIENCES DE LA VIE ET DE LA SANTÉ  
SPÉCIALITÉ : Bio-imagerie

par Solenn TOUPIN

**Cardiac MR thermometry**  
**for the monitoring of radiofrequency ablation**

Sous la direction de : Bruno QUESSON, directeur de recherche CNRS

Soutenue le 7 Décembre 2016

Membres du jury :

M. DE MATHELIN Michel	Professeur	Université de Strasbourg	Rapporteur
M. FELBLINGER Jacques	Professeur	Université de Nancy	Rapporteur
M. PIORKOWSKI Christopher	Docteur	Université de Dresde	Examineur
M. DENIS DE SENNEVILLE Baudouin	Chargé de recherche	Université de Bordeaux	Examineur
M. QUESSON Bruno	Directeur de recherche	Université de Bordeaux	Examineur



**Titre :** Thermométrie IRM pour le suivi des ablations radiofréquences sur le cœur

**Résumé :** Le traitement des arythmies cardiaques par ablation radiofréquence est une procédure thérapeutique permettant de restaurer un rythme normal par destruction thermique des tissus arythmogènes. A l'heure actuelle, l'intervention est réalisée sans imagerie temps réel permettant de visualiser la lésion pendant l'ablation. La thermométrie IRM permet de mesurer la température du tissu en chaque pixel et d'estimer directement l'étendue de la lésion via le calcul de la dose thermique cumulée. Si cette technique est déjà établie pour guider l'ablation de tumeurs dans différents organes, elle reste difficile à mettre en œuvre sur le cœur, notamment à cause des mouvements de respiration et de contraction myocardique. Dans le cadre de cette thèse, une méthode de thermométrie cardiaque a été implémentée pour réaliser une cartographie temps réel de la température du myocarde en condition de respiration libre. Plusieurs séquences IRM rapides ont été développées pour permettre l'acquisition d'environ 5 coupes par battement cardiaque avec une taille de voxel de  $1.6 \times 1.6 \times 3 \text{ mm}^3$ . Plusieurs solutions de réduction des mouvements hors plan de coupe ont été évaluées : positionnement des coupes dans le sens principal du déplacement, suivi dynamique de la position des coupes en fonction de l'état respiratoire (navigateur, mesure de la position du cathéter). Le mouvement résiduel et les artéfacts de susceptibilité associés sont corrigés par des algorithmes temps réels pour permettre une précision de la thermométrie IRM à  $\pm 2^\circ\text{C}$  sur les ventricules. Ce protocole a été utilisé avec succès pour le suivi d'ablations radiofréquences chez la brebis (N=3), permettant une corrélation (R=0.87) entre la dose thermique et la taille réelle des lésions induites. Les résultats sont très prometteurs quant à la pertinence de cette mesure pour une estimation en ligne de l'étendue de la lésion pendant l'ablation. Ces méthodes permettent d'envisager une évaluation clinique à court terme.

**Mots clés :** Thermométrie IRM, Arythmie, Ablation radiofréquence, Cathéter, Correction de mouvement

---

#### **Unité de recherche**

IHU LIRYC, Institut de rythmologie et modélisation cardiaque  
Université de Bordeaux, Centre de Recherche Cardio-Thoracique de Bordeaux, U1045  
Avenue du Haut Lévêque - 33600 Pessac

#### **Entreprise CIFRE**

Siemens Healthineers France - 40 avenue des Fruitiers - 93200 Saint-Denis

**Title:** Cardiac MR thermometry for the monitoring of radiofrequency ablation

**Abstract:** Radiofrequency ablation is a therapeutic procedure for the treatment of cardiac arrhythmia by inducing a local necrosis of the arrhythmogenic tissue. This intervention is currently performed without online imaging of the lesion formation during radiofrequency delivery. MR thermometry provides a monitoring of temperature in the targeted tissue in each pixel and an immediate estimation of lesion via the calculation of the thermal dose. If this technique is well established for the guidance of tumor ablation in various organs, it remains challenging in the heart due to motion (breathing and myocardial contraction). In this work, a cardiac MR thermometry method was developed to perform a real-time temperature mapping of the heart under free-breathing conditions. Several MR pulse sequences were designed to ensure the acquisition of up to 5 slices per heartbeat with a voxel size of  $1.6 \times 1.6 \times 3 \text{ mm}^3$ . Different solutions of minimization of out-of-plane motion were evaluated: alignment of the slices in the main direction of displacement, dynamic update of slice position depending on the respiratory state (echo-navigator, measure of the catheter position). Residual in-plane motion and associated susceptibility artifacts were corrected by real-time algorithms to allow a precision of MR thermometry of  $\pm 2^\circ\text{C}$  in ventricles. This protocol was successfully used for the monitoring of radiofrequency ablation in sheep (N=3), allowing a correlation (R=87) between thermal dose maps and sizes of created lesions. These results are promising regarding the relevance of this measure for an inline estimation of the lesion extent during ablation.

**Keywords:** MR thermometry, Arrhythmia, Radiofrequency ablation, Catheter, Motion compensation

# Remerciements

Au terme de ce doctorat, ma gratitude va tout d’abord à Bruno Quesson qui m’a accueillie au sein de l’institut de rythmologie et modélisation cardiaque (LIRYC) pour effectuer mon stage de fin d’études dans un environnement scientifique stimulant et de très haute qualité. Je lui exprime toute ma reconnaissance pour m’avoir encouragée à poursuivre un doctorat sous sa direction, me témoignant sa confiance pour les trois années qui allaient suivre. Je le remercie d’avoir toujours su se rendre disponible pour répondre à mes questions, partager son savoir et me prêter main forte pour des expérimentations souvent tardives. Sa jovialité, son humour et sa franchise ont amené une touche de bonne humeur très appréciable.

Mes trois années de thèse se sont déroulées dans un environnement chaleureux, convivial et stimulant. Je le dois à tous les membres de l’IHU Liryc et particulièrement à l’équipe “Imagerie”, dans le désordre : Valéry, Pierre, Fabrice, Julie, Mathilde, Thibaud, Jérôme, Alexis, Romain, Olivia, Jasmin, Florent et la toute nouvelle thésarde Marylène. Un grand merci à mes deux co-bureaux préférés, Valéry et Pierre, d’avoir partagé avec moi ces trois années mémorables, des débuts balbutiants aux premiers articles, en passant par les congrès à Milan et à Singapour. Valéry Ozenne, “monsieur Gadgetron”, avec qui j’ai partagé les joies de décrypter et de réimplémenter les techniques de l’état de l’art de la thermométrie IRM au début de ma thèse. C’était le prix à payer pour les premiers arrivants d’un institut nouvellement créé. Je te remercie pour ta bonne humeur à toute épreuve, même face à mes coups de sang certes rares mais sonores. . . “Comme dit” Pierre Bour, dont la passion incompréhensible pour la programmation de séquences IDEA m’a toujours impressionnée ! Merci pour les potins distrayants que tu as ramenés dans le bureau, ta maniaquerie qui nous a encouragés à ranger un peu de temps en temps. De ces trois années en votre compagnie, je retiens une vraie cohésion d’équipe avec des discussions franches et animées, une aide mutuelle sans laquelle aucun résultat n’aurait été possible. Je remercie également Baudouin Denis de Senneville, qui nous a apporté son expertise en correction de mouvement et en thermométrie, avec beaucoup de pédagogie, de patience et de gentillesse. Ses encouragements constants nous ont bien aidés à persévérer face aux difficultés. Je ne sais pas comment aurait fini ce doctorat sans sa contribution inestimable, car comme dirait Baudouin: “le diable est dans les détails”.

Je remercie l’entreprise Siemens Healthcare, désormais Healthineers, ainsi que l’Agence Nationale de la Recherche et de la Technologie (ANRT) pour leur soutien financier via le programme CIFRE. Un grand merci à Matthieu Lepetit-Coiffé, ingénieur application Siemens à Bordeaux, qui m’a aidée à trouver ma place au sein de cette entreprise et qui m’a toujours soutenue tout au long de cette thèse, et même après. Sa connaissance des méthodes d’acquisition IRM et sa force tranquille ont grandement contribué à la réussite de cette thèse. Je le remercie de m’avoir formée à l’IRM cardiaque avec autant de patience et d’avoir toujours répondu présent pour les expérimentations animales, me libérant d’une bonne dose de stress. Je remercie Agnès Malgouyres et Christian Bert pour m’avoir encadrée au sein de Siemens, ainsi qu’Andrea Plank pour son efficacité dans la gestion administrative, qui facilite la vie de beaucoup d’étudiants

CIFRE. Je vous remercie de m'avoir permis de voyager pour présenter mon travail: à Milan, à Edimbourg, à Singapour et enfin à Baltimore. Je remercie également Arne Hengerer pour m'avoir accueillie au sein de son équipe "Advanced Therapy" à Erlangen. Je remercie Rainer Schneider, Dirk Franger et Eva Rothgang avec qui j'ai partagé ces quelques jours de travail et de "Bier Garten".

Un grand merci à Virginie Loyer et Delphine Vieillot, qui ont la très lourde charge de s'occuper des gros animaux lors des expérimentations de l'institut. Ça a été un vrai plaisir de travailler avec elles, toujours dans la bonne humeur. Je remercie également Pierre Jaïs et Arnaud Chaumeil, cardiologues spécialisés en rythmologie cardiaque au CHU de Bordeaux, qui ont trouvé le temps de venir nous assister dans le positionnement des cathéters lors des expérimentations animales. Ce fut l'occasion d'échanges très enrichissants qui nous rapprochent un peu plus du monde clinique.

Je remercie également Jacques Felblinger, Michel de Mathelin et Christopher Piorkowski pour avoir accepté avec enthousiasme de faire partie de mon jury de thèse.

Je remercie ma maman, Malou, mon papa, Christian, et ma sœur Morgane, qui m'ont toujours poussée à me dépasser et à croire en moi. Je remercie ma "Mamie Vet", 99 ans, dont l'intelligence vive aurait mérité bien des diplômes comme celui-ci. Je pense également à tous mes autres grands-parents et à ma marraine Liliane qui auraient été fiers de moi.

Merci de tout mon cœur à Thomas pour son soutien et pour tout le bonheur qu'il m'apporte chaque jour.





# Contents

<b>Abbreviations</b>	<b>13</b>
<b>List of Figures</b>	<b>15</b>
<b>1 Introduction</b>	<b>19</b>
1.1 Cardiac arrhythmia . . . . .	19
1.1.1 Atrial fibrillation . . . . .	20
1.1.2 Ventricular tachycardia . . . . .	21
1.2 Radiofrequency ablation . . . . .	21
1.3 Monitoring of radiofrequency ablation . . . . .	22
1.3.1 Electrode temperature monitoring . . . . .	23
1.3.2 Circuit impedance monitoring . . . . .	23
1.3.3 Electrogram amplitude monitoring . . . . .	24
1.3.4 Contact force monitoring . . . . .	24
1.4 Objectives of this thesis . . . . .	25
1.5 References . . . . .	26
<b>2 Challenges of cardiac Magnetic Resonance thermometry</b>	<b>31</b>
2.1 Principles of Magnetic Resonance thermometry . . . . .	32
2.1.1 Proton Resonance Frequency shift method . . . . .	32
2.1.2 Precision of temperature measurement . . . . .	33
2.1.3 MR dosimetry . . . . .	34
2.2 Fast pulse sequence imaging . . . . .	35
2.2.1 Single-shot Echo Planar Imaging . . . . .	35
2.2.2 Parallel imaging . . . . .	36
2.3 Heart motion . . . . .	39
2.3.1 Effects of heart motion . . . . .	39
2.3.2 MR acquisition methods for compensation of heart-induced motion . . . . .	39
2.3.3 MR acquisition methods for compensation of respiratory-induced motion . . . . .	40
2.3.4 Post-processing methods for in-plane motion compensation . . . . .	44
2.4 Correction of motion-induced $B_0$ changes . . . . .	47
2.4.1 Multi-baseline approach . . . . .	47
2.4.2 Principal Component Analysis (PCA)-based phase modeling approach . . . . .	48
2.4.3 Referenceless approach . . . . .	50

2.4.4	Discussion . . . . .	51
2.5	State-of-the-art of cardiac MR thermometry . . . . .	52
2.6	References . . . . .	54
<b>3</b>	<b>Improved Cardiac Magnetic Resonance Thermometry and Dosimetry for Monitoring Lesion Formation During Catheter Ablation</b>	<b>59</b>
3.1	Preamble . . . . .	60
3.2	Abstract . . . . .	60
3.3	Introduction . . . . .	61
3.4	Methods . . . . .	62
3.4.1	Volunteer study . . . . .	62
3.4.2	Animal study . . . . .	63
3.4.3	RF ablation device and MR-Compatible EP . . . . .	63
3.4.4	Magnetic resonance data acquisition . . . . .	64
3.4.5	Thermometry pipeline . . . . .	65
3.4.6	Image registration . . . . .	65
3.4.7	Correction of respiratory-induced susceptibility changes . . . . .	65
3.4.8	Spatio-temporal phase-drift correction . . . . .	66
3.4.9	Temporal temperature filtering . . . . .	67
3.4.10	Thermal dose calculation . . . . .	67
3.4.11	Statistical analysis . . . . .	67
3.5	Results . . . . .	68
3.5.1	Volunteer temperature imaging . . . . .	68
3.5.2	In vivo RF ablation of the LV in a Sheep . . . . .	70
3.6	Discussion . . . . .	74
3.6.1	Study limitations . . . . .	76
3.7	Conclusions . . . . .	76
3.8	References . . . . .	77
3.9	Technical and practical implementation . . . . .	80
3.9.1	Gadgetron . . . . .	80
3.9.2	Hardware . . . . .	80
3.9.3	Temporal phase unwrapping . . . . .	82
3.9.4	PCA-based implementation for calculation of synthetic background phase	83
<b>4</b>	<b>Combination of Principal Component Analysis and optical-flow motion compensation for improved cardiac MR thermometry</b>	<b>85</b>
4.1	Preamble . . . . .	86
4.2	Abstract . . . . .	86
4.3	Introduction . . . . .	87
4.4	Methods . . . . .	88
4.4.1	MR Thermometry imaging protocol . . . . .	88
4.4.2	Image registration . . . . .	89
4.4.3	Thermometry mapping . . . . .	90

4.4.4	Volunteer study . . . . .	91
4.4.5	Phantom study . . . . .	91
4.4.6	In vivo ablation in the left ventricle of a sheep . . . . .	92
4.5	Results . . . . .	93
4.5.1	Volunteer study . . . . .	93
4.5.2	Phantom study . . . . .	94
4.5.3	In vivo ablation in the left ventricle of a sheep . . . . .	99
4.6	Discussion . . . . .	99
4.7	Conclusion . . . . .	102
4.8	References . . . . .	102
<b>5</b>	<b>Feasibility of real-time MR thermal dose mapping for predicting radiofrequency ablation outcome in the myocardium in vivo</b>	<b>105</b>
5.1	Preamble . . . . .	106
5.2	Abstract . . . . .	107
5.3	Introduction . . . . .	107
5.4	Methods . . . . .	108
5.4.1	Volunteer study . . . . .	108
5.4.2	Animal study . . . . .	108
5.4.3	Radiofrequency ablation device . . . . .	109
5.4.4	Imaging protocol . . . . .	109
5.4.5	MR thermometry pipeline . . . . .	110
5.4.6	Post-ablation visualization . . . . .	113
5.4.7	Macroscopic examination and lesion size measurements . . . . .	113
5.5	Results . . . . .	113
5.5.1	Volunteer study . . . . .	113
5.5.2	In vivo radiofrequency ablations monitoring . . . . .	116
5.5.3	Post-ablation lesion size measurements . . . . .	117
5.6	Discussion . . . . .	119
5.6.1	Limitations . . . . .	121
5.7	Conclusion . . . . .	122
5.8	References . . . . .	122
5.9	Tips and tricks of MR-guided RF ablation in vivo . . . . .	126
5.9.1	Arrhythmia and pacing . . . . .	126
5.9.2	ECG-triggering . . . . .	126
5.9.3	Precise localisation of the catheter tip . . . . .	126
5.9.4	Radiofrequency ablation . . . . .	126
5.9.5	EP recording . . . . .	127
<b>6</b>	<b>Active catheter tracking for improved cardiac MR thermometry</b>	<b>129</b>
6.1	Preamble . . . . .	129
6.2	Abstract . . . . .	130
6.3	Introduction . . . . .	130

6.4	Methods . . . . .	132
6.4.1	Imaging protocol . . . . .	132
6.4.2	MR thermometry processing . . . . .	132
6.4.3	Phantom experiments with catheter ablation . . . . .	133
6.5	Results . . . . .	134
6.6	Discussion . . . . .	137
6.7	Conclusion . . . . .	138
6.8	References . . . . .	138
<b>7</b>	<b>Concluding discussion and project perspectives</b>	<b>141</b>
7.1	Progress related to this PhD thesis . . . . .	141
7.1.1	Real-time implementation of a fast cardiac MR thermometry and dosimetry pipeline . . . . .	142
7.1.2	Implementation of fast MR thermometry pulse sequences . . . . .	142
7.1.3	Improvement of motion estimation and compensation applied to catheter RF ablation . . . . .	142
7.2	Perspectives . . . . .	143
7.2.1	Atrial MR thermometry . . . . .	143
7.2.2	Automatic temperature control . . . . .	146
7.2.3	Cardiac MR thermometry on arrhythmic patients . . . . .	147
7.2.4	Simultaneous Multi-Slice (SMS) MR Thermometry . . . . .	147
7.3	References . . . . .	148
	<b>Summary</b>	<b>151</b>
	<b>Résumé</b>	<b>155</b>
	<b>Publications</b>	<b>161</b>

# Abbreviations

*2D* Two dimensional

*3D* Three dimensional

## Cardiac arrhythmia

*AF* Atrial fibrillation

*AV* Atrioventricular

*bpm* Beats per minute

*ECG* Surface electrocardiogram

*EGM* Intracardiac electrogram

*EP* Electrophysiology

*ICD* Implantable cardioverter-defibrillator

*LV* Left ventricle

*RF* Radiofrequency

*RV* Right ventricle

*SCD* Sudden cardiac death

## MR imaging

*ACS* Autocalibration signal

*b – SSFP* Balanced Steady State Free Precession

*EPI* Echo planar imaging

*FA* Flip angle

*FOV* Field of view

*Gd* Gadolinium

*GRE* Gradient recalled echo

*IR* Inversion recovery

*MRI* Magnetic resonance imaging

*SMS* Simultaneous multi-slice

*T1 – w* T1 weighted

*T<sub>1</sub>* Longitudinal relaxation time

*T<sub>2</sub>* Transversal relaxation time

*TE* Echo time

*TI* Inversion time

*TR* Repetition time

## Motion estimation

*H&S* Horn and Schunck

*I* Image intensity

*u* Horizontal component of motion

*v* Vertical component of motion

## Statistical analysis

*μ<sub>T</sub>* Temporal mean of temperature

*σ<sub>T</sub>* Temporal standard deviation of temperature

*CNR* Contrast-to-noise ratio

*R* Pearson's correlation coefficient

*ROI* Region of interest

*SD* Standard deviation

*SNR* Signal-to-noise ratio

## Thermometry

*α<sub>PRF</sub>* PRF coefficient

*γ* Gyromagnetic ratio

*φ* Current phase image

*φ<sub>REF</sub>* Phase image of reference

*B<sub>j</sub>* *j<sup>th</sup>* PCA eigen vector

*D<sub>j</sub>* *j<sup>th</sup>* Motion descriptor

*HIFU* High intensity focused ultrasound

*LUT* Look-up table

*PCA* Principal component analysis

*PRF* Proton resonance frequency

*SVD* Singular value decomposition

*TD* Thermal dose



# List of Figures

1.1	Electrical conduction system of the normal heart. . . . .	20
1.2	Radiofrequency ablation for the treatment of cardiac arrhythmia. . . . .	21
1.3	Set-up commonly used for RF ablation . . . . .	23
2.1	Basic principle of PRF thermometry method on a static phantom . . . . .	32
2.2	Experimental noise on the phase of the transverse magnetisation vector . . . . .	33
2.3	Evaluation of MR thermometry performance. . . . .	34
2.4	Timing diagram for the blipped EPI sequence and the resulting trajectory in the k-space. . . . .	36
2.5	SENSE parallel imaging . . . . .	37
2.6	Spatial aliasing and SENSE reconstruction . . . . .	38
2.7	GRAPPA reconstruction method . . . . .	38
2.8	ECG-gated imaging. . . . .	39
2.9	ECG-gating acquisition in case of cardiac arrhythmia. . . . .	40
2.10	Crossed-pair echo-navigator positioning. . . . .	41
2.11	Respiratory-gated MR acquisition . . . . .	41
2.12	Rejection of data acquisition outside a user-defined window during respiratory-gated MR acquisition . . . . .	42
2.13	Echo-navigator based slice following technique . . . . .	42
2.14	Examples of basic transformations . . . . .	44
2.15	Optical-flow motion estimation . . . . .	45
2.16	Multi-resolution scheme of optical-flow motion estimation . . . . .	45
2.17	Illustration of the fidelity term of Horn and Schunck (H&S) and Black and Anandan (B&A) optical-flow algorithms . . . . .	46
2.18	Respiratory-induced susceptibility artifacts . . . . .	47
2.19	Diagram of multi-baseline approach for correction of motion-induced susceptibility artifacts with moving phantom data. . . . .	48
2.20	Diagram of the PCA-based phase modeling approach for correction of motion-induced susceptibility artifacts. . . . .	50
2.21	MR thermometry results of RF ablation on a sheep's LV . . . . .	53
3.1	Real-time cardiac magnetic resonance thermometry pipeline. . . . .	64
3.2	Thermometry evaluation on a human volunteer measured at $1.6 \times 1.6 \times 3 \text{ mm}^3$ resolution using the PCA-based method . . . . .	69

3.3	Statistics on 10 healthy volunteers during free-breathing acquisition. . . . .	70
3.4	MR thermometry monitoring during RF ablation at 26 W on the left ventricle. .	71
3.5	Contact electrograms acquired during radiofrequency ablation in sheep. . . . .	73
3.6	Cumulative thermal dose images and gross pathology results for two RF ablations	73
3.7	Integration of Gadgetron framework with a Siemens scanner . . . . .	80
3.8	Biosense Webster catheter . . . . .	81
3.9	Example of artifacts that can occur during RF ablation . . . . .	81
3.10	Hardware design for simultaneous RF ablation and MR thermometry. . . . .	81
3.11	Temporal phase unwrapping . . . . .	82
3.12	Matrix for PCA . . . . .	83
4.1	Calibration of Horn and Schunck (H&S) and PCA-based H&S optical-flow algo- rithms. . . . .	93
4.2	Temperature standard deviation ( $\sigma_T$ ) for both optical-flow methods applied to MR temperature images from free-breathing volunteers. . . . .	94
4.3	Simulation of a local signal decrease on the magnitude image of an agar gel phantom (A) centered on the catheter position. . . . .	95
4.4	Experimental data obtained on a static agar gel phantom. . . . .	96
4.5	Experimental data obtained on an agar gel phantom. . . . .	97
4.6	Simulation of a local signal decrease on the magnitude image in sagittal orien- tation of a sheep LV (A) with a MR-compatible catheter inside (yellow arrow) .	98
4.7	Experimental results of RF ablation under MR temperature imaging in a sheep.	100
5.1	Imaging protocol for catheter navigation (A-D) and fast MR thermometry (E-G) for ablation monitoring. . . . .	111
5.2	MR thermometry evaluation on 5 healthy volunteers in short axis view. . . . .	114
5.3	Real-time MR thermometry during RF ablation in vivo on a sheep LV. . . . .	115
5.4	Endocardial bipolar signal recorded at the tip of the MR-compatible ablation catheter in the LV of a sheep. . . . .	116
5.5	Comparison of lesion dimensions of one representative RF ablation between post- ablation T1-w 3D images (A, C and E), real-time TD map (B) and macroscopic observations with TTC staining (D and F). . . . .	118
5.6	RF lesion dimensions ( $N = 12$ lesions) correlation between measurements on real-time thermal dose maps, post-ablation T1-w images and gross pathology. .	119
6.1	Active catheter tracking interleaved with the MR thermometry imaging pulse sequence. . . . .	133
6.2	Correction of susceptibility artifacts based on the catheter tip position. . . . .	135
6.3	Evaluation of temporal accuracy of MR thermometry on a moving phantom using active catheter tracking. . . . .	136
6.4	Simultaneous monitoring of a RF heating (4 W for 20 s) and catheter tracking on a moving phantom. . . . .	137
7.1	Temperature stability on the atria of a free-breathing volunteer. . . . .	143

7.2 Illustration of endovascular imaging using the coils of the catheter. . . . . 144

7.3 Temperature stability obtained using catheter’s tip micro-coil as imaging coil in  
a static phantom made of agar gel. . . . . 145

7.4 Automatic temperature control during RF ablation . . . . . 146



# Chapter 1

## Introduction

### Contents

---

<b>1.1 Cardiac arrhythmia</b> . . . . .	<b>19</b>
1.1.1 Atrial fibrillation . . . . .	20
1.1.2 Ventricular tachycardia . . . . .	21
<b>1.2 Radiofrequency ablation</b> . . . . .	<b>21</b>
<b>1.3 Monitoring of radiofrequency ablation</b> . . . . .	<b>22</b>
1.3.1 Electrode temperature monitoring . . . . .	23
1.3.2 Circuit impedance monitoring . . . . .	23
1.3.3 Electrogram amplitude monitoring . . . . .	24
1.3.4 Contact force monitoring . . . . .	24
<b>1.4 Objectives of this thesis</b> . . . . .	<b>25</b>
<b>1.5 References</b> . . . . .	<b>26</b>

---

### 1.1 Cardiac arrhythmia

Cardiac arrhythmias occur when the propagation of the electrical impulses that coordinate the mechanical contraction become abnormal. The normal activation sequence of the myocardium is described in Figure 1.1. The electrocardiogram (ECG) records the electrical signals as they travel through the heart. Each wave of the ECG corresponds to a certain event in the cardiac cycle. The conduction system starts in the sinus node, a small area of tissue in the right atrium, which spreads a depolarization wave over the atrium to the atrioventricular (AV) node. This event is called the P-wave. The electrical signal then propagates from the AV over the His-Purkinje system to trigger ventricular contraction (QRS complex). Finally electrical re-polarisation of the ventricular cells is associated to the T wave that corresponds to the ventricular relaxation.

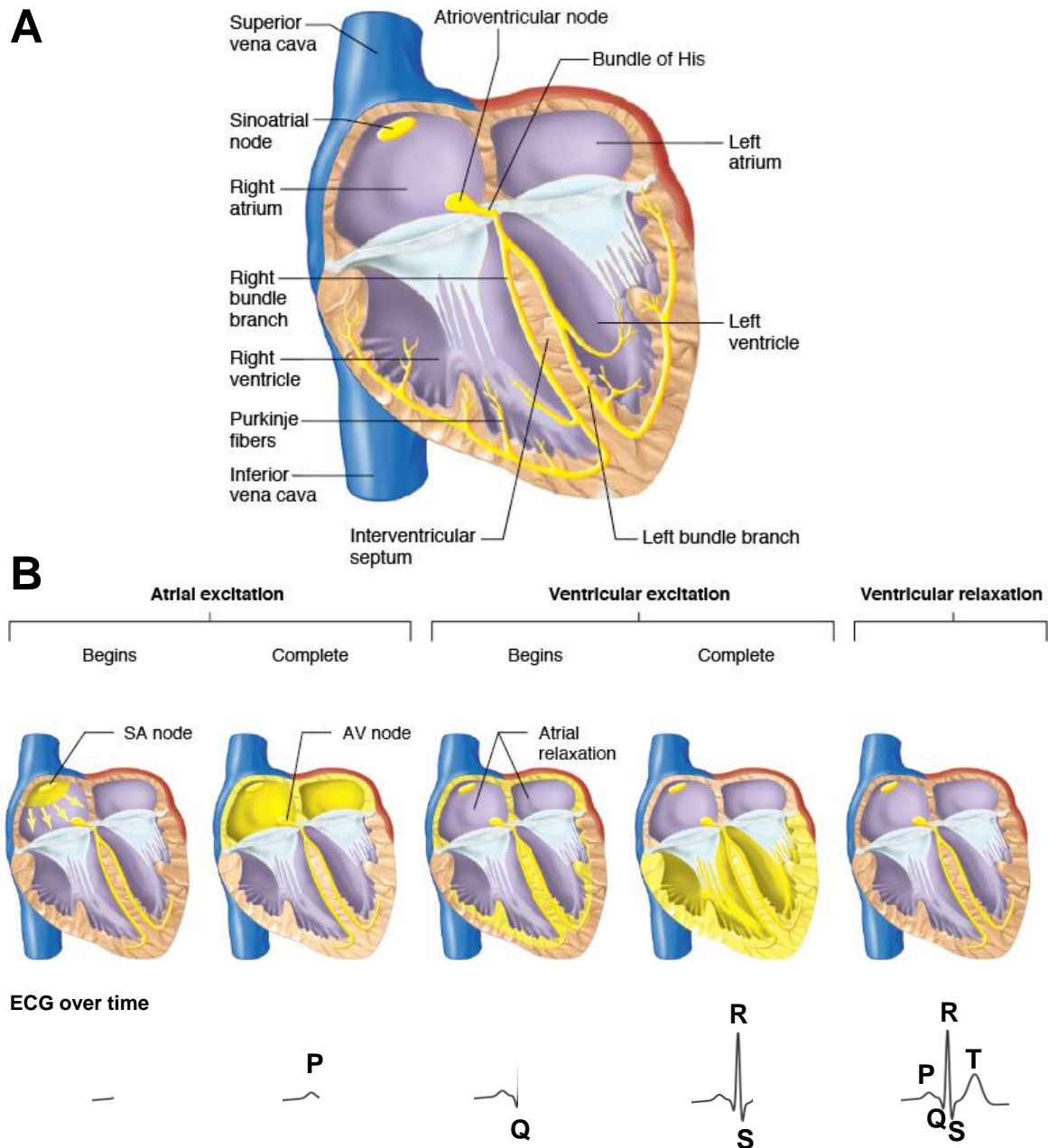


Figure 1.1: Electrical conduction system of the normal heart. (A) Healthy heart anatomy showing the components of the conduction system in yellow. (B) Evolution of the normal conduction system over the cardiac cycle. Each wave of the ECG corresponds to a certain event of the cardiac electrical cycle. (Modified from [www.accessmedicine.com](http://www.accessmedicine.com), The McGraw-Hill Companies)

### 1.1.1 Atrial fibrillation

Atrial fibrillation (AF) being the most common form of cardiac arrhythmia, affects 750,000 people in France and is expected to increase 2.5 fold by 2050 [1]. AF confers a 2.5 fold risk of stroke and 20% of all strokes are attributable to AF [2]. In addition, AF is associated with a 3 fold higher risk of heart failure [2], 2 to 3 times higher likelihood of hospitalization and twice the mortality risk. AF was discovered to be mainly triggered by ectopic foci from the pulmonary veins [3].

### 1.1.2 Ventricular tachycardia

30,000-50,000 sudden cardiac deaths (SCD) are observed in France every year and 300,000-400,000 in the United States [4]. The most common cause of SCD appears to be induced by ventricular tachycardia (VT). In VT, an abnormal acceleration of ventricular rate from 120 to 300 beats per minute (bpm) is observed with no coordination with the atria. If the heart rate increases to more than 300 bpm, VT deteriorates into a ventricular fibrillation that may result in SCD. VT occurs most commonly in patients with a history of myocardial infarction. Scar tissue and fibrosis can interfere with the normal electrical impulse and lead to promoting reentry circuits that can generate ventricular arrhythmia.

## 1.2 Radiofrequency ablation

The common first-line therapeutic approach to treat arrhythmia is the administration of anti-arrhythmic drugs [3] associated with the implantation of a cardioverter-defibrillator (ICD) in patients presenting with prior myocardial infarction. The ICD device administers an electrical discharge to the heart wall and restores the sinus rhythm. It is followed by drug therapy to prevent recurrence of arrhythmia. Although cardioversion therapy has been shown to reduce the risk of SCD, the occurrence of shocks in implanted patients is associated with an altered quality of life, a progression in heart failure symptoms and an increased mortality [5, 6]. Despite a high success rate of effective electrical cardioversion (70% to 90%) [7, 8], less than half of the patients remained in sinus rhythm after one year.

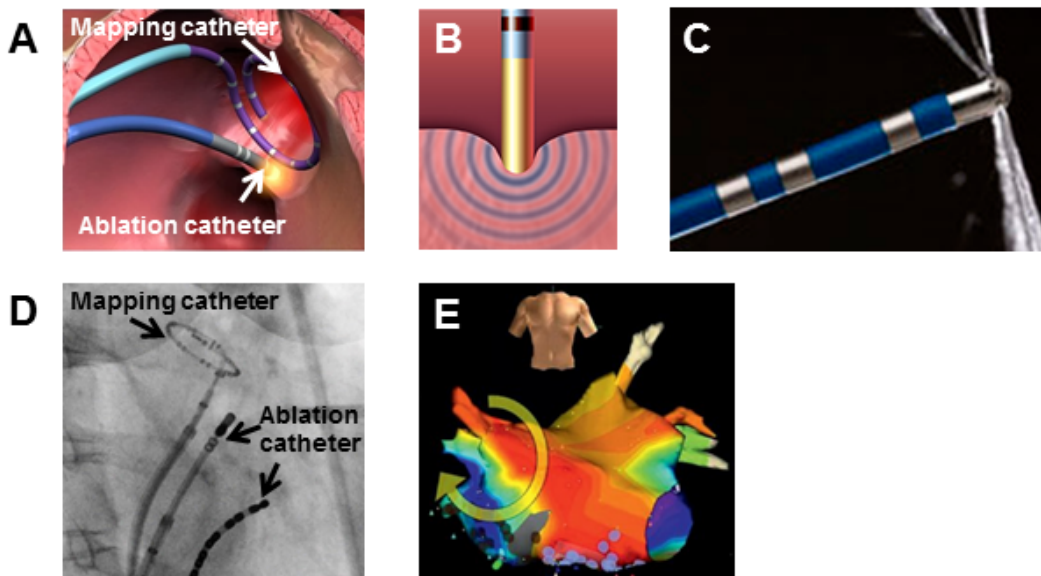


Figure 1.2: Radiofrequency ablation for the treatment of cardiac arrhythmia. (A) For pulmonary veins isolation, a “lasso” catheter is used to proceed to electro-anatomic mapping of the electrical signal in the left atrium. An ablation catheter (B) is used to induce a thermal lesion and isolate abnormal conduction circuit. (C) Example of an irrigated catheter with continuous saline flow ejected from a series of holes at the distal tip of the catheter. (D) Fluoroscopic images showing diagnostic and ablation catheters commonly used for RF ablation procedure. (E) Electro-anatomic map of the left atria using a dedicated clinical software (NavX, St Jude Medical, St Paul, MI, U.S.A.)

Therefore, radiofrequency (RF) ablation has been proposed as a new therapeutic approach. RF energy is applied at the tip of a catheter to induce a necrosis of the targeted cardiac tissue. Critical sites are thus electrically isolated or cauterized to restore a normal conduction. Catheter ablation procedures take place in an electrophysiology (EP) clinical unit, where both diagnosis and ablation are achieved. Catheters are usually inserted through femoral vein and positioned within the heart for intracardiac electrogram (EGM) recording at critical sites. Electro-anatomic mapping is achieved using mapping catheters (Figure 1.2-A,D) and rendered on a dedicated software (Figure 1.2-E) such as NavX (St Jude Medical, St Paul, MI, U.S.A.) or CARTO (Biosense Webster, Diamond Bar, CA, U.S.A.). The therapeutic efficacy of the ablation highly depends on the identification of the site of origin of the arrhythmia. The identification of the trigger sites of AF by Haissaguerre et al. [3] lead for instance to the first successful RF ablation by isolating the arrhythmogenic tissue around the pulmonary veins in the left atrium. Once the site is identified, an ablation catheter is positioned at that location in contact with the myocardium to proceed to the ablation by sending a RF energy for 30-60 s (Figure 1.2-B). The typical RF frequency used for clinical RF ablation is around 500 kHz.

Although RF ablation has become a reference treatment, a significant recurrence rate of arrhythmia is observed: up to 30% of the patients for AF [9] and 37% for VT [10], often requiring redo procedures. Arrhythmia recurrence is mainly caused by incomplete electrical isolation of pathological tissue or by recovery of conduction of previously isolated circuit. The ability to create transmural and permanent lesions is thus of high importance to ensure a durable treatment of the arrhythmia [11]. An optimal RF energy must be delivered to ensure a complete cell destruction of the arrhythmogenic substrate without producing collateral injury, such as atrioesophageal fistulas and tamponade. Typical RF power applied in clinical practice are  $\sim 30$  W without irrigation, and  $>50$  W with irrigated catheter to compensate for the flow cooling.

Ablation procedures are routinely performed under X-ray fluoroscopy guidance, which allows a rapid update of the image (from 10 to 30 frames per second) while navigating the catheter (Figure 1.2-D). X-ray imaging provides essential anatomical information for guidance of catheter positioning but cannot be used for monitoring due to a limited access to tissue information. In addition, limitations in radiation dose are problematic for time-consuming interventions and for paediatric use. Surrogates have been proposed for assessing the completeness of the ablation such as the circuit impedance, the catheter-tip temperature, EGM amplitude and electrode/tissue contact-force.

### 1.3 Monitoring of radiofrequency ablation

One major challenge of RF ablation is the prediction of the size of tissue injury to ensure the efficacy and the safety of the procedure. Catheter orientation, cavities blood flow and catheter/tissue contact are the main factors that significantly influence the created lesion size. Because of the variability of these factors in vivo, energy and duration of the RF delivery remain poor predictors of the final lesion extent.

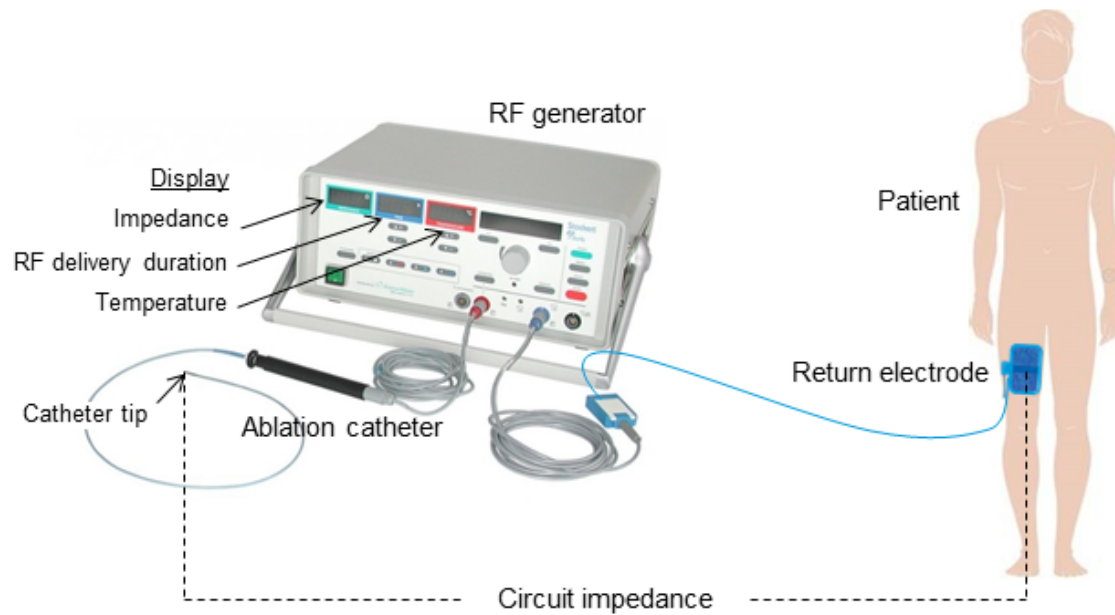


Figure 1.3: Set-up commonly used for RF ablation. The RF current is sent between the ablation catheter tip and a return electrode placed on patient's skin. The circuit impedance is measured and displayed in real-time, as well as the RF delivery duration, power and voltage. If a temperature probe is embedded into the catheter, the temperature of the catheter tip can be displayed. (Source: Stockert)

Figure 1.3 schematizes the clinical set-up commonly used to perform a RF ablation. The RF generator sends an alternative RF current between the catheter tip and a return electrode positioned on patient's skin. The circuit impedance and the parameters of the ablation (power, voltage and duration) are displayed in real-time. The temperature of the catheter tip can also be displayed if the catheter is equipped with a temperature sensor.

### 1.3.1 Electrode temperature monitoring

Temperature sensors were integrated in catheter to monitor the effect of the RF delivery and to prevent coagulum formation. The catheter electrode is not directly heated by the RF energy but by the heated tissue in contact. However, tissue temperature was shown to be significantly higher than the catheter tip temperature due to blood cooling at the tissue surface [12, 13]. Tip-electrode cooling with saline flow (Figure 1.2-C, irrigated catheter) increases even more the risk of tissue overheating. Once the tissue temperature exceeds  $100^{\circ}\text{C}$ , sudden boiling may result in steam formation with subsequent disruption of the myocardial tissue, so-called "pop". These steam pops can cause a perforation especially in thin-walled structures such as the atria. Even if the electrode temperature does not reflect the tissue temperature, electrode temperature feedback may reduce the risk of excessive tissue heating, boiling and wall rupture [11]. However, catheter tip temperature remains poorly correlated to lesion size in vivo.

### 1.3.2 Circuit impedance monitoring

Since electrode temperature monitoring does not directly reflect tissue temperature, surrogate measures have been proposed such as circuit impedance [14]. Impedance is measured through the patient between the catheter tip electrode and the return electrode (Figure 1.3). A decrease

in impedance in the range from 10 to 15  $\Omega$  can be observed during significant RF heating, because of an increase in the mobility of the ions in the tissue with temperature [15]. Absence of impedance drop may indicate inadequate energy delivery due for example to poor catheter-tissue contact. Impedance monitoring can also be used to increase the safety of the procedure [16, 17] by reducing the likelihood of steam pop and associated perforation risk, that have been reported to be followed by a sudden rise in impedance. If impedance control improves the safety of the procedure, it remains a gross measurement that cannot be used to predict the final volume of myocardial necrosis.

### 1.3.3 Electrogram amplitude monitoring

Ablation procedure can also be monitored using EGM amplitude as a marker of the effectiveness of the ablation. As tissue heating causes a decrease of the electrical activity, the amplitude of local EGM recorded at the tip of the catheter decreases during the ablation. A reduction of 50 % in the EGM amplitude can be used in clinical practice as the cut-off point to stop the ablation. No significant reduction of the EGM amplitude or loss of tissue excitability during pacing can be useful indicators of failure of the ablation. However, the EGM amplitude can be affected by a poor catheter/tissue contact and do not directly correlate with the tissue temperature.

### 1.3.4 Contact force monitoring

Since the temperature probe monitoring has become less pertinent with the use of irrigated catheter, additional monitoring of the contact force information was of high interest to create more predictable and reproducible RF lesions. A poor electrode-tissue contact may lead to a low fraction of RF energy effectively delivered to the myocardium.

Recent development of contact force sensing technology provides now real-time feedback of the contact force between the catheter tip and the myocardium. Two different technologies are clinically available: the TactiCath (Endosense/St Jude Medical, St Paul, MI, U.S.A.) catheter that uses three optical fibers to measure deformation of a deformable body in the distal tip of the catheter [18], and the Thermocool Smartouch (Biosense Webster, Diamond Bar, CA, U.S.A.) catheter that uses a small spring connecting the tip electrode to a magnetic transmitter and sensors to measure microdeflection of the spring [19]. Lesion size was shown to be dependent on contact force: greater contact force (30-40 g) produces larger lesions, but increases as well the frequency of steam pop and thrombus formation [18]. The use of contact force sensing technology was evaluated in a multicenter study (TOuCh for CATHeter Ablation – TOCCATA) during pulmonary veins isolation for treatment of AF [20]. The efficacy of the procedure (no recurrence of AF at 12 months) was found to be well correlated with contact force greater than 20 g.

Contact force sensing technology provides a fundamental information for the acquisition of reliable electro-mapping and achievement of ablation lesions, by assuring stable and optimal tissue contact. Further long-term studies are necessary to investigate the improvement in the outcomes of RF ablation. The important hurdle to be overcome remains the visualization of lesion creation during the procedure.

## 1.4 Objectives of this thesis

Significant progress have been done worldwide for the monitoring of catheter RF ablation by increasing number and complexity of sensors embedded in the catheters. However, none of the existing measurements highly correlate with tissue temperature at distance from the contact point of the catheter electrode and thus hardly reflect the final lesion size. Up to now there is a clear lack of lesion formation imaging during the procedure, although RF ablation has become an accepted curative therapy for the treatment of cardiac arrhythmia. X-Ray fluoroscopy remains the reference imaging modality for navigating catheters in cardiac chambers for electrical mapping and delivery of therapeutic RF ablation. However, the intrinsic poor soft tissue contrast of this modality does not allow visualization of myocardial injury.

Magnetic Resonance Imaging (MRI) is nowadays extending from diagnosis to the field of real-time monitoring of therapeutic procedures. In the field of catheter-based RF ablation, most research have focused on pre-ablation arrhythmogenic substrate assessment (scar tissue, fibrosis) [21] and post-ablation lesion characterization [22, 23]. Recent technical advances in MR-compatible catheters permit the emergence of MR-guided catheterization procedures using either passive [24–30] or active [31, 32] catheter tracking for device visualization and location, based on catheter material or on MR receivers embedded into the catheter, respectively. However, no monitoring of lesion formation was performed during RF ablation.

MR thermometry is a non-invasive method to measure the local temperature distribution in tissue during RF energy delivery. This technique is increasingly studies to monitor thermal ablations in various organs: treatment of uterine fibroids [33], prostate cancer [34], liver cancer [35], brain tumours [36]. From quantitative temperature maps, the cumulative thermal dose (TD) can be computed from temperature rise and duration of heating. This metric has been shown to be relevant to predict the final lesion extent, for instance during RF ablation of liver tumours [35].

Cardiac MR thermometry remains very challenging because of the complex motion of the heart (due to contraction and breathing). Preliminary studies demonstrated the technical feasibility of MR thermometry on the heart [37–39] and opened perspectives for real-time guidance of RF ablations. However, the spatial and temporal resolutions of the MR pulse sequence, image processing and catheter technologies need to be improved in order to provide physicians with reliable and quantitative information. To precisely monitor the formation of typical RF lesions (in the range from 3 to 10 millimetres large), cardiac MR temperature images require an improvement in spatial resolution, in order to reach an ideal voxel size of  $1 \times 1 \times 1 \text{ mm}^3$ , while maintaining a high temporal resolution. An adequate update time is necessary to characterize significant change in temperature during RF heating. To precisely map a RF delivery of 30-60 seconds-long, a temporal resolution of  $\sim 1\text{s}$  or less is required. Such an acceleration and a reduction of the voxel size comes at the cost of signal-to-noise ratio (SNR), which directly impacts the temperature uncertainty [40]. With a typical tissue temperature rise higher than  $20^\circ\text{C}$ , temperature precision must be in the range of 1 to  $2^\circ\text{C}$  to allow a precise calculation of the delivered TD and prediction of the therapy outcome. These requirements represent important

technical challenges that must be overcome to ensure a robust, reliable and precise real-time cardiac MR thermometry.

This thesis focuses on new developments for real-time monitoring of RF ablation using cardiac MR thermometry. The manuscript is structured as follows:

- In Chapter 2, the first part presents the challenges and state-of-the-art of performing MR thermometry on a mobile organ, such as the heart.
- In Chapter 3, a complete cardiac MR thermometry pipeline is described, including fast MR acquisition sequence, real-time motion compensation and artifacts correction.
- Chapter 4 proposes to evaluate a robust motion estimation approach to address the issue of intensity variation on magnitude images associated with RF heating, that can significantly bias the calculated motion.
- In Chapter 5, MR thermometry method implemented in Chapter 3 was improved by performing a dynamic update of the slice position depending on the respiratory motion. In vivo validation was conducted in both ventricles of healthy volunteers without heating and in sheep during RF ablation in left ventricle (LV). The feasibility of using thermal dose mapping to estimate the lesion extent is demonstrated.
- In the last part, Chapter 6 proposes to combine active catheter tracking and MR thermometry to update the slice position on the catheter which is directly affected by motion. Preliminary results are presented on a moving phantom.

## 1.5 References

1. Charlemagne, A. *et al.* Epidemiology of atrial fibrillation in France: Extrapolation of international epidemiological data to France and analysis of French hospitalization data. en. *Archives of Cardiovascular Diseases* **104**, 115–124. ISSN: 18752136 (Feb. 2011).
2. Krahn, A. D., Manfreda, J., Tate, R. B., Mathewson, F. A. & Cuddy, T. E. The natural history of atrial fibrillation: Incidence, risk factors, and prognosis in the manitoba follow-up study. en. *The American Journal of Medicine* **98**, 476–484. ISSN: 00029343 (May 1995).
3. Haïssaguerre, M. *et al.* Spontaneous Initiation of Atrial Fibrillation by Ectopic Beats Originating in the Pulmonary Veins. en. *New England Journal of Medicine* **339**, 659–666. ISSN: 0028-4793, 1533-4406 (Sept. 1998).
4. Rubart, M. Mechanisms of sudden cardiac death. en. *Journal of Clinical Investigation* **115**, 2305–2315. ISSN: 0021-9738 (Aug. 2005).
5. Bilge, A. K. *et al.* Depression and Anxiety Status of Patients with Implantable Cardioverter Defibrillator and Precipitating Factors. en. *Pacing and Clinical Electrophysiology* **29**, 619–626. ISSN: 0147-8389, 1540-8159 (June 2006).

6. Larsen, G. K., Evans, J., Lambert, W. E., Chen, Y. & Raitt, M. H. Shocks burden and increased mortality in implantable cardioverter-defibrillator patients. en. *Heart Rhythm* **8**, 1881–1886. ISSN: 15475271 (Dec. 2011).
7. Van Gelder, I. C., Crijns, H. J., Van Gilst, W. H., Verwer, R. & Lie, K. I. Prediction of uneventful cardioversion and maintenance of sinus rhythm from direct-current electrical cardioversion of chronic atrial fibrillation and flutter. en. *The American Journal of Cardiology* **68**, 41–46. ISSN: 00029149 (July 1991).
8. Södermark, T. *et al.* Effect of quinidine on maintaining sinus rhythm after conversion of atrial fibrillation or flutter. A multicentre study from Stockholm. *British heart journal* **37**, 486–492 (1975).
9. Ganesan, A. N. *et al.* Long-term outcomes of catheter ablation of atrial fibrillation: a systematic review and meta-analysis. *Journal of the American Heart Association* **2**, e004549 (2013).
10. Tanner, H. *et al.* Catheter Ablation of Recurrent Scar-Related Ventricular Tachycardia Using Electroanatomical Mapping and Irrigated Ablation Technology: Results of the Prospective Multicenter Euro-VT-Study. en. *Journal of Cardiovascular Electrophysiology* **21**, 47–53. ISSN: 10453873, 15408167 (Jan. 2010).
11. Wittkamp, F. H. & NAKAGAWA, H. RF catheter ablation: lessons on lesions. *Pacing and Clinical Electrophysiology* **29**, 1285–1297 (2006).
12. Kongsgaard, E., Steen, T., JENSEN, Ø., Aass, H. & Amlie, J. P. Temperature guided radiofrequency catheter ablation of myocardium: comparison of catheter tip and tissue temperatures in vitro. *Pacing and clinical electrophysiology* **20**, 1252–1260 (1997).
13. Bruce, G. K. Discrepancies Between Catheter Tip and Tissue Temperature in Cooled-Tip Ablation: Relevance to Guiding Left Atrial Ablation. en. *Circulation* **112**, 954–960. ISSN: 0009-7322, 1524-4539 (Aug. 2005).
14. Harvey, M. *et al.* Impedance monitoring during radiofrequency catheter ablation in humans. *Pacing and Clinical Electrophysiology* **15**, 22–27 (1992).
15. Reithmann, C. *et al.* Different patterns of the fall of impedance as the result of heating during ostial pulmonary vein ablation: implications for power titration. *Pacing and clinical electrophysiology* **28**, 1282–1291 (2005).
16. Seiler, J. *et al.* Steam pops during irrigated radiofrequency ablation: Feasibility of impedance monitoring for prevention. en. *Heart Rhythm* **5**, 1411–1416. ISSN: 15475271 (Oct. 2008).
17. Thiagalingam, A. *et al.* Impedance and Temperature Monitoring Improve the Safety of Closed-Loop Irrigated-Tip Radiofrequency Ablation. en. *Journal of Cardiovascular Electrophysiology* **18**, 318–325. ISSN: 1045-3873, 1540-8167 (Mar. 2007).
18. Yokoyama, K. *et al.* Novel Contact Force Sensor Incorporated in Irrigated Radiofrequency Ablation Catheter Predicts Lesion Size and Incidence of Steam Pop and Thrombus. en. *Circulation: Arrhythmia and Electrophysiology* **1**, 354–362. ISSN: 1941-3149, 1941-3084 (Dec. 2008).

19. Perna, F. *et al.* Assessment of Catheter Tip Contact Force Resulting in Cardiac Perforation in Swine Atria Using Force Sensing Technology. en. *Circulation: Arrhythmia and Electrophysiology* **4**, 218–224. ISSN: 1941-3149, 1941-3084 (Apr. 2011).
20. Reddy, V. Y. *et al.* The relationship between contact force and clinical outcome during radiofrequency catheter ablation of atrial fibrillation in the TOCCATA study. en. *Heart Rhythm* **9**, 1789–1795. ISSN: 15475271 (Nov. 2012).
21. Oakes, R. S. *et al.* Detection and Quantification of Left Atrial Structural Remodeling With Delayed-Enhancement Magnetic Resonance Imaging in Patients With Atrial Fibrillation. en. *Circulation* **119**, 1758–1767. ISSN: 0009-7322, 1524-4539 (Apr. 2009).
22. Dickfeld, T. *et al.* Characterization of Radiofrequency Ablation Lesions With Gadolinium-Enhanced Cardiovascular Magnetic Resonance Imaging. en. *Journal of the American College of Cardiology* **47**, 370–378. ISSN: 07351097 (Jan. 2006).
23. Celik, H. *et al.* Intrinsic contrast for characterization of acute radiofrequency ablation lesions. *Circulation: Arrhythmia and Electrophysiology* **7**, 718–727 (2014).
24. Omary, R. A. *et al.* Real-time MR imaging-guided passive catheter tracking with use of gadolinium-filled catheters. *Journal of Vascular and Interventional Radiology* **11**, 1079–1085 (2000).
25. Nordbeck, P. *et al.* Feasibility of Real-Time MRI With a Novel Carbon Catheter for Interventional Electrophysiology. en. *Circulation: Arrhythmia and Electrophysiology* **2**, 258–267. ISSN: 1941-3149, 1941-3084 (June 2009).
26. Hoffmann, B. A. *et al.* Interactive real-time mapping and catheter ablation of the cavotricuspid isthmus guided by magnetic resonance imaging in a porcine model. en. *European Heart Journal* **31**, 450–456. ISSN: 0195-668X, 1522-9645 (Feb. 2010).
27. Eitel, C., Piorkowski, C., Hindricks, G. & Gutberlet, M. Electrophysiology study guided by real-time magnetic resonance imaging. en. *European Heart Journal* **33**, 1975–1975. ISSN: 0195-668X, 1522-9645 (Aug. 2012).
28. Piorkowski, C. *et al.* Cavotricuspid isthmus ablation guided by real-time magnetic resonance imaging. *Circulation: Arrhythmia and Electrophysiology* **6**, e7–e10 (2013).
29. Sommer, P. *et al.* Feasibility of real-time magnetic resonance imaging-guided electrophysiology studies in humans. en. *Europace* **15**, 101–108. ISSN: 1099-5129, 1532-2092 (Jan. 2013).
30. Settecase, F., Martin, A. J., Lillaney, P., Losey, A. & Hetts, S. W. Magnetic Resonance-Guided Passive Catheter Tracking for Endovascular Therapy. en. *Magnetic Resonance Imaging Clinics of North America* **23**, 591–605. ISSN: 10649689 (Nov. 2015).
31. Nazarian, S. *et al.* Feasibility of Real-Time Magnetic Resonance Imaging for Catheter Guidance in Electrophysiology Studies. en. *Circulation* **118**, 223–229. ISSN: 0009-7322, 1524-4539 (June 2008).
32. Hilbert, S. *et al.* Real-time magnetic resonance-guided ablation of typical right atrial flutter using a combination of active catheter tracking and passive catheter visualization in man: initial results from a consecutive patient series. en. *Europace* **18**, 572–577. ISSN: 1099-5129, 1532-2092 (Apr. 2016).

33. McDannold, N. *et al.* Uterine leiomyomas: MR imaging–based thermometry and thermal dosimetry during focused ultrasound thermal ablation 1. *Radiology* **240**, 263–272 (2006).
34. Ramsay, E. *et al.* MR thermometry in the human prostate gland at 3.0T for transurethral ultrasound therapy: Prostate MR Thermometry at 3T. en. *Journal of Magnetic Resonance Imaging* **38**, 1564–1571. ISSN: 10531807 (Dec. 2013).
35. Lepetit-Coiffé, M. *et al.* Real-time monitoring of radiofrequency ablation of liver tumors using thermal-dose calculation by MR temperature imaging: initial results in nine patients, including follow-up. en. *European Radiology* **20**, 193–201. ISSN: 0938-7994, 1432-1084 (Jan. 2010).
36. Coluccia, D. *et al.* First noninvasive thermal ablation of a brain tumor with MR-guided focused ultrasound. en. *Journal of Therapeutic Ultrasound* **2**, 17. ISSN: 2050-5736 (2014).
37. Kolandaivelu, A. *et al.* Noninvasive Assessment of Tissue Heating During Cardiac Radiofrequency Ablation Using MRI Thermography. en. *Circulation: Arrhythmia and Electrophysiology* **3**, 521–529. ISSN: 1941-3149, 1941-3084 (Oct. 2010).
38. Hey, S. *et al.* Towards optimized MR thermometry of the human heart at 3T: CARDIAC MR THERMOMETRY AT 3T. en. *NMR in Biomedicine* **25**, 35–43. ISSN: 09523480 (Jan. 2012).
39. De Senneville, B. D. *et al.* Feasibility of fast MR-thermometry during cardiac radiofrequency ablation: FEASIBILITY OF FAST MR-THERMOMETRY DURING CARDIAC RF ABLATION. en. *NMR in Biomedicine* **25**, 556–562. ISSN: 09523480 (Apr. 2012).
40. Quesson, B., Vimeux, F., Salomir, R., de Zwart, J. A. & Moonen, C. T. Automatic control of hyperthermic therapy based on real-time Fourier analysis of MR temperature maps. en. *Magnetic Resonance in Medicine* **47**, 1065–1072. ISSN: 0740-3194, 1522-2594 (June 2002).



## Chapter 2

# Challenges of cardiac Magnetic Resonance thermometry

### Contents

---

<b>2.1</b>	<b>Principles of Magnetic Resonance thermometry . . . . .</b>	<b>32</b>
2.1.1	Proton Resonance Frequency shift method . . . . .	32
2.1.2	Precision of temperature measurement . . . . .	33
2.1.3	MR dosimetry . . . . .	34
2.1.3.1	Lethal isotherm . . . . .	34
2.1.3.2	Thermal dose concept . . . . .	35
<b>2.2</b>	<b>Fast pulse sequence imaging . . . . .</b>	<b>35</b>
2.2.1	Single-shot Echo Planar Imaging . . . . .	35
2.2.2	Parallel imaging . . . . .	36
2.2.2.1	SENSE . . . . .	37
2.2.2.2	GRAPPA . . . . .	38
<b>2.3</b>	<b>Heart motion . . . . .</b>	<b>39</b>
2.3.1	Effects of heart motion . . . . .	39
2.3.2	MR acquisition methods for compensation of heart-induced motion . . .	39
2.3.3	MR acquisition methods for compensation of respiratory-induced motion	40
2.3.3.1	Respiratory-gated MR acquisition . . . . .	40
2.3.3.2	Echo-navigator based slice tracking technique . . . . .	42
2.3.3.3	Catheter-based slice tracking technique . . . . .	42
2.3.4	Post-processing methods for in-plane motion compensation . . . . .	44
2.3.4.1	Affine transformation . . . . .	44
2.3.4.2	Optical-flow algorithm . . . . .	44
<b>2.4</b>	<b>Correction of motion-induced <math>B_0</math> changes . . . . .</b>	<b>47</b>
2.4.1	Multi-baseline approach . . . . .	47
2.4.2	Principal Component Analysis (PCA)-based phase modeling approach .	48
2.4.3	Referenceless approach . . . . .	50

2.4.4 Discussion . . . . .	51
<b>2.5 State-of-the-art of cardiac MR thermometry . . . . .</b>	<b>52</b>
<b>2.6 References . . . . .</b>	<b>54</b>

## 2.1 Principles of Magnetic Resonance thermometry

Several MR parameters, such as the longitudinal relaxation time  $T_1$ , the transversal relaxation time  $T_2^*$  and the water proton resonance frequency (PRF) shift, are sensitive to temperature changes [1, 2]. Because the PRF method relies on a linear relationship to temperature from  $0^\circ\text{C}$  to  $100^\circ\text{C}$  and does not depend on tissue type (except adipose tissue), it has become the technique of reference for the monitoring of thermal ablation. In this thesis, all MR thermometry experiments were performed using the PRF shift method.

### 2.1.1 Proton Resonance Frequency shift method

Temperature mapping can be achieved from phase images acquired with a gradient-recalled echo (GRE) pulse sequence. The phase variation  $\Delta\varphi$  is directly proportional to the temperature change  $\Delta T$  as follows:

$$\Delta T = \frac{\Delta\varphi}{\gamma \cdot \alpha_{PRF} \cdot B_0 \cdot TE} = \frac{\varphi - \varphi_{REF}}{\gamma \cdot \alpha_{PRF} \cdot B_0 \cdot TE} \quad (2.1)$$

Where  $\varphi$  is the current acquired phase image,  $\varphi_{REF}$  is the phase of reference (baseline) image acquired prior to heating,  $\gamma$  is the gyromagnetic ratio ( $\sim 42.58\text{MHz/T}$ ),  $\alpha_{PRF}$  is the PRF temperature coefficient ( $-0.0094\text{ ppm}/^\circ\text{C}$  [3]),  $B_0$  is the magnetic field strength and  $TE$  is the echo time of the MR sequence. Figure 2.1 illustrates the MR thermometry method during a RF heating on a static agar gel.

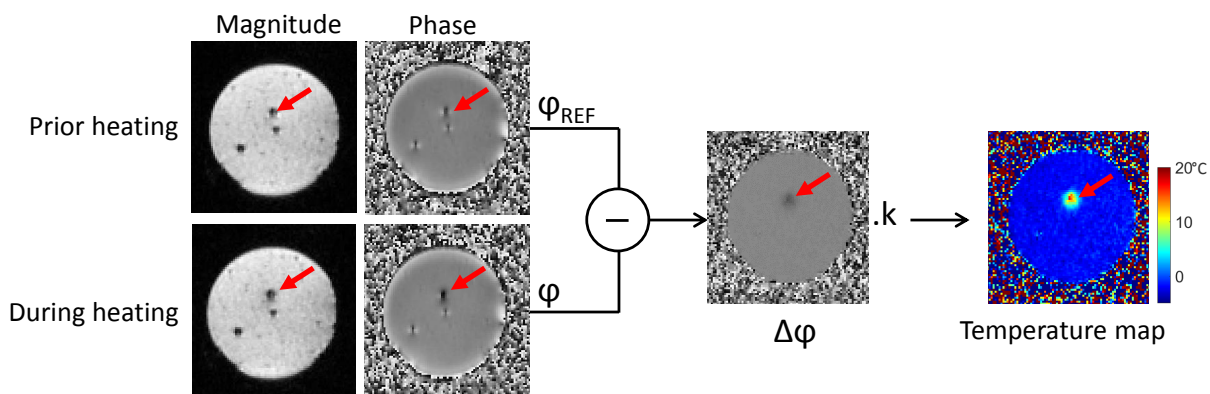


Figure 2.1: Basic principle of PRF thermometry method on a static agar gel phantom. Magnitude and phase images are acquired using a fast EPI pulse sequence. During the heating, the current phase image is subtracted to a phase of reference acquired prior to heating. The temperature map is calculated from the subtracted phase using the PRF formula 2.1. The red arrow depicts the position of the catheter tip positioned perpendicular to the imaging plane.

A simple GRE pulse sequence was mostly used in PRF thermometry applications such as

clinical ablations of brain tumor [4] or uterine fibroids [5]. However, MR thermometry in mobile organs such as the liver, the kidney or the heart, requires fast imaging technique to ensure a sufficient temporal resolution to resolve respiratory motion. For that purpose, echo-planar imaging (EPI) pulse sequence has been increasingly used, for example for the monitoring of tumor ablation in the liver [6, 7]. Further fast imaging techniques will be described in the Section 2.2.

### 2.1.2 Precision of temperature measurement

The real and imaginary parts of the complex MR signal are affected by white gaussian noise with a standard deviation  $\sigma$  (Figure 2.2). It results in Rician noise on the final magnitude and phase images. As the temperature change is proportional to the phase variation (see equation 2.2), the variance of the temperature noise can be calculated using the formula 2.3.

$$\Delta T = \Delta\varphi \cdot k \quad \text{with} \quad k = \frac{1}{\gamma \cdot \alpha_{PRF} \cdot B_0 \cdot TE} \quad (2.2)$$

$$V(\Delta T) = V(\Delta\varphi \cdot k) = V(\Delta\varphi) \cdot k^2 = (V(\varphi_{REF}) + V(\varphi)) \cdot k^2 \quad (2.3)$$

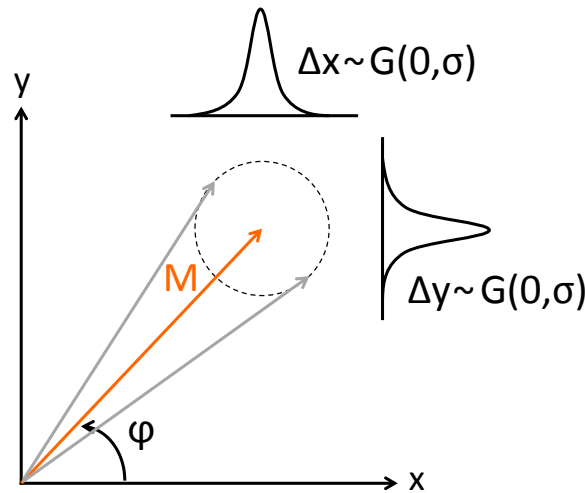


Figure 2.2: Experimental noise on the phase of the transverse magnetisation vector

Thus, the noise of the temperature can be expressed as:

$$\sigma(\Delta T) = \sqrt{\sigma^2(\varphi_{REF}) + \sigma^2(\varphi)} \cdot k = \sigma(\varphi) \cdot \sqrt{2} \cdot k \quad (2.4)$$

Where  $\sigma(\Delta T)$  is the standard deviation of the noise of the phase image. In addition, Conturo et al [8] demonstrated that:

$$\sigma(\varphi) = \frac{1}{SNR} \quad (2.5)$$

Where SNR is the signal-to-noise ratio of the magnitude image. The uncertainty of the temperature measurement  $\sigma(\Delta T)$  can finally be expressed as:

$$\sigma(\varphi) = \frac{\sqrt{2} \cdot k}{SNR} \quad (2.6)$$

The accuracy of the temperature measurement is mainly dependent on the used pulse sequence and on potential artifacts (due to motion or RF delivery).  $\sigma(\varphi)$  is considered as the optimal temperature accuracy that can be obtained by minimizing the artifacts. In this PhD thesis, the accuracy and the stability of the temperature measurements are evaluated by computing, in a pixel-by-pixel basis, the temporal standard deviation  $\sigma_T$  and average  $\mu_T$  of the temperature, respectively (see Figure 2.3).

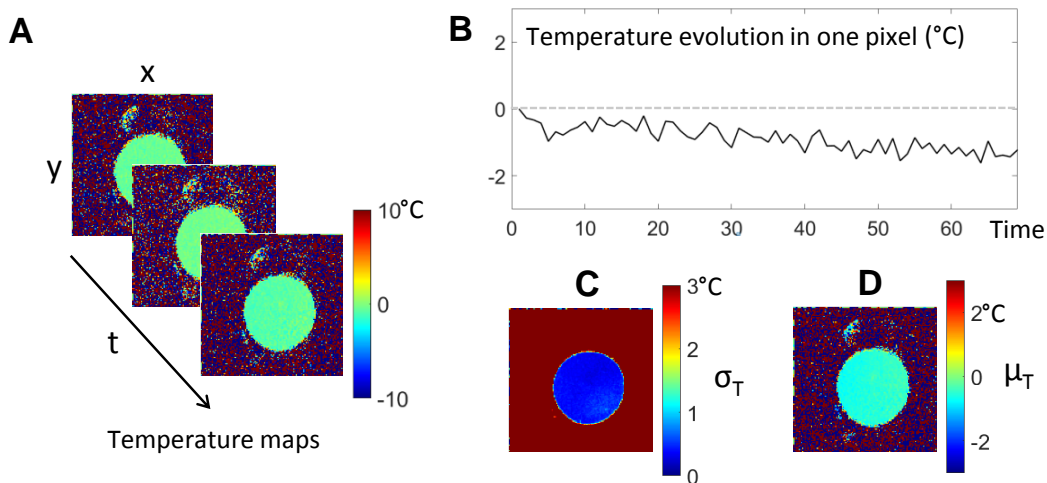


Figure 2.3: Evaluation of MR thermometry performance. (A) Temperature maps are computed over time without heating. Temperature evolution in one pixel centered on the agar gel phantom is plotted in (B). The standard deviation  $\sigma_T$  (C) reflects the noise affecting the temperature over time in each pixel. The temporal average  $\mu_T$  reflects the off-set of the temperature that is supposed to be zero. As shown on (B), the temperature can be impacted by phase drift that must be corrected.

### 2.1.3 MR dosimetry

The goal of MR thermometry is to predict the final outcome of the thermal therapy. During RF ablation, it has to be ensured that the optimal energy has been delivered to completely destroy the targeted myocardium while avoiding collateral damage on surrounding healthy tissue. MR dosimetry aims to give a relation between tissue temperature and resulting cell necrosis. Two different approaches have been proposed in the past: a temperature threshold above which the tissue necrosis is complete, and the thermal dose accounts for both exposure temperature and time.

#### 2.1.3.1 Lethal isotherm

A tissue temperature of  $50^\circ\text{C}$  has been indirectly estimated as the lethal isotherm to create irreversible myocardial damage using spaced thermocouples on excised pig ventricular muscles [9]. This lethal isotherm was used by Kolandaivelu et al. [10] to correlate MR thermometry based temperature measurement and the final lesion transmuralty at gross pathology. Lesion

transmurality by MR thermometry was within 20% of that measured by pathology. However, a recent study demonstrated that 50°C overestimates lesion size [11]. A lethal isotherm of 61°C was proposed by directly measuring the temperature elevation by infrared thermal imaging during RF ablation on the LV of isolated perfused pig hearts. However, the lethal isotherm technique assumes no time-temperature relationship for thermal injury, contrary to the thermal dose concept.

### 2.1.3.2 Thermal dose concept

TD model is widely used in thermal therapy to relate temperature to actual tissue damage. First introduced by Sapareto et al [12], cumulative TD was formulated in each pixel using the following formula:

$$TD = \begin{cases} \int_0^t 2^{T(t)-43} & \text{if } T(t) > 43^\circ C \\ \int_0^t 4^{T(t)-43} & \text{if } T(t) \leq 43^\circ C \end{cases} \quad (2.7)$$

Where  $T(t) = T_{REF} + \Delta T$  is the absolute temperature at the time  $t$ ,  $T_{REF}$  is the temperature offset measured by an external sensor and  $\Delta T$  is the relative temperature change measured by MR thermometry. The lethal threshold for tissue necrosis is equivalent to a constant heating for 240 min at 43°C [13].

Noise impacting MR temperature measurements  $\sigma_T$  must be taken in account for the calculation of the TD. A correction was performed in [6, 14], as follow:

$$TD_{corr}(x, y) = TD(x, y) \cdot e^{-0.5(\ln(2) \cdot \sigma_T(x, y))^2} \quad (2.8)$$

Where  $(x, y)$  depict the TD map coordinates and  $TD_{corr}$  is the corrected TD.

In this PhD thesis, we assume a time-temperature relation with tissue necrosis and the thermal dose model will be evaluated for inline prediction of the ablation outcome.

## 2.2 Fast pulse sequence imaging

Occurrence of motion during the MR acquisition lead to blurring and ghosting artifacts. These effects can be minimized by accelerating the scan time using methods discussed in this section. The employed technique of acquisition and reconstruction must allow a sufficient update rate to avoid latency in temperature map computing.

### 2.2.1 Single-shot Echo Planar Imaging

Single-shot EPI allows the acquisition of images with a scan time in the range of 40-100 ms. This temporal resolution minimizes the issue of intra-scan motion artifacts.

In conventional GRE pulse sequence, one line in k-space is collected within each repetition time (TR). The pulse sequence is repeated to fill the k-space and the scan time is equal to the product of the TR and the number of phase-encoding steps. The single-shot EPI allows the acquisition of all the lines of imaging data after a single RF excitation. The frequency-encoding gradient ( $G_{read}$  in Figure 2.4) forms an echo-train by oscillating rapidly. One line of the k-space is acquired at each oscillation of the frequency-encoding gradient. A short phase-encoding gradient, called “blip”, is used at the zero-crossing point of the frequency-encoding gradient to move to the next line in the k-space.

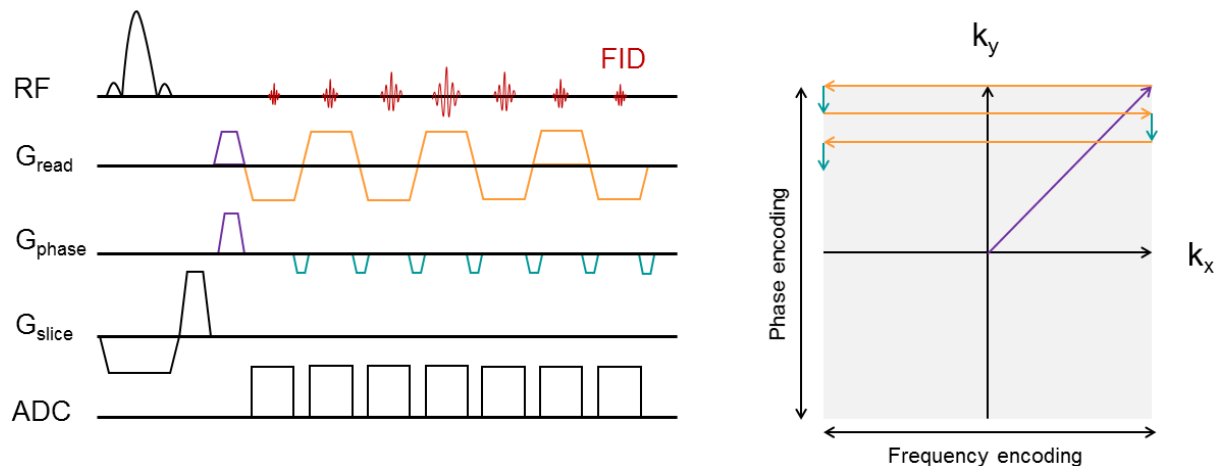


Figure 2.4: Timing diagram for the blipped EPI sequence and the resulting trajectory in the k-space.

Because of the fast oscillation of the frequency-encoding gradient, EPI pulse sequence requires a high gradient strength of 20 mT/m, a minimum rise time of 0.1 ms and a slew rate of 200 T/m per second. These technical requirements have first restricted the development of this technique in routine clinical practice.

EPI is a fast acquisition technique with a reduced scan time and is useful to decrease motion artifact and to image physiologic processes with a high temporal resolution. However, EPI suffers from various artifacts, such as N/2 ghosting and geometric distortion, and is sensitive to susceptibility effects and main magnetic field inhomogeneity.

### 2.2.2 Parallel imaging

Parallel imaging allows an acceleration of the scan time by skipping a part of the lines in the phase-encoding direction of the k-space. However, the reduction of the number of lines results in a reduction of the field of view (FOV), and thus to aliasing on the reconstructed image (see Figure 2.5). In parallel imaging, the MR signal is acquired by multiple receiver coils and weighted by the coil sensitivity. Several methods of reconstruction have been proposed to combine signals from the coils and compute a final unaliased image. In this section are presented the Sensitivity Encoding (SENSE) [15] and the Generalized Autocalibrating Partially Parallel Acquisitions (GRAPPA) [16] methods that are the most widely used techniques.

### 2.2.2.1 SENSE

SENSE involves using the spatial sensitivities of each coil to unwrap aliased images (Figure 2.5). Aliased images are acquired separately from each coil. As illustrated in Figure 2.6 with two receiver coils, one point (P) in the aliased image represents two voxels (V1 and V2) in the body. Using two coils (C1 and C2) with their own sensitivity ( $S_{C1}$  and  $S_{C2}$ ), the system of equations 2.9 can be formulated:

$$\begin{cases} I_{C1}(P) = S_{C1}(V1) * I(V1) + S_{C1}(V2) * I(V2) \\ I_{C2}(P) = S_{C2}(V1) * I(V1) + S_{C2}(V2) * I(V2) \end{cases} \quad (2.9)$$

Where  $I_{C1}(P)$  and  $I_{C2}(P)$  are the signal intensity in the point P recorded with the coil 1 and 2, respectively. From this system of two equations, the two unknowns  $I(V1)$  and  $I(V2)$  can be calculated. This works the same for any number of coils and acceleration factor R, as long as R is lower than the number of coils.

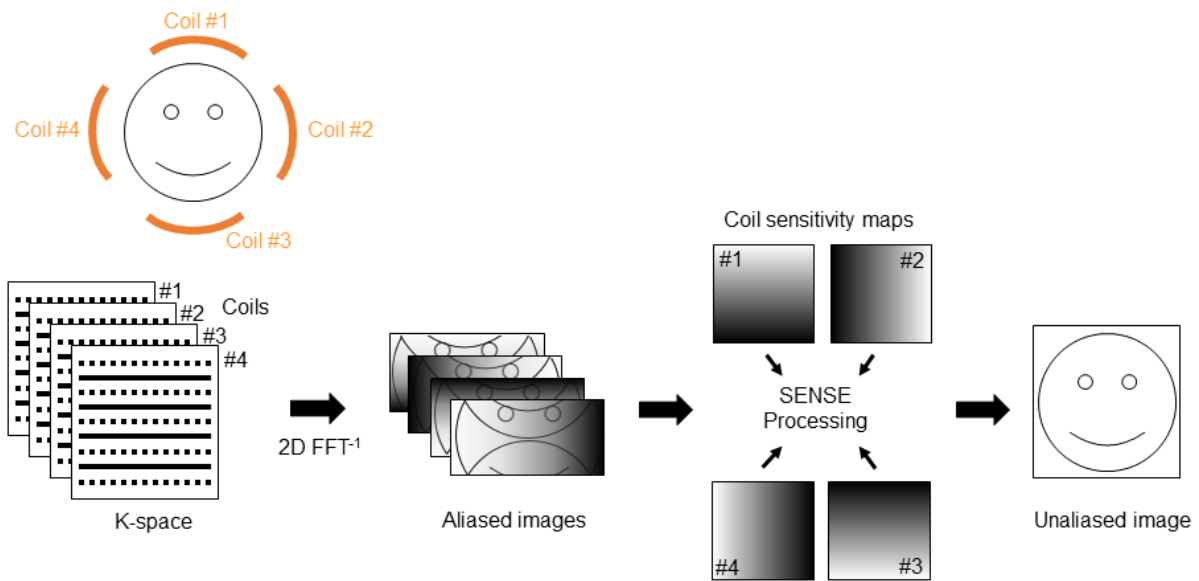


Figure 2.5: SENSE parallel imaging. To accelerate the acquisition time, the k-space is under-sampled (two-fold here, the dashed lines represent unacquired lines). The reconstructed images from each coil present aliasing artifacts caused by the under-sampling. Coil sensitivity maps are used to reconstruct a final unaliased image.

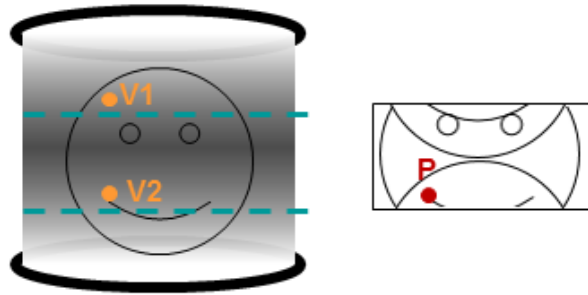


Figure 2.6: Spatial aliasing and SENSE reconstruction. MR signal is acquired by a phased-array of 2 coils. The dashed lines depict the FOV after a two-fold sub-sampling. In the resulting aliased image, the point P is a superposition of two points in the body (voxels V1 and V2).

### 2.2.2.2 GRAPPA

The goal of GRAPPA is the same as of SENSE: to speed up the acquisition by under-sampling the phase-encoding lines and then to solve the aliasing issue using measurements from each individual coil. While SENSE solves the problem in the spatial domain of the image, GRAPPA calculates missing k-space lines before Fourier transform of the raw data.

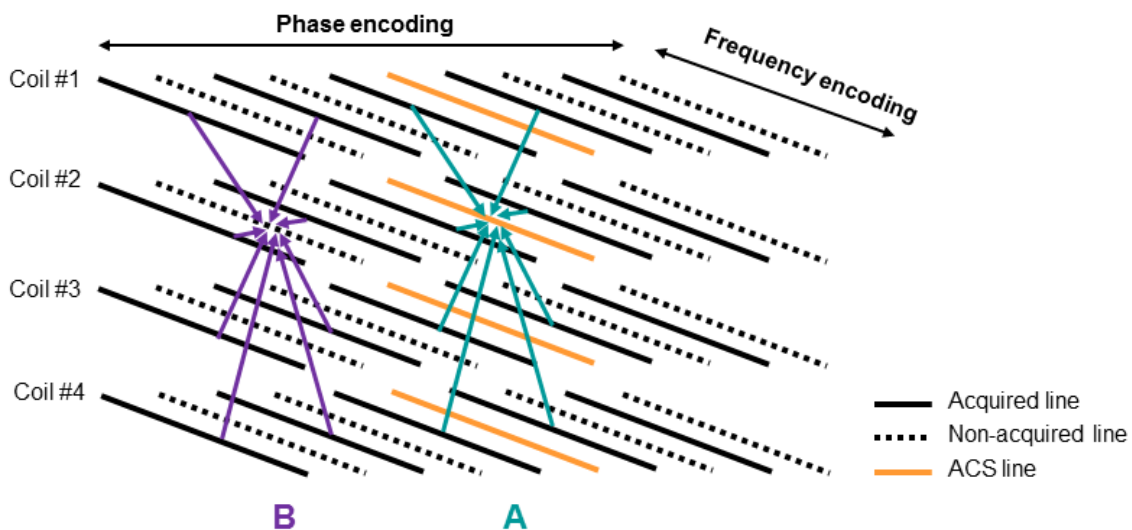


Figure 2.7: GRAPPA reconstruction method with 4 coils and an acceleration factor  $R=2$ . (A) Data acquired in each coil are fit to the ACS line of coil #2. The resulting weights are used to reconstruct the non-acquired lines of the same coil (B).

Autocalibration signal (ACS) is collected in the center of the k-space (orange lines in Figure 2.7). To determine the weights used for reconstruction, a fit is performed between several lines and one ACS line in a single coil (Figure 2.7-A). These weights are then used to generate the missing lines from that coil (Figure 2.7-B). Once all of the lines are reconstructed for each coil, a Fourier transform can be used to generate one unaliased image per coil. The unaliased images are finally combined by sum of square or other methods to generate the final image.

## 2.3 Heart motion

The heart is subject to complex motion-induced by heart contraction and respiratory motion. The breathing induces a mainly 2D periodic linear displacement with a rate in the range from 12 to 18 breaths per minute in humans. The cardiac activity causes elastic deformation of the heart. Each heartbeat is divided in two parts: during diastole the atria and ventricles relax and fill with blood; during systole the heart's ventricles contract and pump the blood out of the heart. A normal resting heart rate ranges from 60 to 100 bpm in adults.

### 2.3.1 Effects of heart motion

- **Intra-scan motion** is induced by motion occurring during the MR acquisition, resulting in image artifacts such as blurring and ghosting when the motion is not compensated.
- **Inter-scan motion** is caused by movement of an object between two consecutive MR acquisitions. As described earlier, PRF-based temperature mapping is performed by subtracting a baseline phase image acquired prior to ablation to the current heating phase image. A misalignment between the acquisitions of the images may lead to strong artifacts in the computed temperature maps.

### 2.3.2 MR acquisition methods for compensation of heart-induced motion

The issue of heart motion can be solved by ECG-gated imaging (Figure 2.8-A). ECG gating synchronizes data acquisition at a specific part of the cardiac cycle, typically during the diastolic phase. The R wave of the ECG signal is detected as the start of the cardiac cycle and the data acquisition is initiated after a user-defined delay. ECG leads are placed on patient chest as described in Figure 2.8-B.

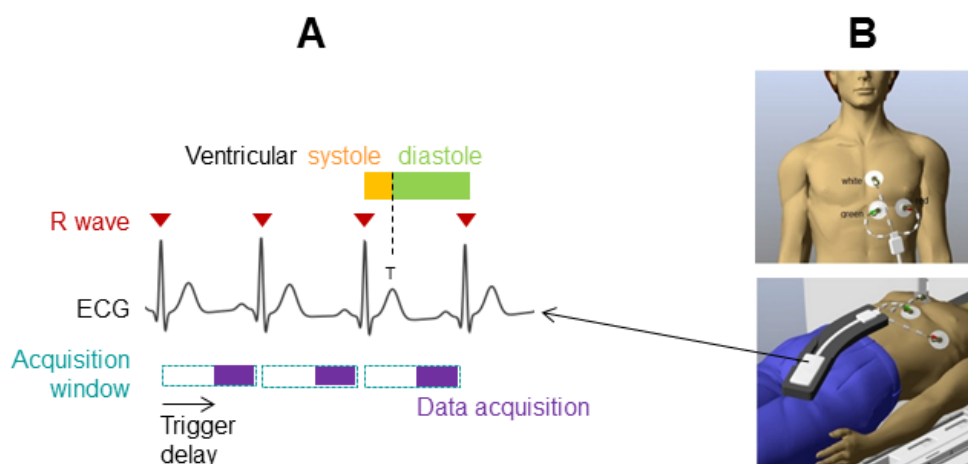


Figure 2.8: ECG gated imaging. (A) The R wave is detected and the data acquisition is run after a trigger delay defined by the user. The trigger delay and the scan duration must not overcome the acquisition window available in the cardiac cycle (R-R interval). The data is typically acquired during the ventricular diastole, when the heart movement is limited. (B) ECG leads placement on human chest with three leads configuration. The leads are connected to a wireless sensor that transmits the ECG signal to the MR scanner.

Gradients and RF pulses can cause interference in ECG. The signal shape of these artifacts can lead to false detection of the R wave and thus to false triggering of the data acquisition. The data may be corrupted with motion and not be synchronized with the other acquisition of the time series. Arrhythmia may cause inappropriate triggering as well. Some imaging softwares incorporate arrhythmia rejection algorithm to discard and re-acquire the corresponding data (Figure 2.9).

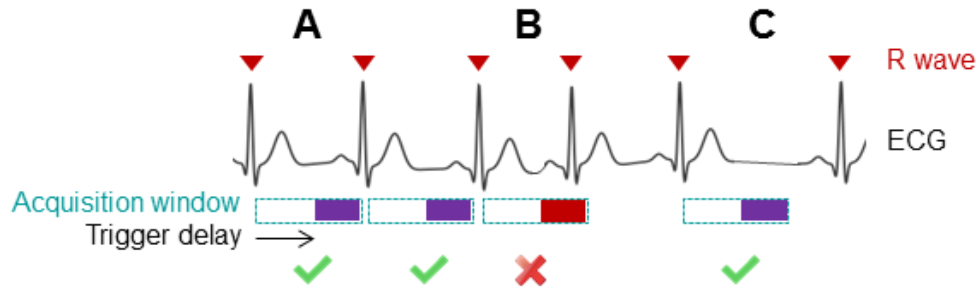


Figure 2.9: ECG gating acquisition in case of cardiac arrhythmia. The acquisition window and the trigger delay are defined by the user based on the heart cycle duration observed before the acquisition (A). If arrhythmia occurs, the R-R interval can be shortened (B) and the data acquisition will be discarded. If the cycle duration is increased (C), the data can be acquired but not at the identical cardiac phase.

### 2.3.3 MR acquisition methods for compensation of respiratory-induced motion

Through-plane heart motion is mainly caused by respiration and can be approximated as a 2D linear displacement in head-foot direction. A motion with a direction perpendicular to the imaging slices may lead to the observation of different part of the heart tissue over time. Because RF ablation procedure duration is in the order of several minutes, MR thermometry imaging cannot be performed in a single breath-hold. Although the acquisition of 3D volumes would be highly valuable, it is hardly feasible with a sufficient temporal resolution and may be prone to intra-scan artifacts described earlier.

#### 2.3.3.1 Respiratory-gated MR acquisition

The MR acquisition is synchronised with the respiratory cycle so that the data is always acquired at the same part of the respiratory cycle. This method requires a monitoring of the patient's respiration. A first approach consisted in the use of a respiratory bellow device fixed to the patient abdomen [17]. It provides a continuous recording of the respiratory signal, independent of field strength. However, bellow signal is not always well correlated with the heart motion due to non-linearities or suboptimal location of the bellow device [18].

A more accurate method is the use of an echo-navigator for the monitoring of temporal changes of the diaphragm position. A column of tissue is excited through the diaphragm using either (1) a pencil-beam echo-navigator based on the excitation of a cylinder shaped volume by a 2D RF pulse with a low flip angle (FA) [19] or (2) a crossed-pair echo-navigator based on the excitation of the intersection volume of two crossed slices [17]. The second method leads to strong saturation artifacts due to high excitation angles ( $90^\circ$  and  $180^\circ$ ). For this reason,

positioning must be done carefully to avoid the two slices to cross the heart. Usually the echo-navigator beam is placed through the peak of the dome of the right hemidiaphragm, as described Figure 2.10.

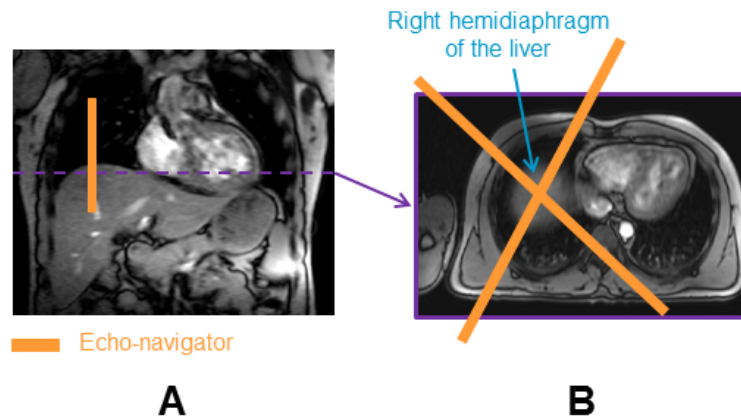


Figure 2.10: Crossed-pair echo-navigator positioning. (A) Coronal view showing the excited volume (orange rectangles) located at the interface between the liver and the lung. The dashed violet line represents the position of the transverse slice (B) used to position the two crossed slices through the peak of the dome of the right hemidiaphragm. Since the two slices create strong saturation artifacts, they are placed in a proper way to not cross the heart

The echo-navigator profile is acquired prior to the acquisition window in the cardiac cycle (Figure 2.11-A) using a prospective technique. The position of the diaphragm is clearly delineated by the contrast between the liver and the lung and can be extracted from echo-navigator profile using real-time edge-detection algorithm [20], correlation or least-squares methods [21]. A gating window is determined by the user at a stable position, typically at end expiration (Figure 2.11-B). If the diaphragm position is included inside the gating window, the data is accepted (Figure 2.12). A large gating window will lead to a high acceptance rate but to a reduced image quality.

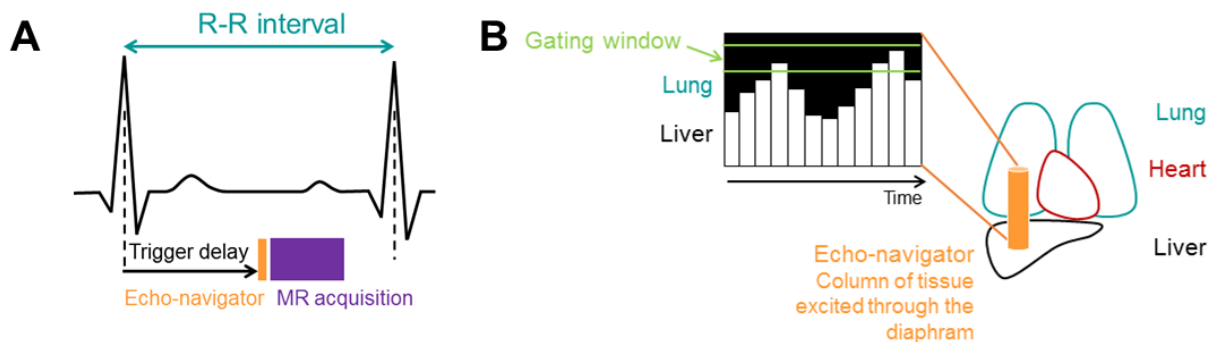


Figure 2.11: Respiratory-gated MR acquisition. (A) The MR acquisition is synchronized with the ECG and an echo-navigator pulse sequence is run prior to the imaging acquisition. (B) Positioned at the liver/lung interface, the echo-navigator allows the detection of the diaphragm. A gating window is defined according to the navigator trace to allow the acquisition only during a stable part of the respiratory cycle. The aim is to minimize the respiratory motion between two successive acquisitions.

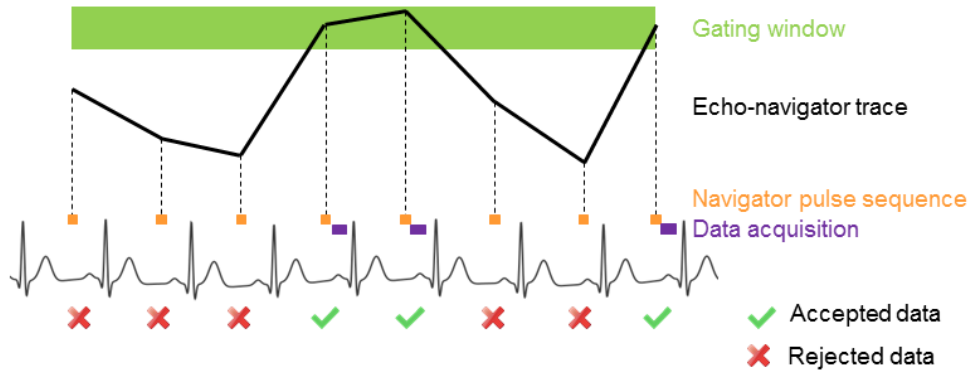


Figure 2.12: Rejection of data acquisition outside a user-defined window during respiratory-gated MR acquisition. If the echo-navigator trace position is included in the user-defined gating window (green region), the data is acquired, otherwise the data is rejected.

### 2.3.3.2 Echo-navigator based slice tracking technique

Similarly to the navigator-gated method, an echo-navigator profile is acquired at each repetition before the imaging pulse sequence. The diaphragm position is detected and used to update the slice position of the next imaging scan, as described Figure 2.13. One major benefit of this technique is the absence of rejected data. Hence, the total scan time is significantly reduced. However, this approach is highly dependent on the tracking factor required to relate the motion of the heart to the motion of the diaphragm. The value of tracking factor used in clinical practice is of 0.57-0.6 [22], but several studies reported high inter-subject variability [22–24]. This issue can be overcome by calculating a subject-specific tracking factor from breath-hold images [25, 26]. It was found to improve quality of coronary arteries imaging.

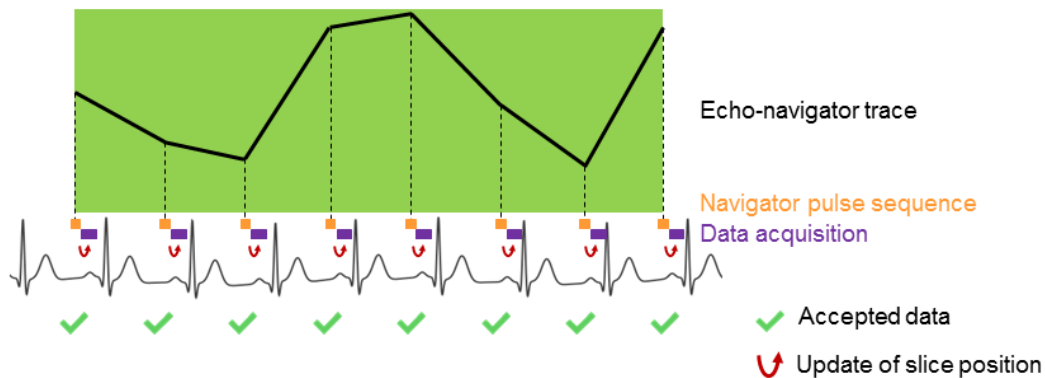


Figure 2.13: Echo-navigator based slice following technique. Slice position is updated depending on the diaphragm position detected by the echo-navigator.

### 2.3.3.3 Catheter-based slice tracking technique

In the case of catheter RF ablation, the catheter itself can be used to update the slice position between two successive MR acquisitions. Currently two major approaches have been investigated to monitor catheter position under MRI: passive tracking [27] and active tracking [28]. Passive tracking relies on the intrinsic material properties of the catheter while active tracking uses modified catheters that incorporate MR receiver coils.

### Passive catheter tracking

Passive catheter devices are made visible under MRI by incorporating markers or material in their construction to create a negative or positive contrast at the tip or along the length of the catheter. Negative contrast can be produced using markers made of ferromagnetic material which cause local susceptibility artifact. A signal void can be visualized on magnitude images. To optimize the visualization, the contrast can be improved by subtracting the image to a prior acquired road-map. However, this technique can induce signal loss from adjacent anatomic structures and be sensitive to inter-scan motion in the case of baseline subtraction. Positive contrast can be generated using a catheter filled with T1-shortening paramagnetic material, such as gadolinium (Gd), associated to T1 weighted (T1-w) imaging.

### Active catheter tracking

Active catheter devices incorporate small RF receiver coils (micro-coil) with limited sensitivity profiles. A dedicated tracking RF pulse sequence allows for the spatial localization of the RF coil. A large volume is excited and a gradient is applied along one direction. The frequency of the MR signal received by the micro-coil linearly depends on the spins' location. As a result, a sharp peak can be visualized on the frequency spectrum and its location indicates the position of the micro-coil along the gradient's direction. The coil 3D coordinates can be generated using the same process along three orthogonal axes (referred as Single-Echo technique).

Several strategies of tracking RF pulse sequence have been proposed to improve the robustness of the coil detection. Distortions in the static magnetic field  $B_0$  may lead to imprecise calculation of the device location. For that purpose, multiplexed Hadamard encoding sequence [29] has been proposed to minimize the resonance such offset errors. It requires four excitations with different gradients' polarity along the three axes. It offers improved accuracy at the expense of temporal resolution due to the acquisition of four echoes. At 1.5 T, where off-resonance effects are limited, the Single-Echo technique has been reported to be sufficiently accurate [30].

### Advantages and disadvantages of passive and active tracking methods

Passive catheter tracking is a simple and inexpensive technique, since no particular instrumentation is required. However, the device 3D coordinates are unknown and imaging plane position and orientation are not automatically updated. Using passive tracking method, the imaging plane must be updated manually with thick slices to keep the marker within the imaging volume. Therefore, passive catheter guided procedures may be time consuming and less precise than active tracking methods.

Active catheter tracking necessitates additional hardware and software and thus may be more expensive. However, it allows for automatic real-time shift of the imaging plane according

to movement of the device. Several softwares of major MR scanner vendors have been developed to visualize a catheter, which is graphically represented and overlaid on incoming MR images. Since the micro-coils are MR receivers, they can easily be visualized in hyper intensity. Several micro-coils can be embedded and detected to accurately measure the position and orientation of steerable catheters. However, incorporation of micro-coils come at a cost of increased device diameter. This approach was mainly investigated for MR-guided EP studies [31, 32] using a balanced Steady State Free Precession (b-SSFP) pulse sequence interleaved with a catheter tracking module.

### 2.3.4 Post-processing methods for in-plane motion compensation

Despite the use of specific MR acquisition method to minimize 3D through-plane motion, 2D in-plane motion between consecutive images may remain. Strategies of motion estimation and correction on MR images have been proposed in the past for the thermal treatment of mobile organs. A rapid overview of these techniques is now presented.

#### 2.3.4.1 Affine transformation

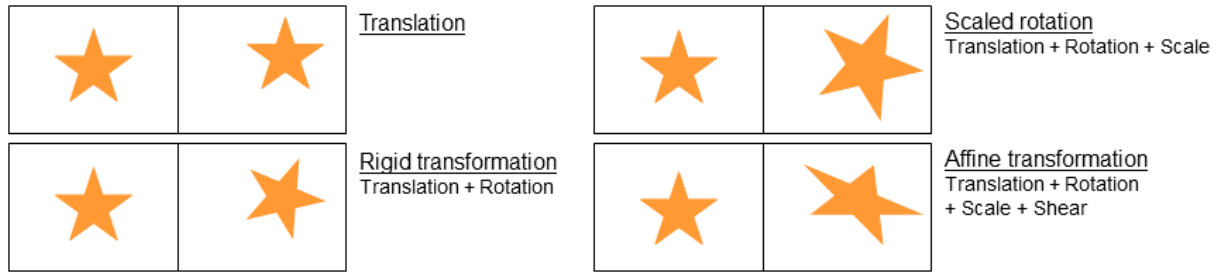


Figure 2.14: Examples of basic transformations

In Hey et al [33], the motion of the heart was estimated as an affine transformation restricted to a user-defined ROI. A gradient driven descent algorithm [34] was performed to maximize the inter-correlation coefficient between the reference magnitude image and each following magnitude image of the time series. The affine transformation leads to six coefficients: two translations, one rotation, two scales and one shear (see Figure 2.14).

#### 2.3.4.2 Optical-flow algorithm

Optical-flow techniques rely on the assumption of intensity conservation. The aim is to calculate  $(u,v)$ , the horizontal and vertical components of the motion field, that depict the displacement of the pixels between two images. The initial approach was proposed by Horn and Schunck (H&S) [35] with the following functional to be minimized:

$$E = \iint_{xy} \left( [I_x u + I_y v + I_t]^2 + \alpha [\|\nabla u\|_2^2 + \|\nabla v\|_2^2] \right) dx dy \quad (2.10)$$

where  $(I_x, I_y, I_t) = \left( \frac{\partial I}{\partial x}, \frac{\partial I}{\partial y}, \frac{\partial I}{\partial t} \right)$ ,  $\|\nabla u\|_2^2 = u_x^2 + u_y^2$  and  $\|\nabla v\|_2^2 = v_x^2 + v_y^2$  with  $u_x = \frac{\partial u}{\partial x}$  and  $v_x = \frac{\partial v}{\partial x}$ .  $\alpha$  is a weighting term that relates the intensity variation and the motion regularity. To minimize this functional, the following iterative scheme can be solved:

$$\begin{cases} u^{n+1} = \bar{u}^n - I_x \frac{\bar{u}^n I_x + \bar{v}^n I_y + i_t}{I_x^2 + I_y^2 + \alpha^2} \\ v^{n+1} = \bar{v}^n - I_x \frac{\bar{u}^n I_x + \bar{v}^n I_y + i_t}{I_x^2 + I_y^2 + \alpha^2} \end{cases} \quad (2.11)$$

where  $n$  is the number of iteration,  $\bar{u}$  and  $\bar{v}$  are the spatial mean values of the motion field. The use of this optical-flow algorithm is illustrated in Figure 2.15.

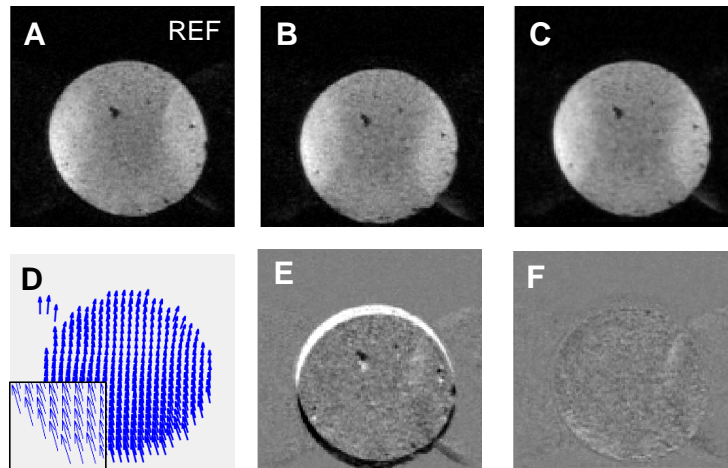


Figure 2.15: Optical-flow motion estimation. The in-plane displacement is estimated between a magnitude of reference (A) and a current magnitude image (B) showing a phantom made of gel. The difference between the two images (E) illustrates the residual motion to correct. An optical-flow algorithm is used to compute the motion field (zoom in D) depicted by one vector per pixel. The registered magnitude image (C) is calculated by applying the motion field on the original magnitude image (B). The motion is well reduced, as demonstrated by the new image difference (F).

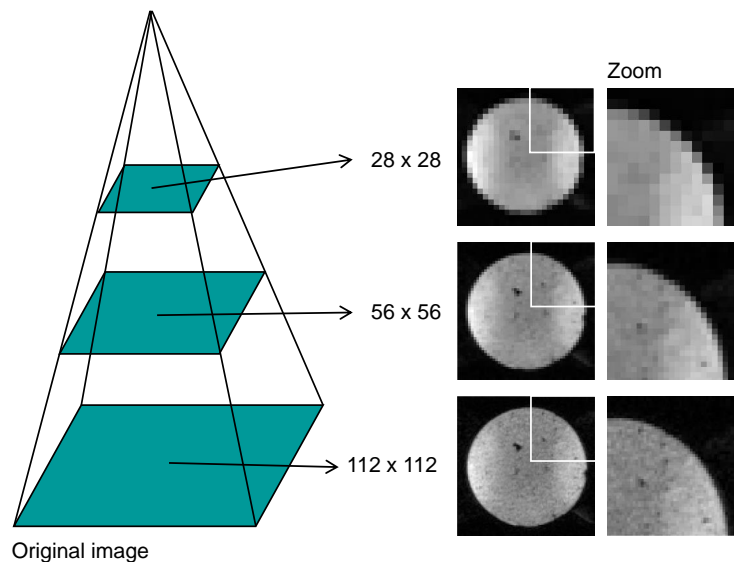


Figure 2.16: Multi-resolution scheme of optical-flow motion estimation

A coarse-to-fine resolution scheme can be performed to ensure the convergence of the motion estimation (Figure 2.16).

Various implementations of the original H&S optical-flow algorithm have been proposed in the literature. For example, Black and Anandan proposed a robust estimator to decrease the influence of pixels corrupted by noise [36]. The fidelity term  $\rho$  is the optical-flow functional (Eq. 2.12) was changed from  $\rho(x) = x^2$  to a Lorentzian estimator  $\rho(x) = \log(1 + \frac{1}{2}(\frac{x}{\sigma})^2)$ .

$$E = \iint_{xy} (\rho(I_x u + I_y v + I_t) + \alpha [\|\nabla u\|_2^2 + \|\nabla v\|_2^2]) dx dy \quad (2.12)$$

The advantage is that the derivative of the Lorentzian tends to zeros for infinity values, whereas the derivative of the quadratic term ( $2x$ ) increases linearly the influence of the corrupted pixel on the estimated motion.

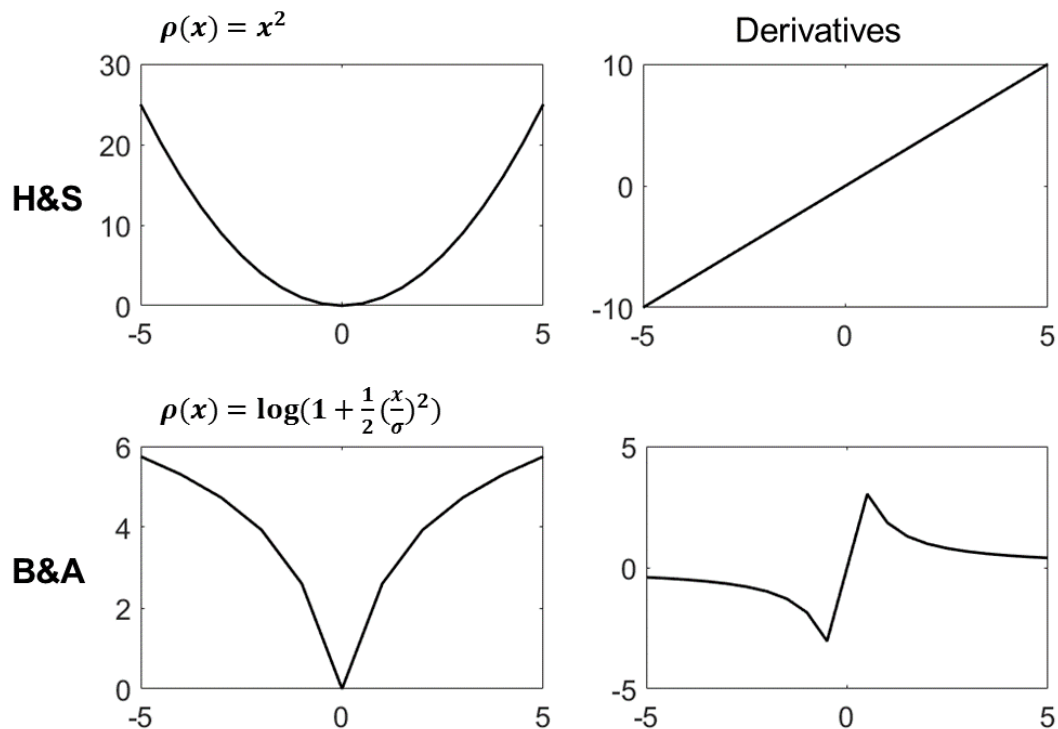


Figure 2.17: Illustration of the fidelity term of Horn and Schunck (H&S) and Black and Anandan (B&A) optical-flow algorithms. The Lorentzian estimator is plotted with  $\sigma=0.2$ .

## 2.4 Correction of motion-induced $B_0$ changes

Respiratory motion induces fluctuations of the magnetic field  $B_0$ , mainly caused by lung volume change. These effects produce local additional shifts on phase images (Figure 2.18), which can bias or mask the PRF-based temperature measurement. Several strategies have been developed to correct for these susceptibility artifacts by determining the reference phase image  $\varphi_{REF}$  used in the PRF equation 2.1.

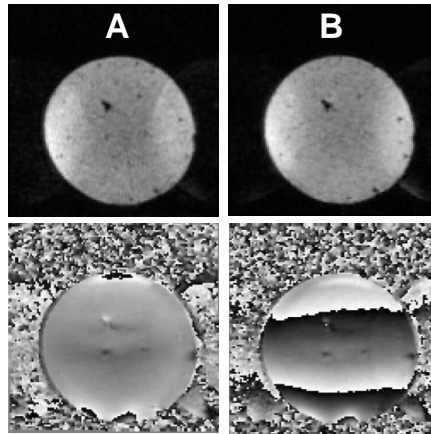


Figure 2.18: Respiratory-induced susceptibility artifacts. Magnitude and phase images of a moving phantom after registration at two different times. Phase variations are visible between (A) and (B).

### 2.4.1 Multi-baseline approach

First introduced on porcine liver [37], the multi-baseline approach consists in the collection of  $N$  images during a learning step before the ablation. The number of images  $N$  is optimized to cover several respiratory cycles (from 2 to 5). Magnitude and phase images are stored in a look-up table (LUT). Motion is depicted by a white line at the border of a gel phantom magnitude images in Figure 2.19. Examples of phase changes attributed to susceptibility variation with breathing are indicated by red arrows. During the interventional procedure, the reference phase  $\varphi_{REF}$  is selected in the LUT dataset to be subtracted to the current phase image  $\varphi$ . For that purpose, the current magnitude image is compared to the LUT magnitude images, using an inter-correlation coefficient (Figure 2.19-A). This coefficient value ranges from 0 to 1. The higher the inter-correlation coefficient is, the greater is the similarity between the two magnitude images. The phase of reference  $\varphi_{REF}$  corresponds to the phase image associated with the magnitude image with the highest inter-correlation coefficient. The subtraction of  $\varphi_{REF}$  and  $\varphi$  is finally performed (Figure 2.19-B) to compute the temperature image (Figure 2.19-C) with the PRF equation 2.1.

The multi-baseline approach is easy to implement and time efficient. However, the correction is intrinsically restrained to positions previously observed during the learning step. The similarity search that computes the best matching between the magnitude images, may introduce an approximation if the exact current position is not present in the LUT, as illustrated in Figure 2.19-A. Susceptibility artifacts caused by spontaneous motion can therefore not be corrected

with this method. A recalibration of the LUT during the intervention could be considered in case of low frame-rate imaging.

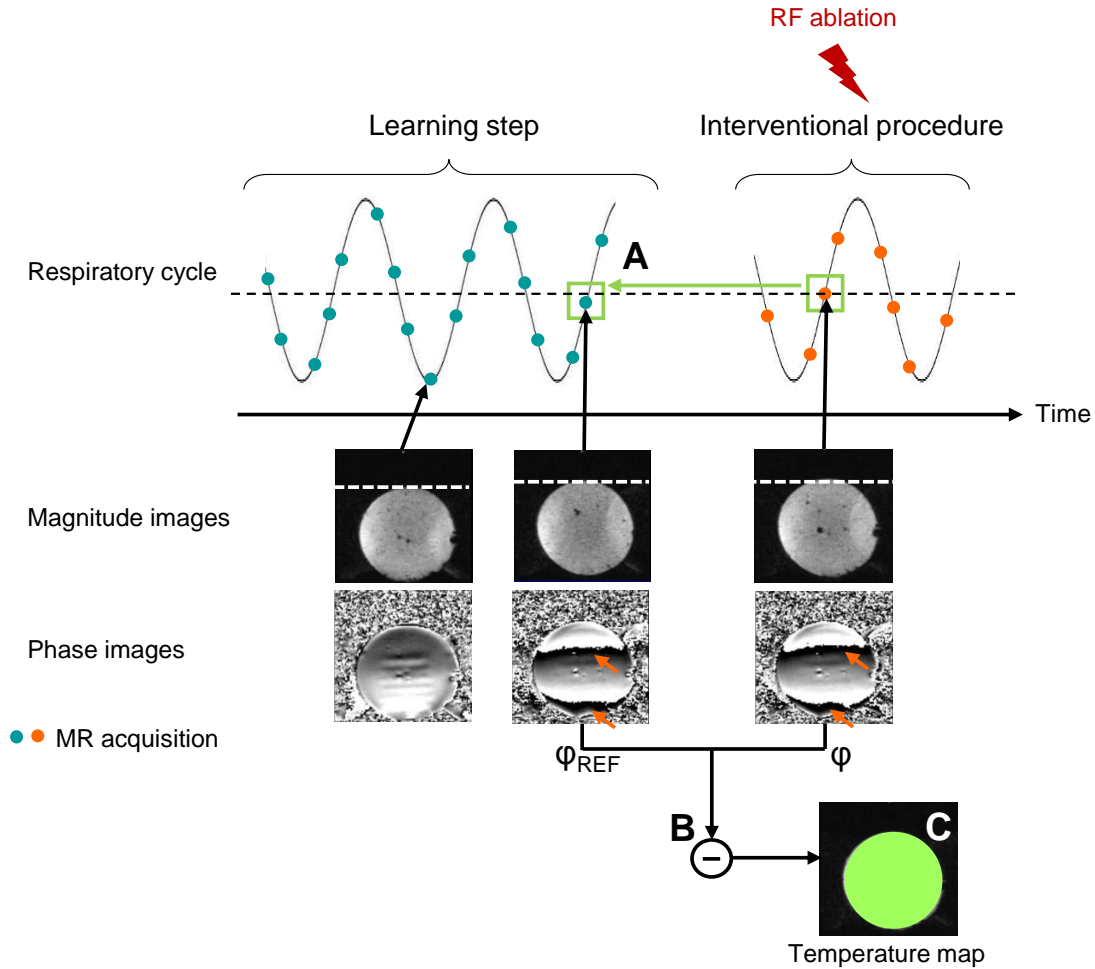


Figure 2.19: Diagram of multi-baseline approach for correction of motion-induced susceptibility artifacts with moving phantom data. During the learning step, magnitude and phase images are collected in a LUT to sample different positions of the respiratory cycle. White lines mark the upper border of the phantom, to show the motion induced to mimic the respiration. Red arrows show examples of phase variation due to susceptibility changes with motion. During the interventional procedure, the current magnitude is compared to each magnitude image of the LUT to find the best matching (A). The dashed line corresponds to the position of the current magnitude image. Note that an approximation can be made by selecting the closest magnitude in the LUT (green square). Finally, the related phase image is used as phase of reference  $\varphi_{REF}$  and is subtracted to the current phase image  $\varphi$  (B). The temperature map is finally computed (C).

#### 2.4.2 Principal Component Analysis (PCA)-based phase modeling approach

Described for the monitoring of thermotherapy of abdominal organs [38, 39], this technique aims to model a linear relation between phase variations and motion changes prior to the intervention. Similarly to the multi-baseline method, the Principal Component Analysis (PCA)-based phase modeling approach requires a learning step before the ablation where the organ motion is estimated on  $N$  magnitude images.

### Parametrized flow model and estimation of the motion descriptors

A PCA algorithm [40] is then used on the set of  $N$  flow-fields to build a parameterized motion flow model. PCA is used to compute an orthonormal basis that spans an  $N$ -dimensional vector space and to depict the characteristic patterns of the motion cycle. To reduce the dimensionality of the original data, only the eigenvectors  $B_j$  associated with the largest eigenvalues  $D_j$  can be conserved to describe the representative spatio-temporal coherence of the motion. Eigenvalues  $D_j$  are referred as “motion descriptors”.

### Modeling of motion-induced phase changes

The  $N$  phase images of the learning step are registered using the motion fields estimated on associated magnitude images. The magnetic field variations were approximated as the sum of linear phase changes of each principal motion eigenvectors on a pixel-by-pixel basis. The parametrized magnetic field model  $P_j$  is computed using a singular value decomposition (SVD) in each pixel.

### Ablation procedure

During the interventional procedure, the parametrized magnetic field model  $P_j$  is used to reconstruct the magnetic field distribution corresponding to the current position of the organ, given by the current motion descriptor  $D_j$ . A synthesized reference non-heated phase image  $\varphi_{REF}$  is calculated as follow:

$$\varphi_{REF} = \sum_{j=0}^{M-1} D_j \cdot B_j(x, y) + B_M(x, y) \quad (2.13)$$

where  $M$  represents the dimension of the PCA-based decomposition (ie, number of eigen vectors and associated eigen values);  $B_j$  are the eigen vectors maps resulting from the PCA on the data acquired during the learning step; and  $B_M$  is the phase value in each pixel that does not vary with respiration.

This method offers the ability to interpolate intermediate positions to reduce discretization errors while the multi-baseline approach is intrinsically restrained to positions observed in the learning step data. Furthermore, since the synthesized phase of reference  $\varphi_{REF}$  is noise-free, the precision of the resulting temperature maps may be improved from a factor  $\sqrt{2}$  compared to the multi-baseline method.

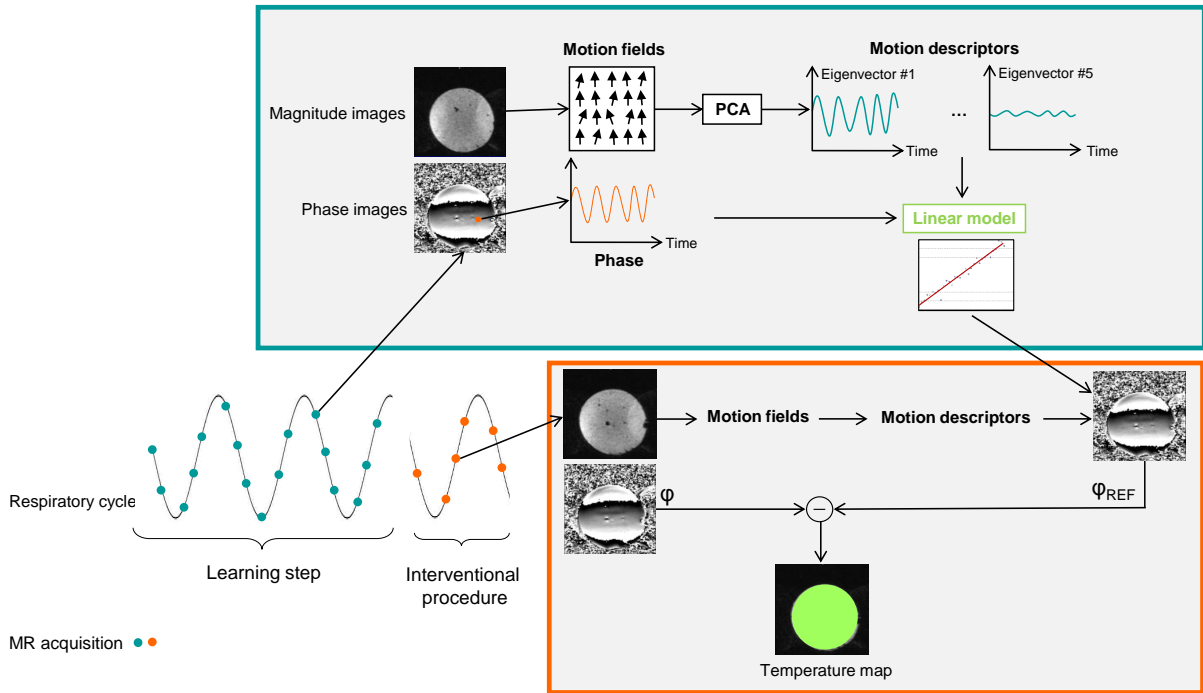


Figure 2.20: Diagram of the PCA-based phase modeling approach for correction of motion-induced susceptibility artifacts.

The linear relation between phase variation and motion can be computed using other motion descriptors than those obtained by optical-flow and PCA. In Hey et al [41], the relation was modeled as a 1<sup>st</sup> order between the phase variation and the diaphragm position detected by an echo-navigator. This was performed in the context of the MR thermometry in breast where the target is static with a background phase affected by the breathing. In Roujol et al [34] in abdominal organs (kidney and liver) and in Hey et al [33] in the heart, the phase changes were expressed as a linear combination of six free parameters (two translations, two scales, a rotation and a shear) obtained from the affine deformation estimation.

### 2.4.3 Referenceless approach

The referenceless method [42] does not require a learning step. The phase of reference  $\varphi_{REF}$  is calculated from the current phase image itself. The measured phase image is fitted by a polynomial function in a region of interest (ROI) surrounding the organ where the heated area is excluded. The selected phase must be spatially unwrapped to avoid fitting issues. After polynomial modeling of the phase, the baseline phase in the heated area is extrapolated and used as  $\varphi_{REF}$  in the PRF equation 2.1.

The referenceless approach is able to correct for susceptibility artifacts induced by any type of motion including non-periodic and spontaneous motion. However, the performance of the correction is highly dependent on the SNR of the magnitude image and on the ROI placement, size and shape. On one hand, the fitting ROI must exclude the ablation area while being sufficiently

close to allow a precise estimation of the background phase in the target area. On the other hand, the fit can be corrupted by heat diffusion if the ROI is not positioned far enough from the ablation zone. Furthermore, spatial phase unwrapping is time-consuming and complicated close to interfaces between tissues with different susceptibilities. Proximity to air-filled lungs is especially problematic.

**Referenceless/Multi-baseline hybrid approach:** Grissom et al [43] proposed to combine the referenceless and the multi-baseline methods. The accuracy of this technique was demonstrated on simulated data and in phantom with high focused ultrasound heating.

#### 2.4.4 Discussion

Table 2.1 summarizes the advantages and drawbacks of the previously presented methods of susceptibility artifacts correction: multi-baseline, phase modeling and referenceless approaches.

	Multi-baseline	Phase modeling	Referenceless
+	Easy	No need of ROI selection	No need of reference images
	No need of ROI selection	Less temperature noise  Interpolation of positions not collected in LUT	Periodic and spontaneous motions
-	Only periodic motion	Only periodic motion	Operator intervention for ROI selection
	Need of reference data	Need of reference data	Highly dependent on the ROI (size, shape, location)
	Restricted to learned positions collected in LUT	Required phase drift correction	Dependent on image quality (SNR)
	Required phase drift correction		Sensitive to large phase fluctuations (ablation area, probe, organ boundaries)
<u>REF</u>	Vigen et al, 2003, liver [37]	Roujol et al, 2010, abdominal organs [34]	Rieke et al, 2004, liver and prostate [42]
	De Senneville et al, 2012, heart [44]	De Senneville et al, 2011, liver and kidney [39]	Rieke et al, 2007, prostate [45]
		De Senneville et al, 2015, liver and kidney [46]	Holbrook et al, 2010, liver [7]

Table 2.1: Comparison of methods of susceptibility artifacts correction

Multi-baseline and phase modeling methods both require pre-heating acquisitions as reference data. Therefore these approaches intrinsically correct only for periodic motion, such as respiratory motion. Compared to standard multi-baseline approach, the phase modeling has

the advantage to not be restricted to discrete positions of the respiratory cycle, sampled during the pre-heating learning step. On the other hand, the referenceless method does not rely on reference data and thus, allows for correction of spontaneous motion.

However, this approach requires the selection of a ROI by the operator to proceed to the background phase polynomial fit. The accuracy highly depends on the size, shape and placement of this ROI. It has to be sufficiently close to the targeted area while sufficiently far to not be contaminated by the heating zone. These requirements are challenging to fulfill in the case of the heart, where only a small part of the image corresponds to myocardium. In addition, it is sensitive to large phase fluctuations, such around a RF probe or near organ boundaries. Therefore, the referenceless technique is more suitable for non-invasive heating modality, such as high intensity focused ultrasounds (HIFU), on area of homogeneous phase distribution. For more precisions, phase modeling and referenceless methods were compared on abdominal organs in [47].

## 2.5 State-of-the-art of cardiac MR thermometry

In this section, previous developments in cardiac MR thermometry are reviewed. Special attention was paid to MR acquisition methods and to motion and susceptibility artifacts compensation strategies. In Table 2.2 are summarised the findings and main characteristics of the reported cardiac MR thermometry techniques, such as the temporal and spatial resolutions and the obtained temperature precision.

First proof of feasibility of cardiac MR thermometry was demonstrated by Kolandaivelu et al. in 2010 using the PRF technique [10]. A conventional GRE acquisition was performed with a spatial resolution of  $1.7 \times 1.7 \times 4 \text{ mm}^3$  to map the temperature during RF ablation on six mongrel dogs. MR acquisition was cardiac-gated and performed during breath-holding. Potential diaphragm motion between images was registered in one direction. To compensate for susceptibility artifacts, three images were acquired prior to heating and used as learned dataset for the multi-baseline method (see section 2.4.1). Temperature rise with RF delivery was successfully visualized and lesion depth observed on temperature maps with an isotherm threshold of  $50^\circ\text{C}$  was found to be in good agreement with Gd delayed enhanced MRI and gross pathology. However, only 3 to 6 temperature maps could be acquired during the procedure due to a scan time from 10 to 20 s per image. Since the typical RF delivery lasts only 1 min, the temporal resolution appeared to be insufficient to precisely characterize the temperature evolution.

In Hey et al [33], the use of conventional GRE and single-shot GRE-EPI pulse sequences was explored in association with parallel imaging and several blood suppression techniques. Through-plane motion was compensated using a slice tracking technique based on a pencil-beam echo-navigator placed on the diaphragm (see Section 2.3.3.2). The EPI pulse sequence, associated with inflow saturation blood suppression, was found to allow the better temperature precision ( $2^\circ\text{C}$  or less in the ventricular septum). To correct for residual in-plane motion, the LV was manually segmented on the reference magnitude image and an affine transformation

(two translations, two scales, one rotation and one shear) was computed using a gradient driven descent algorithm restricted to the selected LV. Susceptibility effects were corrected with a linear phase modeling approach between the six affine coefficients and the registered phase [34]. Using SENSE parallel acquisition technique, the scan time was accelerated to 130 ms per image allowing the acquisition of three slices per heartbeat. However, the spatial resolution was limited to  $3.5 \times 3.5 \times 8 \text{ mm}^3$  due to SNR consideration. Considering the size of typical lesions, a higher spatial resolution is necessary to accurately visualize the lesion formation. This study mainly focused on the optimization of MR thermometry acquisition on the human heart in absence of heating. Hence, no monitoring of RF ablation was performed.

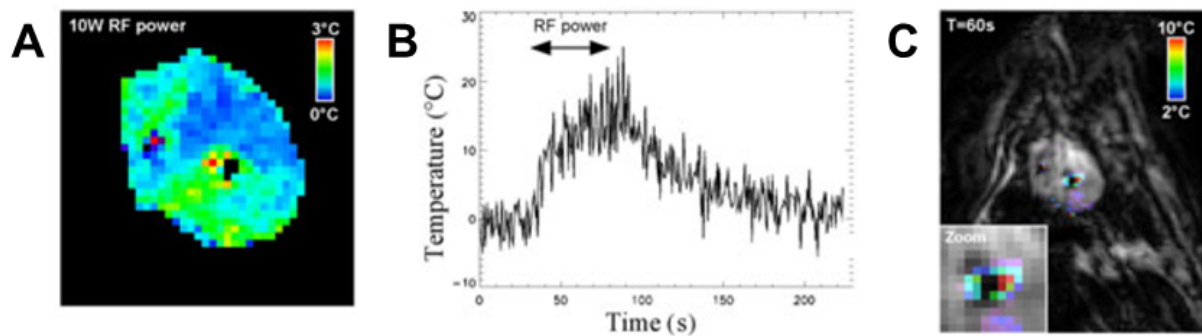


Figure 2.21: MR thermometry results of RF ablation on a sheep's left ventricle. A) Temperature precision before RF delivery. B) Temperature evolution of the temperature rise in the hottest pixel in the myocardium during 10 W RF application. C) Temperature distribution after 1 min of 10 W RF energy delivery overlaid on the anatomical image (From B.D. de Senneville et al [44] with permission).

In De Senneville et al [44], a similar imaging protocol was evaluated on ten volunteers without heating and during RF ablation of the LV of two sheep. Pencil beam slice tracking, ECG triggering and SENSE parallel imaging were combined with a single-shot EPI pulse sequence. The spatial resolution was improved to  $2.5 \times 2.5 \times 6 \text{ mm}^3$  while the temporal resolution of several slices per heartbeat was maintained. As in Hey et al, an affine transformation was estimated between each magnitude image of the time series and the reference image. However, the image registration was improved by using the six affine coefficients to precondition a more complex optical-flow algorithm. The correction of susceptibility artifacts was performed using the multi-baseline approach described in Section 2.4.1. RF ablations were successfully monitored on the LV of two sheep and temporal evolution of the temperature rise in the pixels at the vicinity of the catheter tip could be visualized, as shown in Figure 2.21. However, the voxel size of the thermometry pulse sequence remained too large compared to lesion size. The temperature uncertainty remained important during RF ablation (Figure 2.21-B)) and the heating region was limited to a small number of pixels ( $\sim 20$  pixels, Figure 2.21-C).

<b>Publication</b>	Kolandaveilu et al, 2010	Hey et al, 2012	De Senneville et al, 2012
<b>Field strength</b>	1.5 T	3 T	1.5 T
<b>Pulse sequence</b>	GRE	GRE/EPI	EPI
<b>Voxel size</b>	$1.7 \times 1.7 \times 4 \text{ mm}^3$	$3.5 \times 3.5 \times 8 \text{ mm}^3$	$2.5 \times 2.5 \times 6 \text{ mm}^3$
<b>Temporal resolution</b>	10-20 s/frame	130 ms/frame	130 ms/frame
<b>Human study</b>	×	8 volunteers	10 volunteers
<b>Animal study</b>	6 dogs	×	2 sheep
<b>Out-of-plane respiratory motion</b>	Breath-hold	Pencil-beam navigator slice following	Pencil-beam navigator slice following
<b>In-plane registration</b>	1D diaphragm registration	Affine transformation	Affine transformation + optical-flow
<b>Susceptibility artifacts correction</b>	Multi-baseline	Phase modeling	Multi-baseline
<b>Temperature precision</b>	$3.97 \pm 3.47^\circ\text{C}$ over 3 repetitions around the catheter tip in animal's LV	$1.6 \pm 0.6^\circ\text{C}$ over 50 repetitions with EPI pulse sequence on volunteers' LV	$3.6 \pm 0.9^\circ\text{C}$ over 150 repetitions on volunteers' LV
<b>Other</b>	Good correlation of transmurrity between MR thermometry (threshold $50^\circ\text{C}$ ), Gd-DE and gross pathology	Evaluation of blood suppression techniques for thermometry: inflow saturation was found to be the most robust	×

Table 2.2: State-of-the-art of cardiac MR thermometry

## 2.6 References

1. Quesson, B., de Zwart, J. A. & Moonen, C. T. Magnetic resonance temperature imaging for guidance of thermotherapy. en. *Journal of Magnetic Resonance Imaging* **12**, 525–533. ISSN: 1053-1807, 1522-2586 (Oct. 2000).
2. Rieke, V. & Butts Pauly, K. MR thermometry. en. *Journal of Magnetic Resonance Imaging* **27**, 376–390. ISSN: 10531807, 15222586 (Feb. 2008).
3. De Zwart, J. A., van Gelderen, P., Kelly, D. J. & Moonen, C. T. Fast magnetic-resonance temperature imaging. *Journal of Magnetic Resonance, Series B* **112**, 86–90 (1996).

4. Carpentier, A. *et al.* REAL-TIME MAGNETIC RESONANCE-GUIDED LASER THERMAL THERAPY FOR FOCAL METASTATIC BRAIN TUMORS: en. *Operative Neurosurgery* **63**, ONS21–ONS29. ISSN: 2332-4252 (July 2008).
5. Tempany, C. M. C. *et al.* MR Imaging-guided Focused Ultrasound Surgery of Uterine Leiomyomas: A Feasibility Study. en. *Radiology* **226**, 897–905. ISSN: 0033-8419, 1527-1315 (Mar. 2003).
6. Weidensteiner, C. *et al.* Real-time MR temperature mapping of rabbit liver in vivo during thermal ablation. en. *Magnetic Resonance in Medicine* **50**, 322–330. ISSN: 0740-3194, 1522-2594 (Aug. 2003).
7. Holbrook, A. B., Santos, J. M., Kaye, E., Rieke, V. & Pauly, K. B. Real-time MR thermometry for monitoring HIFU ablations of the liver. en. *Magnetic Resonance in Medicine* **63**, 365–373. ISSN: 07403194, 15222594 (Feb. 2010).
8. Conturo, T. E. & Smith, G. D. Signal-to-noise in phase angle reconstruction: dynamic range extension using phase reference offsets. *Magnetic Resonance in Medicine* **15**, 420–437 (1990).
9. Nath, S., Lynch, C., Wayne, J. G. & Haines, D. E. Cellular electrophysiological effects of hyperthermia on isolated guinea pig papillary muscle. Implications for catheter ablation. en. *Circulation* **88**, 1826–1831. ISSN: 0009-7322, 1524-4539 (Oct. 1993).
10. Kolandaivelu, A. *et al.* Noninvasive Assessment of Tissue Heating During Cardiac Radiofrequency Ablation Using MRI Thermography. en. *Circulation: Arrhythmia and Electrophysiology* **3**, 521–529. ISSN: 1941-3149, 1941-3084 (Oct. 2010).
11. Wood, M. *et al.* Direct Measurement of the Lethal Isotherm for Radiofrequency Ablation of Myocardial Tissue. en. *Circulation: Arrhythmia and Electrophysiology* **4**, 373–378. ISSN: 1941-3149, 1941-3084 (June 2011).
12. Sapareto, S. A. & Dewey, W. C. Thermal dose determination in cancer therapy. *International Contact Lens Clinic* **16**, 340–346 (1989).
13. Dewhirst, M. W., Viglianti, B. L., Lora-Michiels, M., Hanson, M. & Hoopes, P. J. Basic principles of thermal dosimetry and thermal thresholds for tissue damage from hyperthermia. en. *International Journal of Hyperthermia* **19**, 267–294. ISSN: 0265-6736, 1464-5157 (Jan. 2003).
14. Köhler, M. O., Denis de Senneville, B., Quesson, B., Moonen, C. T. & Ries, M. Spectrally selective pencil-beam navigator for motion compensation of MR-guided high-intensity focused ultrasound therapy of abdominal organs. en. *Magnetic Resonance in Medicine* **66**, 102–111. ISSN: 07403194 (July 2011).
15. Pruessmann, K. P., Weiger, M., Scheidegger, M. B., Boesiger, P., *et al.* SENSE: sensitivity encoding for fast MRI. *Magnetic resonance in medicine* **42**, 952–962 (1999).
16. Griswold, M. A. *et al.* Generalized autocalibrating partially parallel acquisitions (GRAPPA). en. *Magnetic Resonance in Medicine* **47**, 1202–1210. ISSN: 0740-3194, 1522-2594 (June 2002).

17. Ehman, R., McNamara, M., Pallack, M., Hricak, H. & Higgins, C. Magnetic resonance imaging with respiratory gating: techniques and advantages. en. *American Journal of Roentgenology* **143**, 1175–1182. ISSN: 0361-803X, 1546-3141 (Dec. 1984).
18. Santelli, C. *et al.* Respiratory bellows revisited for motion compensation: Preliminary experience for cardiovascular MR. en. *Magnetic Resonance in Medicine* **65**, 1097–1102. ISSN: 07403194 (Apr. 2011).
19. Danias, P. G. *et al.* Prospective navigator correction of image position for coronary MR angiography. en. *Radiology* **203**, 733–736. ISSN: 0033-8419, 1527-1315 (June 1997).
20. Liu, Y. L. *et al.* A monitoring, feedback, and triggering system for reproducible breath-hold MR imaging. *Magnetic resonance in medicine* **30**, 507–511 (1993).
21. Wang, Y., Grimm, R. C., Felmlee, J. P., Riederer, S. J. & Ehman, R. L. Algorithms for extracting motion information from navigator echoes. *Magnetic resonance in medicine* **36**, 117–123 (1996).
22. Wang, Y., Riederer, S. J. & Ehman, R. L. Respiratory motion of the heart: kinematics and the implications for the spatial resolution in coronary imaging. *Magnetic Resonance in Medicine* **33**, 713–719 (1995).
23. Danias, P. G. *et al.* Relationship between motion of coronary arteries and diaphragm during free breathing: lessons from real-time MR imaging. *AJR. American journal of roentgenology* **172**, 1061–1065 (1999).
24. Keegan, J., Gatehouse, P., Yang, G.-Z. & Firmin, D. Coronary artery motion with the respiratory cycle during breath-holding and free-breathing: Implications for slice-followed coronary artery imaging. en. *Magnetic Resonance in Medicine* **47**, 476–481. ISSN: 0740-3194, 1522-2594 (Mar. 2002).
25. Taylor, A. M., Jhooti, P., Firmin, D. N. & Pennell, D. J. Automated monitoring of diaphragm end-expiratory position for real-time navigator echo MR coronary angiography. en. *Journal of Magnetic Resonance Imaging* **9**, 395–401. ISSN: 1053-1807, 1522-2586 (Mar. 1999).
26. Moghari, M. H. *et al.* Subject-specific estimation of respiratory navigator tracking factor for free-breathing cardiovascular MR. en. *Magnetic Resonance in Medicine* **67**, 1665–1672. ISSN: 07403194 (June 2012).
27. Settecase, F., Martin, A. J., Lillaney, P., Losey, A. & Hetts, S. W. Magnetic Resonance–Guided Passive Catheter Tracking for Endovascular Therapy. en. *Magnetic Resonance Imaging Clinics of North America* **23**, 591–605. ISSN: 10649689 (Nov. 2015).
28. Wang, W. Magnetic Resonance–guided Active Catheter Tracking. en. *Magnetic Resonance Imaging Clinics of North America* **23**, 579–589. ISSN: 10649689 (Nov. 2015).
29. Dumoulin, C. L., Souza, S. P. & Darrow, R. D. Real-time position monitoring of invasive devices using magnetic resonance. *Magnetic Resonance in Medicine* **29**, 411–415 (1993).
30. Wech, T. *et al.* Measurement accuracy of different active tracking sequences for interventional MRI: Accuracy of Different Tracking Sequences. en. *Journal of Magnetic Resonance Imaging* **40**, 490–495. ISSN: 10531807 (Aug. 2014).

31. Schmidt, E. J. *et al.* Electroanatomic Mapping and Radiofrequency Ablation of Porcine Left Atria and Atrioventricular Nodes Using Magnetic Resonance Catheter Tracking. en. *Circulation: Arrhythmia and Electrophysiology* **2**, 695–704. ISSN: 1941-3149, 1941-3084 (Dec. 2009).
32. Vergara, G. R. *et al.* Real-time magnetic resonance imaging-guided radiofrequency atrial ablation and visualization of lesion formation at 3 Tesla. en. *Heart Rhythm* **8**, 295–303. ISSN: 15475271 (Feb. 2011).
33. Hey, S. *et al.* Towards optimized MR thermometry of the human heart at 3T: CARDIAC MR THERMOMETRY AT 3T. en. *NMR in Biomedicine* **25**, 35–43. ISSN: 09523480 (Jan. 2012).
34. Roujol, S., Ries, M., Quesson, B., Moonen, C. & Denis de Senneville, B. Real-time MR-thermometry and dosimetry for interventional guidance on abdominal organs. en. *Magnetic Resonance in Medicine* **63**, 1080–1087. ISSN: 07403194, 15222594 (Apr. 2010).
35. Horn, B. K. & Schunck, B. G. Determining optical flow. *Artificial intelligence* **17**, 185–203 (1981).
36. Black, M. J. & Anandan, P. *A framework for the robust estimation of optical flow in Computer Vision, 1993. Proceedings., Fourth International Conference on* (IEEE, 1993), 231–236. <[http://ieeexplore.ieee.org/xpls/abs\\_all.jsp?arnumber=378214](http://ieeexplore.ieee.org/xpls/abs_all.jsp?arnumber=378214)> (visited on 08/29/2016).
37. Vigen, K. K., Daniel, B. L., Pauly, J. M. & Butts, K. Triggered, navigated, multi-baseline method for proton resonance frequency temperature mapping with respiratory motion. en. *Magnetic Resonance in Medicine* **50**, 1003–1010. ISSN: 0740-3194, 1522-2594 (Nov. 2003).
38. Maclair, G. *et al.* *PCA-based magnetic field modeling: Application for on-line MR temperature monitoring in International Conference on Medical Image Computing and Computer-Assisted Intervention* (Springer, 2007), 411–419. <[http://link.springer.com/chapter/10.1007/978-3-540-75759-7\\_50](http://link.springer.com/chapter/10.1007/978-3-540-75759-7_50)> (visited on 08/23/2016).
39. De Senneville, B. D., Ries, M., Maclair, G. & Moonen, C. MR-Guided Thermotherapy of Abdominal Organs Using a Robust PCA-Based Motion Descriptor. *IEEE Transactions on Medical Imaging* **30**, 1987–1995. ISSN: 0278-0062, 1558-254X (Nov. 2011).
40. Hotelling, H. Analysis of a complex of statistical variables into principal components. en. *Journal of Educational Psychology* **24**, 417–441. ISSN: 0022-0663 (1933).
41. Hey, S. *et al.* Online correction of respiratory-induced field disturbances for continuous MR-thermometry in the breast. en. *Magnetic Resonance in Medicine* **61**, 1494–1499. ISSN: 07403194, 15222594 (June 2009).
42. Rieke, V. *et al.* Referenceless PRF shift thermometry. *Magnetic resonance in medicine* **51**, 1223–1231 (2004).
43. Grissom, W. A. *et al.* Hybrid referenceless and multibaseline subtraction MR thermometry for monitoring thermal therapies in moving organs. en. *Medical Physics* **37**, 5014. ISSN: 00942405 (2010).

44. De Senneville, B. D. *et al.* Feasibility of fast MR-thermometry during cardiac radiofrequency ablation: FEASIBILITY OF FAST MR-THERMOMETRY DURING CARDIAC RF ABLATION. en. *NMR in Biomedicine* **25**, 556–562. ISSN: 09523480 (Apr. 2012).
45. Rieke, V. *et al.* Referenceless MR Thermometry for Monitoring Thermal Ablation in the Prostate. *IEEE Transactions on Medical Imaging* **26**, 813–821. ISSN: 0278-0062 (June 2007).
46. Denis de Senneville, B., El Hamidi, A. & Moonen, C. A Direct PCA-Based Approach for Real-Time Description of Physiological Organ Deformations. *IEEE Transactions on Medical Imaging* **34**, 974–982. ISSN: 0278-0062, 1558-254X (Apr. 2015).
47. De Senneville, B. D., Roujol, S., Moonen, C. & Ries, M. Motion correction in MR thermometry of abdominal organs: A comparison of the referenceless vs. the multibaseline approach. en. *Magnetic Resonance in Medicine* **64**, 1373–1381. ISSN: 07403194 (Nov. 2010).

## Chapter 3

# Improved Cardiac Magnetic Resonance Thermometry and Dosimetry for Monitoring Lesion Formation During Catheter Ablation

### Contents

---

<b>3.1</b>	<b>Preamble</b> . . . . .	<b>60</b>
<b>3.2</b>	<b>Abstract</b> . . . . .	<b>60</b>
<b>3.3</b>	<b>Introduction</b> . . . . .	<b>61</b>
<b>3.4</b>	<b>Methods</b> . . . . .	<b>62</b>
3.4.1	Volunteer study . . . . .	62
3.4.2	Animal study . . . . .	63
3.4.3	RF ablation device and MR-Compatible EP . . . . .	63
3.4.4	Magnetic resonance data acquisition . . . . .	64
3.4.5	Thermometry pipeline . . . . .	65
3.4.6	Image registration . . . . .	65
3.4.7	Correction of respiratory-induced susceptibility changes . . . . .	65
3.4.8	Spatio-temporal phase-drift correction . . . . .	66
3.4.9	Temporal temperature filtering . . . . .	67
3.4.10	Thermal dose calculation . . . . .	67
3.4.11	Statistical analysis . . . . .	67
<b>3.5</b>	<b>Results</b> . . . . .	<b>68</b>
3.5.1	Volunteer temperature imaging . . . . .	68
3.5.2	In vivo RF ablation of the LV in a Sheep . . . . .	70
<b>3.6</b>	<b>Discussion</b> . . . . .	<b>74</b>
3.6.1	Study limitations . . . . .	76
<b>3.7</b>	<b>Conclusions</b> . . . . .	<b>76</b>

<b>3.8</b>	<b>References</b> . . . . .	<b>77</b>
<b>3.9</b>	<b>Technical and practical implementation</b> . . . . .	<b>80</b>
3.9.1	Gadgetron . . . . .	80
3.9.2	Hardware . . . . .	80
3.9.3	Temporal phase unwrapping . . . . .	82
3.9.4	PCA-based implementation for calculation of synthetic background phase	83

---

### 3.1 Preamble

In this chapter, a number of challenges described in Chapter 2 was addressed to build a cardiac MR thermometry pipeline. At the beginning of this PhD thesis, only a limited number of studies had investigated the feasibility of temperature mapping of the heart. Since no MR thermometry method was available at the IHU LIRYC institute at that time, significant work has been achieved during the 1<sup>st</sup> year of PhD to review the state-of-the-art MR thermometry methods, originally applied on other moving organs. A commercial echo-planar imaging pulse sequence was optimized to fulfill the requirements of fast MR thermometry of the heart. Susceptibility artifacts correction methods and other post-processing algorithms (motion compensation, phase unwrapping, phase drift correction) were first implemented and evaluated in Matlab, as part of this PhD work. The MR thermometry pipeline was then implemented in C++ for real-time execution and integrated to an open-source image reconstruction framework (Gadgetron).

This chapter corresponds to a full paper published by Valery Ozenne, Solenn Toupin et al., in the Magnetic Resonance in Medicine (MRM) journal in February 2016 [1]. Very few modifications were introduced to harmonize the notations of this thesis manuscript.

### 3.2 Abstract

**Purpose:** A new real-time MR-thermometry pipeline was developed to measure multiple temperature images per heartbeat with  $1.6 \times 1.6 \times 3$  mm<sup>3</sup> spatial resolution. The method was evaluated on 10 healthy volunteers and during radiofrequency (RF) ablation in sheep.

**Methods:** Multi-slice, electrocardiogram-triggered, echo planar imaging was combined with parallel imaging, under free breathing conditions. In-plane respiratory motion was corrected on magnitude images by an optical-flow algorithm. Motion-related susceptibility artifacts were compensated on phase images by an algorithm based on Principal Component Analysis. Correction of phase drift and temporal filter were included in the pipeline implemented in the Gadgetron framework. Contact electrograms were recorded simultaneously with MR thermometry by an MR-compatible ablation catheter.

**Results:** The temporal standard deviation of temperature in the left ventricle remained below 2°C on each volunteer. In sheep, focal heated regions near the catheter tip were observed on temperature images (maximal temperature increase of 38°C) during RF ablation, with contact

electrograms of acceptable quality. Thermal lesion dimensions at gross pathology were in agreement with those observed on thermal dose images.

**Conclusion:** This fully automated MR thermometry pipeline (five images per heartbeat) provides direct assessment of lesion formation in the heart during catheter-based RF ablation, which may improve treatment of cardiac arrhythmia by ablation.

### 3.3 Introduction

Catheter ablation using radiofrequency (RF) energy is used commonly to treat cardiac arrhythmia when antiarrhythmic drugs fail, with approximately 200,000 procedures in Europe in 2012 [2]. During this procedure, RF energy is applied to the electrode in contact with the cardiac tissue, inducing a strong current density and an increase in tissue temperature (resistive heating) that may permanently kill the cells when it reaches 60°C [3]. Currently, there is no direct assessment of lesion formation during RF delivery. Some predictions of lesion size and depth have been made based on contact force in bench and in vivo animal studies. However, they are still far from perfect. From both a safety and efficacy stand point, the ideal lesion is transmural, with no extra-cardiac extension and damage, but with complete cell destruction to prevent cell recovery and arrhythmia recurrence. These features are necessary to reduce the likelihood of severe complications such as atriophagial fistulas or tamponade (resulting from a “pop”) and to prevent pulmonary vein reconnections that occur in up to 30% of atrial fibrillation (AF) ablation procedures. These examples taken from AF ablation are also valid for other types of complex arrhythmia such as ventricular tachycardia (VT) or atrial tachycardias (ATs), in which both safety and efficacy are limited by the absence of direct lesion formation monitoring.

Direct monitoring of tissue temperature during RF delivery could dramatically improve both the safety and efficacy of cardiac ablation. MRI thermometry, frequently based on proton resonance frequency (PRF) shift imaging [4], has been developed over the last decade and clinically applied to a wide range of organs (eg, uterus, brain, liver, kidney) for online monitoring of the thermal treatment of various diseases (eg, uterine fibroid, bone metastasis, liver cancer, essential tremor) with demonstrated benefits [5, 6]. Cardiac thermometry is by far the most challenging because of the combined respiratory and cardiac motion that may induce changes in proton phase and therefore errors in temperature measurements.

Furthermore, the blood flow in the cardiac cavities can affect the image quality, thereby reducing the accuracy of temperature mapping. To overcome these problems, several strategies have been proposed, such as hybrid referenceless and multi-baseline subtraction [7], or navigator echoes combined with blood suppression techniques [8]. Hey et al [8] compared several strategies to cancel the blood signal in the cavities to improve image-based registration techniques. Although performed at 3 T, the gain in signal-to-noise ratio (SNR) could not be used to improve the spatial resolution of the thermometry sequence. To be clinically relevant, cardiac MR thermometry should provide imaging at least every second, with at least 2 mm spatial resolution to allow real-time monitoring of tissue temperature and therefore lesion formation. In addi-

tion, dedicated MR-compatible instrumentation must be used to allow RF ablation and contact electrophysiology (EP) signal recording. A number of studies have reported the use of fully MRI-guided clinical electrophysiology, demonstrating that safety issues (eg, risks of catheter heating by MRI pulse sequence) can be solved [9]. Three-dimensional (3D) catheter tracking has also been demonstrated using either passive [10, 11] or active methods [12, 13], and RF ablation inside an MRI bore was also successfully reported recently [14, 15]. Only a limited number of studies [16–18] have reported attempts to address the challenges of cardiac MR thermometry to monitor ablation in real time. Volland et al [16] investigated the feasibility of acquiring limited fields using local MR coils to increase signal sensitivity. In de Senneville et al [18], a single-shot echo planar imaging (EPI) was synchronized with the surface electrocardiogram (ECG) to allow acquisition of several slices per heartbeat. In addition, slice position was continuously updated from echo-navigator readings acquired at the liver-lung interface to reduce respiratory motion and residual in-plane motion, and susceptibility artifacts were compensated with an atlas-based correction technique. However, visualization of temperature increase was restricted to a limited number of pixels in an *in vivo* sheep heart during RF ablation, as a result of insufficient spatial resolution ( $2.5 \times 2.5 \times 6 \text{ mm}^3$ ) and the non-irrigated catheter. Moreover, temperature uncertainty remained too large to evaluate the thermal lesion.

The present study proposes an improved cardiac MR thermometry method operating at 1.5T and displaying several slices per heartbeat with increased spatial resolution ( $1.6 \times 1.6 \times 3 \text{ mm}^3$ ) to resolve temperature distribution in the myocardium during RF ablation. To this end, a fully automated cardiac thermometry pipeline was developed to allow online monitoring of cardiac temperature. The method relies on ECG-triggered EPI acquired under free breathing, associated with parallel imaging and in-plane motion correction using an optical-flow algorithm, allowing voxel-wise registration of all incoming temperature maps on the fly. A principal component analysis (PCA) method was implemented to compensate for any motion-related susceptibility artifacts on phase images that do not require an explicit measurement of all heart positions during the preparation phase. Moreover, real-time correction of phase drift is also proposed and a temporal filter was implemented to increase temperature precision with minimal impact on measurement latency. The method was first evaluated in 10 healthy volunteers under free breathing. This fully automated pipeline compensates for the different sources of artifacts and overcomes the current limitations of cardiac MR thermometry. Online determination of the cumulative thermal dose (TD) was finally evaluated on a large animal model during RF ablation performed with an irrigated, MR-compatible RF ablation catheter, allowing simultaneous recording of contact electrograms and lesion assessment through online MR-thermal dosimetry.

## 3.4 Methods

### 3.4.1 Volunteer study

Ten healthy volunteers ( $31 \pm 6$  years) were scanned to assess temperature stability under free breathing conditions. Each volunteer was informed about the protocol and consented to participate in the study.

### 3.4.2 Animal study

The animal experiment was approved by the ethics committee of the University of Bordeaux. One adult sheep (50 kg) was sedated by intramuscular injection of 1 mg/kg acepromazine (Calmivet, Vetoquinol, Lure, France) and anesthetized by an intravenous injection of ketamine (40 mg/kg/h, IM, Virbac, Carros, France) and 2 mg/kg/h midazolam (Mylan, Canonsburg, Pennsylvania). General anesthesia was maintained using continuous intravenous injection of 40 mg/kg/h ketamine and 2 mg/kg/h midazolam. After induction of anesthesia, the animal was intubated, ventilated, and then installed in a supine position on an MR/X-ray-compatible stretcher (Ferno, SMSp, France). The right femoral vein and artery were cannulated with an 8 French sheath. Two MR-compatible RF ablation catheters (Biosense Webster, Diamond Bar, California) were advanced and positioned into the right ventricle (for cardiac pacing) and the left ventricle (for ablation) under fluoroscopic guidance (Toshiba InfiniX, Toshiba Medical, Nasu, Japan). Each catheter was 2.66 mm in diameter (8 French) with four electrodes located near the tip (a large one at the tip for ablation followed by three smaller rings, all being used for contact EP recordings), identical to standard, non-MR-compatible ablation catheters. Right ventricle (RV) pacing was chosen to reduce the likelihood of commonly observed ventricular arrhythmia induced by catheter ablation in large animal models. After positioning the catheters, the animal was moved to the MR lab for temperature imaging using the stretcher to avoid catheter displacement. Once the MR-guided RF ablation experiment was completed, the animal received a lethal intravenous dose of Dolethal (Vetoquinol, Lure, France), and the heart was excised for gross pathology analysis. The heart sample was dissected in thin (~5 mm) slices from base to apex. Each slice surrounding the different positions of the catheter was photographed. In cases in which a lesion could be identified at visual inspection, its dimensions were measured with a ruler.

### 3.4.3 RF ablation device and MR-Compatible EP

The tip electrode of the catheter inserted into the left ventricle (LV) was connected to a clinical RF ablation generator (Stockert Medical Solution, Freiburg, Germany) located outside the Faraday cage. During ablation, the catheter was irrigated with continuous flow (17 mL/min) using a saline solution (0.9 % concentration) to reduce temperature increase at the catheter-tissue interface and maintain electrical conductivity. The heart was paced to overdrive sinus rhythm using the second catheter with a pulse generator (Agilent, Santa Clara, CA, U.S.A.). Cables from each catheter were extended and connected to a clinical EP acquisition system Bard (Lab-System PRO, Boston Scientific, Marlborough, MA, U.S.A.) located outside the Faraday cage. Band Reject Filters (attenuation  $\geq 40$  dB) tuned to the MR proton resonant frequency (64 MHz) were designed and inserted into the transmission line of each electrode. The voltage between the two distal electrodes (1-4) was displayed continuously on the EP console. Each signal was processed on the EP console using a band rejection filter (bandwidth: 1-250 Hz) and a Butterworth low-pass filter (cutoff frequency: 50 Hz).

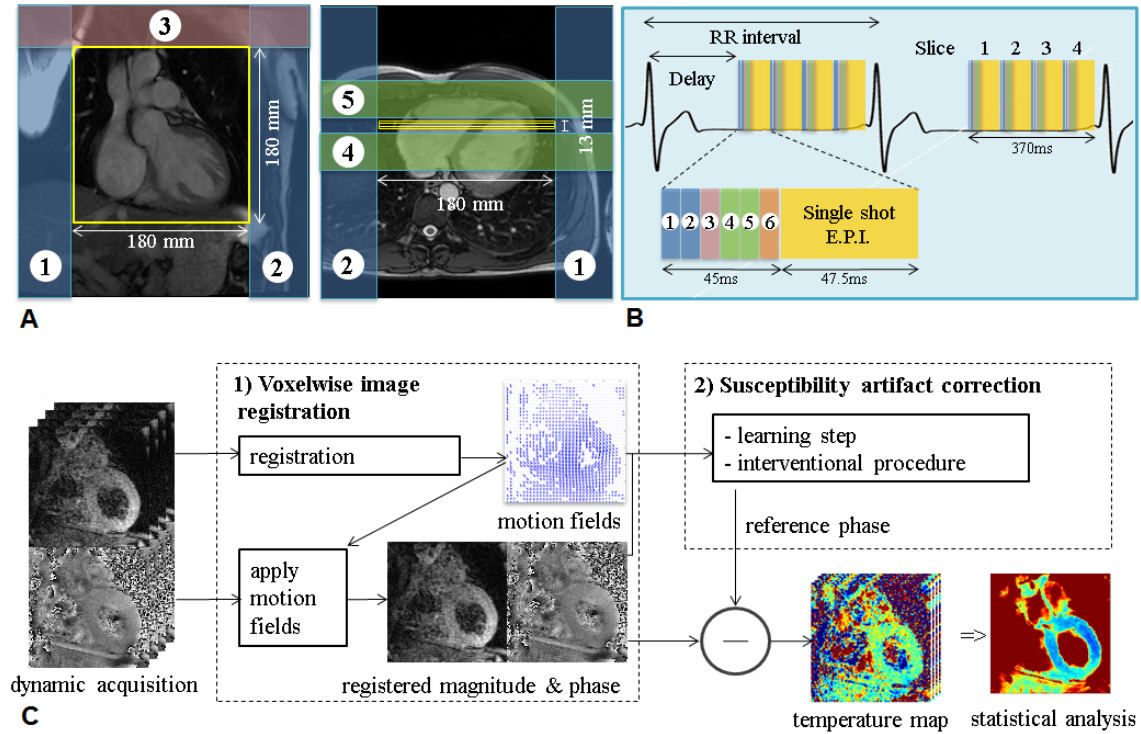


Figure 3.1: Real-time cardiac magnetic resonance thermometry pipeline. (A) b-SSFP images in coronal and transversal orientation on a volunteer showing slice and saturation band positioning for cardiac thermometry in coronal orientation. Two saturation slabs are positioned along the FOV (labeled 1 and 2) in the phase-encoding direction. Additional saturation bands (3, 4, and 5) are set parallel and perpendicular to the imaging slice to reduce the signal from blood. The gap between the sat slabs 4 and 5 and slice stack is 5 mm. (B) Timing of MR thermometry acquisition relative to the RR interval. Labels 1, 2, 3, 4, and 5 on the insert are the saturation slabs and label 6 represents the fat saturation. (C) Dynamic MR imaging is performed using ECG triggering under free breathing. Intrascan motions are compensated for using a nonrigid registration algorithm: Estimation of displacements on a pixel-by-pixel basis results from the analysis of intensity conservation between incoming magnitude image and a reference image. Motion fields are then applied to phase images to follow specific voxel temperature elevation. To address respiratory-induced susceptibility changes, the LUT method or synthetic modeling phase PCA is initialized during a pretreatment period. These reference data are then subtracted from the incoming registered phase during the interventional procedure

### 3.4.4 Magnetic resonance data acquisition

Imaging was performed on a 1.5 T MAGNETOM Avanto MR scanner (Siemens Healthcare, Erlangen, Germany) equipped with two 16-channel cardiac coils. Coils were positioned below and above the thorax on the volunteers, whereas on the animal they were positioned lateral to the thorax to maximize the number of elements near the heart. A dynamic, multi-slice acquisition was performed using a single-shot gradient EPI sequence. Four to five slices in sagittal or coronal orientation (Figure 3.1-A) were acquired sequentially in ascending order within the same heartbeat, over 250 successive cardiac cycles. The following imaging protocol was used:  $180 \times 180 \text{ mm}^2$  field of view (FOV),  $110 \times 110$  matrix (resulting in an in-plane resolution of  $1.6 \times 1.6 \text{ mm}^2$ ), 3 mm slice thickness, 0.3-mm gap between slices, flip angle (FA)  $60^\circ$ , bandwidth = 1568 Hz/pixel, TE = 19 ms, TR = 92.5 ms, GRAPPA acceleration factor of 2 with 75% partial

Fourier acquisition. Two saturation slabs were positioned along the FOV (Figure 3.1-A) in the phase-encoding direction to avoid aliasing, and three additional saturation bands were set parallel and perpendicular to the imaging slice to reduce blood signal, as suggested in [8]. A fat-selective pulse (Gaussian, 5 ms in duration) surrounded by spoiler gradients was used to cancel the lipid signal. All saturation slabs were played before each slice (Figure 3.1-B). The effective slice update time was given by the cardiac cycle duration, as the sequence was ECG-triggered. The delay between QRS detection and the beginning of the acquisition of the first slice were adjusted manually to ensure that all slices could be included within a single heartbeat. Depending on the cardiac cycle duration and number of slices, this corresponded to mid/end diastolic phases.

### 3.4.5 Thermometry pipeline

Raw data were streamed through TCP/IP to the Gadgetron framework for online image reconstruction [19]. The pipeline was run on a Core i7-4790 processor (3.6 GHz, four cores, INTEL Santa Clara, CA, U.S.A.) operating under Linux and including EPI ghost-correction and GRAPPA [20] reconstruction. Several additional modules (“gadgets”) were implemented in house and inserted into this framework for real-time thermometry. This included motion correction using Graphics Processing Unit (GPU) graphic cards (Quadro K620, NVIDIA, Santa Clara, CA, U.S.A.) and susceptibility artifact correction (see subsequently for implementation details). The resulting temperature images were sent to a remote host computer for display on dedicated thermometry software (Thermoguide, IGT, Pessac, France). All data were transferred by TCP/IP networking on a subsecond timescale.

### 3.4.6 Image registration

Through-plane motion was minimized by setting the imaging plane in sagittal or coronal orientation to visualize the heart displacement related to respiratory motion. An optical-flow algorithm [21] was used to register in-plane motion on magnitude and phase images at a fixed position and to compute displacement field  $(u,v)$  for each acquisition as previously published [8, 22]. To deal with large displacement amplitudes ( $\sim 2$  cm for respiration, corresponding to 12 pixels), a coarse-to-fine multi-resolution approach was used, which iterated the optical-flow algorithm on an image pyramid with four levels up to the original image resolution [23, 24]. The reference image was automatically picked at the center of the respiratory cycle using the following method: 1) The first 10 magnitude images were registered on the first image independently for each slice; and 2) the resulting motion fields were averaged and sorted to find the median position in the respiratory cycle in the largest displacement axis. Once this automatic reference image was selected, the temperature calculation was performed iteratively on each new incoming dataset.

### 3.4.7 Correction of respiratory-induced susceptibility changes

Respiratory-related susceptibility effects were corrected using two alternative multi-baseline correction strategies (a “look-up table” (LUT) based method [25] and a PCA-based method [26]) to compare the temperature accuracy in the context of cardiac thermometry. Although the

LUT-based method was solely restrained to positions observed during the learning step, the PCA-based method extended the correction to nonobserved positions. For both methods, a learning step (30 dynamic acquisitions, lasting approximately 30 s) was performed to generate reference data that were used during the interventional procedure (210 dynamic acquisitions, approximately 3'30 min) (Figure 3.1-C). The PCA-based method collected optical-flow fields from registration during the learning step and built a parameterized flow model using the PCA algorithm. The overall magnetic field variations were approximated as the sum of linear phase changes of each motion descriptor (noted as  $d_j$ ) on a pixel-by-pixel basis, giving a parameterized magnetic field model (noted as  $B_j$ ) [26]. During the intervention, the largest PCA-based motion descriptors were estimated from the current flow field of magnitude images and used to reconstruct the background phase ( $\varphi_{REF}$ ) distribution from the parameterized model (details on the PCA component determination (N) can be found in [26]):

$$\varphi_{REF} = \sum_{j=0}^{N-1} d_j \cdot B_j(x, y) + B_N(x, y) \quad (3.1)$$

where N represents the dimension of the PCA-based decomposition (ie, number of eigen vectors and associated eigen values);  $B_j$  are the eigen vectors maps resulting from the PCA on the data acquired during the learning step; and  $B_N$  is the phase value in each pixel that does not vary with respiration. The three eigen vectors with the highest eigen values were selected to compute the synthetic reference phase map. The sum of these three eigen values represented more than 95% of the eigen values resulting from the PCA. The synthetic phase  $\varphi_{REF}$  was subtracted from the experimental phase and the temperature was computed using the PRF shift ( $\alpha_{PRF} = -0.0094$  ppm/°C) [4].

### 3.4.8 Spatio-temporal phase-drift correction

Potential phase drift over the 4 min of acquisition was approximated as a spatio-temporal first-order polynomial function:

$$P(x, y, t) = a \cdot x + b \cdot y + c \cdot t + d \quad (3.2)$$

where a, b, c and d are parameters to be defined from experimental temperature images. For each slice, each new magnitude image registered to the reference position was averaged with all previously acquired images. Regions with low SNR on the resulting averaged magnitude images were masked out using a threshold value equal to three times the standard deviation of the noise. A second mask was computed to remove all voxels with a temporal standard deviation of temperature ( $\sigma_T$ ) higher than a predefined threshold (a typical value of 4°C was employed in this study). For this purpose, the  $\sigma_T$  and temporal mean ( $\mu_T$ ) images were computed iteratively for each slice using the following formulas:

$$\mu_{d+1} = \frac{T_{d+1}}{d+1} + \frac{d}{d+1} \times \mu_d \quad (3.3)$$

$$\sigma_{d+1} = \frac{(T_{d+1} - \mu_{d+1})^2 + d \times \sigma_d}{d+1} \quad (3.4)$$

where  $d$  is the dynamic number and  $\sigma_d$  the temperature map at dynamic number  $d$ .

On the last available temperature image, regions with temperatures over  $5^\circ\text{C}$  were masked out to automatically exclude the heated regions close to the catheter. A resulting mask was computed using the intersection of the three masks (magnitude,  $\sigma_T$  and temperature). The fit to Eq. 3.2 was performed on the last 20 temperature images using pixels included in this mask. A temporal sliding window of 20 dynamic acquisitions starting at the beginning of the interventional procedure (no correction was applied for the first 20 dynamic acquisitions) was used to iteratively update the coefficients ( $a$ ,  $b$ ,  $c$ ,  $d$ ) for each slice, using a root-mean-square error minimization algorithm. Once the coefficients were calculated, a temperature drift map was subtracted to the incoming temperature map and updated by moving the sliding window to the next dynamic acquisition.

### 3.4.9 Temporal temperature filtering

An optional additional temporal temperature filtering was implemented to convert temporal resolution into temperature precision, taking advantage of the registration of all temperature images at a common reference position. For this purpose, a first-order low-pass Butterworth filter with a cutoff frequency of 0.14 Hz was inserted at the end of the pipeline. No spatial filtering was included in the pipeline.

### 3.4.10 Thermal dose calculation

The cumulative TD was computed from the temperature images using the Sapareto equation [27], taking an equivalent dose of 240 min at  $43^\circ\text{C}$  as a lethal threshold. As uncertainty on temperature estimates influences the TD calculation [28, 29], the lethal TD threshold was corrected on each pixel to account for  $\sigma_T$  maps, using the following formula:

$$TD_{corr}(x, y) = TD(x, y) \times e^{-0.5 \times (\ln(2) \times \sigma_T(x, y))^2} \quad (3.5)$$

$\sigma_T$  was estimated on each pixel surrounding the catheter before RF delivery (over 20 dynamic acquisitions).

### 3.4.11 Statistical analysis

To assess the quality of the temperature measurements without heating, the  $\sigma_T$  and  $\mu_T$  were calculated for each pixel. For this evaluation, during the intervention procedure all 210 dynamic acquisitions of the four slices for the 10 volunteers and two orientation planes (in total 16 800 images) were used. For each slice, motion-registered magnitude images were averaged over all dynamic acquisitions. Then, a region of interest (ROI) surrounding the ventricle was manually drawn on each resulting slice. The  $\mu_T$  and  $\sigma_T$  distributions integrating all slices were plotted with a box and whisker graphical representation using five different distribution percentages: T10, T25, T50, T75, and T90, corresponding to 10, 25, 50, 75, and 90 % of the distribution of the  $\sigma_T$  values, respectively. The same analysis was repeated after temporal filtering.

## 3.5 Results

### 3.5.1 Volunteer temperature imaging

The mean standard deviation (SD) heart rate across all volunteers was  $67 \pm 10$  bpm, with minimal and maximal values of 44 and 83 bpm, respectively. Figure 3.2 shows an example of thermometry results obtained on a volunteer at  $1.6 \times 1.6 \times 3$  mm<sup>3</sup> resolution using the PCA-based method to compensate for respiratory-related susceptibility artifacts. Figures 3.2-A and 3.2-B display the averaged (over 240 dynamic acquisitions) registered magnitude images in coronal and sagittal views, respectively. In each slice, the image showed a well-delimited frontier between the myocardium and adjacent organs (liver, lungs). The proximal aorta, left atrium, and aortic valve could be identified, which is indicative of a successful image registration. Residual blood signal could be observed on each slice, with increased suppression for the last images acquired at the end of diastole.

Figures 3.2-C and 3.2-D display the  $\sigma_T$  maps for the corresponding slices, overlaid on an averaged registered magnitude image (Figure 3.2-A and 3.2-B). In the coronal view, most of the pixels displayed a  $\sigma_T$  at approximately  $2^\circ\text{C}$  over the myocardium, including a large part of the LV and only the inferior part of the RV. In the sagittal view, temperatures in both the LV and RV could be mapped.

In the coronal view, the  $\sigma_T$  (mean  $\pm$  SD) in each slice was  $2.42 \pm 0.93^\circ\text{C}$ ,  $2.26 \pm 1.05^\circ\text{C}$ ,  $2.11 \pm 1.22^\circ\text{C}$ , and  $2.23 \pm 1.09^\circ\text{C}$  ( $2.25 \pm 1.10^\circ\text{C}$  over all slices). In the sagittal view, the  $\sigma_T$  was  $2.10 \pm 0.75^\circ\text{C}$ ,  $2.08 \pm 0.75^\circ\text{C}$ ,  $1.86 \pm 0.90^\circ\text{C}$ , and  $1.90 \pm 0.90^\circ\text{C}$  ( $1.90 \pm 0.90^\circ\text{C}$  over all slices), respectively. The sizes of the ROIs were  $1265 \pm 245$  pixels and  $952 \pm 168$  pixels, respectively. The temporal mean of temperature for the corresponding datasets were  $-0.07 \pm 2.50^\circ\text{C}$  and  $-0.05 \pm 0.40^\circ\text{C}$ , respectively. Additional temporal filtering with the Butterworth low-pass filter resulted in a  $\sigma_T$  of  $1.12 \pm 1.3^\circ\text{C}$  in coronal view and  $0.82 \pm 0.40^\circ\text{C}$  in sagittal view (Figure 3.2-E and 3.2-F), with a temporal mean of temperature of  $0.10 \pm 2.30^\circ\text{C}$  and  $0.01 \pm 0.4^\circ\text{C}$ , respectively. Figure 3.2-G displays the temporal evolution of the temperature in a single voxel at each step of the image processing pipeline. Large amplitude oscillations (approximately higher than  $10^\circ\text{C}$ ) remain visible after motion correction (orange curve), as a result of respiratory-related susceptibility effects. After PCA correction, these oscillations are reduced, showing the temporal phase drift (yellow curve) that is corrected by the processing method (blue curve).  $\sigma_T$  is improved by additional low-pass Butterworth temporal filtering (green curve). The  $\mu_T \pm \sigma_T$  values in the pixel at each step were  $-2.7 \pm 5.7^\circ\text{C}$ ,  $-1.4 \pm 0.9^\circ\text{C}$ ,  $-0.1 \pm 0.9^\circ\text{C}$ , and  $-0.1 \pm 0.4^\circ\text{C}$ , respectively.

The statistical analysis of temperature distribution over all volunteers is presented in Figure 3.3 using box and whisker plots, for the three motion-related susceptibility-correction methods (LUT, PCA, and PCA with temporal filtering). Nonuniform phases were observed at the heart-liver-lung interface in all volunteers. This small region (less than 4% of the ROI) containing

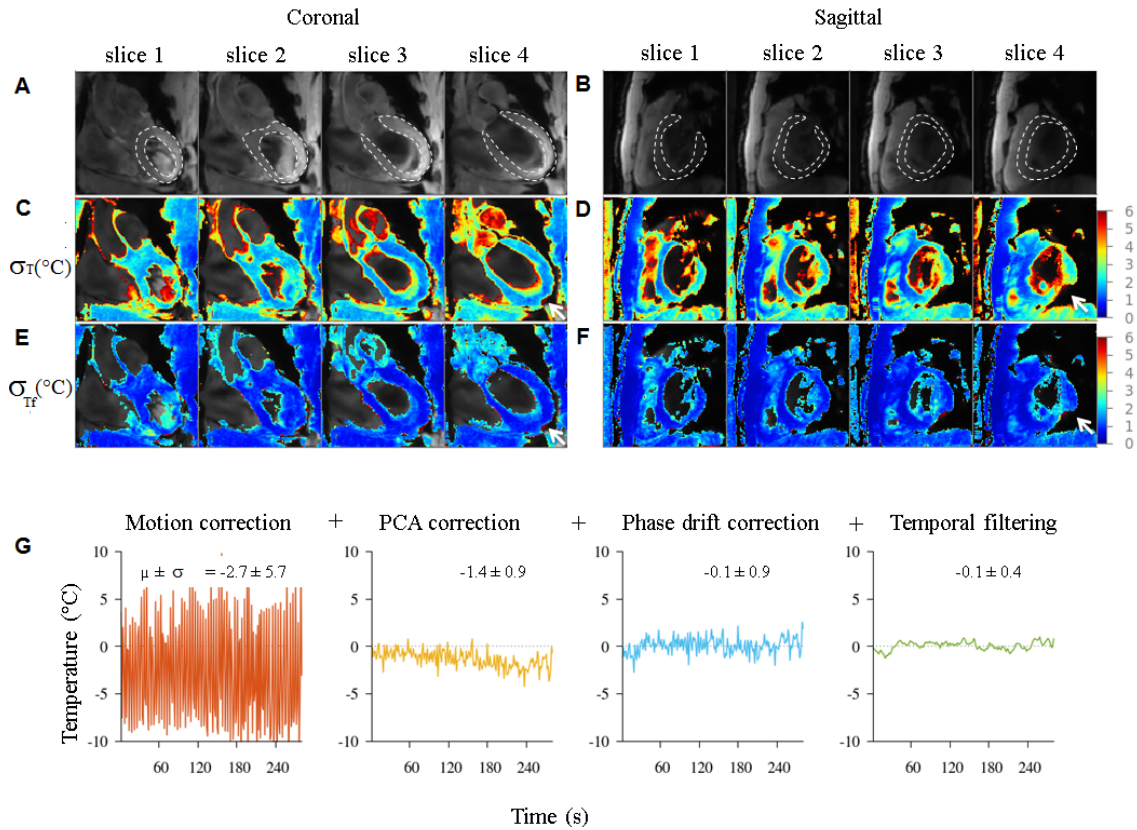


Figure 3.2: Thermometry evaluation on a human volunteer measured at  $1.6 \times 1.6 \times 3 \text{ mm}^3$  resolution using the PCA-based method, in coronal and sagittal views. Temporal standard deviation temperature maps (C and D) are overlaid on averaged registered magnitude images (A and B). A total of 210 dynamic acquisitions were used for calculating  $\sigma_T$  temperature and for averaging the registered magnitude images. Dotted lines in (A) and (B) show contour of the myocardium used for the statistical analysis of temperature data. Presence of large phase variations or low SNRs resulted in increased  $\sigma_T$  only in small areas (white arrow). Images (C) and (D) are  $\sigma_T$  using the PCA-based method and temporal filtering (low-pass Butterworth filter with 0.14-Hz cutoff frequency). (E) Temperature evolution versus time in a single voxel (taken from the sagittal view, slice # 2) at different steps of the pipeline: after motion correction (orange curve), after PCA correction of susceptibility artifacts (yellow curve), after phase drift correction (blue), and after temporal filtering (green curve). At each step, the temporal mean and  $\sigma_T$  values within this voxel are also indicated.

unwanted artifacts was removed from the analysis. Across all correction methods, the temperature offset (Figure 3.3-B) remained close to zero for both image orientations. The  $\sigma_T$  was systematically higher with the LUT-based method as compared with the PCA-based method (Figure 3.3-A). In the sagittal view, the T50/T75 values were 3.35/4.52 $^{\circ}\text{C}$  and 2.74/3.55 $^{\circ}\text{C}$ , respectively. In the coronal view, the T50/T75 values were 3.17/3.93 $^{\circ}\text{C}$  and 2.60/3.25 $^{\circ}\text{C}$ , respectively. The  $\sigma_T$  distributions resulting from the LUT and PCA methods were statistically different (Student's t-test,  $P < 0.001$ ). Temporal filtering had a negligible effect on the temperature offset, but reduced the temporal standard deviation of temperature by a factor of two or more, with T50/T75 values of 1.36/1.72 $^{\circ}\text{C}$  in the sagittal view and 0.90/1.15 $^{\circ}\text{C}$  in the coronal view.

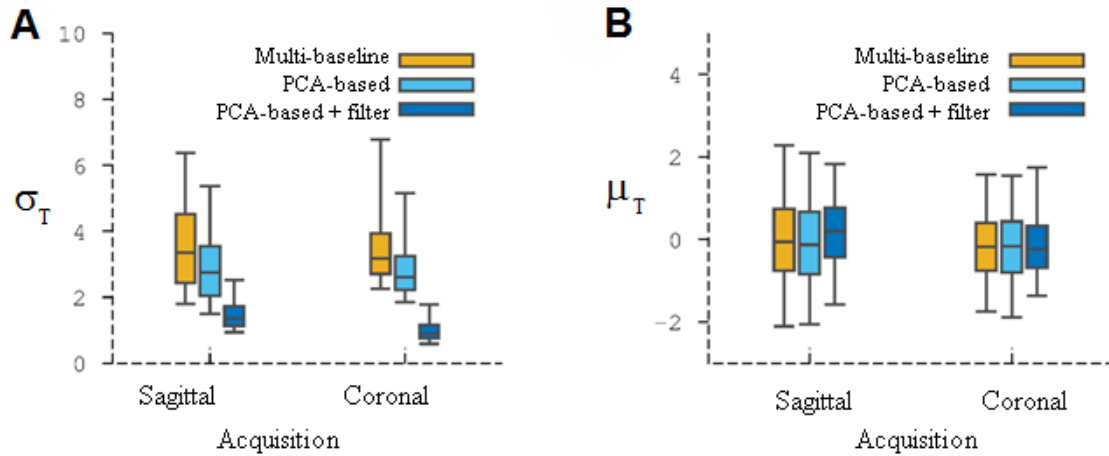


Figure 3.3: Statistics on 10 healthy volunteers during free-breathing acquisition. Box-and-whisker plots of the distribution of temperature  $\sigma_T$  (A) and offset  $\mu_T$  (B) over all volunteers, with the LUT method, PCA, and PCA+filtering methods. The data were retrieved from ROIs (see Figure 3.2-A and 3.2-B) surrounding the left ventricle using all dynamic images for each orientation plane.

### 3.5.2 In vivo RF ablation of the LV in a Sheep

During the intervention, the heart was paced at 86 bpm (700 ms cycle length) to reduce the risk for ventricular arrhythmia during RF ablation. Four RF ablations of 60 s each were performed successively at different locations in the LV with a progressive increase of RF power from 15 to 30 W in each.

Figure 3.4-A shows one example of thermometry data during RF ablation, with the catheter visible in slice #2 on the time-averaged registered magnitude images. Phase distribution in pixels surrounding the catheter tip did not show phase wraps that could alter temperature precision (Figure 3.4-B).  $\mu_T$  and  $\sigma_T$  maps were computed before the interventional procedure over 20 consecutive dynamic acquisitions for the five slices acquired in a sagittal orientation on the myocardium (zoomed view in Figure 3.4-C), using the PCA method for susceptibility compensation and temporal filtering. The resulting values (mean  $\pm$  SD) were  $\mu_T = -0.13 \pm 0.41^\circ\text{C}$  and  $\sigma_T = 0.67 \pm 0.24^\circ\text{C}$ , respectively. The sizes of the ROIs shown in Figure 4a were  $517 \pm 152$  pixels. Figure 3.4-D displays the five temperature images after 42 s of heating at 26 W. A local temperature increase can be observed in the myocardium at the contact of the catheter tip with a less intense temperature increase at the same level in adjacent slices. In Figure 3.4-E, temporal evolution of temperature in slice #2 are plotted on a  $6 \times 6 \text{ mm}^2$  voxel area centered on the heated region (red curves), together with temperature values away from the catheter area (black curves). On each pixel, a progressive heating with a maximal temperature increase of  $28^\circ\text{C}$  at the contact with the catheter can be observed. After switching off the RF energy, the temperature decreased in all pixels. However, the temperature decrease was faster in the three pixels at the point of catheter contact, with a final temperature lower than the pre-ablation temperature in two of them. This was attributed to the catheter tip cooling with saline solution

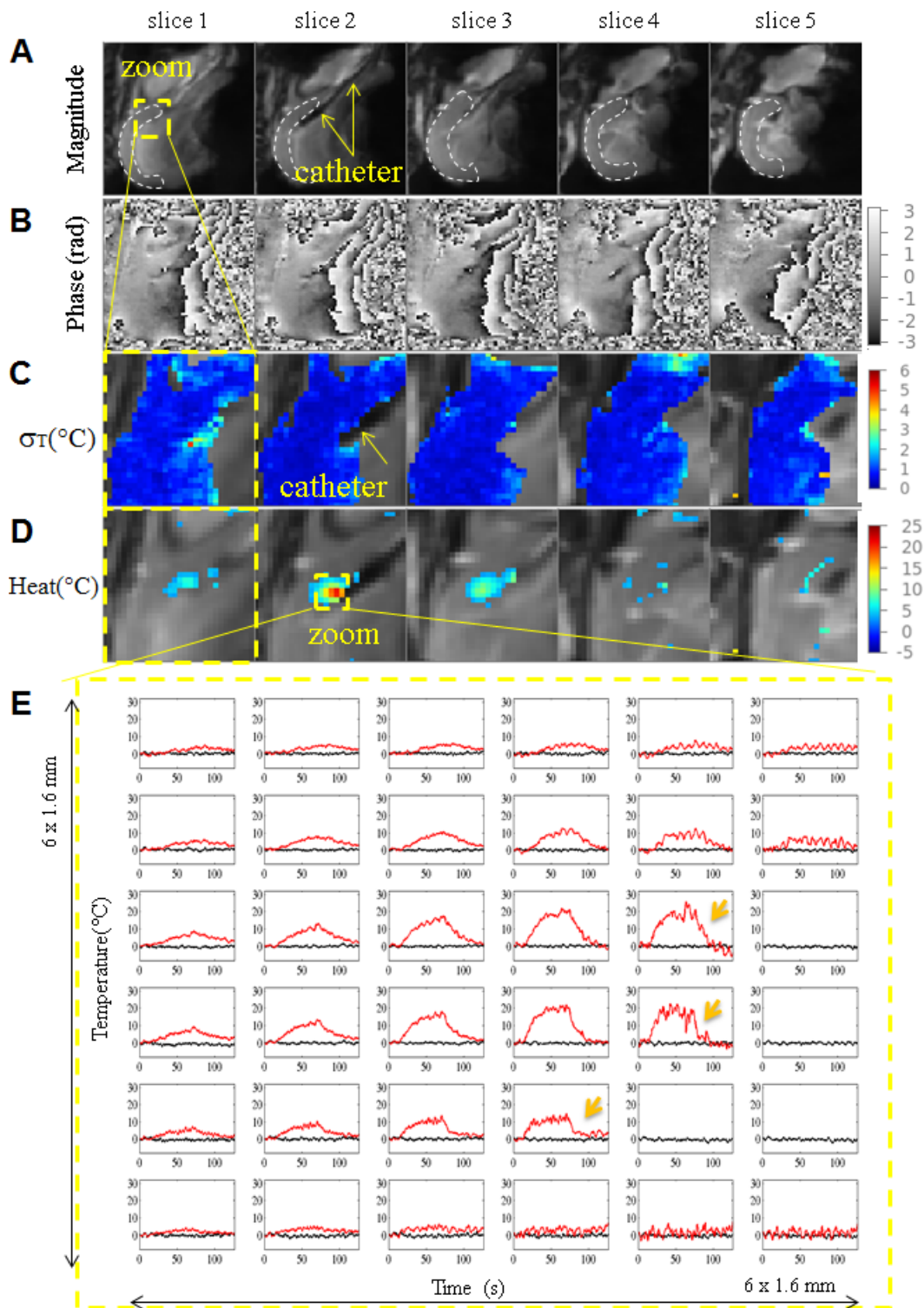


Figure 3.4: MR thermometry monitoring during RF ablation at 26 W on the left ventricle. Averaged registered magnitude images (A). Dotted lines show contour of the myocardium used for statistical analysis of temperature data before RF ablation. Reference phase images (B).  $\sigma_T$  map (over 20 dynamic acquisitions) in sagittal view overlaid on averaged registered magnitude images before the interventional procedure (C). Instantaneous temperature at acquisition #120 (D). A second zoom view (E) shows temperature elevation as a function of time for each voxel surrounding the catheter (in red). Temperature baseline (in black) from a myocardium region away from the catheter is superimposed as a reference. Orange arrows show rapid temperature decrease in the pixel at the vicinity of the catheter tip

infusion at room temperature. In pixels located away from the contact zone, the temperature decrease was slower and returned to its initial value.

Table 3.1 reports the thermometry results for the four RF procedures performed on the sheep. The maximal temperature rise in the three slices surrounding the catheter tip increased with the applied RF power from 13°C (15 W) to 38.9°C (30 W). The cumulative TD was computed for each experiment. The temperature increase was insufficient in the experiments performed at 15 and 17 W to reach the lethal threshold. At 26 W, only 6 pixels in the central slice reached the lethal value, but at 30 W the lethal TD was reached in 21 pixels in the central slice and in 7 and 10 pixels in the adjacent slices, respectively.

RF power (W)	Maximal temperature increase (°C)			Number of pixels reaching lethal TD		
	Slice (n-1)	Slice (n)	Slice (n+1)	Slice (n-1)	Slice (n)	Slice (n+1)
15	7	13	5	0	0	0
17	9.8	18.7	11.5	0	0	0
26	13.5	27.7	17.4	0	6	0
30	25.8	38.9	27	10	21	7

Table 3.1: Temperature data for several RF ablations performed in one sheep. Each ablation was performed over 60 s at the power indicated in the first column. The maximal temperature increases are reported in the three slices surrounding the catheter (n-1, n, and n+1). The last three columns provide the number of pixels having reached the lethal TD threshold.

Figure 3.5 shows the electrograms recorded with the ablation catheter, before, during and after RF ablation, for the experiment reported in Figure 3.4. Slight changes in signal could be observed as the ablation advanced; however, there were limited artifacts during RF delivery and/or MR sequence acquisition, demonstrating excellent feasibility.

Figure 3.6 displays the TD images (A and B) and gross pathology (C and D) for the experiments performed at 26 W (left column) and 30 W (right column) on the sheep. Neither focal ablation nor hemorrhage could be visualized from the endocardial surface for the two RF deliveries performed at 15 and 17 W (data not shown). The experiment performed at 26 W resulted in 6 pixels reaching the TD (Figure 3.6-A) and showed traces of hemorrhage (Figure 3.6-C) at the surface of the endocardium. The experiment performed at 30 W resulted in 21 pixels reaching the lethal TD threshold (Figure 3.6-B) and showed a focal, semicircular, ablated area with a central white zone surrounded by a red hemorrhagic ring (Figure 3.6-D) at gross pathology. Dimensions of this lesion were approximately  $6 \times 8 \text{ mm}^2$ , which is in good agreement with the dimensions observed on the TD image.

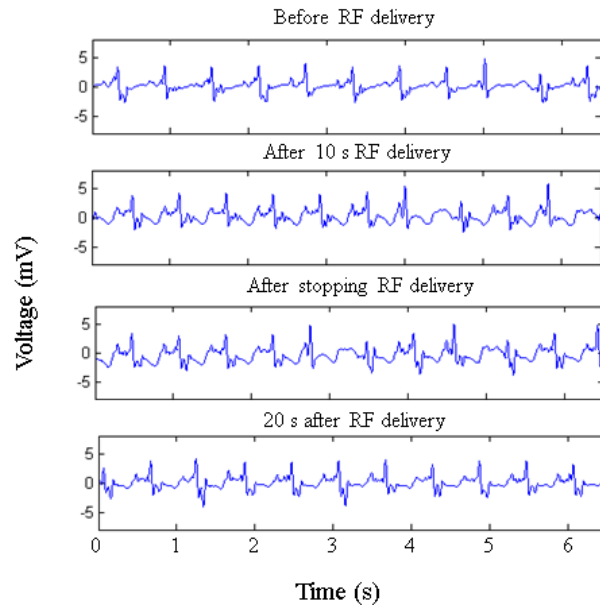


Figure 3.5: Contact electrograms acquired during radiofrequency ablation in sheep. Electrograms recorded between the two distal electrodes (1–4) of the MR-compatible catheter for approximately 6 s, before (top trace) RF delivery, after 10 s RF delivery at 26 W (second trace), immediately after stopping RF delivery (third trace), and 20 s after the end of RF delivery (bottom trace).

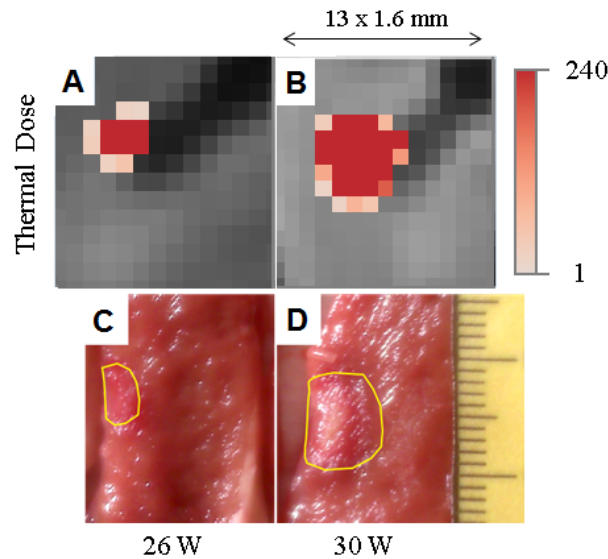


Figure 3.6: Cumulative TD images and gross pathology results for the two RF ablations performed at 26 and 30 W. Pixels having reached the lethal TD threshold superposed on the averaged motion registered magnitude image, for the two ablations performed at 26 W (A) and 30 W (B). Photographs of sections (from endocardium to epicardium) of the LV immediately after sacrifice of the animal, for the corresponding RF power conditions: yellow contours (C and D) delineate the thermal lesion and scale at the right of (D) in millimeters (same zoom factor used in (C) and (D)).

### 3.6 Discussion

In this study, we demonstrate the possibility of mapping temperature distribution in the myocardium during free breathing in humans with only  $1^\circ\text{C}$  of uncertainty, an update rate given by the cardiac cycle duration (1-s time scale), an in-plane spatial resolution of  $1.6 \times 1.6 \text{ mm}^2$ , and a slice thickness of 3 mm. Compared with the published data (15,17) in which the voxel size was  $2.5 \times 2.5 \times 6 \text{ mm}^3$  or more, the spatial resolution in the present work improved five-fold and the temperature precision improved to  $1^\circ\text{C}$  uncertainty. Therefore, this precision allows better visualization of the temperature distribution during RF ablation on an animal model. This thermometry pipeline combines rapid imaging with online reconstruction (including GRAPPA reconstruction and EPI corrections), motion correction, and susceptibility compensation using the two different methods. The quantitative analysis of  $\sigma_T$  showed that the LUT-based and PCA-based susceptibility compensations can provide reliable thermometry, although the PCA method was found to be slightly superior. In an animal model, very regular breathing (12 Hz) imposed by mechanical ventilation ensured reliable temperature estimates with lower  $\sigma_T$  values ( $\text{SD} = 0.67 \pm 0.24^\circ\text{C}$ ). The adjunction of temporal filtering with a conventional low-pass Butterworth filter improved the  $\sigma_T$  with a resulting temperature distribution below  $2^\circ\text{C}$  in 75% of the pixels located in the myocardium. Simulations of the latency induced by this filter revealed limited impact (delay of three dynamic acquisitions), making it appropriate for online temperature monitoring and potential development of automatic feedback algorithms for optimized energy delivery [30, 31] to avoid excessive heating of the myocardium. Although this filter theoretically reduced the temporal resolution of the thermometry method to several seconds, its effect on actual temperature estimates during RF ablation can be considered negligible because of the slow evolution of temperature in the tissue (Figure 3.4-E). This pipeline was developed into the Gadgetron reconstruction framework [19], which is being used increasingly in the MRI research community. The process incorporating reconstruction, motion correction, susceptibility compensation, phase drift correction, and temporal filtering was implemented in GPU or C++ in dedicated software modules (“gadgets”), resulting in an overall image latency of 75 ms in its current implementation. The pipeline ensures real-time monitoring for at least 10 slices/s.

In this study, imaging planes were positioned in coronal or sagittal orientations to visualize respiratory motion. Image-based algorithms were then applied to register all images at fixed positions and respiratory-related susceptibility changes were also compensated for. In previous studies, respiratory motion during acquisition was compensated by using slice tracking from navigator readings and images that were oriented in short axis. This method could be advantageous for blood signal cancellation, as blood flow should be better attenuated with inflow saturation using saturation slabs parallel to the imaging plane [8]. In the present work, blood signal was attenuated with the same technique, playing saturation slabs 45 ms before each slice. However, the signal remained visible inside the cavities (see slice #1 and #2 in Figure 3.2-A) primarily for the first slices acquired in the cardiac cycle, due to limited time for saturated blood to enter the slice. Nevertheless,  $\sigma_T$  were not altered, and comparable thermometry quality could be reported (see Figure 3.2). For the animal experiment, the blood signal in the cavities remained visible in all slices but did not affect the thermometry results. Averaging the motion-registered mag-

nitide images allowed the visualization of small anatomical structures such as cardiac valves, illustrating the robustness of the image-based correction method. Different strategies have been proposed to remove potential temporal phase drift, such as subtraction of a global temperature offset from a ROI [22]. In this study, an automatic phase drift correction was implemented using a first-order spatio-temporal polynomial model. This technique was shown to be efficient in all of the experiments. The first-order spatio-temporal model used to fit the drift may be suboptimal in some locations within the heart, leading to a standard deviation of the mean temperature ( $\mu_T$ ) value in the range of  $\pm 2^\circ\text{C}$  (for the volunteer data in Figure 3.2 in the coronal orientation). More complex fitting models could be applied to improve the thermometry pipeline, but with the current implementation, residual mean temperature values over all volunteers were found to be acceptable (see distribution in Figure 3.3-B).

The irrigated, MR-compatible ablation catheter did not produce large artifacts even though a single-shot EPI sequence was used. The effect of the saline infusion flowing from the catheter tip electrode did not alter the temperature image quality, and the effect of local cooling at myocardium contact could be observed on temperature maps demonstrating the performance of temperature monitoring. Increasing the spatial resolution allowed characterization of the temperature distribution in each slice, reducing the influence of the partial volume effect. Right-ventricle pacing of the sheep helped to maintain a stable rhythm during ablation. The high incidence of ventricular arrhythmia during RF delivery is specific to large animals such as pigs or sheep and is not an issue in patients.  $\sigma_T$  showed superior results to volunteer data and was attributed to a better control of breathing conditions.

Electrograms recording from the ablation catheter could be successfully performed during the whole procedure with a preserved quality, including during MRI acquisition and/or RF ablation, using analog and numerical filters.

The ultimate objective of this cardiac thermometry pipeline is to provide the physician with a quantitative map of the thermal damage induced by RF ablation through a direct calculation of the cumulative TD. The two experiments performed at low RF power did not produce thermal damage as reported by the gross pathology analysis. For these experiments, no pixels reached the TD threshold on MR-thermal dosimetry images. In contrast, when the TD threshold was reached on MR-thermal dosimetry, tissue alteration was observed at gross pathology. In the experiment performed at 26 W, only 6 pixels reached the lethal TD and limited superficial damage was observed at gross pathology. In the cases of such moderate heating, the voxel size may be considered too large to assess the TD deposition with sufficient precision to predict the lesion size. For the experiment performed at 30 W, a larger region was heated and a semicircular region of 5 pixels in diameter reached the lethal threshold. With the 1.6-mm in-plane resolution of MR thermometry sequence, this leads to a predicted thermal lesion of 8 mm in diameter, which corresponds well with the gross pathology results ( $6 \times 8 \text{ mm}^2$  in Figure 3.6-D).

This online temperature monitoring enables direct lesion mapping and should be compared

with strategies such as the calculation of a lesion index [32], which integrate power, time, and contact force values to estimate the RF lesion size.

### 3.6.1 Study limitations

Although clinical cardiac MR thermometry appears to be feasible with the proposed method, the present study shows a number of limitations. The thermometry method was evaluated on 10 healthy volunteers and showed accurate temperature estimates on the LV. Although MR thermometry was found to be reliable in more than 90% of the pixels ( $\sigma_T$  values below  $2^\circ\text{C}$  in Figure 3.3-A) included into the ROI surrounding the LV, a few pixels exhibited spatial phase wraps that remained uncompensated with the current processing pipeline (white arrows in Figure 3.2). Further image processing methods are under consideration to compensate for this artifact, to retrieve exploitable temperature estimates in these pixels located at the liver-lung-heart interface.

Coronal and sagittal orientations were assumed to fully encompass respiratory motion. However, more refined positioning of the imaging slices may be necessary to increase robustness of the thermometry by reducing potential residual through plane motion, depending on patient anatomy. Future work will investigate the precision of MR thermometry on patients suffering from arrhythmia, allowing quantitative evaluation of motion correction and susceptibility artifact compensation. In this study, a limited number of RF ablations were performed in only one animal. Therefore, no statistical correlation between TD and actual lesion size could be performed, although a good correspondence was observed between the TD image and gross pathology analysis for the experiment performed at 30 W. Further studies are needed on a larger number of animals to demonstrate the value of this lesion monitoring strategy. However, this was out of the scope of the present work, which aimed to provide a proof of concept of an improved cardiac MR thermometry method for monitoring tissue temperature during RF ablation simultaneously with electrogram recording.

## 3.7 Conclusions

This study proposes a significant step forward toward the clinical applicability of cardiac MR thermometry for online monitoring of temperature changes during RF ablation. Cardiac MR thermometry will be of benefit if catheter ablation under MR is adopted in clinical practice. It could provide online lesion formation monitoring and would complement postablation lesion imaging by other MR modalities. This approach should allow for significant improvements in safety and efficacy of catheter ablation.

### 3.8 References

1. Ozenne, V. *et al.* Improved cardiac magnetic resonance thermometry and dosimetry for monitoring lesion formation during catheter ablation. *Magnetic resonance in medicine*. <<http://onlinelibrary.wiley.com/doi/10.1002/mrm.26158/pdf>> (visited on 06/07/2016) (2016).
2. Arribas, F. *et al.* Statistics on the use of cardiac electronic devices and electrophysiological procedures in 55 ESC countries: 2013 report from the European Heart Rhythm Association (EHRA). en. *Europace* **16**, i1–i78. ISSN: 1099-5129, 1532-2092 (Apr. 2014).
3. Wood, M. *et al.* Direct Measurement of the Lethal Isotherm for Radiofrequency Ablation of Myocardial Tissue. en. *Circulation: Arrhythmia and Electrophysiology* **4**, 373–378. ISSN: 1941-3149, 1941-3084 (June 2011).
4. Quesson, B., de Zwart, J. A. & Moonen, C. T. Magnetic resonance temperature imaging for guidance of thermotherapy. en. *Journal of Magnetic Resonance Imaging* **12**, 525–533. ISSN: 1053-1807, 1522-2586 (Oct. 2000).
5. *MRI-guided focused ultrasound surgery* eng (eds Jolesz, F. A. & Hynynen, K. H.) OCLC: 836507003. ISBN: 978-0-8493-7370-1 (Informa Healthcare, New York, 2008).
6. Schlesinger, D. *et al.* MR-guided focused ultrasound surgery, present and future. en. *Medical Physics* **40**, 080901. ISSN: 0094-2405 (Aug. 2013).
7. Grissom, W. A. *et al.* Hybrid referenceless and multibaseline subtraction MR thermometry for monitoring thermal therapies in moving organs. en. *Medical Physics* **37**, 5014. ISSN: 00942405 (2010).
8. Hey, S. *et al.* Towards optimized MR thermometry of the human heart at 3T: CARDIAC MR THERMOMETRY AT 3T. en. *NMR in Biomedicine* **25**, 35–43. ISSN: 09523480 (Jan. 2012).
9. Nazarian, S. *et al.* Feasibility of Real-Time Magnetic Resonance Imaging for Catheter Guidance in Electrophysiology Studies. en. *Circulation* **118**, 223–229. ISSN: 0009-7322, 1524-4539 (June 2008).
10. Campbell-Washburn, A. E. *et al.* Dual echo positive contrast bSSFP for real-time visualization of passive devices during magnetic resonance guided cardiovascular catheterization. en. *Journal of Cardiovascular Magnetic Resonance* **16**. ISSN: 1532-429X. doi:10.1186/s12968-014-0088-7. <<http://jcmr-online.biomedcentral.com/articles/10.1186/s12968-014-0088-7>> (visited on 07/29/2016) (Dec. 2014).
11. Hoffmann, B. A. *et al.* Interactive real-time mapping and catheter ablation of the cavotricuspid isthmus guided by magnetic resonance imaging in a porcine model. en. *European Heart Journal* **31**, 450–456. ISSN: 0195-668X, 1522-9645 (Feb. 2010).
12. Vergara, G. R. *et al.* Real-time magnetic resonance imaging-guided radiofrequency atrial ablation and visualization of lesion formation at 3 Tesla. en. *Heart Rhythm* **8**, 295–303. ISSN: 15475271 (Feb. 2011).

13. Ranjan, R. *et al.* Identification and Acute Targeting of Gaps in Atrial Ablation Lesion Sets Using a Real-Time Magnetic Resonance Imaging System. en. *Circulation: Arrhythmia and Electrophysiology* **5**, 1130–1135. ISSN: 1941-3149, 1941-3084 (Dec. 2012).
14. Sommer, P. *et al.* Feasibility of real-time magnetic resonance imaging-guided electrophysiology studies in humans. en. *Europace* **15**, 101–108. ISSN: 1099-5129, 1532-2092 (Jan. 2013).
15. Grothoff, M. *et al.* MR Imaging-guided Electrophysiological Ablation Studies in Humans with Passive Catheter Tracking: Initial Results. en. *Radiology* **271**, 695–702. ISSN: 0033-8419, 1527-1315 (June 2014).
16. Volland, N. A., Kholmovski, E. G., Parker, D. L. & Hadley, J. R. Initial feasibility testing of limited field of view magnetic resonance thermometry using a local cardiac radiofrequency coil: Limited FOV MR Thermometry with Local Coil. en. *Magnetic Resonance in Medicine* **70**, 994–1004. ISSN: 07403194 (Oct. 2013).
17. Kolandaivelu, A. *et al.* Noninvasive Assessment of Tissue Heating During Cardiac Radiofrequency Ablation Using MRI Thermography. en. *Circulation: Arrhythmia and Electrophysiology* **3**, 521–529. ISSN: 1941-3149, 1941-3084 (Oct. 2010).
18. De Senneville, B. D. *et al.* Feasibility of fast MR-thermometry during cardiac radiofrequency ablation: FEASIBILITY OF FAST MR-THERMOMETRY DURING CARDIAC RF ABLATION. en. *NMR in Biomedicine* **25**, 556–562. ISSN: 09523480 (Apr. 2012).
19. Hansen, M. S. & Sørensen, T. S. Gadgetron: An open source framework for medical image reconstruction: Gadgetron. en. *Magnetic Resonance in Medicine* **69**, 1768–1776. ISSN: 07403194 (June 2013).
20. Griswold, M. A. *et al.* Generalized autocalibrating partially parallel acquisitions (GRAPPA). en. *Magnetic Resonance in Medicine* **47**, 1202–1210. ISSN: 0740-3194, 1522-2594 (June 2002).
21. Black, M. J. & Anandan, P. *A framework for the robust estimation of optical flow in Computer Vision, 1993. Proceedings., Fourth International Conference on* (IEEE, 1993), 231–236. <[http://ieeexplore.ieee.org/xpls/abs\\_all.jsp?arnumber=378214](http://ieeexplore.ieee.org/xpls/abs_all.jsp?arnumber=378214)> (visited on 08/29/2016).
22. Roujol, S., Ries, M., Quesson, B., Moonen, C. & Denis de Senneville, B. Real-time MR-thermometry and dosimetry for interventional guidance on abdominal organs. en. *Magnetic Resonance in Medicine* **63**, 1080–1087. ISSN: 07403194, 15222594 (Apr. 2010).
23. Pratikakis, I., Barillot, C., Hellier, P. & Memin, E. Robust Multiscale Deformable Registration of 3D Ultrasound Images. en. *International Journal of Image and Graphics* **03**, 547–565. ISSN: 0219-4678, 1793-6756 (Oct. 2003).
24. Maclair, G. *et al.* en. in *Medical Image Computing and Computer-Assisted Intervention – MICCAI 2007* (eds Ayache, N., Ourselin, S. & Maeder, A.) 411–419 (Springer Berlin Heidelberg, Berlin, Heidelberg, 2007). ISBN: 978-3-540-75758-0. <[http://link.springer.com/10.1007/978-3-540-75759-7\\_50](http://link.springer.com/10.1007/978-3-540-75759-7_50)> (visited on 07/29/2016).

25. Vigen, K. K., Daniel, B. L., Pauly, J. M. & Butts, K. Triggered, navigated, multi-baseline method for proton resonance frequency temperature mapping with respiratory motion. en. *Magnetic Resonance in Medicine* **50**, 1003–1010. ISSN: 0740-3194, 1522-2594 (Nov. 2003).
26. De Senneville, B. D., Ries, M., Maclair, G. & Moonen, C. MR-Guided Thermotherapy of Abdominal Organs Using a Robust PCA-Based Motion Descriptor. *IEEE Transactions on Medical Imaging* **30**, 1987–1995. ISSN: 0278-0062, 1558-254X (Nov. 2011).
27. Sapareto, S. A. & Dewey, W. C. Thermal dose determination in cancer therapy. *International Contact Lens Clinic* **16**, 340–346 (1989).
28. Weidensteiner, C. *et al.* Real-time MR temperature mapping of rabbit liver in vivo during thermal ablation. en. *Magnetic Resonance in Medicine* **50**, 322–330. ISSN: 0740-3194, 1522-2594 (Aug. 2003).
29. Köhler, M. O., Denis de Senneville, B., Quesson, B., Moonen, C. T. & Ries, M. Spectrally selective pencil-beam navigator for motion compensation of MR-guided high-intensity focused ultrasound therapy of abdominal organs. en. *Magnetic Resonance in Medicine* **66**, 102–111. ISSN: 07403194 (July 2011).
30. Quesson, B., Vimeux, F., Salomir, R., de Zwart, J. A. & Moonen, C. T. Automatic control of hyperthermic therapy based on real-time Fourier analysis of MR temperature maps. en. *Magnetic Resonance in Medicine* **47**, 1065–1072. ISSN: 0740-3194, 1522-2594 (June 2002).
31. Mougnot, C. *et al.* Three-dimensional spatial and temporal temperature control with MR thermometry-guided focused ultrasound (MRgHIFU). en. *Magnetic Resonance in Medicine* **61**, 603–614. ISSN: 07403194, 15222594 (Mar. 2009).
32. Squara, F. *et al.* Contact force and force-time integral in atrial radiofrequency ablation predict transmuralty of lesions. en. *Europace* **16**, 660–667. ISSN: 1099-5129, 1532-2092 (May 2014).

## 3.9 Technical and practical implementation

### 3.9.1 Gadgetron

The Gadgetron is an open-source reconstruction software compatible with several MR vendors [19]. Two modules “Emitter” and “Injector” are added into the vendor reconstruction pipeline as shown Figure 3.7. The raw data are sent via TCP/IP to a remote computer for image reconstruction using a list of self-containing modules called “Gadgets”. The source code of each gadget is written in C++ and can be found on the Sourceforge Open Source distribution website (<http://gadgetron.sourceforge.net>). A XML configuration file defines the desired reconstruction chain that will be used for image reconstruction. Our MR thermometry pipeline was integrated as gadgets inside the Gadgetron, at the end of the reconstruction pipeline, when magnitude and phase images are available. Gadgetron relies on a common vendor-neutral raw data format called ISMRMRD, proposed by the NIH. Each segment of the k-space is labelled using flags (k-space\_encoding\_step\_1, slice, etc).

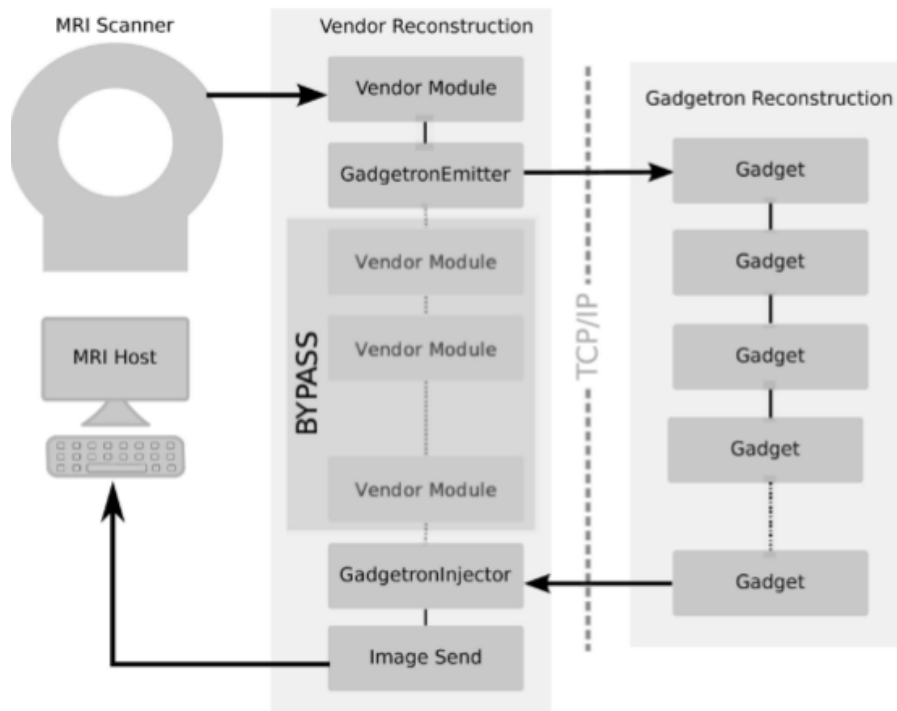


Figure 3.7: Integration of Gadgetron framework with a Siemens scanner.

### 3.9.2 Hardware

#### MR-compatible catheter

The deflectable MR-compatible catheter used for this study was provided by Biosense Webster (Figure 3.8). Four electrodes allow EP recording and the distal one was used for RF ablation. No temperature sensor was available.

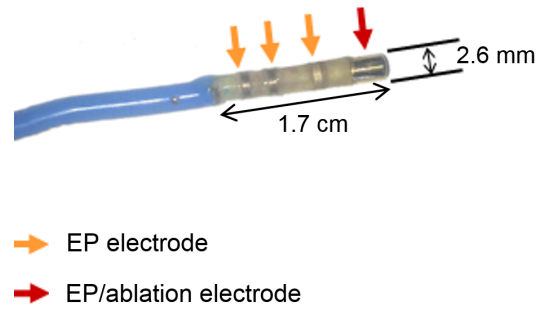


Figure 3.8: Prototype of an MR-compatible catheter equipped with 4 electrodes provided by Biosense Webster.

### Filters

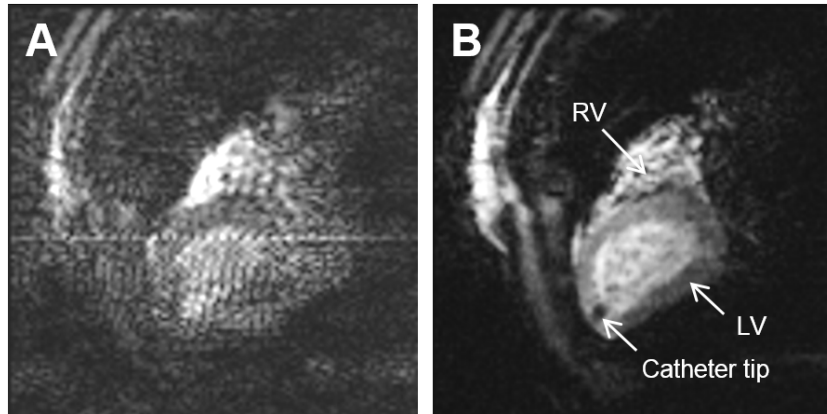


Figure 3.9: Example of artifacts that can occur during RF ablation. (A) Magnitude image before RF delivery showing a catheter inside the LV of a sheep. (B) Without proper filtering the RF ablation can cause severe artifacts.

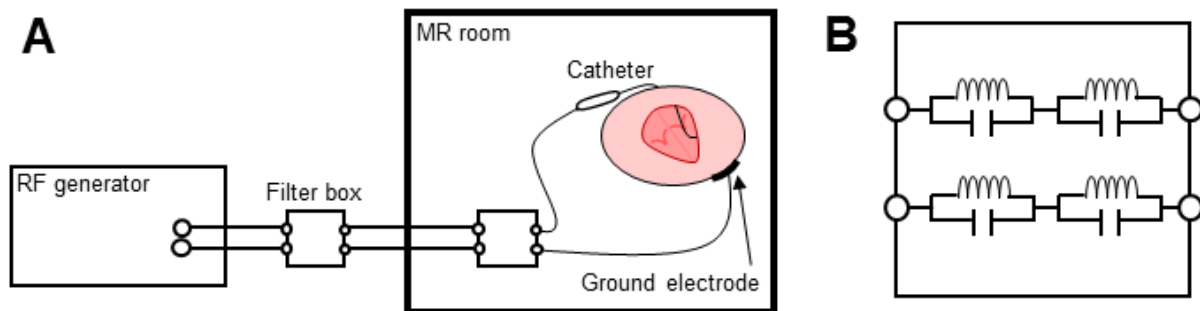


Figure 3.10: Hardware design for simultaneous RF ablation and MR thermometry. (A) The output of the RF generator is filtered by several filter boxes outside and inside the Faraday cage. (B) Each filter is made of band-rejection filters tuned at 63 MHz consisting in two couples of inductors ( $L = 206 \text{ nH}$ ) and capacitors ( $C = 27 \text{ pF}$ ) arranged in parallel for each line.

Since MR scanners are susceptible to interferences caused by the RF device, appropriate filtering had to be implemented and inserted into the transmission line between the RF generator and the catheter electrodes. An example of RF artifacts are shown in Figure 3.9. The aim is to

attenuate harmonics of the RF ablation signal (500 kHz) around 63 MHz (Larmor frequency at 1.5 T). For that purpose, a band-rejection filter made of capacitors and inductance (scheme in Figure 3.10) was added in the transmission line.

### 3.9.3 Temporal phase unwrapping

The  $2\pi$  periodicity of the phase image can lead to phase jump from  $-\pi$  to  $\pi$  between two successive acquisitions. A temporal phase unwrapping is performed on a pixel-by-pixel basis to prevent bias in temperature mapping. Figure 3.11-A shows phase evolution in one pixel. Motion of the object induces phase variations due to susceptibility changes. The phase unwrapping algorithm (Eq 3.6) is applied by calculating the difference between the current phase  $\varphi_t$  and the previous phase  $\varphi_{t-1}$ .

$$\varphi_{uw} = \begin{cases} \varphi_t + 2\pi & \text{if } \varphi_t - \varphi_{t-1} < -\pi \\ \varphi_t - 2\pi & \text{if } \varphi_t - \varphi_{t-1} \geq \pi \end{cases} \quad (3.6)$$

As the result, the unwrapped phase  $\varphi_{uw}$  is obtained as shown in Figure 3.11-B.

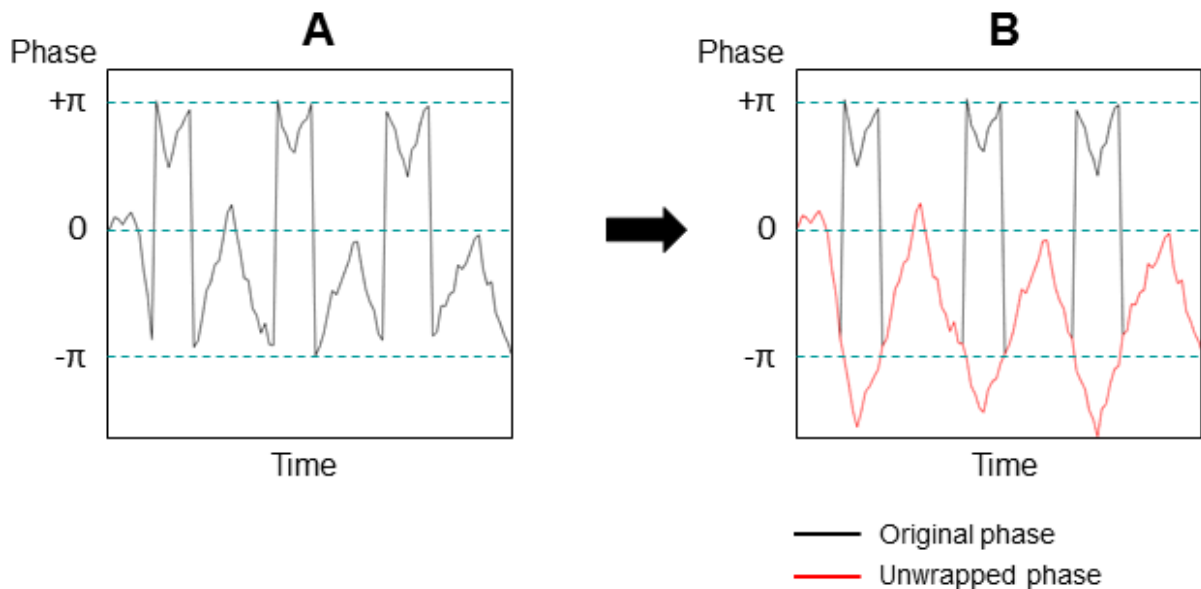


Figure 3.11: Temporal phase unwrapping

One error in this temporal phase unwrapping may spread over the following MR acquisitions and impact the temperature mapping. This is one of the reasons why the MR thermometry accuracy is degraded in regions prone to high susceptibility variations and local spatial phase wraps.

### 3.9.4 PCA-based implementation for calculation of synthetic background phase

#### Learning step

A subset of the dynamic images are used to learn the relation between the motion and the phase variations impacted by susceptibility artifacts. For that purpose the motion field  $(u,v)$  is estimated on the first  $n$  images covering several respiratory cycles (equivalent to around 20-30 frames) with an optical-flow algorithm. Since the motion is periodic, most information is redundant. The principal component analysis (PCA) is used to reduce the dimension of the motion fields. For each image  $i$ , we have a vector  $f_i$  composed by an horizontal component  $u_i$  and vertical component  $v_i$  of  $s$  elements each for an image of  $s$  pixels. A matrix  $F$  is filled with the  $n$   $f_i$  to obtain a final size of  $n \times 2s$  (Figure 3.12).

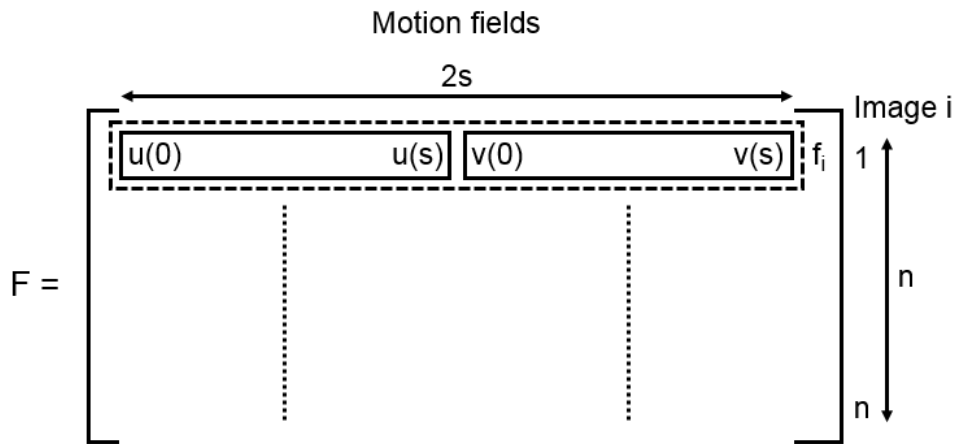


Figure 3.12: Matrix filled with motion fields of the first  $n$  images of the preparative learning step.

A singular value decomposition (SVD) is performed on this matrix  $F$  so that  $F_{n \times 2s} = U_{n \times n} S_{n \times 2s} V_{2s \times 2s}$ . Each column of the matrix  $V$  is an eigenvector of the matrix  $F$ , ie one of the principal components. In order to reduce the dimension of the initial dataset, we select the first  $N$  components associated with the largest eigenvalues. We finally obtain  $V_{2s \times N}$ , a sub-matrix of  $V$ , which is the motion basis. The following formula is used to calculate the eigenvalues  $d_{N \times n}$  of the images in the learning step:

$$d = (V^T V)^{-1} * V^T * F \quad (3.7)$$

At that step, we can now describe the respiratory motion using a small amount of numbers:  $N$  eigenvalues per image, also called motion descriptors. Then, we want to learn the relation between the motion and the phase variations. All the phase images of the atlas are registered at a fixed position, using the  $(u,v)$  computed on the equivalent magnitude images. Each registered phase image is vectorized and stored in a matrix  $Pre_{s \times n}$ . The relation between the eigenvalues and the phase is calculated as a basis of phase  $B$ :

$$B = (d^T d)^{-1} * d^T * P_{reg} \quad (3.8)$$

### Interventional procedure

During the intervention, the current motion field  $(u,v)$  is estimated from the current magnitude image and filled in a matrix  $F_{1 \times 2s} = (u(0) \dots u(s), v(0) \dots v(s))$ . The current motion descriptor  $d$  is calculated using the learned motion basis  $V$  (see Eq 3.7). The background phase  $\varphi_{REF}$  is then computed using the motion descriptors  $d$  and the phase basis  $B$  learned during the atlas.

$$\varphi_{REF} = \sum_{j=0}^{N-1} d_j \cdot B_j(x, y) + B_N(x, y) \quad (3.9)$$

The synthetic phase of reference  $\varphi_{REF}$  is finally used to calculate the current temperature map:

$$\Delta T = \frac{\Delta \varphi}{\gamma \cdot \alpha_{PRF} \cdot B_0 \cdot TE} = \frac{\varphi - \varphi_{REF}}{\gamma \cdot \alpha_{PRF} \cdot B_0 \cdot TE} \quad (3.10)$$

Where  $\gamma$  is the gyromagnetic ratio ( $= 42.58 \text{ MHz/T}$ ),  $\alpha_{PRF}$  is the PRF temperature coefficient ( $= -0.0094 \text{ ppm/}^\circ\text{C}$ ),  $B_0$  is the magnetic field strength ( $= 1.5 \text{ T}$ ) and  $TE$  is the echo time. The use of the PRF shift technique on moving organs such as the heart requires motion and associated susceptibility artifacts correction.

## Chapter 4

# Combination of Principal Component Analysis and optical-flow motion compensation for improved cardiac MR thermometry

### Contents

---

<b>4.1</b>	<b>Preamble</b> . . . . .	<b>86</b>
<b>4.2</b>	<b>Abstract</b> . . . . .	<b>86</b>
<b>4.3</b>	<b>Introduction</b> . . . . .	<b>87</b>
<b>4.4</b>	<b>Methods</b> . . . . .	<b>88</b>
4.4.1	MR Thermometry imaging protocol . . . . .	88
4.4.2	Image registration . . . . .	89
4.4.3	Thermometry mapping . . . . .	90
4.4.4	Volunteer study . . . . .	91
4.4.5	Phantom study . . . . .	91
4.4.6	In vivo ablation in the left ventricle of a sheep . . . . .	92
<b>4.5</b>	<b>Results</b> . . . . .	<b>93</b>
4.5.1	Volunteer study . . . . .	93
4.5.2	Phantom study . . . . .	94
4.5.3	In vivo ablation in the left ventricle of a sheep . . . . .	99
<b>4.6</b>	<b>Discussion</b> . . . . .	<b>99</b>
<b>4.7</b>	<b>Conclusion</b> . . . . .	<b>102</b>
<b>4.8</b>	<b>References</b> . . . . .	<b>102</b>

---

## 4.1 Preamble

This chapter focuses on the method of motion estimation used to correct in-plane motion in the MR thermometry pipeline, described in the previous chapter. Baudouin Denis de Senneville et al. [1] recently proposed an adapted optical-flow algorithm that addressed the issue of mis-registration induced by the local intensity variations not related to motion. Indeed, thermal ablation may lead to intra-voxel temperature gradients and changes in tissue properties that result in intensity decrease on magnitude images. The novel optical-flow algorithm was found to be more robust to such effects in liver and kidney of healthy volunteers with simulated high intensity focused ultrasound (HIFU) heating area.

The aim of this chapter was to evaluate this adapted optical-flow method in the particular case of RF ablation in the heart. For that purpose, the novel method, provided in Matlab by B.D. de Senneville, was implemented in C++ to be integrated into the automated MR thermometry pipeline (2<sup>nd</sup> year of PhD). This method was first evaluated on healthy volunteers, using datasets acquired with the MR thermometry protocol explained in Chapter 3. Experimental validation was performed during controlled RF ablation on a moving phantom, where the reference temperature could be measured using a probe. As the motion estimation bias depends on the pattern of signal decrease (amplitude and thickness), several configurations were investigated by simulation. The impact of mis-registration was finally evaluated in an experimental case of RF ablation in the LV of a sheep.

This chapter corresponds to a full paper submitted by Solenn Toupin et al., in the journal of Physics in Medicine and Biology (PMB-104718). Very few modifications were introduced to harmonize the notations of this thesis manuscript.

## 4.2 Abstract

The use of Magnetic Resonance (MR) thermometry for the monitoring of thermal ablation is rapidly expanding. However, this technique remains challenging for the monitoring of the treatment of cardiac arrhythmia by radiofrequency ablation due to the heart displacement with respiration and contraction. Recent studies have addressed this problem by compensating in-plane motion in real-time with optical-flow based tracking technique. However, these algorithms are sensitive to local variation of signal intensity on magnitude images associated with tissue heating. In this study, an optical-flow algorithm was combined with a principal component analysis method to reduce the impact of such effects. The proposed method was integrated to a fully automated cardiac MR thermometry pipeline, compatible with a future clinical workflow. It was evaluated on nine healthy volunteers under free breathing conditions, on a phantom and in vivo on the left ventricle of a sheep. The results showed that local intensity changes in magnitude images had lower impact on motion estimation with the proposed method. Using this strategy, the temperature mapping accuracy was significantly improved.

### 4.3 Introduction

Catheter-based radiofrequency (RF) ablation has become a reference therapy to treat cardiac arrhythmia. Abnormal electrical pathways that trigger for unwanted cardiac contractions can be isolated from the healthy myocardium by creating a local thermal lesion surrounding the pathologic region. RF energy is delivered through an electrode located at the tip of a catheter advanced into the heart. However, the risk of arrhythmia recurrence remains significant [2, 3], mainly due to incomplete isolation of circuit or by recovery of previously isolated circuit. Hence, one major challenge of RF ablation is the ability to create permanent and transmural lesions to ensure the efficacy and the safety of the procedure. The success rate of the therapy may be improved by directly monitoring the myocardial necrosis formation to predict the size of the final tissue injury [4]. Catheter orientation, blood flow in the cardiac cavities and catheter/tissue contact are the main factors that significantly influence the lesion size. Because of the variability of these factors in vivo, energy and duration of the RF delivery can hardly predict the therapy outcome. Since the electrode temperature does not reflect the temperature of the tissue at distance of the contact point, surrogate measures have been proposed such as changes of circuit impedance, electrogram amplitude and catheter/tissue contact force. These techniques were found to help to prevent excessive heating and associated complications (perforation, thrombus, atrioesophageal fistulas... ). However, none of them correlated with tissue temperature and final lesion size.

Magnetic Resonance (MR) thermometry, using the water Proton Resonance Frequency (PRF) shift technique, is a non-invasive technique to measure the temperature distribution in tissue. This method has been of growing interest in recent years for the monitoring of thermal ablation in various organs such as liver [5, 6], prostate [7], uterus [8] and brain [9, 10]. However, cardiac MR thermometry remains very challenging because of complex organ motion resulting from heart contraction and respiratory motion. The three following hurdles must be overcome. 1) MR acquisition must be fast enough to avoid intra-scan motion, resulting in blurring and ghosting artifacts. 2) All images in the time series must be registered at an identical position, to allow the reliable calculation of temperature and cumulative thermal dose [11], based on the temporal integration of the temperature on a pixel-by-pixel basis. 3) Change in lung volume during the breathing cycle modifies the local magnetic field in the heart and induces additional periodic variations on phase images in the heart. Since the PRF thermometry method is based on the linearity between the temperature variations and the phase changes, these effects cause significant artifacts that can bias the temperature measurements.

To overcome these issues, several techniques have been proposed in the past. 1) Fast imaging, such as single-shot Echo Planar Imaging (EPI), was combined with electrocardiogram (ECG) triggering to allow the acquisition of several slices per heartbeat with limited intra-scan motion and heart contraction motion [12, 13]. 2) All magnitude and phase images in the time series are registered accordingly to a selected reference data. Since temperature information is encoded into the phase image, magnitude image can be used to estimate and compensate organ displacement between consecutive images using optical-flow algorithm. 3) To correct for

susceptibility artifacts, a number of MR images are usually acquired before starting the thermal ablation (learning step) to create a set of reference data that can be used to remove susceptibility related phase variations [14]. Using such a strategy, cardiac MR thermometry was recently reported with a spatial resolution of  $1.6 \times 1.6 \times 3 \text{ mm}^3$  and an imaging time of  $\sim 100 \text{ ms}$  per slice [13].

In this previous study, an optical-flow algorithm [15] was used to compute vector fields representing displacement between each new magnitude image and the image at a reference position. This algorithm requires the calibration of only one parameter and ensures a fast convergence which is advantageous for applications with real-time processing requirements. However, it relies on the assumption of conservation of local intensity that can be violated during RF ablation due to changes in tissue properties with heating [16]. MR relaxation times, such as T1, T2 and T2\*, can indeed vary with temperature and tissue may also change when a thermal lesion is created (e.g. edema). These effects can result in local intensity variations on the magnitude images, also depending on the MR acquisition pulse sequence. As a result, these local intensity changes may be interpreted as motion and lead to local erroneous displacement vector field. Since this motion field is used to register the phase images used by the PRF method, the MR thermometry precision may thus be compromised as well.

To overcome potential issues of the Horn and Schunck (H&S) optical-flow algorithm in the context of MR thermometry, a new technique has recently been proposed [1]. The method consists in applying conventional H&S algorithm over the data collected during the learning step before ablation, since no intensity variation induced by heating is expected. Then, a Principal Component Analysis (PCA) is performed over the resulting motion field vectors to extract eigenvectors and eigenvalues that are related to motion. During thermal ablation, the motion is estimated from each new image as a linear combination of these eigenvectors, making the method less sensitive to potential variations of intensity when tissue temperature is locally changing.

This present work focuses on the evaluation of this optical-flow based method associated with PCA, called PCA-based H&S, in the context of cardiac MR thermometry during RF ablation. The performance of the method was evaluated on simulated intensity variations on magnitude images, on experimental data obtained on a static/mobile phantom during RF ablation, on experimental images from 9 healthy volunteers under free breathing conditions without heating and during cardiac RF ablation performed in vivo on the left ventricle (LV) of a sheep.

## 4.4 Methods

### 4.4.1 MR Thermometry imaging protocol

Dynamic MR thermometry was performed at 1.5 T (Avanto, Siemens Healthcare, Germany) using two standard 16-channel cardiac coils. A fat-saturated, single-shot EPI pulse sequence was combined with GRAPPA (acceleration factor of 2) to achieve a spatial resolution of  $1.6 \times 1.6 \times 3 \text{ mm}^3$ , TE/TR/Flip angle (FA) = 18-20 ms/110 ms/60°, bandwidth = 1576 Hz/px, Field of view (FOV)

= 180x180 mm<sup>2</sup>. Through-plane motion was minimized by setting the imaging slices parallel to the principal respiration direction (head-feet). Saturation slabs were positioned along the FOV in the phase encoding direction to avoid aliasing. Acquired EPI raw data were streamed online via TCP/IP to a remote computer for image reconstruction [17] and for real-time computation of temperature maps.

#### 4.4.2 Image registration

For each image in the time series, displacement field (u,v) was estimated from magnitude images (see Figure 4.1-A) and used to register both magnitude and phase images at a fixed position (the first image in the time series was taken as the reference position). Conventional H&S optical-flow algorithm is based on the minimization of the energy E (Eq. 4.1).

$$E = \iint_{xy} \left( [I_x u + I_y v + I_t]^2 + \alpha [\|\nabla u\|_2^2 + \|\nabla v\|_2^2] \right) dx dy \quad (4.1)$$

Where x and y are the pixel coordinates, u and v the horizontal and vertical displacement vector components,  $I_{x,y,t}$  the spatio-temporal partial derivatives of the intensity and  $\alpha$  a tunable weighting factor. Since this method relies on the local conservation of the intensity, the drop in signal intensity induced by heating and changes in tissue properties may introduce errors in the estimated motion (u,v).

The PCA-based H&S method requires a preparative learning step which covers several breathing cycles before the ablative procedure (typically 20 frames). 2D estimated motion fields (u,v) together with registered phase images are collected using the conventional H&S method (Eq. 4.1) since local variations of intensity are unexpected prior heating. Then a PCA is performed on the motion fields of the learning step:

$$\begin{pmatrix} u(x,y) \\ v(x,y) \end{pmatrix} = \sum_{k=1}^M d_k \begin{pmatrix} \Phi_k(x,y) \\ \Psi_k(x,y) \end{pmatrix} \quad (4.2)$$

Where  $\Phi_{k=1...M}$  and  $\Psi_{k=1...M}$  are the horizontal and vertical components of the eigenvector #k,  $d_{k=1...M}$  are the eigenvalues representing motion descriptors and M is the number of eigenvectors.

During the interventional procedure, for each new incoming image, the 2D motion is estimated as a linear combination of the previously calculated eigenvectors. For that purpose, the following PCA-based H&S equation (Eq. 4.3) is minimized:

$$\begin{aligned}
E & \left( \sum_{k=1}^M d_k \Phi_k(x, y), \sum_{k=1}^M d_k \Psi_k(x, y) \right) \\
& = \int_{xy} \left( (I_x \sum_{k=1}^M d_k \Phi_k(x, y) + I_y \sum_{k=1}^M d_k \Psi_k(x, y) + I_t)^2 \right. \\
& \quad \left. + \alpha \left( \left\| \nabla \sum_{k=1}^M d_k \Phi_k(x, y) \right\|_2^2 + \left\| \nabla \sum_{k=1}^M d_k \Psi_k(x, y) \right\|_2^2 \right) \right) dx dy
\end{aligned} \tag{4.3}$$

The minimization of the functional  $E$  was described in [1] and provided in the RealTITracker<sup>1</sup> free toolbox. Conventional H&S and PCA-based H&S methods were both used to register magnitude/phase images in order to evaluate the impact of the algorithms on MR thermometry performance. To improve the estimation of large displacements, a coarse-to-fine multi-resolution scheme was performed with three levels up to the original image resolution (112×112 px). To ensure the convergence of the optical-flow algorithms,  $(\sqrt{u^2 + v^2})$  was averaged over all the pixels of the image between two successive iterations and compared to a convergence criteria given by  $(\frac{0.1}{l+1})$ , where  $l$  is the level of the multi-resolution scheme. At the last level of the pyramid, where the image size is maximal,  $l$  value is 0 and the convergence criteria value is 0.1.

The weighting factor  $\alpha$  regulates the link between intensity variation and motion field regularity and must be experimentally determined to optimize the robustness of the motion estimation on representative MR images. Values of  $\alpha$  range between 0 and 1 and large values close to 1 lead to a smoother flow. The number of eigenvectors used in the PCA basis can influence the robustness of the motion estimation as well. The first eigenvector represents the main contribution of the motion, while the eigenvectors associated with lower eigenvalues encode for local deformations and for the noise.

The optical-flow algorithms were implemented in C++ and evaluated on a Core i7-4790 processor (3.6 GHz, four cores, INTEL, Santa Clara, CA, U.S.A.) without GPU implementation.

### 4.4.3 Thermometry mapping

The PRF thermometry method computes temperature change  $\Delta T$  from difference between a given phase image  $\varphi$  acquired during treatment and a reference phase image  $\varphi_{REF}$  acquired prior to heating:

$$\Delta T = \frac{\Delta\varphi}{\gamma \cdot \alpha_{PRF} \cdot B_0 \cdot TE} = \frac{\varphi - \varphi_{REF}}{\gamma \cdot \alpha_{PRF} \cdot B_0 \cdot TE} \tag{4.4}$$

Where  $\gamma$  is the gyromagnetic ratio ( $\sim 42.58$  MHz/T),  $\alpha_{PRF} = -0.0094$  ppm. $^{\circ}C$  is the PRF

<sup>1</sup><http://bsenneville.free.fr/RealTITracker>

temperature coefficient,  $B_0$  is the magnetic field strength (= 1.5 T) and TE is the echo time. The registered phase images of the learning step were used to build a parameterized flow model using a PCA algorithm on a pixel-by-pixel basis. During the intervention, the background phase  $\varphi_{REF}$  is computed with the learned model and subtracted to the current registered phase image  $\varphi$ . Details on this method can be found in [14]. Temperature maps computation was followed by temporal temperature filtering using a low-pass Butterworth filter (first order, cutoff frequency of 0.14 Hz), as described in [13].

#### 4.4.4 Volunteer study

Thermometry performance was evaluated with both algorithms by computing the temporal standard deviation of the temperature ( $\sigma_T$ ) in each pixel over a 2-3 minutes acquisition (250 successive acquisitions triggered on the cardiac cycle). A region of interest (ROI) surrounding the LV was manually drawn to select pixels included in the analysis. The regularization term  $\alpha$  and the number of PCA eigenvectors M were experimentally determined on one dataset from volunteer #5. Performances of the algorithms were then compared on nine healthy volunteers under free-breathing conditions with the same value of  $\alpha$ . The significance between the  $\sigma_T$  obtained with H&S and PCA-based H&S optical-flow methods was evaluated using a t-test with a significance level of 1%. Each pixels of the ROI surrounding the LV was included in the statistical analysis.

#### 4.4.5 Phantom study

##### Simulation of intensity variation on MR images of an agar phantom

A first study was performed on a home-made cylindrical tissue-mimicking phantom (3% dry-weight agar) as described in [18]. To evaluate the robustness of PCA-based H&S algorithm in the case of local variation of intensity on magnitude images, several patterns of signal decrease were added to the magnitude image of the phantom into which a catheter was inserted. A Gaussian function of amplitude A (expressed in percent of the maximal image intensity from native experimental images) and variance  $\mu$  was computed and subtracted to the original magnitude image to mimic the impact of a typical RF lesion. The resulting bias in image registration was computed for different values of A (ranging from 10% to 100%) and  $\mu$  (ranging from 0.5 to 2.9 pixels) by calculating the average and the maximal endpoint error (EE) (see Eq. 4.5) over a ROI of  $9 \times 9$  pixels centered on simulated area.

$$EE = \sqrt{(u - u_{ref})^2 + (v - v_{ref})^2} \quad (4.5)$$

Where  $(u, v)$  and  $(u_{ref}, v_{ref})$  are the estimated and the reference motion, respectively.  $(u_{ref}, v_{ref})$  is the motion estimated on the original image and is considered as the gold standard motion while  $(u, v)$  is the motion estimated on the modified image including simulated signal change. EE maps were computed individually with the PCA-based H&S and the conventional H&S optical-flow methods for comparison of the robustness of the proposed method with the original

one.

### Experimental validation on a gel phantom

A RF ablation was run at 10 W for 60 s with simultaneous temperature mapping on the phantom without motion. A MR-compatible catheter (Biosense Webster, Diamond Bar, CA) inserted into the gel was connected to a clinical RF generator (Stockert Medical Solution, Freiburg, Germany) located outside the Faraday cage. An optical probe (Luxtron probe, LumaSense technologies, Santa Clara, CA) was positioned close to the catheter tip to measure the absolute temperature evolution.

The gold standard temperature map  $\Delta T_{ref}$  was first calculated by simple phase subtraction 4.4 without image registration, since the phantom is static. Then, temperature maps were calculated after image registration using H&S and PCA-based H&S optical-flow methods. The potential artifact, introduced by the motion correction due to signal intensity variation on magnitude images, was quantified by calculating the motion fields  $EE$  (Eq. 4.5) and the temperature errors  $\delta T$  (Eq. 4.6) relative to reference temperature data  $\Delta T_{ref}$  for each method:

$$\delta T = \frac{1}{N} \sum_{t=1}^N |\Delta T(t) - \Delta T_{ref}(t)| \quad (4.6)$$

Where  $\delta T$  is the temperature elevation measured with an optical-flow based motion estimation,  $\Delta T_{ref}$  is the reference temperature increase computed without motion compensation and  $N$  is the number of dynamic acquisitions in the time series.

After a cooling period was observed, an identical RF ablation was performed while the phantom underwent a periodic motion (15 cycles per minute) of  $\sim 8$  mm amplitude along  $z$  axis of the magnet using an inflated balloon strapped to the phantom and driven by a MR-compatible ventilator (Aestivia, General Electric, Fairfield, CT, U.S.A.). Temperature maps were computed and compared for the two different methods of motion estimation and correction. The calculation of the gold standard temperature  $\Delta T_{ref}$  was not possible because of the phantom movement.

#### 4.4.6 In vivo ablation in the left ventricle of a sheep

Animal experiment was conducted in vivo on a sheep after approval of the protocol by the ethic committee of the University of Bordeaux. Identical MR-compatible catheter was advanced into the LV under fluoroscopy (Toshiba InfiniX, Toshiba Medical, Nasu, Japan). The animal was then installed in a supine position in the MRI scanner and maintained under controlled respiration (15 cycles per minute). Cardiac triggered MR temperature images were acquired prior and during a RF ablation at 30 W for 60 s.

### Simulation of intensity variation on MR images of a sheep heart

As a first test, local intensity variations were added in the vicinity of the catheter tip on one magnitude image of the time series without heating, using identical methodology as on agar gel phantom. The resulting bias was quantified by calculating the average and the maximal EE (Eq. 4.5) over a ROI of  $9 \times 9$  pixels centered on the simulated area.

### Experimental validation in the left ventricle of a sheep

MR images acquired during RF ablation were computed in post-processing using the two different motion estimation algorithms and resulting temperature images were compared.

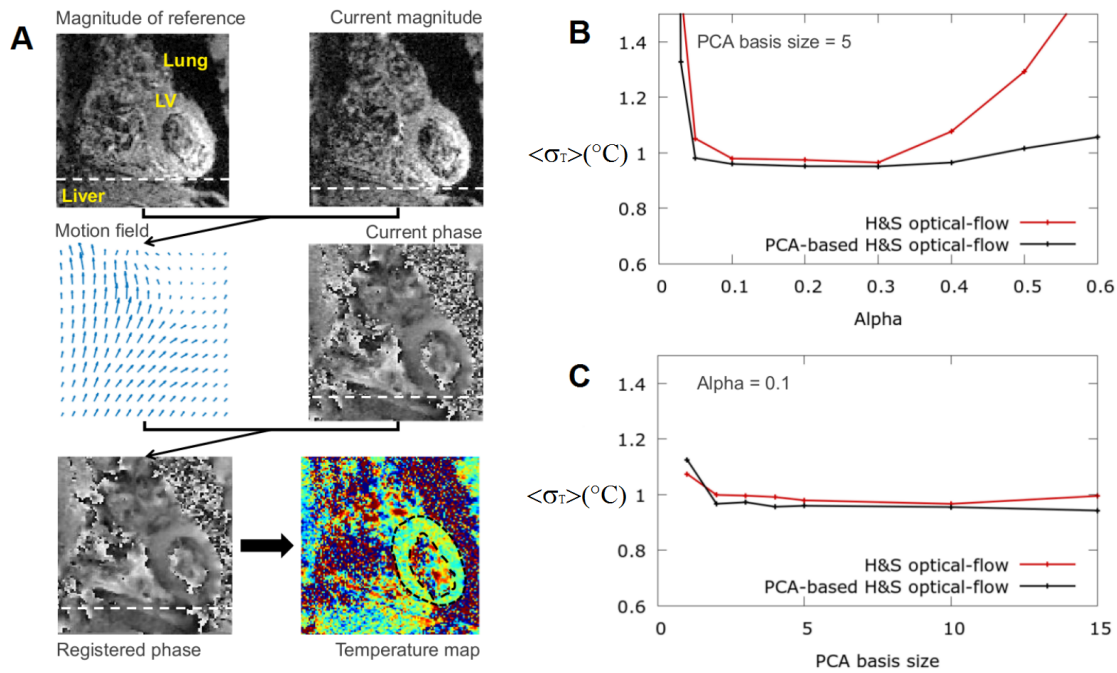


Figure 4.1: Calibration of Horn and Schunck (H&S) and PCA-based H&S optical-flow algorithms. A) The motion is estimated between each current magnitude image and a magnitude image of reference using either H&S or PCA-based H&S optical-flow algorithms. The resulting motion field is used to register the current phase image. Finally the temperature map is calculated from the registered phase using the PRF method. Calibration is computed depending on the regularization term  $\alpha$  (B) and the size of PCA basis (C), i.e. the number of eigenvectors used in the PCA algorithm. Performance of algorithms is evaluated in term of MR thermometry accuracy, given by the standard deviation of the temperature evolution in time ( $\sigma_T$ ) on average over the LV of one typical volunteer (ROI surrounding by the black dashed line on temperature map).

## 4.5 Results

### 4.5.1 Volunteer study

Figure 4.1 depicts the calibration of H&S and PCA-based H&S optical-flow algorithms on a typical experimental dataset of one volunteer (volunteer #5). Regularization term  $\alpha = 0.1$

was found to minimize the  $\sigma_T$  with resulting values of  $0.98 \pm 0.36$  °C and  $0.96 \pm 0.35$  °C for conventional H&S and PCA-based H&S optical-flow algorithms, respectively (Figure 4.1-B).  $\sigma_T$  remained nearly identical when the number of eigenvectors was larger than one (Figure 4.1-C). For all data obtained on volunteers, the number of eigenvectors was set to 5, which represented more than 99% of the total energy (sum of the eigenvalues).

Figure 4.2 compares the performances of conventional H&S and PCA-based H&S algorithms on MR temperature images from all volunteers.  $\sigma_T$  maps obtained on volunteer #5 are reported with the conventional H&S optical-flow approach (Figure 4.2-A) and with the proposed PCA-based H&S method (Figure 4.2-B). Over all volunteers, the temperature stability remained similar for both motion correction strategies, with averaged  $\sigma_T$  over the pixels of the LV ROI of  $1.06 \pm 0.35$ °C (H&S) and  $1.05 \pm 0.40$ °C (PCA-based H&S), respectively. The t-test showed a statistically non-significant difference between the two methods ( $p > 0.01$ ).

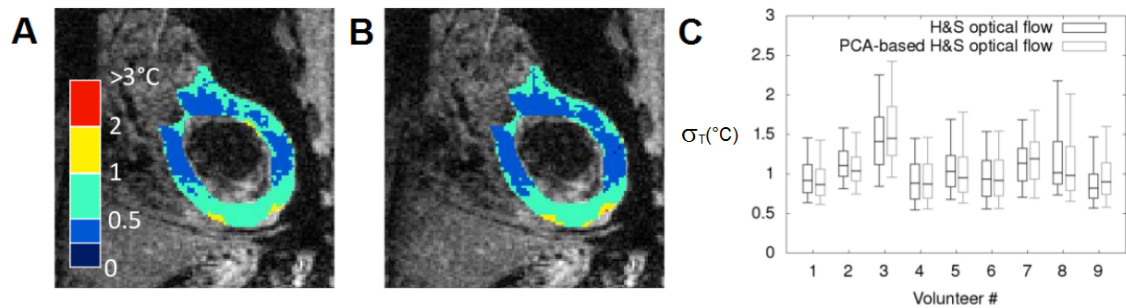


Figure 4.2: Temperature standard deviation ( $\sigma_T$ ) for both optical-flow methods applied to MR temperature images from free-breathing volunteers. The  $\sigma_T$  is computed on a pixel-by-pixel basis over the 2-3 min of dynamic acquisition.  $\sigma_T$  is compared when H&S and PCA-based H&S methods are employed for in-plane motion registration. Typical results obtained on the LV of a healthy volunteer (colored pixels, volunteer #5) are displayed in (A) H&S and (B) PCA-based H&S. Both methods were tested with a weighting factor  $\alpha = 0.1$ , a number of eigenvectors of 5 and identical temperature mapping data processing. Boxplots (C) relate the distribution of  $\sigma_T$  in a ROI surrounding the LV for images from the nine tested volunteers.

#### 4.5.2 Phantom study

Figure 4.3 shows EE of flow fields computed on simulated signal variations around a catheter tip inserted in the static phantom (Figure 4.3-A), without heating. Examples of simulated patterns with  $A = 80\%$  of maximal signal decrease are shown in Figure 4.3-B and applied to the MR images of the gel in Figure 4.3-C. The conventional H&S optical-flow displayed higher EE than PCA-based H&S. With a signal decrease  $A$  of 80 %, the maximal EE was in the range of 1.1-3.5 mm with H&S (Figure 4.3-D) and of 0.03-0.2 mm with PCA-based H&S (Figure 4.3-E), for values of  $\mu$  ranging from 0.9 to 2.9 pixels. As shown on contour plots, EE increased with the amplitude  $A$  and the variance  $\mu$  of the simulated signal drop. On average on the  $9 \times 9$  pixels ROI, the mean EE value increased up to 2 mm with H&S method, whereas it remained around 0.1 mm with the PCA-based method.

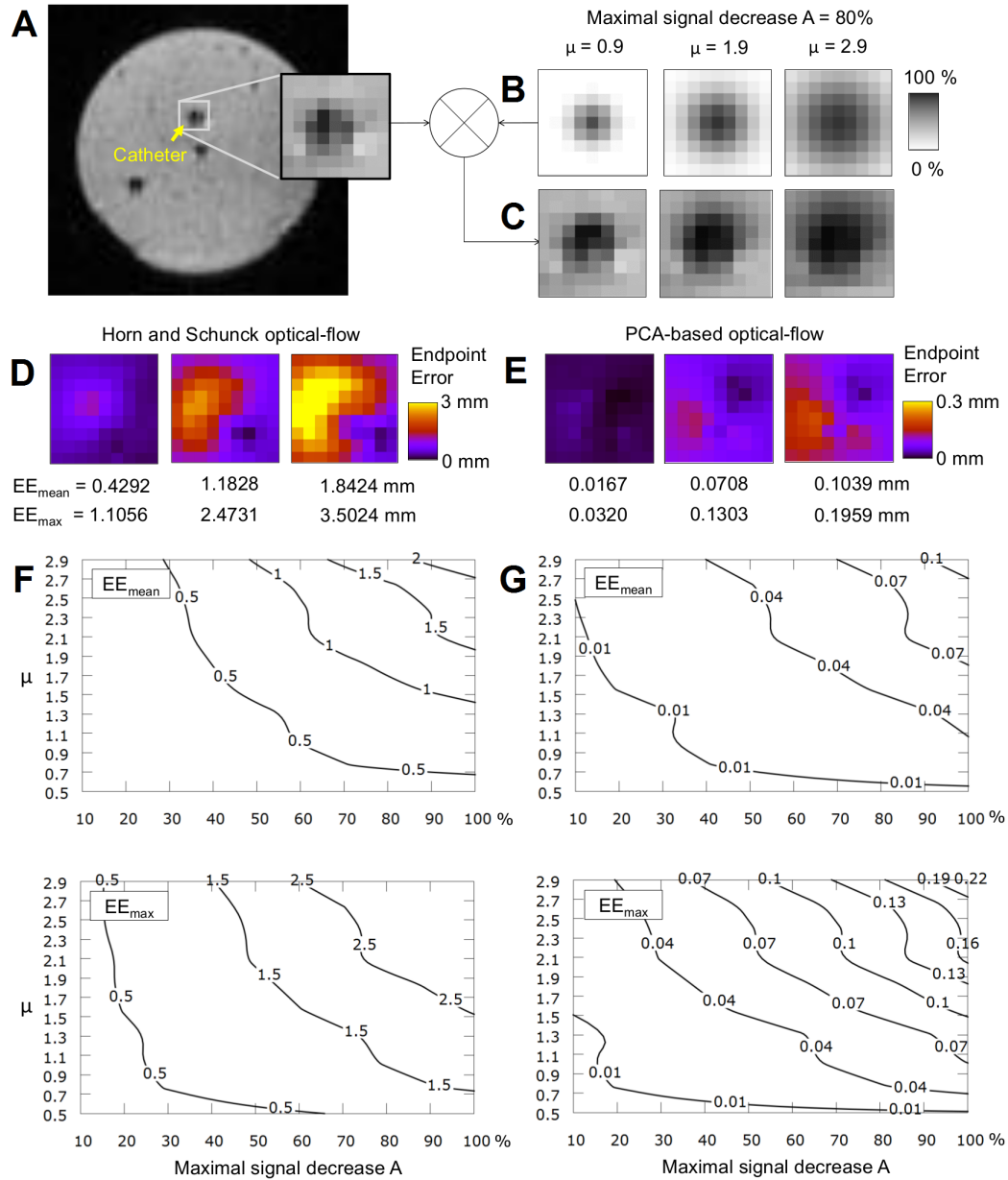


Figure 4.3: Simulation of a local signal decrease on the magnitude image of an agar gel phantom (A) centered on the catheter position. The imaging plane was positioned perpendicular to the catheter, near the tip. Several patterns of signal drop were computed depending on the variance  $\mu$  in pixels and the maximal decrease  $A$  in percentage. Example of patterns is shown in (B) with 80% of signal loss in the central pixel of the ROI ( $9 \times 9$  pixels). Motion estimation was performed on the resulting simulated magnitude images (C). The motion fields Endpoint Error (EE) was computed in millimeters (1 pixel = 1.6 mm) with H&S (D) and PCA-based H&S (E) optical-flow methods. Average and maximal values over the ROI are annotated below. Averaged and maximal EE were calculated for each pattern and summed up on contour plots (F) H&S and (G) PCA-based H&S.

The impact of flow field errors on temperature measurement was measured by performing a RF ablation at 10 W for 60 s. The magnitude decrease during the ablation is illustrated by

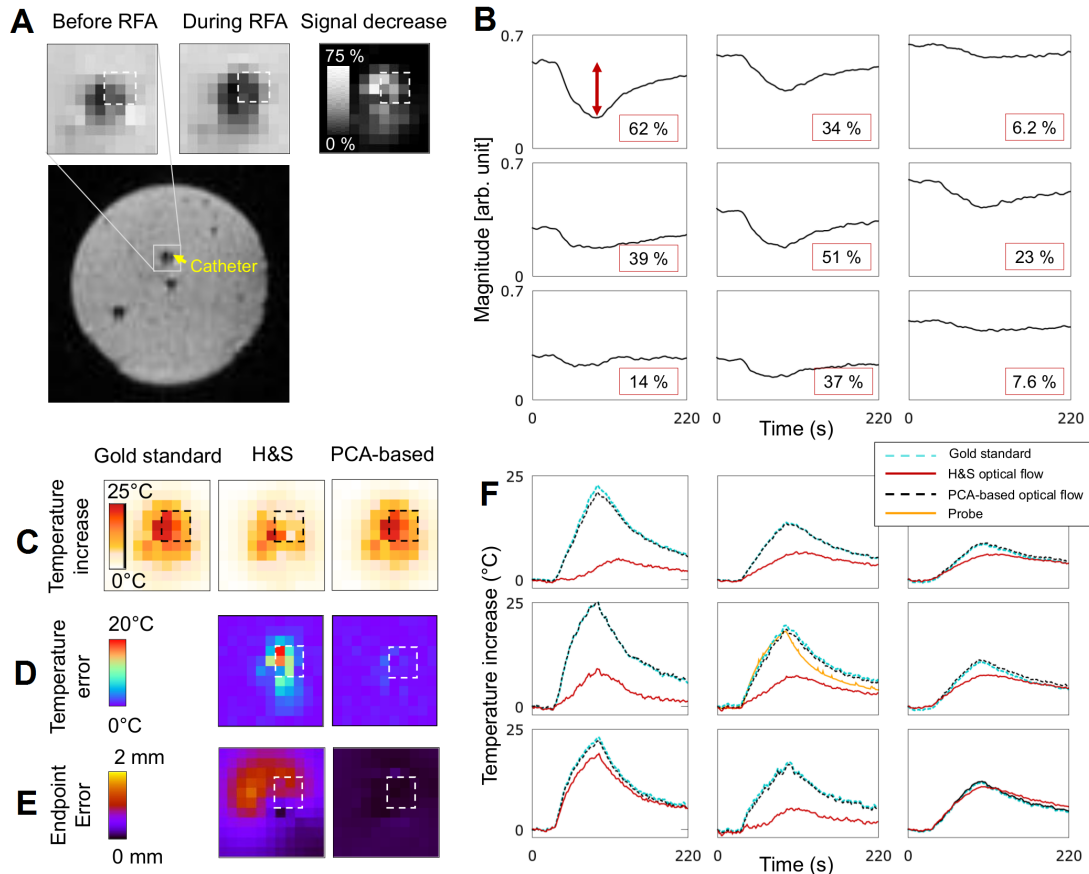


Figure 4.4: Experimental data obtained on a static agar gel phantom. A RF ablation was run for 60 s at 10 W using a MR-compatible catheter inserted in agar gel (A). A decrease of the magnitude signal was observed during the RF ablation. The pixels corresponding to the white dashed box are plotted in (B). (C) Temperature elevation calculated with H&S optical-flow and with PCA-based optical-flow algorithm was compared with temperature measured without any motion correction (Gold standard). Bias introduced by motion registration was evaluated in terms of temperature error (D) and motion fields EE in millimeters (1 pixel = 1.6 mm) (E). Evolution of temperature (F) in time in pixels of a ROI of  $3 \times 3$  pixels (dashed box) was plotted. The curve resulting from optical fiber temperature probe measurements is plotted in the central pixel which corresponds to the closest location of the probe.

performing the difference between two images, before and during the ablation (Figure 4.4-A). Evolution of magnitude in time in  $3 \times 3$  pixels is described in Figure 4.4-B and is correlated with the phantom properties changes during the heating. Temperature maps measured with each method were compared to gold standard temperature map, computed without motion correction (Figure 4.4-C). Heating zone was highly distorted by the errors of the flow field estimated with H&S optical-flow, with a temperature error up to  $15^\circ\text{C}$  (Figure 4.4-D) due to a EE in motion estimation of 1.5 mm (Figure 4.4-E). Maximal intensity decrease was about 60 % and the thickness of the spot was equivalent to  $\mu = 1.3$  pixels. EE was thus in agreement with simulation results displayed in Figure 4.3. In contrast, using the PCA-based method, the EE was found below 0.05 mm and the temperature error below  $1.5^\circ\text{C}$ . Temperature evolution in

time in a ROI of  $3 \times 3$  pixels was plotted in Figure 4.4-F and illustrated the bias introduced by each tested methods.

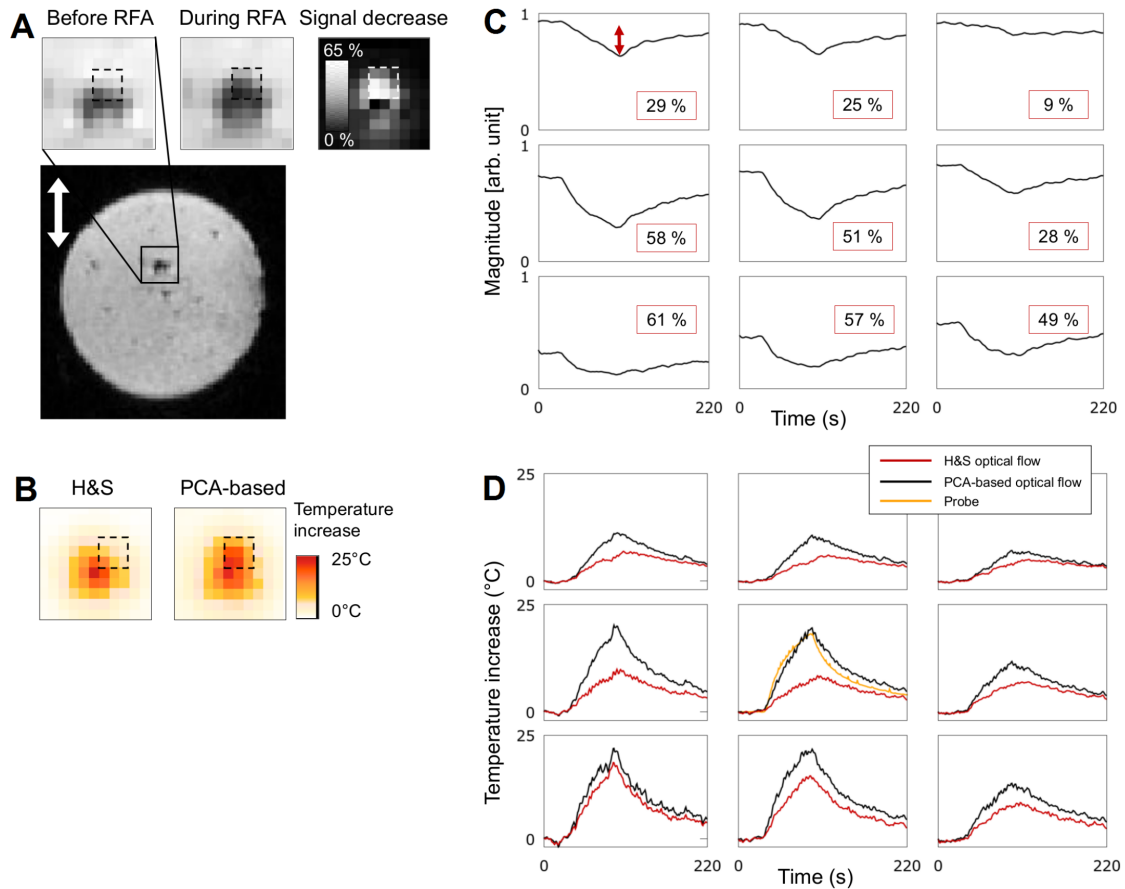


Figure 4.5: Experimental data obtained on an agar gel phantom. A RF ablation (10 W for 60 s) was run on a mobile phantom (translation induced by a mechanical ventilator) and monitored by MR thermometry. Heating induced local intensity variation around the catheter tip (A). Signal loss in  $3 \times 3$  pixels of a ROI (dashed box) is plotted in (B). (C) Temperature map at the end of the RF delivery using H&S and PCA-based H&S algorithms in a  $11 \times 11$  pixels area centered on the catheter tip. (D) Temperature evolution in time on pixels of the dashed black boxes, centered on optical probe location.

During RF ablation on the gel and in presence of motion (Figure 4.5), similar drop in signal intensities near the catheter tip was observed (Figure 4.5-A,B), with a maximal decrease of 60 % and a variance of 1.1 pixel. Temperature maps computed with the conventional H&S method showed an underestimation of up to  $15^\circ\text{C}$  (Figure 4.5-C,D) while temperature from the PCA-based H&S algorithm followed readings from the temperature probe (see central plot in Figure 4.5-D). The presence of motion affected slightly the temperature accuracy (additional noise in temperature signals) despite the use of optical-flow motion registration and susceptibility artifact correction algorithm. However, obtained temperature measurements were similar to those computed on a phantom without motion. Note that the presence of motion prevents the calculation of the gold standard temperature by simple phase subtraction.

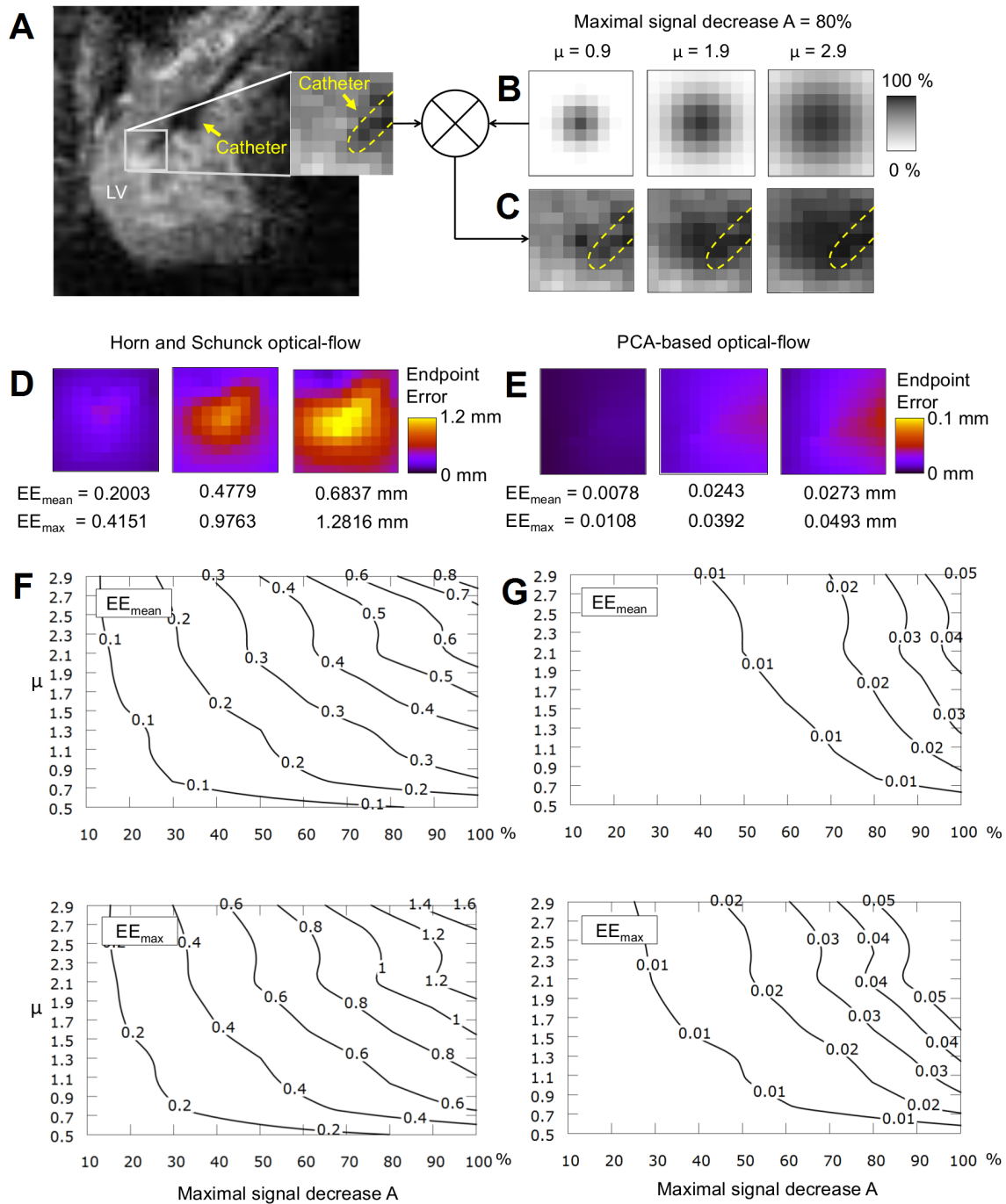


Figure 4.6: Simulation of a local signal decrease on the magnitude image in sagittal orientation of a sheep LV (A) with a MR-compatible catheter inside (yellow arrow). Several patterns of signal drop were computed depending on the variance  $\mu$  in pixels and the maximal decrease  $A$  in percentage. Example of patterns is shown in (B) with a maximal decrease at the center of the ROI of 80%. Motion estimation was performed on the resulting simulated magnitude images (C). The motion fields EE was computed in millimeters (1 pixel = 1.6 mm) with H&S (D) and PCA-based H&S (E) optical-flow methods (mean and maximal values over the ROI annotated below). Averaged and maximal EE were calculated for each pattern and summed up on contour plots (F) H&S and (G) PCA-based H&S in millimeters.

### 4.5.3 In vivo ablation in the left ventricle of a sheep

Figure 4.6-A shows one magnitude image of the time series, where the MR-compatible ablation catheter is visible in hypo-intensity inside the sheep LV (yellow arrow). A ROI of  $9 \times 9$  pixels was selected at the distal tip of the catheter for the simulation of several patterns of signal intensity drop. Examples of these patterns are shown in Figure 4.6-B with a maximal signal decrease  $A$  of 80 % and various values of variance  $\mu$  from 0.9 to 2.9 pixels. These patterns were applied to the original magnitude image to simulate a change in myocardial tissue properties with heating (Figure 4.6-C). Corresponding EE maps were computed with H&S (Figure 4.6-D) and PCA-based H&S (Figure 4.6-E) motion estimation method, showing that the misregistration were higher using the H&S algorithm. For example, a signal decrease pattern ( $A, \mu$ ) of (80% 1.9 pixels) resulted in a maximal EE of  $\sim 0.98$  mm with the H&S algorithm compared to  $\sim 0.04$  mm with the PCA-based H&S method. Contour plots displayed in Figure 4.6-F and 4.6-G confirm that the latter method is more robust in terms of mean and maximal EE values.

To evaluate the impact of motion estimation errors, original experimental data with RF ablation heating on the LV was used to compute the temperature maps using the two different methods for motion estimation. The signal decrease in the pixels around the catheter tip (Figure 4.7-A) is displayed in Figure 4.7-B. Motion-induced susceptibility artifacts were successfully corrected with both methods and a heating spot is clearly visible near the tip of the catheter, as shown in Figure 4.7-C. However, a difference in temperature elevation (up to  $5^\circ\text{C}$ ) was observed in the 3 hottest pixels with the PCA-based H&S algorithm (Figure 4.7-D). The signal drop in these pixels was about 40% with a variance  $\mu = 0.7$  pixel in a limited area in the vicinity of the catheter tip.

## 4.6 Discussion

Real-time cardiac thermometry was achieved with a spatial resolution of  $1.6 \times 1.6 \times 3$  mm<sup>3</sup> and a temporal resolution of  $\sim 4$ -5 slices/heartbeat, as already reported [13]. However, the accuracy of temperature measurements relies on the efficiency of the motion registration algorithm together with the correction of the susceptibility artifacts. The standard method for motion estimation in the context of MR thermometry on moving organs is the use of optical-flow algorithms that interpret intensity variation on magnitude images as local displacement of the pixels. In this paper, the impact of signal decrease during RF ablation on the motion estimation was quantitatively investigated, and the PCA-based optical-flow algorithm was demonstrated more robust against potential local intensity of magnitude images during heating.

The required learning step does not increase the duration of the standard MR thermometry procedure since collection of data prior to heating is also necessary for compensating susceptibility artifacts on phase images. Since only a limited number of respiratory cycles is required to collect learning data (typically 20 s scanning were found sufficient to cover two to three respiratory cycles), such a method remains compatible with clinical practice. Moreover, the MR

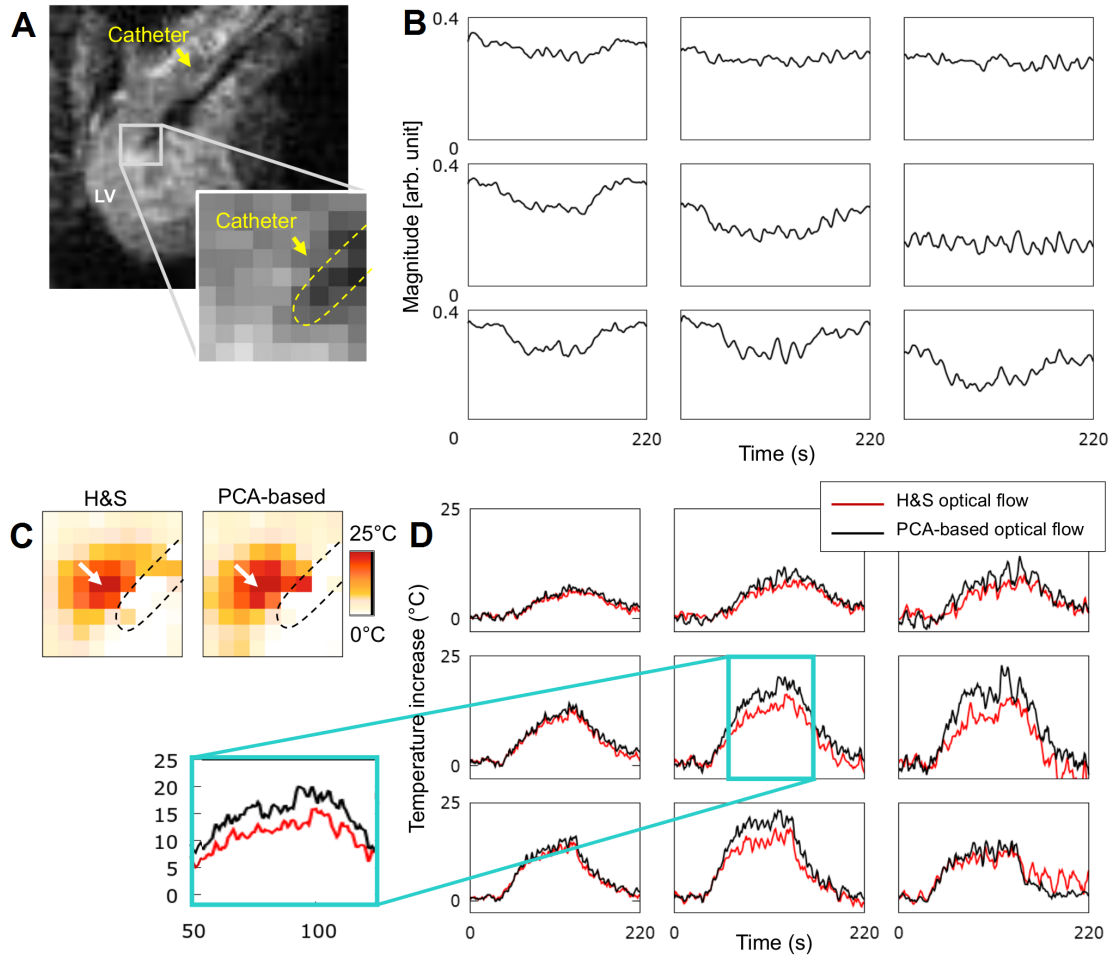


Figure 4.7: Experimental results of RF ablation under MR temperature imaging in a sheep. A RF ablation was run for 60 s at 30 W. Free-breathing dynamic magnitude images (A) were acquired during RF ablation and used to compensate for respiratory motion. Magnitude signal loss over time in  $3 \times 3$  pixels close to the catheter tip is plotted in (B). Temperature maps (C) were computed using H&S and PCA-based H&S optical-flow algorithms for motion estimation. Temperature evolution in time in  $3 \times 3$  pixels (centered on the pixel indicated by the white arrow) was plotted in (D) to compare results achieved with both tested methods.

thermometry pipeline is fully automated and does not require the intervention of an operator (for ROI segmentation for example). The calibration is limited to only two parameters (number of eigenvectors and regularization term) and can be performed only once on a representative image dataset. The same parameters can be used for an unlimited number of similar data. For the tested images in this study, we showed that any value of  $\mu$  in the range of 0.1 to 0.4 combined with a minimum number of 2 eigenvectors (Figure 4.1) were sufficient to ensure good results. Compared with the conventional H&S optical-flow, the PCA-based technique provided similar results on all volunteers in term of  $\sigma_T$  (value around  $1^\circ\text{C}$  on the LV, see Figure 4.2), which is sufficient to accurately measure the temperature evolution during RF ablation that typically results in temperature increase higher than  $20^\circ\text{C}$  in the myocardium.

In this paper, a simulation protocol was presented to quantify the impact of different patterns of signal loss on motion estimation. EE contour plots were computed by comparing the estimated motion on the original image with the motion calculated on images containing signal intensity variations that were not observed during the pre-heating learning step. Results showed that conventional PCA-based H&S optical-flow algorithm was less impacted by local intensity variation with a motion field EE 20-fold lower than with the standard H&S method. The conventional H&S motion fields' error was more significant on the phantom than in vivo on sheep LV images:  $\sim 2$  mm and  $\sim 0.8$  mm of averaged EE (see Figure 4.3 and 4.6), respectively. Such a difference can be attributed to the different features of the magnitude images in both situations. The gel phantom image presented a rather uniform disk clearly delineated from the background and only a limited number of pixels were hypointense near the catheter tip. On the contrary, cardiac MR images were noisier, with a much lower number of pixels covering the myocardium on the LV and a larger number of hypointense pixels were visible since the catheter was included into the imaging plane. Therefore, the same simulated patterns may result in different contributions on misregistration using optical flow algorithms.

The impact of misregistration using conventional H&S algorithm was then investigated on experimental data during RF delivery. The resulting temperature error could be computed on a static phantom since the reference temperature could be measured. Conventional H&S was found to sharply impact the calculated temperature map (up to  $15^{\circ}\text{C}$  of temperature error) while the PCA-based H&S allows for an accurate temperature calculation (below  $1.5^{\circ}\text{C}$  of temperature error). The motion fields' EE was in good agreement with the prediction of the simulation, considering the fact that experimental intensity change was not as isotropic as simulated one. The simulated signal drop patterns were designed to mimic the aspect of catheter-based RF ablation, but other patterns may be implemented to simulate different heating sources (e.g. Laser, high intensity focused ultrasound, microwave) [19].

Comparison of temperature maps obtained with both optical-flow methods was finally performed in presence of motion on a phantom and in vivo in sheep LV during RF ablation. As on static phantom, temperature maps were sharply different by only changing the optical-flow algorithm. The temperature increase using PCA-based H&S motion estimation was close to the optical fiber probe located near the catheter tip. The impact of intensity drop on final temperature maps was found larger on the gel phantom (up to  $15^{\circ}\text{C}$ ) than on the sheep LV (up to  $5^{\circ}\text{C}$ ). These results were consistent with simulated motion fields' EE considering the amplitude and the variance of the intensity variation that were smaller in vivo than in phantom. Therefore, the methodology presented in this work could be applied for each particular situation and does not require particular assumptions.

In order to be clinically applicable, computation time of the algorithms must be shorter than 100 ms (scan-time per image) to avoid latency in the real-time processing. Using the parameter 0.1 and five eigenvectors with the PCA-H&S algorithm, computation time was of 25 ms per image, which was approximately 2.5 times shorter than the conventional H&S algorithm (63

ms). Computation time may be shortened by adjusting the regularization parameter (reducing increases the motion estimation computation time) whereas the number of eigenvectors has no influence on the computation time. A GPU-based implementation may also allow a significant reduction of the processing time per slice. However it was found sufficiently fast with its current implementation with the frame-rate of the thermometry pulse sequence for monitoring cardiac RF ablation.

The proposed technique is constrained to displacements that can be characterized as a linear combination of the prior learned motion. However, a complete re-calibration may be required in case of significant changes in the motion pattern and/or in the image features, such as the modification of the catheter position than can occur during the RF ablation procedures. Similarly, the use of this method on patients suffering from cardiac arrhythmia need to be evaluated. In presence of arrhythmia, image acquisition can occur at different cardiac phases due to a change in synchronization related to the ECG. Cardiac contraction patterns that have never been observed during the learning step may therefore be difficult to compensate. Adaptive PCA algorithms should be investigated to automatically adapt in real-time without stopping the acquisition and reacquire a new learning data set.

Imaging slices positioned in coronal and sagittal orientations were assumed to fully encompass respiratory motion. However, residual through-plane motion may remain, depending on the patient anatomy and breathing pattern. Integration of an echo-navigator to the thermometry pulse sequence followed by slice repositioning may help to overcome this limitation [12, 20].

## 4.7 Conclusion

In this paper, the robustness of the PCA-based H&S method was evaluated in the context of tissue MR properties changes during RF ablation in the perspective of cardiac treatment of arrhythmia. This algorithm accurately estimates the heart motion in presence of signal intensity variations due to heating and remains compatible with a frame rate of 10 images per second. The PCA-based H&S algorithm is faster and less sensitive to local variations of signal intensities associated with temperature than conventional H&S algorithm.

## 4.8 References

1. Denis de Senneville, B., El Hamidi, A. & Moonen, C. A Direct PCA-Based Approach for Real-Time Description of Physiological Organ Deformations. *IEEE Transactions on Medical Imaging* **34**, 974–982. ISSN: 0278-0062, 1558-254X (Apr. 2015).
2. Tanner, H. *et al.* Catheter Ablation of Recurrent Scar-Related Ventricular Tachycardia Using Electroanatomical Mapping and Irrigated Ablation Technology: Results of the Prospective Multicenter Euro-VT-Study. en. *Journal of Cardiovascular Electrophysiology* **21**, 47–53. ISSN: 10453873, 15408167 (Jan. 2010).

3. Weerasooriya, R. *et al.* Catheter Ablation for Atrial Fibrillation. en. *Journal of the American College of Cardiology* **57**, 160–166. ISSN: 07351097 (Jan. 2011).
4. Wittkamp, F. H. & NAKAGAWA, H. RF catheter ablation: lessons on lesions. *Pacing and Clinical Electrophysiology* **29**, 1285–1297 (2006).
5. Holbrook, A. B., Santos, J. M., Kaye, E., Rieke, V. & Pauly, K. B. Real-time MR thermometry for monitoring HIFU ablations of the liver. en. *Magnetic Resonance in Medicine* **63**, 365–373. ISSN: 07403194, 15222594 (Feb. 2010).
6. Seror, O. *et al.* Real time monitoring of radiofrequency ablation based on MR thermometry and thermal dose in the pig liver in vivo. en. *European Radiology* **18**, 408–416. ISSN: 0938-7994, 1432-1084 (Feb. 2008).
7. Ramsay, E. *et al.* MR thermometry in the human prostate gland at 3.0T for transurethral ultrasound therapy: Prostate MR Thermometry at 3T. en. *Journal of Magnetic Resonance Imaging* **38**, 1564–1571. ISSN: 10531807 (Dec. 2013).
8. McDannold, N. *et al.* Uterine leiomyomas: MR imaging–based thermometry and thermal dosimetry during focused ultrasound thermal ablation 1. *Radiology* **240**, 263–272 (2006).
9. De Senneville, B. D., Mougenot, C. & Moonen, C. T. Real-time adaptive methods for treatment of mobile organs by MRI-controlled high-intensity focused ultrasound. *Magnetic Resonance in Medicine* **57**, 319–330 (2007).
10. Lipsman, N. *et al.* MR-guided focused ultrasound thalamotomy for essential tremor: a proof-of-concept study. *The Lancet Neurology* **12**, 462–468 (2013).
11. Sapareto, S. A. & Dewey, W. C. Thermal dose determination in cancer therapy. *International Contact Lens Clinic* **16**, 340–346 (1989).
12. De Senneville, B. D. *et al.* Feasibility of fast MR-thermometry during cardiac radiofrequency ablation: FEASIBILITY OF FAST MR-THERMOMETRY DURING CARDIAC RF ABLATION. en. *NMR in Biomedicine* **25**, 556–562. ISSN: 09523480 (Apr. 2012).
13. Ozenne, V. *et al.* Improved cardiac magnetic resonance thermometry and dosimetry for monitoring lesion formation during catheter ablation. *Magnetic resonance in medicine*. <<http://onlinelibrary.wiley.com/doi/10.1002/mrm.26158/pdf>> (visited on 06/07/2016) (2016).
14. Roujol, S., Ries, M., Quesson, B., Moonen, C. & Denis de Senneville, B. Real-time MR-thermometry and dosimetry for interventional guidance on abdominal organs. en. *Magnetic Resonance in Medicine* **63**, 1080–1087. ISSN: 07403194, 15222594 (Apr. 2010).
15. Horn, B. K. & Schunck, B. G. Determining optical flow. *Artificial intelligence* **17**, 185–203 (1981).
16. Graham, S. J., Bronskill, M. J. & Henkelman, R. M. Time and temperature dependence of MR parameters during thermal coagulation of ex vivo rabbit muscle. *Magnetic resonance in medicine* **39**, 198–203 (1998).

17. Hansen, M. S. & Sørensen, T. S. Gadgetron: An open source framework for medical image reconstruction: Gadgetron. en. *Magnetic Resonance in Medicine* **69**, 1768–1776. ISSN: 07403194 (June 2013).
18. Rickey, D., Picot, P., Christopher, D. & Fenster, A. A wall-less vessel phantom for Doppler ultrasound studies. en. *Ultrasound in Medicine & Biology* **21**, 1163–1176. ISSN: 03015629 (Jan. 1995).
19. Lepetit-Coiffé, M. *et al.* Real-time monitoring of radiofrequency ablation of liver tumors using thermal-dose calculation by MR temperature imaging: initial results in nine patients, including follow-up. en. *European Radiology* **20**, 193–201. ISSN: 0938-7994, 1432-1084 (Jan. 2010).
20. Köhler, M. O., Denis de Senneville, B., Quesson, B., Moonen, C. T. & Ries, M. Spectrally selective pencil-beam navigator for motion compensation of MR-guided high-intensity focused ultrasound therapy of abdominal organs. en. *Magnetic Resonance in Medicine* **66**, 102–111. ISSN: 07403194 (July 2011).

## Chapter 5

# Feasibility of real-time MR thermal dose mapping for predicting radiofrequency ablation outcome in the myocardium in vivo

### Contents

---

<b>5.1</b>	<b>Preamble</b>	<b>106</b>
<b>5.2</b>	<b>Abstract</b>	<b>107</b>
<b>5.3</b>	<b>Introduction</b>	<b>107</b>
<b>5.4</b>	<b>Methods</b>	<b>108</b>
5.4.1	Volunteer study	108
5.4.2	Animal study	108
5.4.3	Radiofrequency ablation device	109
5.4.4	Imaging protocol	109
5.4.5	MR thermometry pipeline	110
5.4.6	Post-ablation visualization	113
5.4.7	Macroscopic examination and lesion size measurements	113
<b>5.5</b>	<b>Results</b>	<b>113</b>
5.5.1	Volunteer study	113
5.5.2	In vivo radiofrequency ablations monitoring	116
5.5.3	Post-ablation lesion size measurements	117
<b>5.6</b>	<b>Discussion</b>	<b>119</b>
5.6.1	Limitations	121
<b>5.7</b>	<b>Conclusion</b>	<b>122</b>
<b>5.8</b>	<b>References</b>	<b>122</b>
<b>5.9</b>	<b>Tips and tricks of MR-guided RF ablation in vivo</b>	<b>126</b>
5.9.1	Arrhythmia and pacing	126

5.9.2	ECG-triggering . . . . .	126
5.9.3	Precise localisation of the catheter tip . . . . .	126
5.9.4	Radiofrequency ablation . . . . .	126
5.9.5	EP recording . . . . .	127

---

## 5.1 Preamble

In this chapter, the initial cardiac MR thermometry pipeline described in Chapter 3 was improved with the following features:

- The commercial single-shot EPI pulse sequence was modified to integrate an echo-navigator between two successive slices. Positioned on the diaphragm, this echo-navigator provided the 1D respiratory trace which was used to update the position of the EPI imaging slices. This “slice following” technique was described in Section 2.3.3.2 of this thesis. A similar technique was reported in previous studies of cardiac MR thermometry [1, 2]. It offers a free positioning of slices instead of being restricted to the main direction of motion. It allows to access to additional anatomical structures, such as the right ventricle in short axis orientation, while limiting out-of-plane motion.
- In addition to a small acquired voxel size of  $1.6 \times 1.6 \times 3 \text{ mm}^3$ , zero filling was added in image reconstruction to achieve a final in-plane resolution of  $0.8 \times 0.8 \text{ mm}^2$ . Without bringing any additional information, this technique makes heating area easier to visualize, in view of the limited size of thermal lesions.
- The motion estimation algorithm described in Chapter 4 was used for in-plane registration of magnitude and phase images to reduce the impact of signal decrease induced by heating on calculated motion fields.

In addition to these technical developments, new MR-compatible catheters were available at the IHU LIRYC institute (middle of 2<sup>nd</sup> year, beginning of 3<sup>rd</sup> year). Embedded micro-coils made catheter navigation and location more straightforward, using active catheter tracking. The position of the catheter was detected and used to update the position of a localization slice. Thanks to these improvements, pre-clinical animal study was significantly advanced compared to Chapter 3 and state-of-the-art studies in cardiac MR thermometry (see Section 2.5). Over twelve RF ablations successfully monitored by MR thermometry in sheep, thermal dose (TD) mapping could be evaluated as a tool of real-time visualization of where tissue necrosis occurred. For that purpose, lesion sizes measured on TD maps were correlated to those measured on 3D post-ablation imaging, that relied on intrinsic tissue properties without contrast agent. The relevance of thermal dose mapping for prediction of lesion extent is a very important point that could lead to a superior clinical outcome in the future.

This chapter corresponds to a full paper submitted by Solemn Toupin et al., in the Journal of Cardiovascular Magnetic Resonance (JCMR-D-16-00197). Very few modifications were introduced to harmonize the notations of this thesis manuscript.

## 5.2 Abstract

**Purpose:** Clinical treatment of cardiac arrhythmia by radiofrequency (RF) ablation currently lacks quantitative and precise visualization of lesion formation in the myocardium during the procedure. This study aims at evaluating thermal dose (TD) imaging obtained from real-time magnetic resonance (MR) thermometry on the heart as a relevant indicator of the thermal lesion extent.

**Methods:** MR temperature mapping based on the Proton Resonance Frequency (PRF) shift method was performed at 1.5 T on the heart, with 4 to 5 slices acquired per heartbeat. Respiratory motion was compensated using navigator-based slice tracking. Residual in-plane motion and related magnetic susceptibility artifacts were corrected online. The standard deviation of temperature was measured on healthy volunteers ( $N = 5$ ) in both ventricles. On animals, the MR-compatible catheter was positioned and visualized in the left ventricle (LV) using a b-SSFP pulse sequence with active catheter tracking. Twelve MR-guided RF ablations were performed in three sheep in vivo at various locations in left ventricle (LV). The dimensions of the thermal lesions measured on thermal dose images, on 3D T1-weighted (T1-w) images acquired immediately after the ablation and at gross pathology were correlated.

**Results:** MR thermometry uncertainty was  $1.5^{\circ}\text{C}$  on average over more than 96 % of the pixels covering the left and right ventricles, on each volunteer. On animals, catheter repositioning in the LV with active slice tracking was successfully performed and each ablation could be monitored in real-time by MR thermometry and thermal dosimetry. Thermal lesion dimensions on TD maps were found to be highly correlated with those observed on post-ablation T1-w images ( $R = 0.87$ ) that also correlated ( $R = 0.89$ ) with measurements at gross pathology.

**Conclusion:** Quantitative TD mapping from real-time rapid cardiac MR thermometry during catheter-based RF ablation is feasible. It provides a direct assessment of the lesion extent in the myocardium with precision in the range of one millimeter. Real-time MR thermometry and thermal dosimetry may improve safety and efficacy of the RF ablation procedure by offering a reliable indicator of therapy outcome during the procedure.

## 5.3 Introduction

Radiofrequency (RF) ablation is a well-established procedure to treat cardiac arrhythmias by inducing small thermal lesions in the myocardium. When the area responsible for the arrhythmia is isolated or destructed, durable sinus rhythm is restored and the mechanical function of the heart may even improve in some cases. To prevent recurrence of the arrhythmia, created lesions must be transmural and permanent. Success rate of this procedure is currently limited by a lack of visualization of lesion formation during the procedure [3, 4]. To date, X-Ray fluoroscopy remains the reference imaging modality for navigating catheters in cardiac chambers for electrical mapping and delivery of therapeutic RF ablation. However, the intrinsic poor soft tissue contrast of this modality does not allow visualization of myocardial injury. Catheter tip

temperature rise, changes in tissue electrical impedance and delivered power showed poor correlation with the actual lesion size [5]. On the other hand, an excessive temperature exposure may translate into extra cardiac damages in organs such as lungs, bronchi, phrenic nerves or esophagus [6]. Therefore, there is a need to develop new strategies to offer a more reliable monitoring lesion formation for increased patient safety and improvement of the therapeutic efficiency.

Magnetic Resonance (MR) thermometry using the Proton Resonance Frequency (PRF) shift method has been shown to be a relevant technique for the monitoring of the thermal treatment in a number of organs including liver [7, 8], prostate [9], uterus [10] and brain [11, 12]. In addition, it has been demonstrated that MR thermometry-derived cumulative thermal dose (TD) mapping provides a good correspondence between temperature increases for a given time of exposure and the resulting thermal lesion dimensions, using a lethal TD threshold equivalent to a constant heating at 43°C for 240 min [13].

Recent studies demonstrated the feasibility of cardiac MR thermometry with electrocardiogram (ECG) and echo-navigator triggering to address challenges inherent to heart contraction and respiratory motion [2, 14, 15]. Correction strategies were proposed to compensate for susceptibility artifacts associated with magnetic field changes due to breathing [16, 17]. A spatial resolution of  $1.6 \times 1.6 \times 3 \text{ mm}^3$  was recently reported with an imaging time of  $\sim 100 \text{ ms}$  per slice [15]. However, visualization of temperature increase remained limited to a small number of pixels and in vivo data were reported on a limited number of preclinical experiments. To our knowledge, no studies reported correlation between the TD maps derived from MR thermometry and the RF ablation lesion sizes in the context of the treatment of cardiac arrhythmia.

This study aims at demonstrating the feasibility of simultaneous RF thermal ablation and real-time MR TD mapping for predicting ablated lesion extent.

## 5.4 Methods

### 5.4.1 Volunteer study

MR thermometry was evaluated on 5 healthy volunteers under free-breathing conditions. Each volunteer was informed about the protocol and consented to participate to this study.

### 5.4.2 Animal study

Animal experiments were conducted in vivo on sheep ( $N = 3$ ) weighting 46-54 kg. The experimental protocol was approved by the ethics committee of the University of Bordeaux. Anesthesia was induced and maintained with an intravenous injection of ketamine (40 mg/kg/h, IM, Virbac, Carros, France) and 2 mg/kg/h midazolam (Mylan, Canonsburg, PA, U.S.A.). Two MR-compatible catheters were positioned using X-ray angiography system (Toshiba InfiniX, Toshiba Medical, Nasu, Japan). An eight-French MR-compatible catheter (Biosense Webster, Diamond Bar, CA, U.S.A.) was inserted into the right ventricle (RV) for cardiac pacing. A ten-French MR-compatible catheter (MRI Interventions, Irvine, CA, U.S.A.) was positioned into the

LV for RF ablation. This catheter was equipped with 4 MR micro-coils to allow active device tracking under MRI (Figure 5.1-A red arrows, and Figure 5.1-B) and with 2 electrophysiological (EP) electrodes (Figure 5.1-A, blue arrows). The animals were installed in a supine position in the MR scanner and were ventilated using a MR-compatible ventilator (Aestivia, General Electric, Fairfield, CT, U.S.A.) with a respiratory rate of 15 breaths per minute (bpm). Vital signs including cardiac rhythm, intra-arterial pressure, capnometry and rectal temperature, were monitored during all the experiments (Carescape, General Electric, Fairfield, CT, U.S.A.).

### 5.4.3 Radiofrequency ablation device

The LV catheter was connected to a clinical RF generator (Stockert Medical Solution, Freiburg, Germany) located outside the Faraday cage, using the ClearTrace system [18] (MRI Interventions, Irvine, CA, U.S.A.). A RF current at 500 kHz was sent between the catheter tip electrode and an adhesive return electrode (MONOPlate, ERBE, Tübingen, Germany) positioned on animal skin. Electrical isolation between RF generator and MR scanner was achieved by low pass filters introduced in the transmission line [2] to prevent RF artifacts on MR acquisitions due to possible interferences between RF ablation device and MR receivers. The catheter was irrigated with a saline solution (0.9 % concentration) with a flow rate of 3 mL/min during all the procedure and 10-12 mL/min during RF ablation. The heart was paced with the catheter located into the RV to reduce the risk of inducing ventricular arrhythmia commonly observed in large animal models during RF ablation. EP signals were measured between the tip electrode and the 2<sup>nd</sup> electrode of catheters in both ventricles and displayed on a clinical EP acquisition system (Bard, LabSystem PRO, Boston Scientific, Marlborough, MA, U.S.A.). A numerical low-pass Butterworth filter (cutoff frequency = 30 Hz, 8th order) was applied to LV signal for denoising.

### 5.4.4 Imaging protocol

MR acquisition was performed on a 1.5 T MR system (Avanto, Siemens Healthcare, Erlangen, Germany) using two clinically used 16-channel cardiac coils (Invivo Corporation, Gainesville, FL, U.S.A.). After scout views were acquired, the imaging protocol was set as follow:

In volunteers, the receiver coils were positioned anterior and posterior around the chest . MR temperature images were acquired in short axis orientation under free breathing.

In animals, the receiver coils were positioned left and right to the chest. Catheter navigation was performed under MR guidance to position the catheter at different locations within the LV. Then, MR temperature images were acquired under assisted ventilation during RF ablation. 3D T1-weighted images were acquired after completion of the ablations to assess lesion sizes. Details on each acquisition sequence are provided below.

#### Catheter navigation

Real-time guidance of the catheter was performed using an interactive sequence made of a balanced steady state free precession (b-SSFP) pulse sequence (TE/TR = 1.93/183 ms, resolu-

tion =  $1.8 \times 1.8 \times 4 \text{ mm}^3$ , Field of view (FOV) =  $225 \times 225 \text{ mm}^2$ , Flip angle (FA) =  $45^\circ$ ) interleaved with a catheter tracking module (BEAT IRTTT: Interactive Real Time Tip Tracking, Siemens Healthcare, Erlangen, Germany). This module consisted in a 3D encoding of the micro-coils position (Figure 5.1-C) along three successive gradient orientations with a total duration of 20 ms. The 3D position of the catheter coils was computed online and three slices were automatically repositioned accordingly to align the center of the slice on the catheter tip (Figure 5.1-D). MR images were displayed on a remote monitor inside the MR room to provide visual feedback to the operator.

### Dynamic temperature mapping

A fat-saturated, single-shot Echo Planar Imaging (EPI) sequence was combined with GRAPPA parallel acquisition technique (acceleration factor of 2) to achieve a  $1.6 \times 1.6 \times 3 \text{ mm}^3$  spatial resolution, TE/TR/FA = 18-20 ms/110 ms/ $60^\circ$ , bandwidth = 1576 Hz/px, FOV =  $180 \times 180 \text{ mm}^2$ , 6/8 partial Fourier. Up to five slices (spacing between slices = 0.3 mm) were acquired at each heartbeat during 250-300 consecutive cardiac cycles with ECG triggering (Figure 5.1-E). Saturation slabs were positioned along the FOV in the phase encoding direction to avoid aliasing and two additional saturation bands were set parallel to the imaging slices to reduce the signal of blood inside the cavities (Figure 5.1-F), as proposed in [1]. A crossed-pair navigator was positioned on the dome of the liver to adjust the slice position in real-time for compensating through-plane respiratory motion (Figure 5.1-G) [19]. A tracking factor of 0.6 was used to relate the motion of the liver with the heart displacement. On volunteers, the group of slices was positioned in short axis orientation at the medium part of the heart to evaluate the precision of the method on both ventricles. On sheep, the group of slices was positioned accordingly to intersect the catheter tip, previously visualized during the MR-guided navigation. Before the RF ablation, a series of 70 repetitions was first acquired to assess the MR thermometry stability in the myocardium surrounding the catheter tip. Then an identical EPI acquisition was run for 250-300 repetitions and RF energy was started at the 50<sup>th</sup> image.

#### 5.4.5 MR thermometry pipeline

Acquired EPI raw data were streamed online via TCP/IP to a remote computer for image reconstruction using the Gadgetron framework [20]. Reconstruction pipeline included EPI ghost-correction using three central line of k-space, followed by GRAPPA parallel reconstruction [15]. Zero filling was applied prior to Fourier transform of MR data, resulting in a matrix size of  $224 \times 224 \text{ px}$  and a reconstructed pixel size of  $0.8 \times 0.8 \text{ mm}^2$  in plane.

The PRF shift thermometry method computes temperature change  $\Delta T$  from difference between phase image  $\varphi$  and a reference phase image  $\varphi_{REF}$  acquired prior to heating:

$$\Delta T = \frac{\Delta \varphi}{\gamma \cdot \alpha_{PRF} \cdot B_0 \cdot TE} = \frac{\varphi - \varphi_{REF}}{\gamma \cdot \alpha_{PRF} \cdot B_0 \cdot TE} \quad (5.1)$$

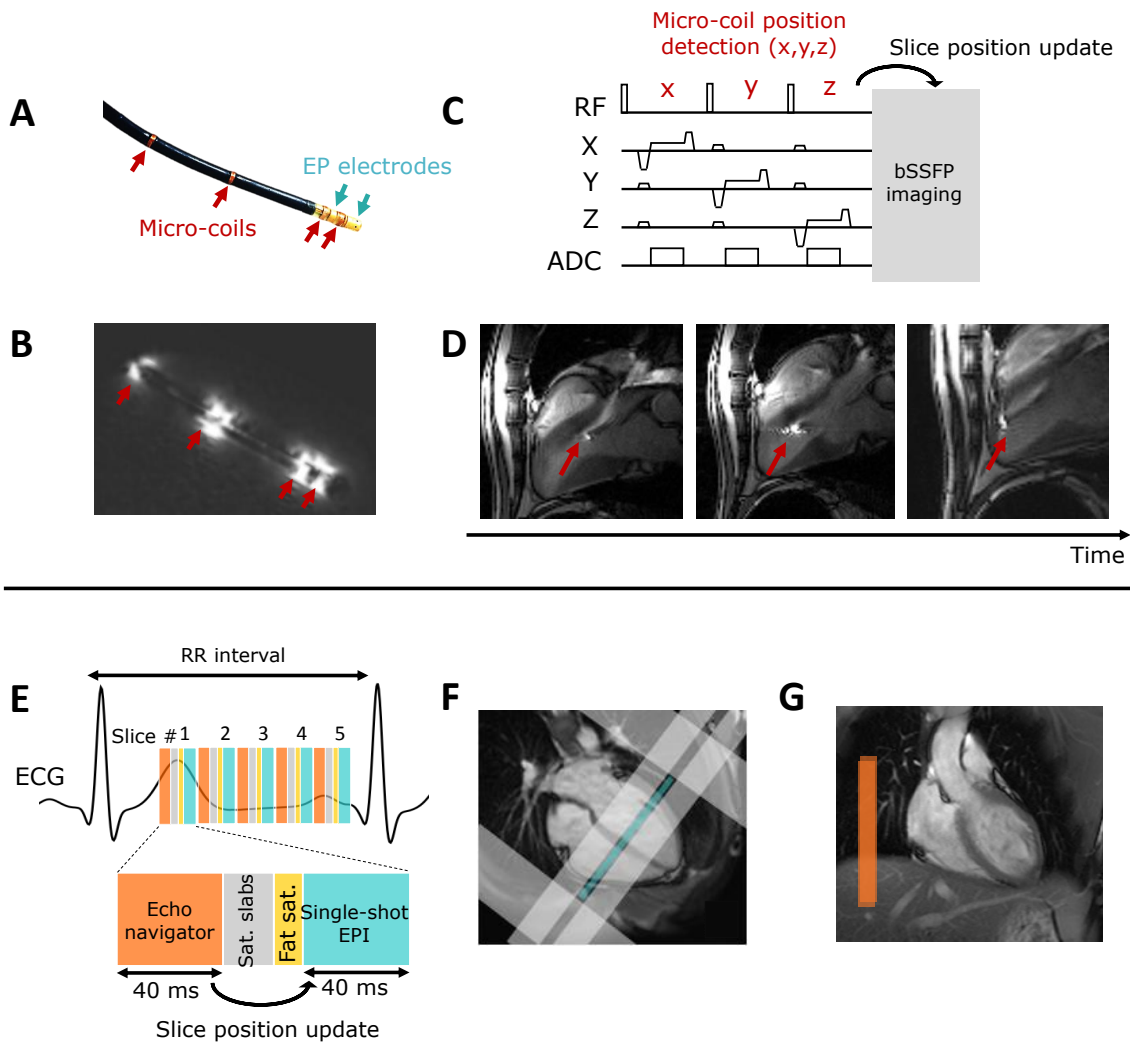


Figure 5.1: Imaging protocol for catheter navigation (A-D) and fast MR thermometry (E-G) for ablation monitoring. (A) displays photograph of the MR-compatible catheter equipped with 2 EP electrodes (blue arrows) and 4 micro-coils (red arrows). EP signals were measured between the two electrodes and the RF current was sent through the tip electrode. The associated magnitude image (B) of the catheter in water illustrates the utility of the 4 active markers which appear hyperintense whereas the catheter body stays hypointense. An interactive sequence (C) was run during the catheter manipulation. The micro-coil position was detected and used to update the position of the b-SSFP imaging slices. Catheter tip (red arrows) could be visualized and followed as shown in (D). MR thermometry was performed using a single-shot EPI triggered on ECG (E). Up to 5 slices were acquired depending on heart cycle duration. On healthy volunteers, imaging slices were positioned in short axis orientation (4 chambers view F, blue rectangle) and surrounded by saturation slabs (image F, gray rectangles): 2 along the FOV in the phase encoding direction to limit aliasing effect and 2 parallels to the imaging slices to reduce the signal of blood. A crossed-pair navigator was positioned on the dome of the liver (image G, orange rectangle on coronal view) to monitor respiratory motion at the lung/liver interface. The echo-navigator pulse sequence was run before each slice and the detected breathing stage was used to update the position of the following slice.

Where  $\gamma$  is the gyromagnetic ratio ( $= 42.58 \text{ MHz/T}$ ),  $\alpha_{PRF}$  is the PRF temperature coefficient ( $= -0.0094 \text{ ppm/}^\circ\text{C}$ ),  $B_0$  is the magnetic field strength ( $= 1.5 \text{ T}$ ) and TE is the echo time. The use of the PRF shift technique on moving organs such as the heart requires motion and associated susceptibility artifacts correction.

### Motion correction

Through-plane respiratory motion was compensated by a real-time update of slice position from the echo-navigator readings measured at the liver-lung interface. A Principal Component Analysis (PCA)-based optical-flow algorithm was used to estimate residual in-plane motion on magnitude images [21]. Phase images were registered at a fixed position using the calculated motion fields.

### Correction of respiratory-induced phase variations

Due to magnetic field variations associated with respiration, susceptibility artifacts induce variations on phase images. Thus direct computation of temperature maps from registered phase images may lead to significant errors. A PCA-based method was performed to build a parameterized flow model that establishes a relationship between motions fields and phase variations over the 30 first repetitions of the time series (learning step). This model was then used to correct artifacts of the following repetitions during the interventional procedure. This correction method was introduced in an earlier study [22].

Phase drift compensation was also performed to minimize the effect of fluctuations of magnetic field induced by the heating of magnet components during EPI scanning [15, 23]. Finally, temperature maps were temporally filtered on a pixel-by-pixel basis with a low-pass Butterworth filter (cutoff frequency of 0.14 Hz), taking advantage of the high temporal resolution (<1 s) compared to the slow evolution of the temperature in tissue.

To assess the thermometry precision, the temporal average  $\mu_T$  and the temporal standard deviation  $\sigma_T$  were computed on each pixel over  $\sim 2$  min 30 s of acquisition without heating on healthy volunteers. Regions of interest (ROIs) were hand-drawn around the LV and the RV to perform statistical analysis.

### Thermal dose mapping

First introduced by Sapareto et al. [13], cumulative TD was formulated in each pixel as follows:

$$TD = \begin{cases} \int_0^t 2^{T(t)-43} & \text{if } T(t) > 43^\circ C \\ \int_0^t 4^{T(t)-43} & \text{if } T(t) \leq 43^\circ C \end{cases} \quad (5.2)$$

Where  $T(t) = T_{REF} + \Delta T$  is the absolute temperature at the time  $t$ . Rectal temperature served as a reference temperature value  $T_{REF}$ . The dose corresponding to a constant heating at  $43^\circ C$  for 240 min was considered as the lethal threshold. Computed TD maps were corrected to take in account the uncertainty of the temperature measurement  $\sigma_T$ , using the following formula [24]:

$$TD_{corr}(x, y) = TD(x, y) \times e^{-0.5 \times (\ln(2) \times \sigma_T(x, y))^2} \quad (5.3)$$

Where  $\sigma_T$  is the temperature standard deviation map, calculated on each pixel before RF ablation over 20 repetitions ( $\sim 20$  s). Computed temperature and TD maps were sent in real-time to a dedicated thermometry software (Thermoguide, Image Guided Therapy, Pessac, France) for display and online monitoring of the ablation.

#### 5.4.6 Post-ablation visualization

After each RF ablation, a 3D navigator-gated Turbo Flash IR pulse sequence was performed with long inversion time (TI) for blood suppression in order to visualize the lesion without the use of contrast agents, as proposed by Guttman et al. [25]. The parameters of the sequence were: TI = 700 ms, resolution =  $1.3 \times 1.3 \times 2.5$  mm<sup>3</sup>, FOV =  $360 \times 360$  mm<sup>2</sup>, matrix =  $288 \times 288$  px, ECG-triggered every two heartbeats, FA = 11°, 31 segments, 60 slices. The contrast-to-noise ratio (CNR) was measured as the inner lesion signal intensity minus surrounding tissue signal intensity divided by the standard deviation of the noise measured in a ROI located outside the body (SyngoVia software package, Siemens Healthcare, Erlangen, Germany). Apparent lesion sizes measured on the resulting images will be referred as 3D T1-w dimensions.

#### 5.4.7 Macroscopic examination and lesion size measurements

After completion of the MR-guided RF ablation and 3D imaging, the animals were euthanized with a lethal intravenous dose of Dolethal (Vetoquinol, Lure, France) until complete cardiac arrest was attested. The heart was rapidly excised and dissected to expose each ablation lesion. Each lesion sample was stained at 37°C with tetrazolium chloride (TTC) solution to assess the range of ablation area. Lesions were measured with a ruler and dimensions were correlated to dimensions observed on 2D TD maps and on 3D T1-w images.

To compare 2D TD map and 3D T1-w lesion sizes, the equivalent 2D slice of the MR thermometry sequence displaying the largest TD dimensions was reconstructed from the 3D T1-w volume. Largest and smallest dimensions of the apparent lesion were measured on both images. To compare 3D T1-w and macroscopic lesion sizes, two slices were reconstructed from the 3D volume to approach the orientation of the heart sample dissection. Three measurements were performed: largest and smallest dimensions from endocardium side and depth into the myocardium.

## 5.5 Results

### 5.5.1 Volunteer study

The rate and maximal amplitude of breathing were  $24 \pm 2$  bpm and  $9.2 \pm 4.2$  mm, respectively. The use of saturation slabs apart the imaging slice group resulted in effective blood suppression in three out of five slices, as shown in Figure 5.2-A on averaged magnitude images. Phase images showed significant phase wraps in all volunteers at the heart-liver-lung interface, depicted by the red arrows in Figure 5.2-B. The results of the evaluation of the accuracy  $\sigma_T$  and average

of temperature  $\mu_T$  in the myocardium of one typical volunteer are shown as an overlay on the averaged registered magnitude images in Figure 5.2-C and D, respectively.

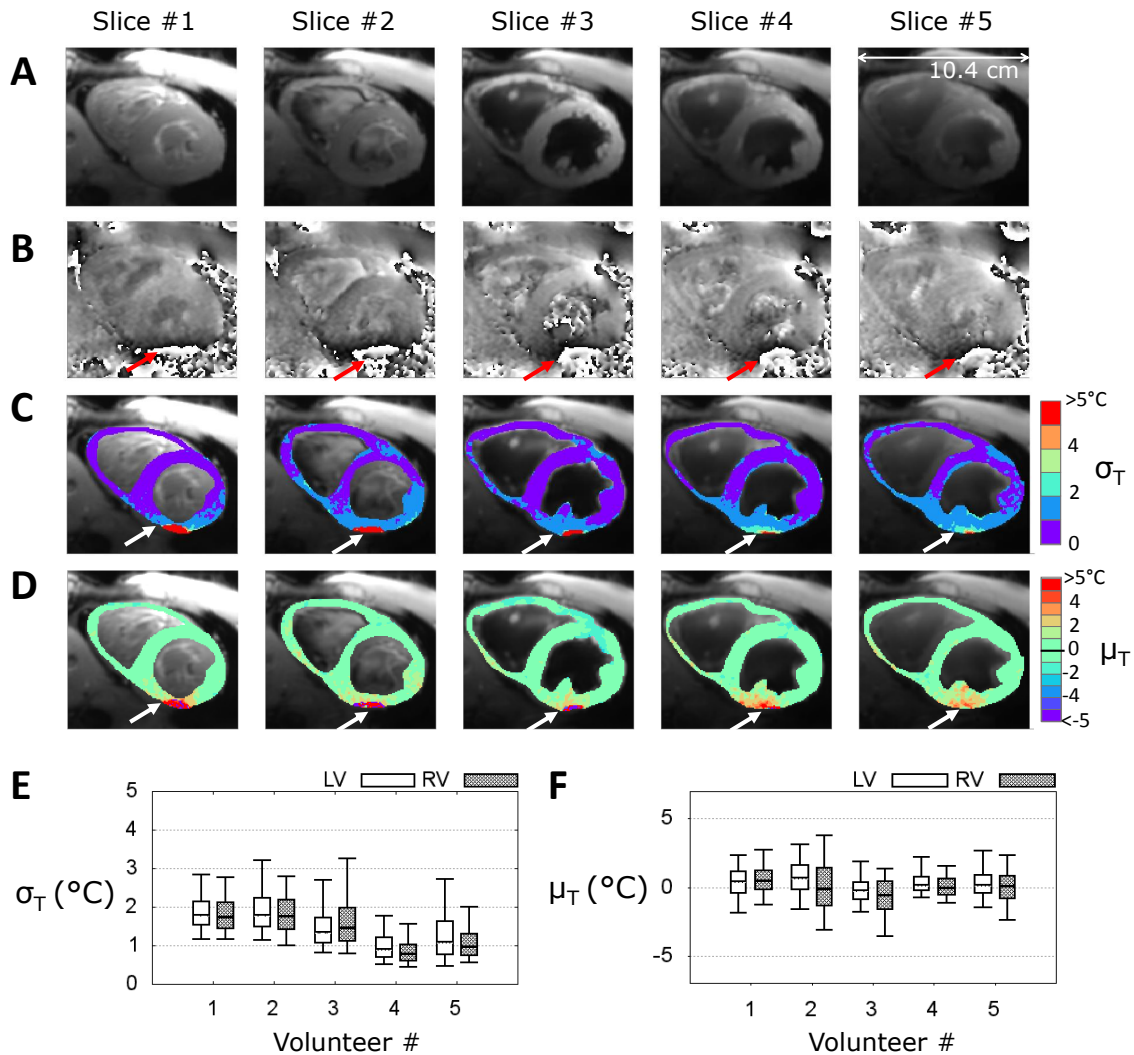


Figure 5.2: MR thermometry evaluation on 5 healthy volunteers in short axis view. Typical results obtained on a volunteer (#5) are displayed: (A) averaged registered magnitude over 2 min 30 s of acquisition and (B) phase image presenting spatial wraps at the heart-liver-lung interface (red arrows). Temporal standard deviation  $\sigma_T$  (C) and mean  $\mu_T$  (D) temperature maps are overlaid on averaged magnitude in a handmade ROI surrounding the all myocardium. White arrows indicate degraded MR thermometry performance induced by remaining phase wraps, despite temporal phase unwrapping processing. Pixels of this area with aberrant results ( $\sigma_T > 7^\circ\text{C}$ ) were excluded from the statistical analysis presented in (E-F). Box-and-whisker plots of standard deviation  $\sigma_T$  (E) and mean  $\mu_T$  (F) of the distribution of temperature in handmade ROIs surrounding the LV and the RV. For each graph, the levels of temperature correspond to 10% (lower horizontal bar), 25% (lower limit of the box), median value (horizontal line inside the box), 75% (upper limit of the box) and 90% (upper horizontal bar) of the distribution.

A reduced temperature precision was observed in the area with remaining phase wraps. The statistical analysis of temperature distribution over all volunteers is presented in Figure 5.2 (E-F) using box and whisker plots for LV and RV ROIs. Over all the volunteers, the standard deviation of temperature  $\sigma_T$  for 2 min 30 s was  $1.5 \pm 0.4^\circ\text{C}$  in LV and  $1.5 \pm 0.5^\circ\text{C}$  in RV, excluding pixels where the thermometry performance was too much degraded ( $\sigma_T > 7^\circ\text{C}$ ),

representing  $3.7 \pm 0.9$  % of the pixels of the myocardium ( $627 \pm 240$  pixels were excluded over a total of  $16 \times 10^4 \pm 3.2 \times 10^3$  pixels). The temporal average was  $0.3 \pm 0.3^\circ\text{C}$  in the LV and  $0.7 \pm 0.5^\circ\text{C}$  in the RV, illustrating the efficiency of phase drift correction (up to  $5^\circ\text{C}$  over 2-3 min of dynamic acquisition) of the MR thermometry pipeline. Thickness of heart walls measured on conventional cine images (resolution  $1.5 \times 1.5 \times 7$  mm<sup>3</sup>, 25 phases/cardiac cycle with retrospective reconstruction) at the medium part of the heart were of  $4.3 \pm 0.7/2.7 \pm 1.3$  mm (mean  $\pm$  sd in Systolic/Diastolic phases) in RV and  $11.6 \pm 3.4/7.4 \pm 2.1$  mm in LV.

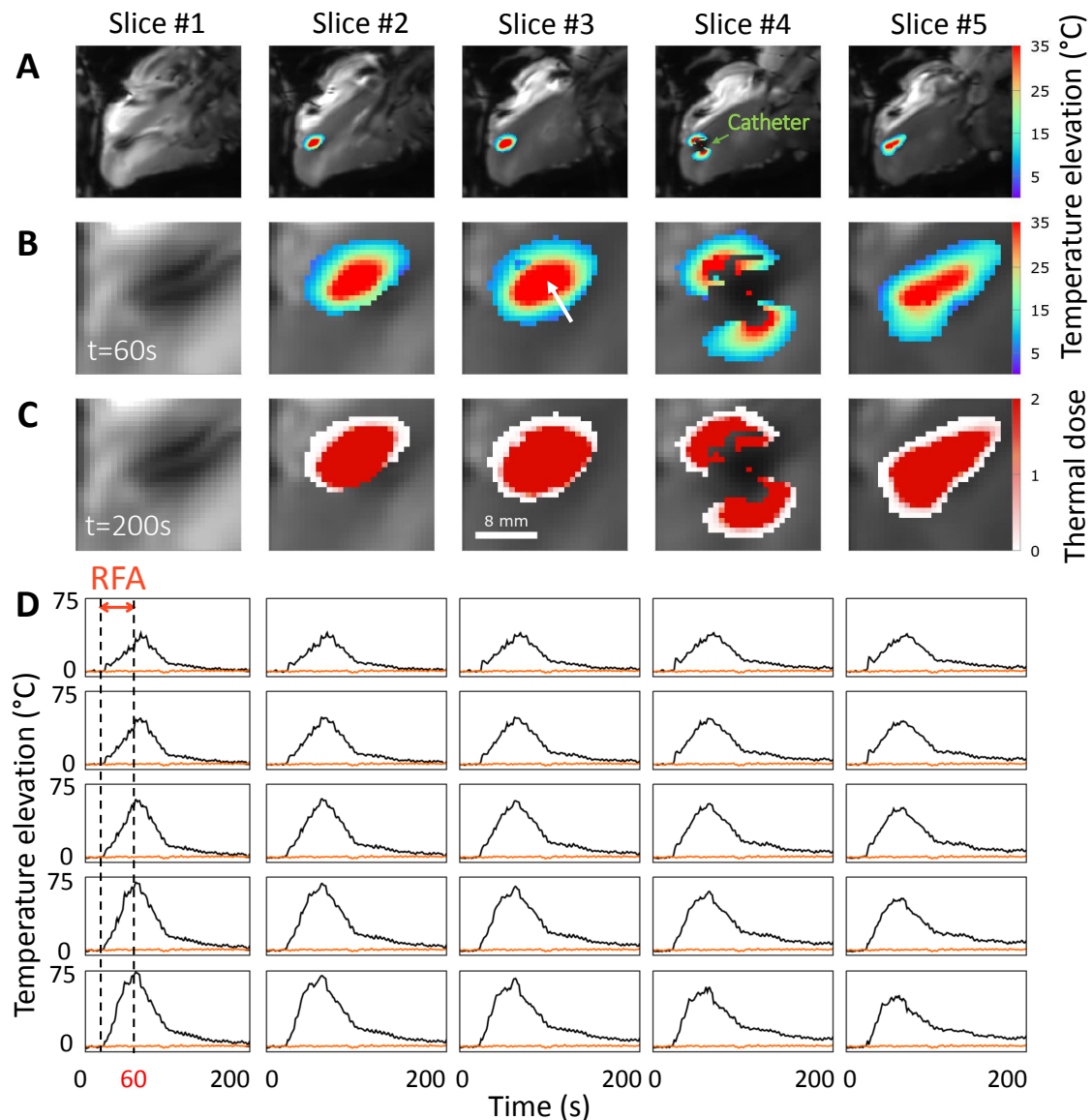


Figure 5.3: Real-time MR thermometry during RF ablation in vivo on a sheep LV. Dynamic MR thermometry was performed in real-time during a RF ablation (70 W for 40 s, RF ablation #4 on sheep #3). A) Temperature maps at  $t = 60$  s, corresponding to 40 s of RF delivery, are overlaid on averaged registered magnitude images within a hand-drawn ROI surrounding the heating zone. Heating zone and associated TD ( $t = 200$ s) are zoomed on (B) and (C) in a  $30 \times 30$  pixels ROI. The value 1 refers to one time the lethal TD threshold equivalent to  $43^\circ\text{C}$  for 240 min. D) Temperature evolution in time in  $5 \times 5$  pixels of slice #3 centered on the white arrow. Orange line depicts baseline temperature in a single pixel outside heating zone.

### 5.5.2 In vivo radiofrequency ablations monitoring

For each animal, the MR-compatible catheter could be successfully navigated and visualized at a frame rate of 3 Hz, with automatic realignment of the imaging stack on the catheter tip. The catheter could be repositioned to a new location in the LV in less than 5 min. 12 RF procedures were performed at different locations in the endocardium of the 3 sheep. The standard deviation of the temperature  $\sigma_T$  before RF ablation was  $1^\circ\text{C}$  or below on the LV. Catheter appeared as a hypointense area with a larger diameter (6 mm) than the actual catheter dimension (3 mm). However, thermometry remained precise enough to monitor the temperature evolution in surrounding myocardial tissue.

Figure 5.3 presents typical MR thermometry results of a RF application at 70 W for 40 s. The local temperature evolution around the catheter tip showed a progressive rise during energy delivery with a maximal relative temperature increase of  $75^\circ\text{C}$  on the central slice, followed by tissue cooling after completion of RF delivery (Figure 5.3-A, zoom on heating zone in Figure 5.3-B). TD maps were computed online with the lethal dose colored in red (Figure 5.3-C). The temperature increase in  $5 \times 5$  pixels centered on the heating spot is displayed in Figure 5.3-D.

ECG recording from the ablation catheter could be performed during the procedure. As displayed on Figure 5.4, changes in ECG signals acquired post-ablation (Figure 5.4-B) differed from the signals observed before the procedure (Figure 5.4-A). During the ablation, the simultaneous MR thermometry acquisition caused significant artifacts and ECG signals were barely readable during the RF ablation.

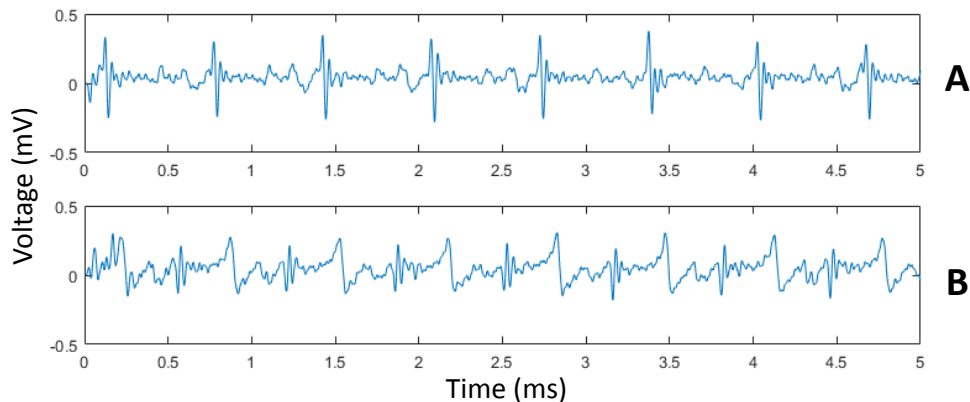


Figure 5.4: Endocardial bipolar signal recorded at the tip of the MR-compatible ablation catheter in the LV of a sheep: (A) before the ablation and (B) after the ablation, showing voltage abatement.

Table 5.1 reports MR thermometry results of 12 RF procedures performed on 3 sheep. The 12 RF procedures resulted in induction of a thermal lesion and were successfully monitored by MR thermometry and dosimetry. Remaining spatial phase wraps at the apex prevented efficient MR thermometry for one ablation that was not reported on Table 5.1. An average of  $59.2 \pm 7.9$  W of RF power was delivered for  $72.5 \pm 18$  seconds, leading to a total RF energy delivery

ranging from 2.8 to 7.0 kJ (mean  $\pm$  sd =  $4.3 \pm 1.3$  kJ).

Sheep #	RFA #	Power (W)	Duration (s)	Energy (J)	Temp max (°C)	Lesion sizes in 2D	
						TD map (mm <sup>2</sup> )	T1-w (mm <sup>2</sup> )
1	1	60	60	3600	30	9×4	9×5
	2	60	90	5400	55	6.5×4	7×4
	3	70	100	7000	30	8×3	9×3
	4	70	90	6300	40	7.5×5	6.5×4
2	1	60	60	3600	40	11×4	11×5
	2	60	60	3600	45	12.5×6	11×5.5
	3	50	90	4500	35	5×8	6×6
	4	60	60	3600	45	10×6	9×5
3	1	50	90	4500	55	12×10	10×7
	2	50	60	3000	30	8×8	8×6
	3	50	70	3500	55	10.5×7	10×7
	4	70	40	2800	75	10×7	10×7

Table 5.1: In vivo MR thermometry results in 3 sheep. Parameters of 12 RF ablations are reported in this Table: the power, the duration and the energy of the RF delivery, the maximal temperature reached in the LV and the 2D dimensions of each lesion created. Lesion extent maximal dimensions were measured in 2D on the cumulative TD maps and on the equivalent slice of the 3D T1-w volume.

### 5.5.3 Post-ablation lesion size measurements

Figure 5.5-A displays typical lesion visualization on 2D slice reconstructed from the 3D T1-w volume after a RF ablation, together with the cumulative TD map (Figure 5.5-B) obtained in real-time during the ablation. The 3D T1-w images obtained with an IR pulse sequence with a TI of 700 ms allowed visualization of lesion core in hyper signal with a CNR of  $88.8 \pm 38.3$  with the surrounding tissue. The volume was acquired after each new ablation with an acquisition time in the range of 15 min to 25 min, depending on the acceptance rate of the echo-navigator and the heart cycle duration. The dimensions of this lesion performed at 60 W for 60 s were  $9 \times 5$  mm<sup>2</sup> on T1-w image and  $10 \times 6$  mm<sup>2</sup> on TD map. Correlation between ablation size on T1-w images and TD maps is shown in Figure 5.6-A with a Pearson's coefficient  $R = 0.87$  and a linear regression slope of 1.01 and an offset of 0.58 mm. In Figure 5.5 are presented T1-w volume (Figure 5.5-C) and macroscopic views (Figure 5.5-D) of the same representative lesion for purpose of comparison. The three measured dimensions were  $8 \times 6 \times 3$  mm<sup>3</sup> and  $7 \times 6 \times 3$  mm<sup>3</sup>, respectively.

Correlation study between T1-w volume and macroscopic measurements is presented Figure 5.6-B with a Pearson's coefficient  $R = 0.89$  and a linear regression slope of 0.92 and an offset of 0.00 mm. The Bland-Altman analysis displayed in Figures 5.6-C and 5.6-D showed no bias depending on the ablation size. Only five measurements were found outside the 95% confidence interval. 2D lesion size estimation from TD maps was found larger than T1-w images measurements:  $0.63 \pm 1.3$  mm (Figure 5.6-C) and 3D lesion size measurements on T1-w volume was found larger than macroscopic measurement:  $0.46 \pm 1.2$  mm (Figure 5.6-D). No correlation analysis could be performed between 2D TD maps and macroscopic measurements since no reliable 3D correspondence could be performed between orientation/position of 2D MR slice and gross pathology dissection.

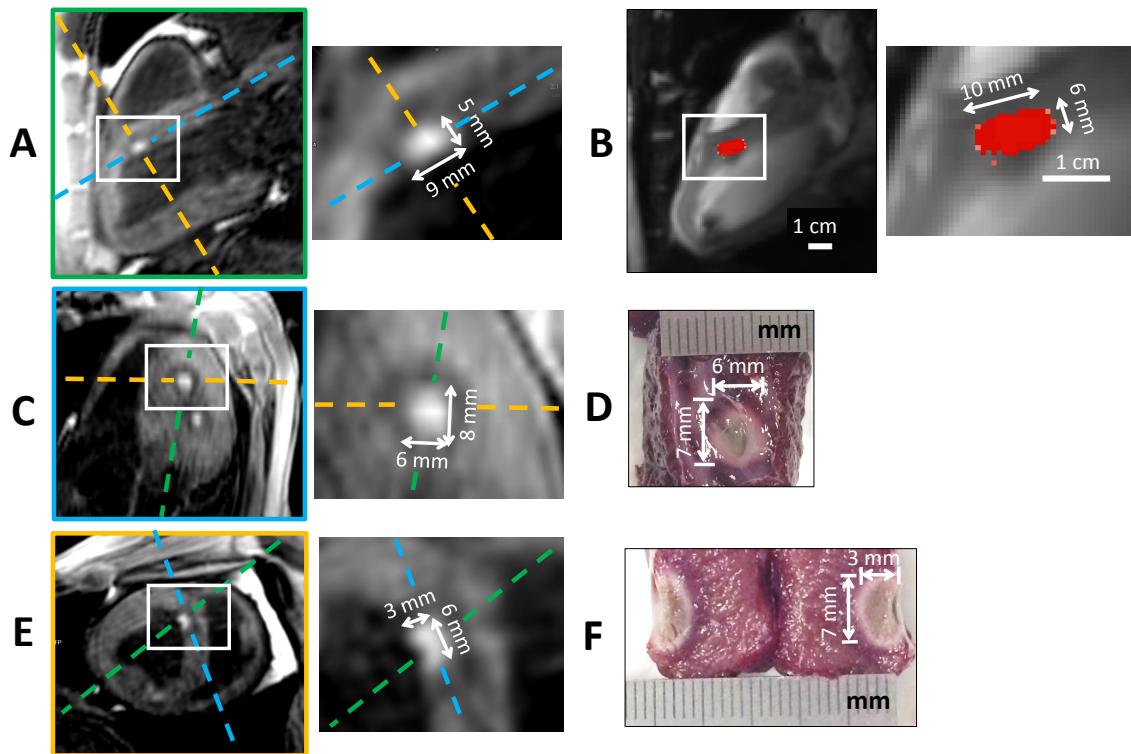


Figure 5.5: Comparison of lesion dimensions of one representative RF ablation between post-ablation T1-w 3D images (A, C and E), real-time TD map (B) and macroscopic observations with TTC staining (D and F). Cumulative TD was computed in real-time simultaneously to a RF ablation of 60 s at 60 W (RF ablation #4 on sheep #2), given the TD map (B) at the end of the procedure. After the ablation, a 3D T1-w IR volume was acquired and the created lesion could be visualized in hyper signal compared to the surrounding tissue attributed to edema. To compare 2D TD map and 3D-IR lesion sizes, the equivalent 2D slice was reconstructed from the 3D T1-w volume, resulting in the image (A, green dashed line perpendicular to other views C and E) with the same position, orientation and zoom than (B). After the intervention, the animal was euthanized and the heart was dissected to expose the lesion. The macroscopic view from the endocardium side is shown in (D) and the equivalent slice (C) was reconstructed from the 3D T1-w volume (blue dashed line perpendicular to other views A and E). The lesion sample was finally cut to expose the extent in depth in the myocardium (F) and the equivalent slice (E) was reconstructed from the 3D T1-w volume (yellow dashed line perpendicular to other views A and C).

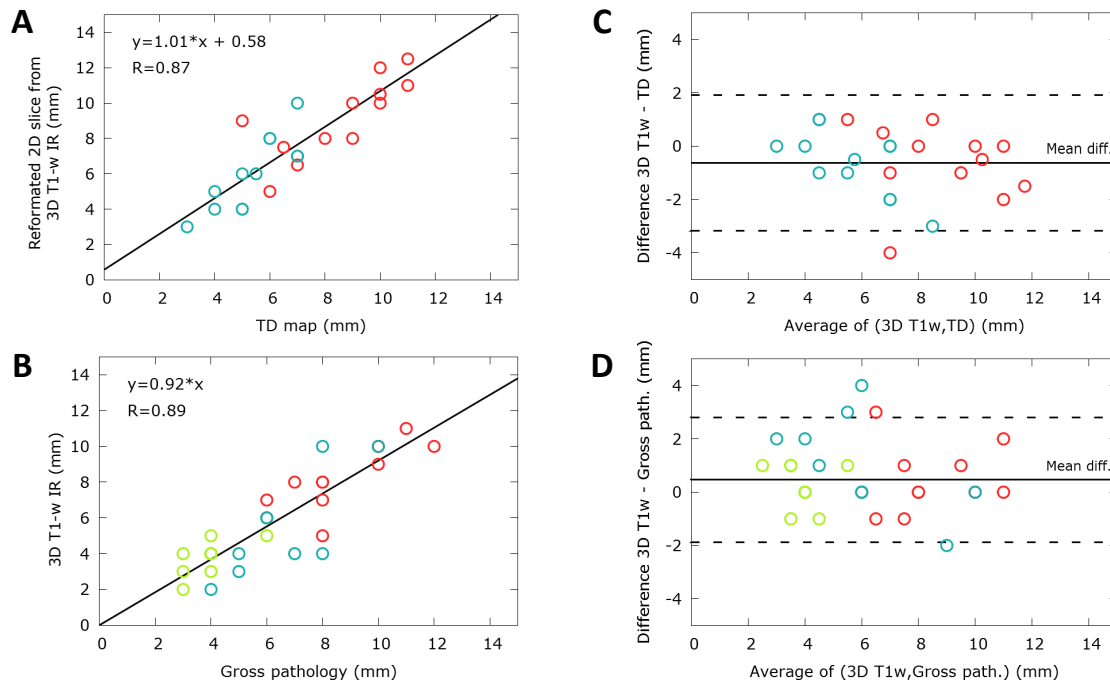


Figure 5.6: RF lesion dimensions ( $N = 12$  lesions) correlation between measurements on real-time thermal dose maps, post-ablation T1-w images and gross pathology. Pearson's linear correlation on (A) reformatted 2D slices from T1-w IR images and TD maps (2 dimensions per lesion,  $N = 24$ ), and (B) T1-w IR images and macroscopic measurements (3 dimensions per lesion,  $N = 36$ ). Dimensions are colour-coded: red for largest dimensions, blue for smallest dimensions and green for depth dimensions (B and D graphs only). It must be noted that several points correspond to more than one measure, since some lesions had identical dimensions. Pearson's correlation coefficient  $R$  and coefficients of the linear regression are indicated on the graphs. Bland and Altman representation of the agreement between the lesion dimensions of the T1-w IR images and TD maps (C) and between the T1-w IR images and gross pathology measurements (D). Dashed lines indicate 95 % confidence limits.

## 5.6 Discussion

One major challenge of RFA for the treatment of cardiac arrhythmia is the ability to visualize the lesion formation in the myocardium in real-time. Objectives of this mini-invasive therapy are to achieve a transmural ablation of the arrhythmogenic substrate while preserving the surrounding healthy tissues and to create a continuous electrical isolation through multiple adjacent RFA performed sequentially. This study demonstrates that i) MR thermometry using our pipeline allows real-time tissue temperature monitoring, including during RF delivery, ii) thermal dosimetry predicts myocardial lesion size. To achieve this goal, we developed a rapid ( $\sim 110$  ms/image), multi-slice echo-navigated MR thermometry method with a spatial resolution in the range of one millimeter, including real-time motion correction and compensation of associated susceptibility artifacts on phase images.

Compared to the recent paper from Ozenne et al [15], an echo-navigated slice following technique was implemented to compensate for respiratory motion in free-breathing conditions, providing full flexibility in the slice orientation. This improvement allowed for the evaluation of

MR thermometry in five volunteers in short axis orientation and resulted in an uncertainty of approximately  $1.5^{\circ}\text{C}$  in the myocardium over 2.5 min of acquisition. Although the wall thickness is thinner in the RV than in the LV, similar temperature precision could be achieved in both ventricles. To our knowledge, this is the first study to report temperature measurements in the RV. The echo-navigator based slice following approach was first reported by Denis de Senneville et al. [2] for CMR thermometry. However, the proposed acquisition protocol suffered from an insufficient spatial resolution (voxel size of  $2.5 \times 2.5 \times 6 \text{ mm}^3$ ) to precisely monitor RF ablation and temperature measurements in the RV. Moreover, only two RF ablations were performed in vivo in animals.

In this work, lesion sizes measured on TD, 3D T1-w imaging and gross pathology from 12 RF ablations performed in 3 sheep were compared. One procedure did not produce a lesion that was attributed to a poor electrode-tissue contact. The results showed an excellent correlation (slopes close to unity and off-set lower than 1 mm) between apparent lesion sizes measured in 2D on TD maps vs T1-w images and in 3D on T1-w images vs macroscopic measurements. Differences between lesion sizes remained in the range of image spatial resolution (0.8 mm). Thus, TD mapping can be used as a reliable surrogate for assessing lesion size in real-time during RF ablation. However, direct comparison between TD maps and gross pathology was not performed since the slice thickness of thermometry sequence (3 mm) was considered too large to assess the TD deposition in 3D with a sufficient precision, regarding the lesion size dimensions reported in Table 1.

Interestingly enough, this study shows that identical RFA parameters (Table 1, duration and power of RF delivery) can lead to different thermal lesion sizes. This may be explained by a number of factors such as the quality of the contact between the catheter tip and the tissue, potential local differences in tissue electrical and thermal conductivities, influence of blood flow, and efficiency of catheter cooling. This has been suspected clinically but the current method now provides an accurate and reliable way to directly measure the actual temperature in the myocardium and accumulated thermal dose, and thereby guide RF delivery in a much more effective way to achieve the desired end point [26]. This strategy should be compared to indirect means such as lesion index algorithm using contact force information.

Kolandaivelu et al. [14] proposed to use an isotherm lethal threshold of  $50^{\circ}\text{C}$  assuming no time-temperature relation. They studied the correlation of the transmural depth of the lesions (depth in short axis orientation) between MR thermometry, LGE MRI and gross pathology over 6 RF ablations in dogs. They reported that lesion transmural depth by thermography was within 20% of that measured by pathology and LGE MRI. However, the insufficient temporal resolution of 10 to 20 s per image associated with breath-holding prevented an accurate and continuous monitoring of the temperature evolution. Moreover, such an approach remains hardly applicable to patients. Visualization of lesion using LGE MRI was found to overestimate the pathological lesion size [14, 27]. In the present study, we performed 3D IR T1-w imaging to visualize the lesions after the procedure without injection of contrast agent. The lesions appeared as an area

of hyperintensity, well demarcated ( $\text{CNR} = 88.8 \pm 38.3$ ) from the surrounding edema appearing as hypointense [28] and healthy tissue. Image contrast did not change significantly (data not shown) over the time course of the experiment ( $> 3$  hours). These findings were consistent with results obtained by other groups with the same MR acquisition pulse sequence [25, 29]. This method offers the advantage of providing a high CNR without injection of a contrast agent, allowing to visualize previously created lesions at once. This is of particular interest to detect potential gaps between successive RF ablations that can result in arrhythmia recurrence. Redo procedure to create a continuous lesion can therefore be facilitated without requiring to wait for contrast agent elimination [27]. However, the sequence remained relatively time consuming ( $\pm 15\text{-}25$  min depending on the heart rate and the breathing cycle duration) and should not be used too often to avoid increasing total procedure time. Recent improvement in acceleration techniques, such as iterative reconstruction [30, 31], could help in reducing the acquisition time for potential clinical practice.

### 5.6.1 Limitations

This study aimed to investigate if the thermal dose can predict the actual lesion size. However, it was not designed to demonstrate that MR thermometry can guide RF delivery in order to achieve transmural and contiguous lesions that are mandatory for efficient curative treatment of arrhythmia. As a consequence and considering this study as a first step, we chose to perform several ablations at distinct locations within the LV, to allow to characterize each RF delivery without bias from overlapping lesions.

Although reliable thermometry stability was achieved in 96 % of the voxels located on the myocardium, the region near the liver-heart-lung interface remained prone to stronger spatial and temporal susceptibility variations that lead to higher temperature standard deviation  $\sigma_T$  ( $> 7^\circ\text{C}$ ). Such an observation was already reported in previous studies [2, 15, 16]. Further improvement in image processing might compensate for this artifact to retrieve accurate temperature measurements in this area.

The proposed MR thermometry method needs to be evaluated on patients suffering from cardiac arrhythmia. Under these conditions, synchronization between the image acquisition and the ECG may be prone to errors and increased temperature uncertainty. Unobserved cardiac contraction pattern during the learning step may be difficult to compensate and justify further investigations and optimization of correction algorithms.

Echo-navigator based slice tracking was assumed to fully correct for through-plane respiratory motion. However, free-breathing patients could present more erratic respiratory motion than healthy volunteers and mechanically ventilated animals. The performance of the slice following should be evaluated under such conditions. The implementation of simultaneous active catheter tracking [32, 33] and RF ablation could address this limitation with a slice always positioned on the catheter tip during MR thermometry.

The first results of thermometry stability on the RV of healthy volunteers are promising for future monitoring of RF ablation in this ventricle. However, the spatial resolution remains insufficient for atrial RF ablation considering the thickness of the atrial wall ( $\sim 2\text{-}3$  mm). Recently, the use of endovascular coils embedded in the catheter was proposed and may be explored to achieve high spatial resolution [34, 35] for monitoring temperature change in the atria.

The current MR compatible catheters did not allow precise EP recording during RF ablation while MRI scanning, due to perturbation induced by MRI gradient switching. Only two contact EP electrodes were available close to the catheter tip due to the presence of MR receiver coils, providing limited contact EP measurements. Thus, improvement of catheter design and associated instrumentation is also mandatory before clinical evaluation.

## 5.7 Conclusion

This study demonstrates that reliable thermometry can be achieved on line on both ventricles using a multi-slice fast imaging sequence combined with slice tracking for respiratory motion compensation. In addition, the thermal dose mapping is highly correlated with post-ablation 3D T1-w images that were also correlated with actual lesion sizes measured at gross pathology. This real-time thermal dosimetry may provide guidance during RF delivery and therefore improve safety and efficacy of catheter ablation.

## 5.8 References

1. Hey, S. *et al.* Towards optimized MR thermometry of the human heart at 3T: CARDIAC MR THERMOMETRY AT 3T. en. *NMR in Biomedicine* **25**, 35–43. ISSN: 09523480 (Jan. 2012).
2. De Senneville, B. D. *et al.* Feasibility of fast MR-thermometry during cardiac radiofrequency ablation: FEASIBILITY OF FAST MR-THERMOMETRY DURING CARDIAC RF ABLATION. en. *NMR in Biomedicine* **25**, 556–562. ISSN: 09523480 (Apr. 2012).
3. Tanner, H. *et al.* Catheter Ablation of Recurrent Scar-Related Ventricular Tachycardia Using Electroanatomical Mapping and Irrigated Ablation Technology: Results of the Prospective Multicenter Euro-VT-Study. en. *Journal of Cardiovascular Electrophysiology* **21**, 47–53. ISSN: 10453873, 15408167 (Jan. 2010).
4. Weerasooriya, R. *et al.* Catheter Ablation for Atrial Fibrillation. en. *Journal of the American College of Cardiology* **57**, 160–166. ISSN: 07351097 (Jan. 2011).
5. Eick, O. J. Temperature controlled radiofrequency ablation. *Indian pacing and electrophysiology journal* **2**, 66 (2002).
6. Cappato, R. *et al.* Updated Worldwide Survey on the Methods, Efficacy, and Safety of Catheter Ablation for Human Atrial Fibrillation. en. *Circulation: Arrhythmia and Electrophysiology* **3**, 32–38. ISSN: 1941-3149, 1941-3084 (Feb. 2010).

7. Seror, O. *et al.* Real time monitoring of radiofrequency ablation based on MR thermometry and thermal dose in the pig liver in vivo. en. *European Radiology* **18**, 408–416. ISSN: 0938-7994, 1432-1084 (Feb. 2008).
8. Holbrook, A. B., Santos, J. M., Kaye, E., Rieke, V. & Pauly, K. B. Real-time MR thermometry for monitoring HIFU ablations of the liver. en. *Magnetic Resonance in Medicine* **63**, 365–373. ISSN: 07403194, 15222594 (Feb. 2010).
9. Ramsay, E. *et al.* MR thermometry in the human prostate gland at 3.0T for transurethral ultrasound therapy: Prostate MR Thermometry at 3T. en. *Journal of Magnetic Resonance Imaging* **38**, 1564–1571. ISSN: 10531807 (Dec. 2013).
10. McDannold, N. *et al.* Uterine leiomyomas: MR imaging–based thermometry and thermal dosimetry during focused ultrasound thermal ablation 1. *Radiology* **240**, 263–272 (2006).
11. De Senneville, B. D. *et al.* MR thermometry for monitoring tumor ablation. en. *European Radiology* **17**, 2401–2410. ISSN: 0938-7994, 1432-1084 (Sept. 2007).
12. Lipsman, N. *et al.* MR-guided focused ultrasound thalamotomy for essential tremor: a proof-of-concept study. *The Lancet Neurology* **12**, 462–468 (2013).
13. Sapareto, S. A. & Dewey, W. C. Thermal dose determination in cancer therapy. *International Contact Lens Clinic* **16**, 340–346 (1989).
14. Kollandaivelu, A. *et al.* Noninvasive Assessment of Tissue Heating During Cardiac Radiofrequency Ablation Using MRI Thermography. en. *Circulation: Arrhythmia and Electrophysiology* **3**, 521–529. ISSN: 1941-3149, 1941-3084 (Oct. 2010).
15. Ozenne, V. *et al.* Improved cardiac magnetic resonance thermometry and dosimetry for monitoring lesion formation during catheter ablation. *Magnetic resonance in medicine*. <<http://onlinelibrary.wiley.com/doi/10.1002/mrm.26158/pdf>> (visited on 06/07/2016) (2016).
16. Grissom, W. A. *et al.* Hybrid referenceless and multibaseline subtraction MR thermometry for monitoring thermal therapies in moving organs. en. *Medical Physics* **37**, 5014. ISSN: 00942405 (2010).
17. De Senneville, B. D., Ries, M., Maclair, G. & Moonen, C. MR-Guided Thermotherapy of Abdominal Organs Using a Robust PCA-Based Motion Descriptor. *IEEE Transactions on Medical Imaging* **30**, 1987–1995. ISSN: 0278-0062, 1558-254X (Nov. 2011).
18. Vergara, G. R. *et al.* Real-time magnetic resonance imaging–guided radiofrequency atrial ablation and visualization of lesion formation at 3 Tesla. en. *Heart Rhythm* **8**, 295–303. ISSN: 15475271 (Feb. 2011).
19. Köhler, M. O., Denis de Senneville, B., Quesson, B., Moonen, C. T. & Ries, M. Spectrally selective pencil-beam navigator for motion compensation of MR-guided high-intensity focused ultrasound therapy of abdominal organs. en. *Magnetic Resonance in Medicine* **66**, 102–111. ISSN: 07403194 (July 2011).
20. Hansen, M. S. & Sørensen, T. S. Gadgetron: An open source framework for medical image reconstruction: Gadgetron. en. *Magnetic Resonance in Medicine* **69**, 1768–1776. ISSN: 07403194 (June 2013).

21. Denis de Senneville, B., El Hamidi, A. & Moonen, C. A Direct PCA-Based Approach for Real-Time Description of Physiological Organ Deformations. *IEEE Transactions on Medical Imaging* **34**, 974–982. ISSN: 0278-0062, 1558-254X (Apr. 2015).
22. Roujol, S., Ries, M., Quesson, B., Moonen, C. & Denis de Senneville, B. Real-time MR-thermometry and dosimetry for interventional guidance on abdominal organs. en. *Magnetic Resonance in Medicine* **63**, 1080–1087. ISSN: 07403194, 15222594 (Apr. 2010).
23. Bing, C. *et al.* Drift correction for accurate PRF-shift MR thermometry during mild hyperthermia treatments with MR-HIFU. en. *International Journal of Hyperthermia*, 1–15. ISSN: 0265-6736, 1464-5157 (May 2016).
24. Weidensteiner, C. *et al.* Real-time MR temperature mapping of rabbit liver in vivo during thermal ablation. en. *Magnetic Resonance in Medicine* **50**, 322–330. ISSN: 0740-3194, 1522-2594 (Aug. 2003).
25. Guttman, M., Kolandaivelu, A., Fink, S., Halperin, H. & Herzka, D. A. Towards MRI-guided cardiac ablation procedures with no contrast agent: safety and efficacy considerations. en. *Journal of Cardiovascular Magnetic Resonance* **18**, P213. ISSN: 1532-429X (2016).
26. Ikeda, A. *et al.* Relationship Between Catheter Contact Force and Radiofrequency Lesion Size and Incidence of Steam Pop in the Beating Canine Heart: Electrogram Amplitude, Impedance, and Electrode Temperature Are Poor Predictors of Electrode-Tissue Contact Force and Lesion Size. en. *Circulation: Arrhythmia and Electrophysiology* **7**, 1174–1180. ISSN: 1941-3149, 1941-3084 (Dec. 2014).
27. Dickfeld, T. *et al.* Characterization of Radiofrequency Ablation Lesions With Gadolinium-Enhanced Cardiovascular Magnetic Resonance Imaging. en. *Journal of the American College of Cardiology* **47**, 370–378. ISSN: 07351097 (Jan. 2006).
28. Celik, H. *et al.* Intrinsic contrast for characterization of acute radiofrequency ablation lesions. *Circulation: Arrhythmia and Electrophysiology* **7**, 718–727 (2014).
29. Kholmovski, E., Ranjan, R., Angel, N., Vijayakumar, S. & Marrouche, N. F. Visibility of RF ablation lesions in native T1-weighted MRI reduces with time after ablation. en. *Journal of Cardiovascular Magnetic Resonance* **18**, P196. ISSN: 1532-429X (2016).
30. Lustig, M., Donoho, D. & Pauly, J. M. Sparse MRI: The application of compressed sensing for rapid MR imaging. en. *Magnetic Resonance in Medicine* **58**, 1182–1195. ISSN: 07403194, 15222594 (Dec. 2007).
31. Forman, C. *et al.* Reduction of respiratory motion artifacts for free-breathing whole-heart coronary MRA by weighted iterative reconstruction: Weighted Iterative Reconstruction for CMRA. en. *Magnetic Resonance in Medicine* **73**, 1885–1895. ISSN: 07403194 (May 2015).
32. Dumoulin, C. L., Souza, S. P. & Darrow, R. D. Real-time position monitoring of invasive devices using magnetic resonance. *Magnetic Resonance in Medicine* **29**, 411–415 (1993).
33. Wang, P. & Unal, O. Motion-compensated real-time MR thermometry augmented by tracking coils: Real-time MR Thermometry. en. *Journal of Magnetic Resonance Imaging* **41**, 851–857. ISSN: 10531807 (Mar. 2015).

34. Volland, N. A., Kholmovski, E. G., Parker, D. L. & Hadley, J. R. Initial feasibility testing of limited field of view magnetic resonance thermometry using a local cardiac radiofrequency coil: Limited FOV MR Thermometry with Local Coil. en. *Magnetic Resonance in Medicine* **70**, 994–1004. ISSN: 07403194 (Oct. 2013).
35. Ertürk, M. A., Hegde, S. S. & Bottomley, P. A. Radiofrequency Ablation, MR Thermometry, and High-Spatial-Resolution MR Parametric Imaging with a Single, Minimally Invasive Device. *Radiology*, 151447 (2016).

## 5.9 Tips and tricks of MR-guided RF ablation in vivo

### 5.9.1 Arrhythmia and pacing

Large animals, such as pigs and sheep, are more prone to arrhythmia triggered by RF ablation than humans. Pigs are very prone to ventricular tachycardia and fibrillation with a high risk of death after a single ablation. For that reason, animal experiment was performed on sheep with pacing of the RV to prevent arrhythmia during RF ablation. It was accomplished by delivering pulses of short duration (eg 2 ms) of electric current through the catheter tip, which stimulates the heart and triggers mechanical contractions. The frequency was chosen so that the resulting heart-rate was a bit faster than the sinus rhythm. The voltage amplitude depends on the catheter/tissue contact quality. It was adjusted in the range from 1 to 3 V, until the pacing threshold is reached to successfully initiate a heartbeat.

However, the pacing may sometimes fail for various reasons such as a bad contact between the RV catheter and the tissue. If this issue cannot be solved during an animal experiment, an arrhythmia may occur during the ablation. This can result in a change in the ECG signal that prevent the MRI to trig and finally to acquire images for MR thermometry. In worse cases a fibrillation may occur and must be stopped using a defibrillator outside the magnet.

### 5.9.2 ECG-triggering

The MR acquisition is synchronised on the ECG signal, recorded by electrodes placed on animal's skin. To optimise the signal quality, animal's skin is previously shaved. The signal is analysed by the MR software to successfully detect the QRS complex. However, the shape of the ECG signal may be corrupted during the ablation so that the R wave is not well detected anymore. As a result, the MR acquisition would be stopped, preventing any MR thermometry monitoring. For that reason, we'd rather use the pacing signal as an external trigger for MR acquisition, if available, to prevent such a failure in image acquisition.

### 5.9.3 Precise localisation of the catheter tip

MR thermometry requires a precise localisation of the catheter tip for slices positioning at the targeted area. The use of active catheter equipped with micro-coils facilitated the localisation of the catheter. However, the fact that the ablation electrode is 3 mm away from the distal micro-coil has to be taken in account for slices positioning. Several MR acquisition of 70 repetitions were performed to ensure that the heating zone will be included in the slice group during ablation.

### 5.9.4 Radiofrequency ablation

A clinical ablation generator (Stockert) was used to deliver the RF energy to the myocardium through the catheter tip. The catheter mode "Manual unipolar" was selected using the rotary knob on the front panel. A safety cutoff based on the circuit impedance has to be disabled. The RF frequency was 500 kHz and the impedance was in a range from 150 to 250  $\Omega$  in vivo.

### 5.9.5 EP recording

In clinical practice, EP recording is performed by connecting each catheter electrodes to an acquisition system Bard. A software (LabSystem) displays EP signals in real-time. EP recording under MRI requires rejection filters to reduce artifacts induced by the gradients of the MR acquisition. Since the MR-compatible catheter (MRI Interventions) is equipped with only two EP electrodes, only one EP voltage signal can be recorded. It was successfully recorded with reduced artifacts from gradients during MR acquisition. However, one important issue that we met, is a loss of this EP signal while the catheter was still in contact with the cardiac wall (successful ablation). It was mainly due to a lack of robustness of the catheter, with broken wires and irrigation flow leak inside the catheter's handle. EP recording should be improved in the future with optimised designed of MR-compatible catheters that should fit standards of devices used in conventional cathlabs.



## Chapter 6

# Active catheter tracking for improved cardiac MR thermometry

### Contents

---

<b>6.1</b>	<b>Preamble</b>	<b>129</b>
<b>6.2</b>	<b>Abstract</b>	<b>130</b>
<b>6.3</b>	<b>Introduction</b>	<b>130</b>
<b>6.4</b>	<b>Methods</b>	<b>132</b>
6.4.1	Imaging protocol	132
6.4.1.1	Catheter design and tip tracking method	132
6.4.1.2	Fast MR thermometry imaging	132
6.4.2	MR thermometry processing	132
6.4.2.1	Statistical analysis	133
6.4.3	Phantom experiments with catheter ablation	133
<b>6.5</b>	<b>Results</b>	<b>134</b>
<b>6.6</b>	<b>Discussion</b>	<b>137</b>
<b>6.7</b>	<b>Conclusion</b>	<b>138</b>
<b>6.8</b>	<b>References</b>	<b>138</b>

---

### 6.1 Preamble

In this chapter, preliminary results achieved at the end of this PhD thesis on simultaneous active catheter tracking and MR thermometry are presented. Despite good temperature precision of the echo-navigated MR thermometry method detailed in Chapter 5, one limitation is the relation between liver and heart motions that relies on a tracking factor. This tracking factor may highly depend on the patient anatomy and on the location of both the echo-navigator at the liver/lung interface and the imaging slices in the heart. To address this issue, we propose to directly track the catheter position, which is equipped with micro-coils, to update the slices position. For that purpose, the commercial single-shot EPI pulse sequence was modified in collaboration with

Siemens Healthcare to integrate an active catheter tracking scheme to update the position of the EPI slices according to the detected position of the catheter tip. Evaluation of this method on a moving phantom is presented in this chapter.

## 6.2 Abstract

**Purpose:** To combine active catheter tracking with automatic update of slice position and real-time proton resonance frequency (PRF) shift MR thermometry.

**Methods:** A MR-compatible catheter equipped with MR receivers (micro-coils) was inserted into a phantom (agar gel) for radiofrequency (RF) ablation experiments on a 1.5 T MR scanner. A catheter tracking scheme was inserted before a single-shot echo-planar imaging (EPI) pulse sequence (less than 100 ms per slice), with a spatial resolution of  $2 \times 2 \times 3$  mm<sup>3</sup>. Residual in-plane motion was corrected using an optical flow algorithm and motion-related susceptibility artifacts were corrected on-line by performing phase modeling based on the updated slice position derived from catheter readings. Performance of the developed MR thermometry method was assessed on a mobile phantom in sagittal, coronal and transverse orientations without heating to calculate the temporal standard deviation of temperature over 3 min of acquisition. The same protocol was then used during RF ablation.

**Results:** Displacement computed from catheter MR signals were consistent with the actual motion. The temporal standard deviation of temperature without heating remained below 2°C whatever the slice orientation. The online monitoring of a RF ablation with an update frequency of 2 Hz was successfully performed using the proposed method.

**Conclusion:** The combination of catheter tracking and online motion and susceptibility correction allows accurate monitoring of temperature while minimizing out-of-plane motion. This method is promising for further application of minimally invasive MR guided cardiac RF ablation.

## 6.3 Introduction

Catheter-based radiofrequency (RF) ablation is widely used for the treatment of cardiac arrhythmia by inducing coagulation necrosis of the arrhythmogenic substrate. Over the last decade, magnetic resonance imaging (MRI) has been increasingly used for the guidance of thermal ablation. Quantitative real-time temperature imaging provides access to thermal dose computation that has been shown to correlate with induced tissue damage. The proton resonance frequency (PRF) shift has become the method of reference due to its linearity in most tissue (except adipose tissue) and its simplicity of implementation in static organs. Temperature change using the PRF shift method is computed using the following formula:

$$\Delta T = \frac{\Delta\varphi}{\gamma \cdot \alpha_{PRF} \cdot B_0 \cdot TE} = \frac{\varphi - \varphi_{REF}}{\gamma \cdot \alpha_{PRF} \cdot B_0 \cdot TE} \quad (6.1)$$

Where  $\varphi$  is the current phase image,  $\varphi_{REF}$  is the phase of reference acquired prior heating,  $\gamma$  is the gyromagnetic ratio ( $= 42.58 \text{ MHz/T}$ ),  $\alpha_{PRF}$  is the PRF temperature coefficient ( $= -0.0094 \text{ ppm/}^\circ\text{C}$ ),  $B_0$  is the magnetic field strength ( $= 1.5 \text{ T}$ ) and TE is the echo time. However, since the PRF technique relies on the subtraction of two phase images acquired at different times, it is highly sensitive to motion and magnetic field variations induced by moving organs.

Several MR acquisition strategies have been investigated to compensate for motion, such as respiratory-gating [1] or slice following techniques [2, 3]. In both methods, an echo-navigator is used to track the diaphragm position at the liver-lung interface. However, the respiratory-gating solution suffers from a limited temporal resolution, since the data is only acquired on the expiration phase of the respiratory cycle. On the other hand, the slice following method allows for a real-time update of the slices position along one direction. However, the effectiveness of this technique highly depends on the relationship between the movements of the diaphragm and the targeted organ. A coefficient, called the tracking factor, must be determined in each patient to give the relation between these two movements. Although several methods have been proposed to determine accurately this tracking factor in each patient [4], a coefficient of 0.6 is commonly used in clinical cardiac MRI [5]. However, this value may differ between patients depending on their anatomy and breathing pattern. In this study, we propose to directly track the catheter position using a dedicated pulse sequence and to automatically update the slice position accordingly. This technique relies on active catheter tracking that has been increasingly used during MR-guided catheterization procedures [6, 7].

MR thermometry requires the correction of susceptibility artifacts induced by motion-related magnetic field changes on mobile organs. The multi-baseline [8] and the referenceless [9] methods are the two commonly used techniques. Because of the sensitivity of the referenceless method to sharp magnetic field perturbations, the multi-baseline method has become the reference technique used in presence of RF probe. It requires a set of pre-heating data to analyze the relation between the motion and the variations of the phase of the MR signal in each pixel. From this analysis, a synthetic phase  $\varphi_{REF}$  can be reconstructed and subtracted to the experimental phase. Wang et al. recently demonstrated the feasibility to use the catheter position to evaluate the relation between motion and local phase variations [10].

In this study, we combine active catheter tracking with automated update of slice position and real-time multi-slice MR thermometry imaging including susceptibility compensation for the monitoring of RF ablation.

## 6.4 Methods

### 6.4.1 Imaging protocol

#### 6.4.1.1 Catheter design and tip tracking method

A MR-compatible catheter (MRI Intervention, Irvine, CA, U.S.A.) equipped with four MR micro-coil receivers (Figure 6.1-A, red arrows) was used and connected to a 1.5T MR scanner (Magnetom Aera, Siemens Healthineers Global, Erlangen, Germany). A single-echo active tracking pulse sequence was implemented in which linear gradients  $G_x$ ,  $G_y$  and  $G_z$  were simultaneously applied along three orthogonal axes (Figure 6.1-B). MR signal received by the micro-coil results in a sharp peak in the frequency spectrum. The 3D coordinates (X,Y,Z) of each coil are then calculated on the fly from the frequency of each peaks (Figure 6.1-C) and the slice position is updated accordingly.

#### 6.4.1.2 Fast MR thermometry imaging

A 2D multi-slice single-shot echo-planar imaging (EPI) was to achieve a spatial resolution of  $2 \times 2 \times 3 \text{ mm}^3$  and a temporal resolution of 100 ms per slice (echo time [TE] = 17 ms, repetition time [TR] = 100 ms, flip angle [FA] =  $60^\circ$ , field of view [FOV] =  $224 \times 224 \times 3 \text{ mm}^3$ , acquisition matrix =  $112 \times 112$ , space between slices = 10% of slice thickness, i.e. 0.3 mm). Four to five slices were acquired and interleaved with the tracking scheme previously described. The position of the each slice was automatically updated so that the slice group was centered on the distal micro-coil located near the catheter tip. Two surface coils with 18 channels each were positioned laterally to the phantom and allowed GRAPPA acceleration (factor 2). The MR raw data were streamed to a remote computer for inline reconstruction of the magnitude and phase images using the Gadgetron framework [11].

### 6.4.2 MR thermometry processing

Potential remaining small in-plane motion was estimated from magnitude images using a fast optical-flow algorithm [12, 13], taking the first stack of slices in the time series as the reference. The computed motion fields were used to register both magnitude and phase images at this reference position. Although images were corrected in position, motion of the object in the static field induces local magnetic field variations in phase images that may be misinterpreted as temperature changes. Thus, a correction algorithm was implemented by performing a linear phase modeling approach as following.

The first N registered magnitude and phase images in the time series were stored in a look-up table, along with the slice position (X,Y,Z), corresponding to the catheter tip position. Then, the overall magnetic field variations were approximated as the linear combination of the slice position (X,Y,Z) on a pixel-by-pixel basis, giving a parametrized magnetic field model (noted as B). For each image acquired after this learning step, the slice position (X,Y,Z) was used with the model B to compute a synthetic phase of reference  $\varphi_{REF}$  as follows:

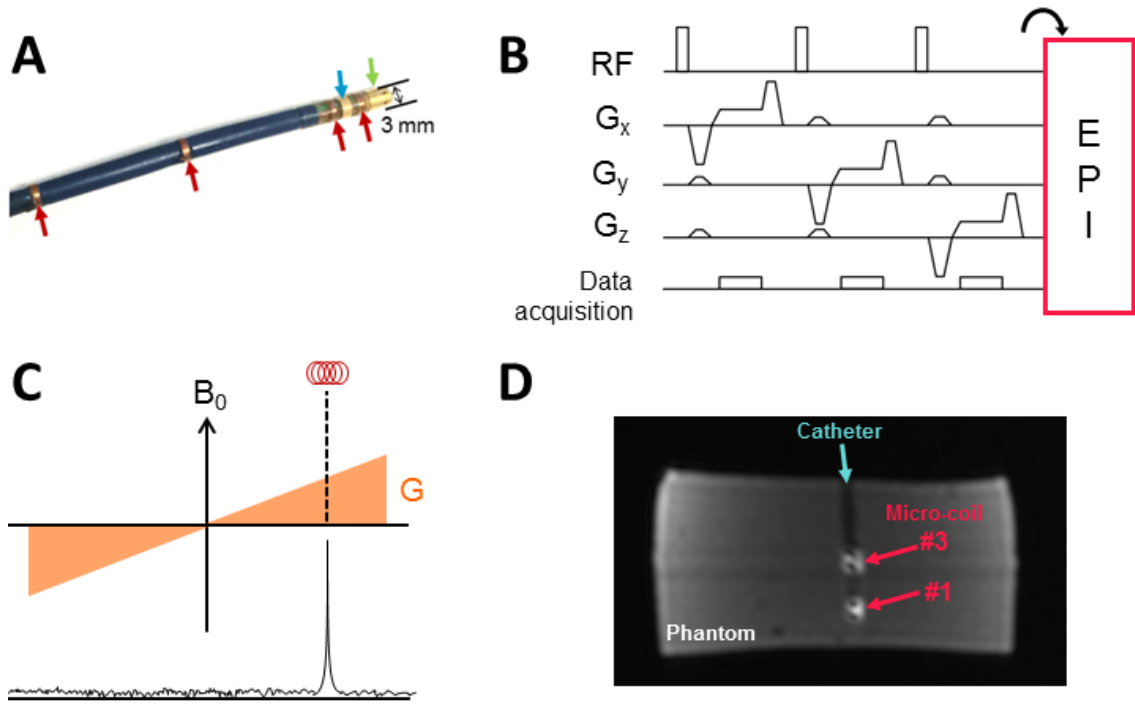


Figure 6.1: Active catheter tracking interleaved with the MR thermometry imaging pulse sequence. (A) A catheter equipped with four micro-coil receivers (red arrows) and two EP electrodes (green and blue arrows) including the ablation tip (green arrow). (B) Basic single-echo catheter tracking scheme, used to detect the 3D coordinates of the tip micro-coil. A non-selective RF is applied before a linear gradient is played along one direction. This scheme is repeated 3 times before EPI with gradients applied along the X, Y and Z axes. (C) The signal received by the micro-coil shows a sharp peak in the frequency spectrum that is proportional to the spatial location of the micro-coil along the applied gradient direction. (D) MR image of a Phantom showing the Catheter and two Micro-coils labeled #1 and #3.

$$\varphi_{REF}(x, y) = X.B_1(x, y) + Y.B_2(x, y) + Z.B_3(x, y) + B_4(x, y) \quad (6.2)$$

Where  $(x, y)$  denotes the pixel coordinates,  $(X, Y, Z)$  the 3D coordinates of the slice positioned on the catheter tip,  $B_j$  with  $1 \leq j \leq 4$  is the parameterized magnetic field model.  $B_4$  is the phase value in each pixel that does not vary with motion. This reference phase image is then subtracted to the current registered phase image to compute the temperature map  $\Delta T$  using the PRF equation.

#### 6.4.2.1 Statistical analysis

To assess the performance of the thermometry method, temporal average  $\mu_T$  and standard deviation  $\sigma_T$  were computed in a pixel-by-pixel basis over 300 temperature maps without heating (corresponding to 2.5 min of dynamic acquisition with a TR of 500 ms).

#### 6.4.3 Phantom experiments with catheter ablation

The MR-compatible catheter was inserted in a cylindrical phantom made of agar gel (3% dry-weight), as visible on a localization image Figure 6.1-D. A periodic motion was produced by a home-made rocker along the magnet direction (z axis). The amplitude was set to 10 mm with a

speed of  $\sim 7$  mm/s to simulate respiratory motion at rest. Four slices were positioned in coronal or sagittal orientations to include catheter displacement in the imaging plane. Then, additional experiment was performed with the four slices in transverse orientation (i.e. perpendicular to the motion direction) in order to evaluate the precision of the slice tracking method in presence of through-plane motion. The MR acquisition was performed simultaneously to motion for a total duration of 3 min. The first 60 images ( $= 30$  s) were used to calculate the phase model during the preparative learning step. Then, the incoming images were used to compute temperature maps.

The MR thermometry performance was first evaluated in absence of heating to compute  $\mu_T$  and  $\sigma_T$  maps for the three different slice orientations. Then a RF ablation was run for 20 s at 4 W using a clinical RF generator (Stockert Medical Solution, Freiburg, Germany) located outside the Faraday cage. RF energy deposition was started after 1 min of data acquisition (i.e. 30 seconds after the end of the learning step).

## 6.5 Results

Figure 6.2-A shows the  $z$  temporal evolution of the position measured from the catheter tip tracking pulse sequence during the rocker-driven motion. The amplitude of  $\sim 10$  mm was in agreement with the rocker set-up. A remaining motion was still visible on the updated magnitude images. This can be attributed to signal disturbance and to the small delay between the catheter tracking and the image acquisition ( $\sim 50$  ms). This in-plane remaining motion was estimated and corrected using an optical-flow algorithm. As expected, the phase image was impacted by the motion due to magnetic field changes, as shown in Figure 6.2-B (one pixel). In addition, a linear phase drift in time is observed. The first 60 acquisition in the time series, corresponding to 30 s of acquisition, were used to analyze the relation between motion and phase variations. The pre-heating phase model was then used during the interventional procedure to compute the background phase  $\varphi_{REF}$  (see Figure 6.2-B, dashed line). A nearly constant temperature curve was observed (Figure 6.2-C) after phase drift correction. Standard deviation of temperature was  $1.0 \pm 0.5^\circ\text{C}$  under these experimental conditions and  $0.4 \pm 0.12^\circ\text{C}$  on the same phantom under static conditions (in coronal orientation). Temperature accuracy was assessed during motion without heating using different configurations of slice orientation. In each case,  $\sigma_T$  was found below  $2^\circ\text{C}$  in most of the pixels (Figure 6.3), except in small regions prone to spatial phase wrapping and distortions (visible on the four corners of the phantom surrounded by circles in Figure 6.3-C). The temporal offset  $\mu_T$  maps illustrated the quality of the phase drift correction and remained below  $0.3^\circ\text{C}$  on average over all the pixels located in the phantom. These results demonstrate similar quality in temperature mapping between in-plane and through-plane motions.

To perform RF ablation in the phantom with simultaneous catheter tracking, several RF energy were tested while plotting in real-time the frequency spectrum computed from the signal of the catheter coils. Interferences were generated when RF power was higher than 4 W using

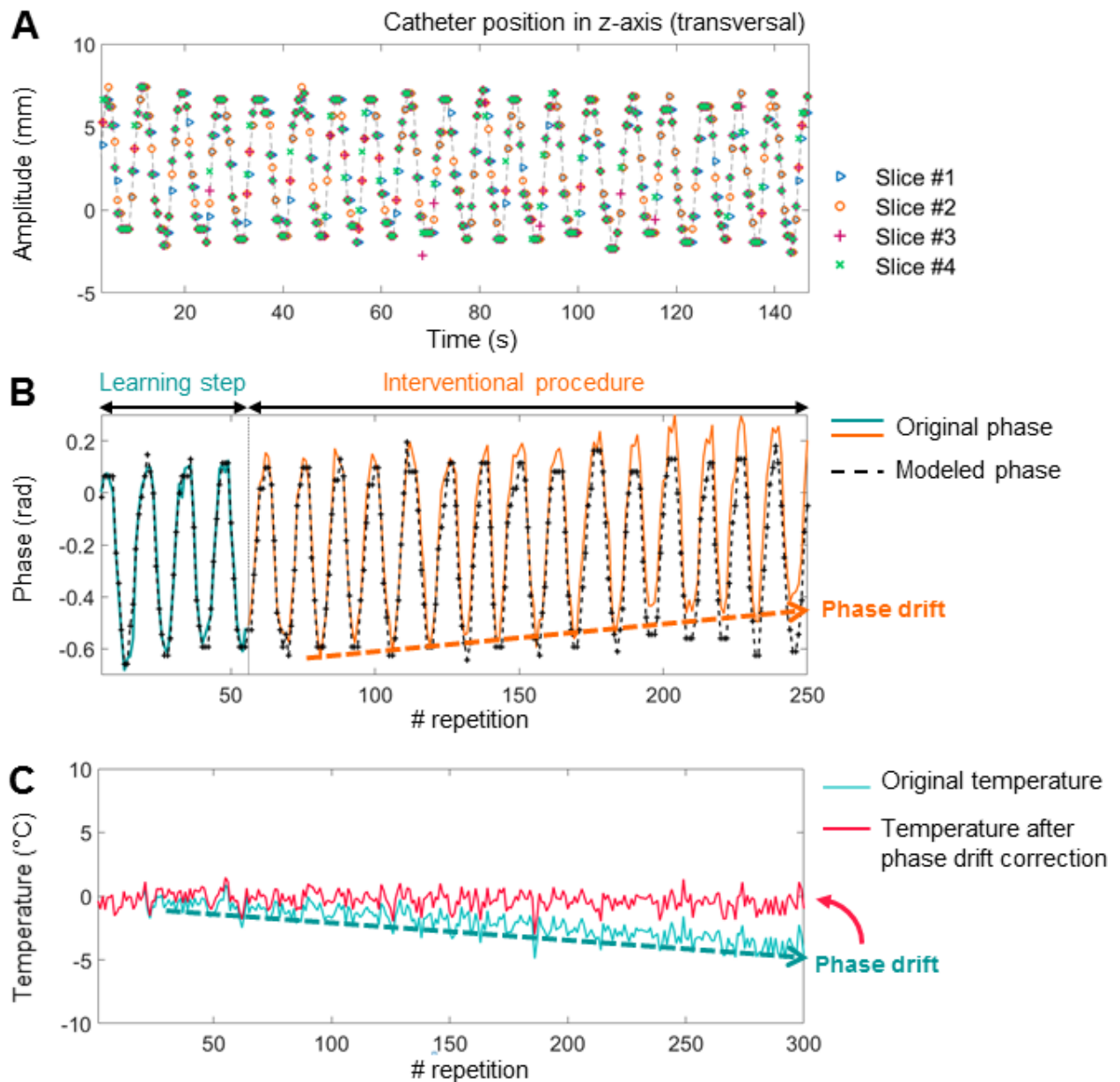


Figure 6.2: Correction of susceptibility artifacts based on the catheter tip position. (A) Position of the catheter in z-axis over time with an amplitude maximal of  $\sim 1$  cm. No variation of position was recorded in x and y axes. (B) Phase variation in one pixel induced by the motion. The relation between the motion (A) and the phase variation was analyzed during a preparative learning step (blue line). The background phase was then modeled from the catheter position (dashed line). Note that a linear phase drift was observed during the intervention (orange line). The modeled background phase was subtracted to the current phase to compute the PRF-based temperature (C, blue line). The drift was finally corrected.

the clinical RF generator operating at 500 kHz. For that reason, the RF delivery was limited to 4 W for 20 s. Figure 6.4 shows the maximal temperature changes at the end of the RF delivery during rocker-driven motion. Temperature evolution in the hottest pixel is plotted at different steps of the correction pipeline: after the image registration (Figure 6.4-B), after the susceptibility artifacts and drift correction (Figure 6.4-C) and finally after additional temporal filtering (Figure 6.4-D).

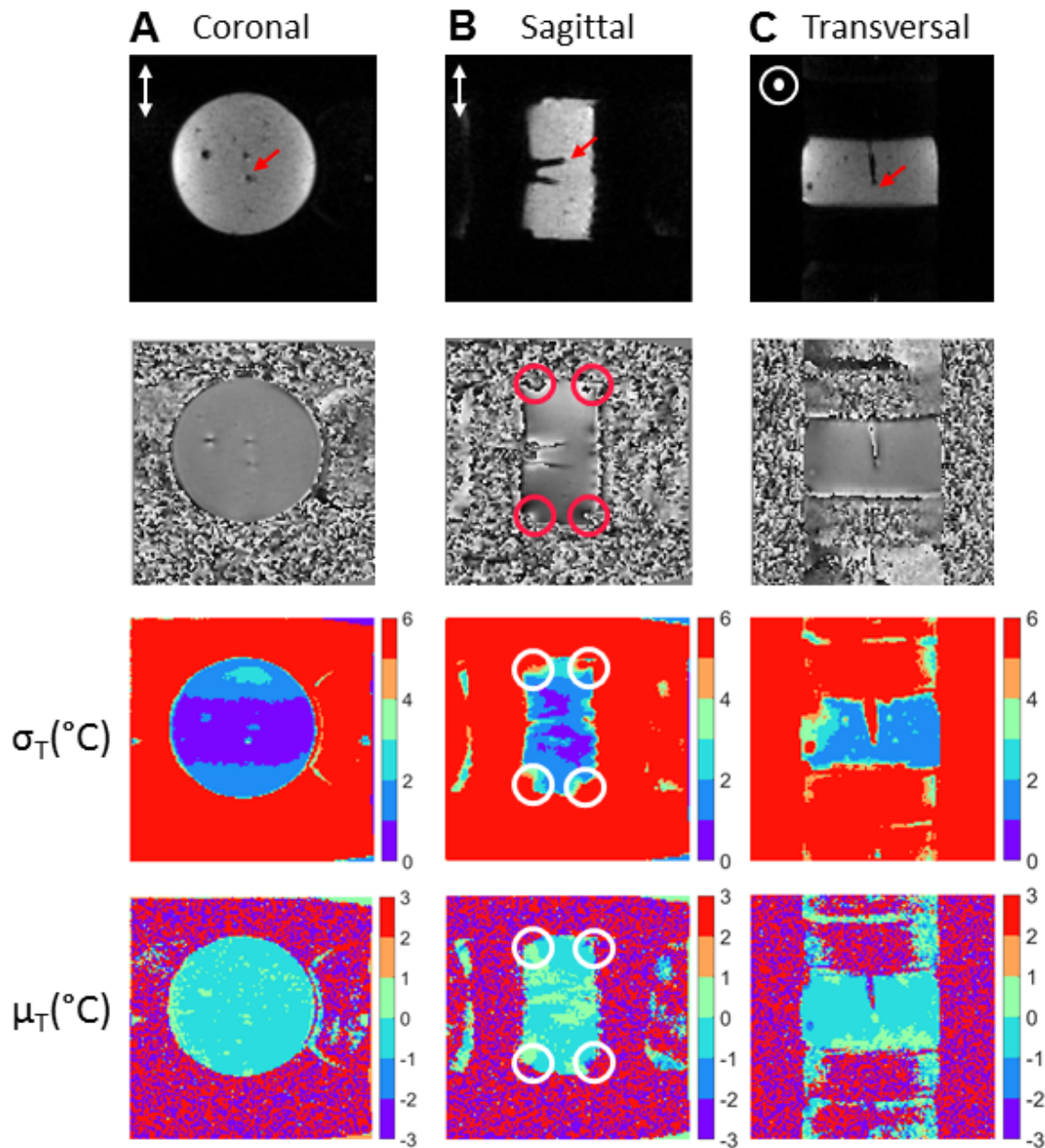


Figure 6.3: Evaluation of temporal accuracy of MR thermometry on a moving phantom using active catheter tracking. The motion was induced by a home-made rocker in the  $z$ -axis direction of the magnet. Three dynamic MR thermometry acquisition of 3 minutes-long each were performed with three different slice positioning. The motion was in-plane to coronal (A) and sagittal (B) imaging slices whereas it was through-plane the transversal imaging slice (C). The imaging plane position was updated according to the catheter tip micro-coil position. The position of the catheter is visible on magnitude (red arrow) and phase images. Temporal standard deviation  $\sigma_T$  and average  $\mu_T$  of the temperature illustrates the performance of the MR thermometry pipeline including catheter-based susceptibility artifacts correction. Circles surround small regions prone to spatial phase wrapping and distortions at the four corners of the phantom in sagittal orientation (B). These areas were associated with a degraded thermometry accuracy  $\sigma_T$ .

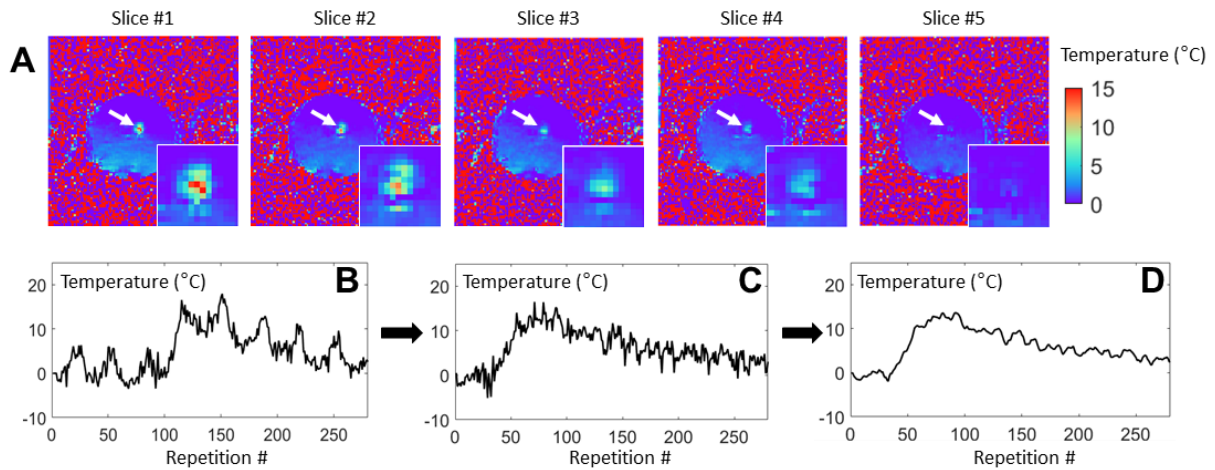


Figure 6.4: Simultaneous monitoring of a RF heating (4 W for 20 s) and catheter tracking on a moving phantom. (A) Multi-slice temperature maps (repetition #78) at the end of the RF delivery. The temperature evolution of the hottest pixel is plotted after image registration without susceptibility artifacts compensation in (B). The susceptibility artifacts are corrected using the catheter position given the temperature evolution (C) without temporal filtering and (D) with temporal filtering (Butterworth low-pass filter).

## 6.6 Discussion

In this study, we demonstrated the feasibility of MR thermometry using active catheter tracking with good performances in case of in-plane and through-plane motions. This method is promising to improve the ease of MR-guided mini-invasive procedures 1) by positioning automatically the imaging slices on the micro-coil positioned close to the device tip and 2) by keeping the heating spot in the imaging plane despite the motion. This technique would be compatible not only with catheters, but with every devices equipped with a micro-coil, for example a needle for RF ablation of tumors in the liver. The proposed slice following technique using the micro-coil position is advantageous over echo-navigator based method, which tracks the respiratory motion in 1D at the liver interface and may require a patient-dependent tracking factor to relate to the motion of the targeted organ. In addition, the use of crossed-pair echo-navigator [ref] impacts the magnitude image with signal suppression and may be an issue in the context of RF ablation of hepatic tumors.

A limitation of our study is the amplitude and the speed of the motion that must be higher to fully mimic the respiratory motion. This technique is currently applicable to respiratory motion with a period of  $\sim 6$  s. In addition, more complex motion patterns must be evaluated. Temperature changes during RF heating in the case of in-plane motion was well monitored. However, another method such as basic multi-baseline should be perform in the future for comparison of the temperature measurements. An optical fiber temperature probe could also be used as reference, even if it cannot reflect the spatial distribution around the tip.

Another shortcoming is the interferences between the RF current delivered at the catheter tip and the frequency peaks used for catheter tracking, despite the use of 64 MHz band-rejection filters in the transmission line. For further in vivo evaluation of this method, a RF power of more than 30 W must be delivered to induce a tissue necrosis. For that purpose, refinement of the filters or the use of another RF generator producing less interferences at the Larmor frequency.

## 6.7 Conclusion

This new active catheter tracking MR thermometry method is promising and offers several advantages for the monitoring of mini-invasive procedures, such as catheter-based RF ablation of the myocardium. This technique allows an automated update of the imaging plane using the catheter tip micro-coil measurements. The motion-related susceptibility artifacts were successfully corrected by performing phase modeling between the phase variations and the tracked catheter motion. The proposed MR thermometry pipeline that integrates in-plane image registration and correction algorithms, is fully compatible with real-time monitoring of procedures (less than 100 ms per image). Further developments must be performed to allow delivery of a standard clinical RF ablation power (higher than 50 W) without interfering with catheter tracking.

## 6.8 References

1. Ehman, R., McNamara, M., Pallack, M., Hricak, H. & Higgins, C. Magnetic resonance imaging with respiratory gating: techniques and advantages. en. *American Journal of Roentgenology* **143**, 1175–1182. ISSN: 0361-803X, 1546-3141 (Dec. 1984).
2. Köhler, M. O., Denis de Senneville, B., Quesson, B., Moonen, C. T. & Ries, M. Spectrally selective pencil-beam navigator for motion compensation of MR-guided high-intensity focused ultrasound therapy of abdominal organs. en. *Magnetic Resonance in Medicine* **66**, 102–111. ISSN: 07403194 (July 2011).
3. Ries, M. *et al.* Real-time 3D target tracking in MRI guided focused ultrasound ablations in moving tissues. en. *Magnetic Resonance in Medicine* **64**, 1704–1712. ISSN: 07403194 (Dec. 2010).
4. Moghari, M. H. *et al.* Subject-specific estimation of respiratory navigator tracking factor for free-breathing cardiovascular MR. en. *Magnetic Resonance in Medicine* **67**, 1665–1672. ISSN: 07403194 (June 2012).
5. Wang, Y., Riederer, S. J. & Ehman, R. L. Respiratory motion of the heart: kinematics and the implications for the spatial resolution in coronary imaging. *Magnetic Resonance in Medicine* **33**, 713–719 (1995).
6. Hilbert, S. *et al.* Real-time magnetic resonance-guided ablation of typical right atrial flutter using a combination of active catheter tracking and passive catheter visualization in man: initial results from a consecutive patient series. en. *Europace* **18**, 572–577. ISSN: 1099-5129, 1532-2092 (Apr. 2016).

7. Nazarian, S. *et al.* Feasibility of Real-Time Magnetic Resonance Imaging for Catheter Guidance in Electrophysiology Studies. en. *Circulation* **118**, 223–229. ISSN: 0009-7322, 1524-4539 (June 2008).
8. Vigen, K. K., Daniel, B. L., Pauly, J. M. & Butts, K. Triggered, navigated, multi-baseline method for proton resonance frequency temperature mapping with respiratory motion. en. *Magnetic Resonance in Medicine* **50**, 1003–1010. ISSN: 0740-3194, 1522-2594 (Nov. 2003).
9. Rieke, V. *et al.* Referenceless PRF shift thermometry. *Magnetic resonance in medicine* **51**, 1223–1231 (2004).
10. Wang, P. & Unal, O. Motion-compensated real-time MR thermometry augmented by tracking coils: Real-time MR Thermometry. en. *Journal of Magnetic Resonance Imaging* **41**, 851–857. ISSN: 10531807 (Mar. 2015).
11. Hansen, M. S. & Sørensen, T. S. Gadgetron: An open source framework for medical image reconstruction: Gadgetron. en. *Magnetic Resonance in Medicine* **69**, 1768–1776. ISSN: 07403194 (June 2013).
12. Horn, B. K. & Schunck, B. G. Determining optical flow. *Artificial intelligence* **17**, 185–203 (1981).
13. Denis de Senneville, B., El Hamidi, A. & Moonen, C. A Direct PCA-Based Approach for Real-Time Description of Physiological Organ Deformations. *IEEE Transactions on Medical Imaging* **34**, 974–982. ISSN: 0278-0062, 1558-254X (Apr. 2015).



## Chapter 7

# Concluding discussion and project perspectives

### Contents

---

<b>7.1</b>	<b>Progress related to this PhD thesis</b>	<b>141</b>
7.1.1	Real-time implementation of a fast cardiac MR thermometry and dosimetry pipeline	142
7.1.2	Implementation of fast MR thermometry pulse sequences	142
7.1.3	Improvement of motion estimation and compensation applied to catheter RF ablation	142
<b>7.2</b>	<b>Perspectives</b>	<b>143</b>
7.2.1	Atrial MR thermometry	143
7.2.2	Automatic temperature control	146
7.2.3	Cardiac MR thermometry on arrhythmic patients	147
7.2.4	Simultaneous Multi-Slice (SMS) MR Thermometry	147
<b>7.3</b>	<b>References</b>	<b>148</b>

---

## 7.1 Progress related to this PhD thesis

The objective of this thesis was to demonstrate the feasibility of precise PRF MR thermometry and dosimetry for the monitoring of RF ablation in the heart. State-of-the-art studies showed major limitations in spatial resolution (compared to a typical RF lesion size smaller than 1 cm), or in temporal resolution (relative to the duration of a standard RF ablation duration, ranging from 30 to 60 seconds). Furthermore, only few preclinical evaluation of the developed methods were conducted due to the limited capabilities of the MR-compatible instrumentation for MR-guided catheter ablation. To overcome these hurdles, a fast MR thermometry and dosimetry pipeline has been developed from scratch in this thesis, since no cardiac MR thermometry methodology was available in the laboratory at the beginning of the PhD. A brief summary of the contributions of this thesis are presented below.

### 7.1.1 Real-time implementation of a fast cardiac MR thermometry and dosimetry pipeline

A pipeline of MR thermometry and dosimetry was designed to allow a real-time monitoring of temperature in the heart. The MR raw-data were streamed to a remote computer for image reconstruction using the recent Gadgetron framework [1]. The algorithms were implemented on GPU and integrated as “gadgets” to ensure real-time conditions. Several state-of-the-art strategies for susceptibility artifacts correction were implemented and evaluated on the heart of free-breathing volunteers.

### 7.1.2 Implementation of fast MR thermometry pulse sequences

Standard single-shot EPI pulse sequence was available on the 1.5 T scanner. Parameters were optimized to allow a sufficient spatial resolution ( $1.6 \times 1.6 \times 3 \text{ mm}^3$ ) while preserving a sufficient image SNR ( $> 10$ ). GRAPPA parallel reconstruction was employed to accelerate the temporal resolution ( $< 100 \text{ ms}$  per slice). Since no compensation of through-plane motion technique was implemented in this commercial pulse sequence, the imaging plane was positioned in order to observe the main direction of the respiratory motion in the imaging plane (head-feet direction). This strategy was used in Chapter 3 along with the developed MR thermometry pipeline.

Two different through-plane motion compensation strategies were then added to the standard single-shot EPI pulse sequence. An automatic update of the imaging group was performed in real-time based 1) on an echo-navigator located at the liver/lung interface (reported in Chapter 5) and 2) on the localization of the catheter tip using an active tracking MR pulse sequence (reported in Chapter 6). 1) Compared to the original EPI pulse sequence, this method offers a full flexibility of the orientation of the imaging slices. Echo-navigated EPI was evaluated in free-breathing volunteers in short axis orientation and showed good results of stability on both ventricles. MR thermometry results obtained with this pulse sequence were detailed in Chapter 5. In addition, zero filling was performed to improve the visualization of the RF lesions by increasing the matrix size of the reconstructed images. 2) Proof-of-concept of simultaneous catheter tracking and MR thermometry was demonstrated in Chapter 6 on a moving phantom of agar gel.

### 7.1.3 Improvement of motion estimation and compensation applied to catheter RF ablation

The performance of the optical-flow motion estimation was proved to be biased by intensity variations associated with the RF heating, mostly due to changes in relaxation times T1 and T2 with temperature of the tissue together with intra-voxel temperature gradients. In this thesis, a protocol of simulation of heating zone on experimental magnitude images was proposed to quantify the impact of such changes on registration process. Then, a novel optical-flow method has been found to solve this issue, by analyzing the motion fields of the first images of the time series with a PCA. The motion of the next images was calculated as a linear combination of the learned PCA eigenvectors. This algorithm showed equivalent performances on volunteers’

data, while being less impacted by intensity variations in the vicinity of the catheter tip, where temperature increase is the most important.

## 7.2 Perspectives

### 7.2.1 Atrial MR thermometry

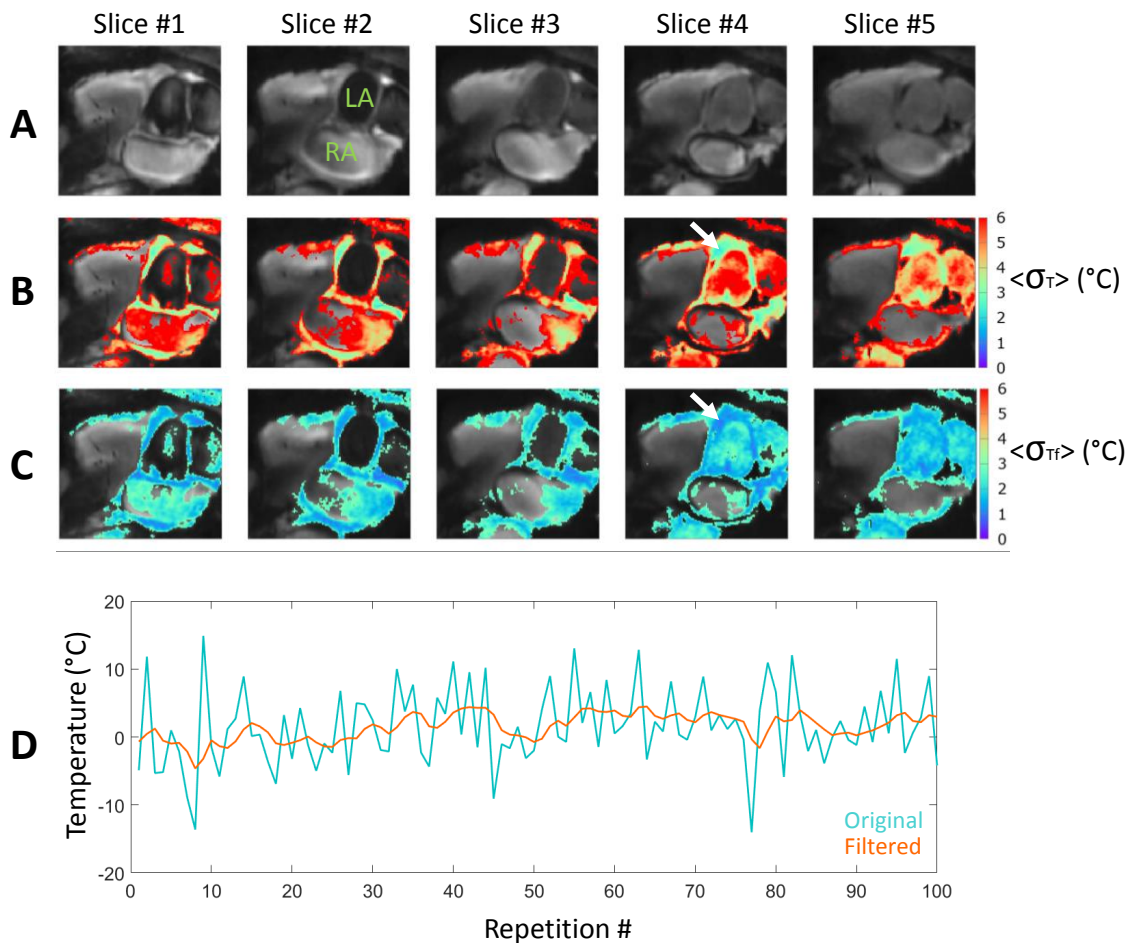


Figure 7.1: Temperature stability on the atria of a free-breathing volunteer. (A) Averaged registered magnitude image in transversal orientation showing the left and right atria. An echo-navigated single-shot EPI pulse sequence was used with slice following to compensate for through-plane respiratory motion. Temperature stability  $\sigma_T$  without filter (B) and with temporal filter  $\sigma_{Tf}$  (C) over 220 repetitions. The colored pixels correspond to pixels  $\sigma_{Tf} < 3^\circ\text{C}$ . The temperature evolution in one pixel pointed by the white arrow on slice #4 is plotted in (D). A temperature stability of  $\sim 3^\circ\text{C}/1.5^\circ\text{C}$  was obtained in the left atrium without/with temporal filter, respectively.

The MR thermometry experiments presented in this thesis were carried out in the LV. However, one major target of RF ablation is the atrium which is much more challenging because of its thickness ranging from 1 to 3 mm. The use of navigator-based slice following along with zero filling provided a stability of  $\sim 1.5^\circ\text{C}$  in the RV of free breathing volunteers (see Chapter

4). This is a significant advancement towards atrial MR thermometry.

Figure 7.1 shows MR thermometry stability obtained in atria on a free-breathing volunteer. The imaging slices were located in transversal orientation to cross the atria. Slices position was updated in real-time according to the respiratory motion observed with an echo-navigator (see Chapter 5). A temperature precision  $\sigma_T$  of  $\sim 3^\circ\text{C}$  was obtained on the left atrium. A temporal filter was added to improve the stability to  $\sim 1.5^\circ\text{C}$ . However, the atria remained hardly distinguishable on magnitude images, due to insufficient spatial resolution.

Several recent studies demonstrated the feasibility of MR thermometry using intravascular coil embedded in a catheter. In Volland et al. [2], an initial study was performed by positioning a local loop MR coil (2 cm of diameter) on the outer surface (epicardium) of the RV during open-chest animal experiment. MR thermometry was measured using this coil and a limited FOV while catheter-based RF ablation was performed in the endocardium of the RV. The increase in SNR brought by the local coil allowed a temperature precision of  $\sim 1^\circ\text{C}$  with a spatial resolution of  $1 \times 1 \times 3 \text{ mm}^3$ . This work was a first validation to pursuit efforts in developing deployable coils that could be inserted into the heart. Ertürk et al. recently developed a single device to perform MR thermometry with high in-plane resolution (voxel size of  $0.3 \times 0.3 \times 8 \text{ mm}^3$ ) using transmit/receive catheter at 3 T. This result opens interesting perspectives for future high resolution MRI of the atria.

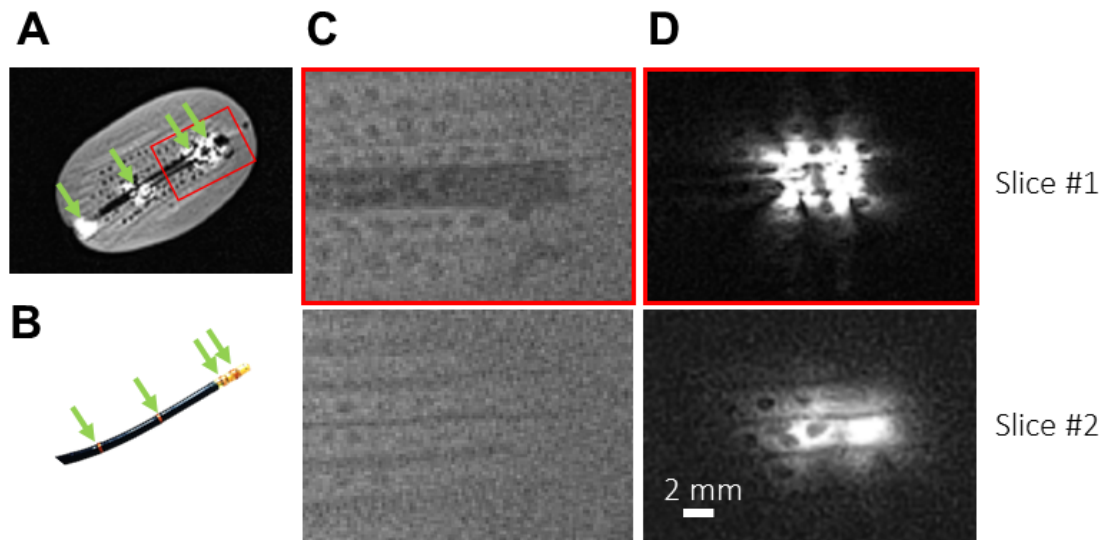


Figure 7.2: Illustration of endovascular imaging using the coils of the catheter. A MR-compatible catheter (B) was inserted inside a kiwi fruit (A). The 4 MR receivers are depicted by the green arrows. Two slices of the kiwi using a Turbo Spin Echo pulse sequence was acquired with an external loop coil (C) and with the two distal coils of the catheter (D). A spatial resolution of  $0.24 \times 0.24 \times 3 \text{ mm}^3$  was achieved.

The MR-compatible catheter (MRI Interventions, Irvine, CA, U.S.A.) available at the IHU-

LIRYC institute was equipped with 4 MR receivers. To illustrate the interest of local imaging coils, the catheter was inserted inside a kiwi (see Figure 7.2). High-resolution images were acquired with an external loop coil (11 cm diameter) and with the two distal micro-coils of the catheter for comparison. A spatial resolution of  $0.24 \times 0.24 \times 3 \text{ mm}^3$  was achieved on a small FOV of  $30 \times 30 \times 3 \text{ mm}^3$  using body coil for excitation. The use of the micro-coils allows a high SNR in approximately 1 cm around the catheter tip. In this particular case, a six-fold increase of SNR was achieved between external and catheter coils. However, the coils configuration was not designed for imaging purpose and the shape of the coil sensitivity should be optimized to allow the visualization of cardiac wall structures.

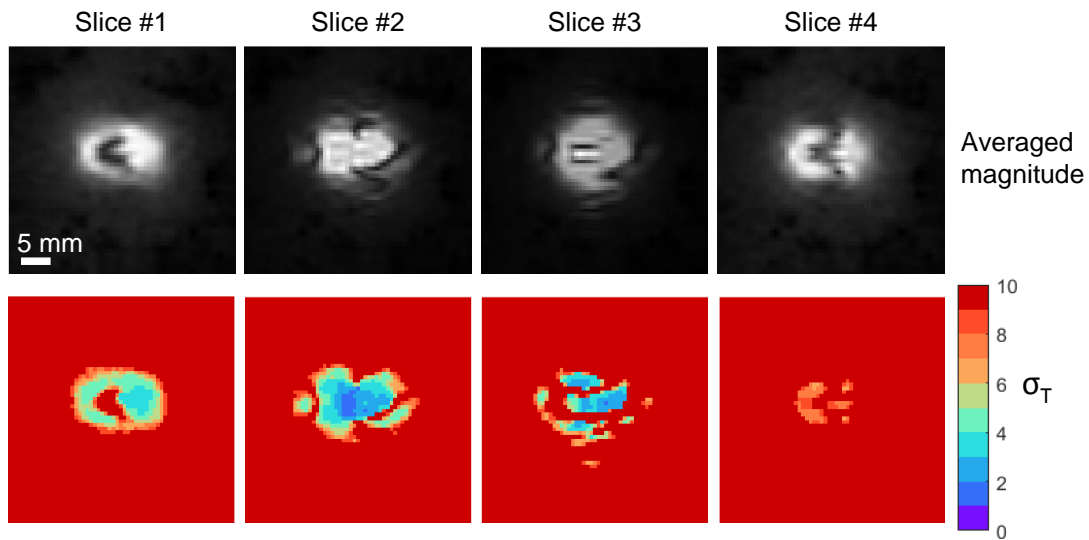


Figure 7.3: Temperature stability obtained using catheter's tip micro-coil as imaging coil in a static phantom made of agar gel. Four slices were acquired in coronal orientation (transverse to the catheter tip) over 300 repetitions. The first row shows the averaged magnitude image obtained after in-plane zero-filling (reconstructed  $0.63 \times 0.63 \text{ mm}^2$  pixel size). Temperature maps were computed by basic PRF-based phase subtraction, without any correction. Temperature accuracy  $\sigma_T$  is shown on the second row in degree Celsius.

In Figure 7.3, MR thermometry stability using the two distal micro-coils was evaluated by inserted the MR-compatible catheter inside a home-made agar phantom. Single-shot EPI sequence was used to acquire 4 slices over 300 repetitions with a limited FOV of  $16 \times 16 \times 3 \text{ mm}^3$  and a voxel size of  $1.25 \times 1.25 \times 3 \text{ mm}^3$ , reconstructed  $0.63 \times 0.63 \times 3 \text{ mm}^3$  with zero-filling. The reduction of the FOV and voxel size are limited by the TE, that must be close to the  $T2^*$  to ensure a good temperature uncertainty [3]. The spatial distribution of the signal around the catheter tip was heterogeneous. According to this signal distribution, the temperature stability was found in the range of  $1.5^\circ\text{C}$  in pixels close to the micro-coil vicinity and up to  $8^\circ\text{C}$  at 5 mm from the tip, without temporal filtering. These results were not sufficient to accurately measure a RF heating, mainly due to the inherent noise induced by the small voxel size and to the inhomogenous spatial distribution of the signal. To overcome the issue of sensitivity, Anderson et al. designed a novel coil configuration, using two orthogonal solenoid coils, to allow a

forward-looking intra-vascular catheter [4]. Such strategy may be highly interesting to improve the ability to accurately measure temperature with the catheter’s micro-coils.

### 7.2.2 Automatic temperature control

Once reliable temperature information is available, there is a need of automatic temperature control to ensure a complete temperature necrosis without inducing collateral damages, such as “pop” or wall perforation. Proportional, integral and derivative (PID) combined with the bioheat transfert law has been proposed in the past to control hyperthermia by high intensity focused ultrasound (HIFU) [5]. RF intensity power ( $P$ ) was derived from PID differential equation:

$$P = \frac{1}{\alpha} \left[ \frac{\partial T}{\partial t} - D \cdot \nabla^2 T + \alpha \cdot (\theta - T) + \frac{\alpha^2}{4} \int_t (\theta - T) \right] \quad (7.1)$$

Where  $\theta$  and  $T$  are the target and the measured temperatures, respectively.  $\alpha$  is the absorption of the tissue and  $D$  is the thermal diffusion coefficient.

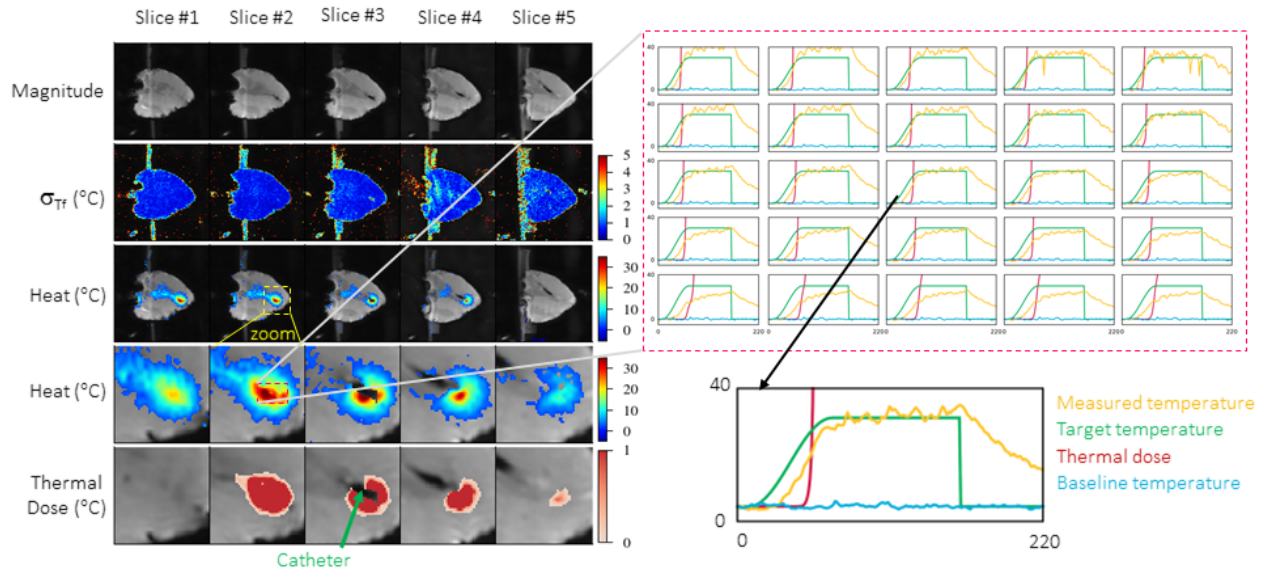


Figure 7.4: Automatic temperature control during RF ablation (Target temperature of 30°C for 90 s) on a perfused beating heart of a sheep. RF power was adjusted in real-time to reach the target temperature (green plot) using PID control. (Results presented by Valéry Ozenne et al. at ISMRM congress in May 2016)

One perspective of this PhD thesis work is to insert automatic control feedback into the developed real-time cardiac MR thermometry pipeline. Temperature control of catheter-based ablation is challenging because of the presence of the catheter that can corrupt pixels in time due to remaining small motion. First results were obtained on ex-vivo beating heart of a sheep [6] by adjusting energy deposition from online temperature images using a programmable RF generator (Image Guided Therapy, Pessac, France). Temperature maps were computed in real-

time using the pipeline described in Chapter 3. An algorithm was performed to control the RF delivery depending on the mean temperature value of  $3 \times 3$  ROI (selected manually before ablation at the vicinity of the catheter). As shown on Figure 7.4, the target temperature could be reached in less than 30 s. Few oscillations of  $\sim 1^\circ\text{C}$  remained, once the temperature reached the targeted one.

These results are promising for a further in vivo application, which is more challenging because of respiratory motion and potential artifact of temperature imaging during ablation. However, phase-related artifacts may induce non-safe adjustment of power which may lead to excessive or insufficient heating. For that purpose, new strategies have to be developed to discard inconsistent phase images corrupted with such artifacts.

### 7.2.3 Cardiac MR thermometry on arrhythmic patients

In this PhD thesis, feasibility of accurate cardiac MR thermometry was demonstrated in healthy volunteers and on animal with normal rhythm. However, performance of this technique has not yet been investigated on patients presenting potential arrhythmia episodes. Irregular rhythm (RR interval) may alter the MR thermometry accuracy that relies on ECG-triggered imaging protocol.

A first study was performed by acquiring MR thermometry data on patients under free-breathing conditions, using the protocol described in Chapter 3 [7]. The MR thermometry accuracy  $\sigma_T$  was computed without discarding data while recording the ECG signal. In post-processing, episodes of arrhythmia were characterized for each patient using duration of current RR interval versus duration of the previous loading beat, as proposed by Contijoch et al. [8]. Over sixteen patients, ten presented episodes of arrhythmia while six were in sinus rhythm during 4 min of temperature mapping. Over all patients, an average  $\sigma_T$  of  $1.94^\circ\text{C}$  was ensured in the LV using temporal filtering. No clear correlation was found between arrhythmia and unstable thermometry.

These results are promising but further developments are required to refine motion compensation and susceptibility artifacts correction depending on ECG readings received in real-time with MR raw data. MR thermometry acquisitions will be performed in absence of heating on a larger cohort of patients. The improved echo-navigated MR thermometry protocol described in Chapter 5 is planned to be used on patients to evaluate its performance in clinical practice.

### 7.2.4 Simultaneous Multi-Slice (SMS) MR Thermometry

Simultaneous Multi-Slice (SMS) imaging offers an acceleration of data acquisition by exciting simultaneously several slices (see review [9]). This technique is rapidly expanding in time critical applications, such as functional MRI (fMRI), abdominal and cardiac imaging. It was shown to be compatible with EPI acquisition [10] and standard parallel reconstruction methods. A first study recently demonstrated the feasibility of MR thermometry with SMS [11], validated on

agar gel during HIFU heating.

In the case of cardiac PRF-based MR thermometry, this technique could be highly advantageous by allowing the acquisition of the slices at the same cardiac phase, instead of sequentially. The blood flow cancellation, ensured by saturation slabs apart the imaging slices, could be achieved similarly in all slices. Thus, motion estimation at the heart cavity boundaries would be less impacted by sporadic blood flow signal.

### 7.3 References

1. Hansen, M. S. & Sørensen, T. S. Gadgetron: An open source framework for medical image reconstruction: Gadgetron. en. *Magnetic Resonance in Medicine* **69**, 1768–1776. ISSN: 07403194 (June 2013).
2. Volland, N. A., Kholmovski, E. G., Parker, D. L. & Hadley, J. R. Initial feasibility testing of limited field of view magnetic resonance thermometry using a local cardiac radiofrequency coil: Limited FOV MR Thermometry with Local Coil. en. *Magnetic Resonance in Medicine* **70**, 994–1004. ISSN: 07403194 (Oct. 2013).
3. Quesson, B., de Zwart, J. A. & Moonen, C. T. Magnetic resonance temperature imaging for guidance of thermotherapy. en. *Journal of Magnetic Resonance Imaging* **12**, 525–533. ISSN: 1053-1807, 1522-2586 (Oct. 2000).
4. Anderson, K. J. T., Leung, G., Dick, A. J. & Wright, G. A. Forward-looking intravascular orthogonal-solenoid coil for imaging and guidance in occlusive arterial disease. eng. *Magnetic Resonance in Medicine: Official Journal of the Society of Magnetic Resonance in Medicine / Society of Magnetic Resonance in Medicine* **60**, 489–495. ISSN: 1522-2594 (Aug. 2008).
5. Salomir, R. *et al.* Automatic feedback control of the temperature for MRI-guided therapeutic ultrasound in (IEEE, Aug. 2007), 222–225. ISBN: 978-1-4244-0787-3 978-1-4244-0788-0. doi:10.1109/IEMBS.2007.4352263. <<http://ieeexplore.ieee.org/document/4352263/>> (visited on 10/19/2016).
6. Vaillant, F. *et al.* Magnetic resonance-compatible model of isolated working heart from large animal for multimodal assessment of cardiac function, electrophysiology, and metabolism. en. *American Journal of Physiology - Heart and Circulatory Physiology* **310**, H1371–H1380. ISSN: 0363-6135, 1522-1539 (May 2016).
7. Ozenne, V. *et al.* Improved cardiac magnetic resonance thermometry and dosimetry for monitoring lesion formation during catheter ablation. *Magnetic resonance in medicine*. <<http://onlinelibrary.wiley.com/doi/10.1002/mrm.26158/pdf>> (visited on 06/07/2016) (2016).
8. Contijoch, F. *et al.* Quantification of Left Ventricular Function With Premature Ventricular Complexes Reveals Variable Hemodynamics. *Circulation: Arrhythmia and Electrophysiology* **9**, e003520 (2016).

9. Barth, M., Breuer, F., Koopmans, P. J., Norris, D. G. & Poser, B. A. Simultaneous multislice (SMS) imaging techniques: SMS Imaging. en. *Magnetic Resonance in Medicine* **75**, 63–81. ISSN: 07403194 (Jan. 2016).
10. Setsompop, K. *et al.* Blipped-controlled aliasing in parallel imaging for simultaneous multislice echo planar imaging with reduced g-factor penalty. en. *Magnetic Resonance in Medicine* **67**, 1210–1224. ISSN: 07403194 (May 2012).
11. Borman, P. T. S. *et al.* Towards real-time thermometry using simultaneous multislice MRI. *Physics in Medicine and Biology* **61**, N461–N477. ISSN: 0031-9155, 1361-6560 (Sept. 2016).



# Summary

This thesis describes recent developments in MR-guided treatment of cardiac arrhythmia by catheter-based radiofrequency ablation. MR thermometry intends to improve the efficacy and safety of the procedure by providing physicians with real-time temperature maps of the targeted myocardium.

In the introduction, the topic of this thesis is positioned in the general context of the monitoring of radiofrequency ablation. A general overview of the monitoring methods used in clinical practice and their limitations is included: temperature at the tip electrode, EGM amplitude, circuit impedance and catheter-tissue contact force. It was shown that none of the existing techniques clearly relate with the final tissue necrosis extent. Compared to X-ray fluoroscopy, MRI guidance offers an excellent soft-tissue contrast that allows target imaging and real-time temperature mapping.

Chapter 2 is dedicated to challenges of cardiac MR thermometry based on the water PRF shift method. The principle of this technique is provided in the first section of this chapter along with the thermal dose concept, which gives us the relation between temperature, duration of exposure and resulting tissue damage. An important challenge of cardiac MR thermometry is to provide a temperature map with a sufficiently small voxel size while preserving a high update rate. Further on, fast imaging acquisition techniques are described, in particular single-shot EPI pulse sequence combined with parallel imaging techniques. The use of fast imaging allows minimizing image artifacts that may be induced by intra-scan motion from heart contraction and respiration. Heart motion is the subject of the following section, where MR acquisition methods to compensate heart-induced and respiratory-induced motions were presented. A short overview of post-processing techniques are then presented to correct for remaining in-plane motion, such as optical-flow algorithms, which are based on the analysis of pixels intensity changes in time. However, despite an effective motion compensation of both magnitude and phase images, motion induces additional variations on phase images due to magnetic field changes in the heart with respiration. These susceptibility effects can bias or mask the temperature measurements and must thus be corrected. An overview of state-of-the-art methods for on-line correction of susceptibility artifacts is given. Drawbacks and advantages of each methods were presented in this section. Finally, a summary of recent studies on cardiac MR thermometry was presented with special attention given to the methods for motion compensation, to temporal and spatial

resolutions of the imaging protocol and to results in term of MR thermometry stability and monitoring of radiofrequency ablation on animal's LV.

An imaging protocol and on-line processing pipeline was described in Chapter 3, which corresponds to a study published on Magnetic Resonance in Medicine (MRM) journal in February 2016 by Valery Ozenne, Solenn Toupin et al. We described a technical solution and implementations to allow a fast MR thermometry acquisition and on-line correction of motion and susceptibility artifacts. A single-shot EPI pulse sequence was combined with GRAPPA parallel imaging and partial Fourier acquisition to ensure a scan time less than 100 ms per slice. Cardiac-induced motion was compensated by synchronizing the acquisition on the surface ECG signal. Up to 5 slices could be acquired within one heartbeat, ensuring a fast update rate for the sampling of temperature evolution. A voxel size of  $1.6 \times 1.6 \times 3 \text{ mm}^3$  could be achieved, which represents a significant improvement compared to the current state-of-the-art methods. Through-plane respiratory motion was minimized by orientating imaging slices parallel to the main displacement direction (head-feet direction). Acquired raw data were reconstructed using an open-source reconstruction framework, Gadgetron, where real-time post-processing algorithms were added: optical-flow algorithm to correct for in-plane motion, susceptibility artifacts correction, computation of temperature and thermal dose maps, phase drift correction and temporal filtering. Performance of this pipeline was first evaluated on healthy free-breathing volunteers and was then used to successfully monitor RF ablations on sheep.

In Chapter 4, a novel approach for in-plane motion estimation and compensation was evaluated in the context of cardiac MR thermometry. The performance of standard motion estimation, using Horn and Schunck optical-flow algorithm, was found biased by intensity changes induced by RF heating. To overcome this issue, a Principal Component Analysis (PCA) was performed on the H&S motion fields of the pre-heating data-set (acquired for the multi-baseline method). For each new incoming image, the motion was calculated as a linear combination of the PCA eigenvectors. This technique has been found to not impact the quality of the motion estimation while being more robust against local intensity variations in the heated region. In addition, this PCA-based optical-flow technique was faster than the previous method, and therefore was still compatible with the real-time execution of the MR thermometry pipeline described in Chapter 3.

In Chapter 5, an echo-navigator was added between two successive acquisitions of single-shot EPI to perform a slice tracking according to the respiratory motion. This significant improvement allows the free positioning of the imaging slices while ensuring to lock the imaging stack on the catheter position. The in-plane pixel size of  $1.6 \times 1.6 \text{ mm}^2$  was improved to  $0.8 \times 0.8 \text{ mm}^2$  by performing basic zero filling during reconstruction. This method brings no additional information but facilitates the visualization of the RF heating zone. The performance of this novel protocol was first evaluated on free-breathing volunteers with five slices positioned in short axis orientation thanks to the echo-navigator slice following. An accuracy of  $\sim 1\text{-}2^\circ\text{C}$  was obtained in the LV, as well as in the RV. These first results of MR thermometry in the right ventricle were possible thanks to the use of the slice tracking technique. This part of the heart was not

accessible with the pipeline reported in Chapter 3, where the slices were positioned in sagittal or coronal orientations. This improved pipeline was then successfully used to monitor in real-time twelve RF ablations on sheep. The created lesions were then visualized in hyper-intensity using a 3D inversion recovery T1-weighted pulse sequence. Lesion sizes measured on the 3D volume was found in good agreement with those estimated on the thermal dose maps and measured on gross pathology after heart dissection. These findings are promising for further MR-guided RF ablation, since the thermal dose mapping could be used as a reliable indicator of the lesion formation in the myocardium of the LV.

The Chapter 6 reports preliminary results on fast cardiac MR thermometry combined with active catheter tracking. The position of a catheter micro-coil could be tracked using non-selective RF and linear gradients in each orthogonal direction. The frequency peak received by the micro-coil directly relates to its position in each axis. The 3D coordinates of this micro-coil were used to update the position slice center and to correct for susceptibility artifacts. This method allows a slice tracking based on the catheter position to minimize the out-of-plane motion of the targeted myocardium. Compared to the echo-navigator based technique (see Chapter 5), this method has the advantage to not necessitate any tracking factor. However, the proximity of the RF electrode with the tip micro-coil may cause interference in the tracking peak frequency. In this chapter, the ability to accurately measure MR thermometry was investigated in a moving gel phantom, in which the catheter tip was inserted. Susceptibility artifacts were effectively corrected and a temperature stability of  $\sim 1\text{-}2^\circ\text{C}$  was obtained (without temporal filtering) whatever the slice orientation. Temperature evolution up to  $15^\circ\text{C}$  was successfully measured during a RF ablation at low power. These results are promising and further investigations of this technique will be performed in vivo in sheep in the future.

The last chapter includes the conclusion of this thesis together with discussions on the project perspectives, outlining research topics which remains to be investigated in the future. Preliminary results were presented on some of these topics.



# Résumé

Les arythmies cardiaques sont des pathologies courantes constituant une gêne quotidienne pour les patients qui souffrent d'une qualité de vie dégradée et d'une morbidité élevée. L'ablation radiofréquence s'est développée en pratique clinique comme traitement visant à éliminer la source de l'arythmie. Pour cela, un cathéter est amené par voie endovasculaire jusqu'au tissu ciblé. Un courant radiofréquence est ensuite émis pour induire un échauffement local et détruire les cellules responsables de l'arythmie. Le taux de réussite est important dans les cas d'arythmies dites simples, où seul intervient un nombre limité de foyers ou circuits, telle que la fibrillation auriculaire qui est principalement déclenchée par des foyers ectopiques autour des veines pulmonaires. Cependant, dans le cas d'arythmies plus complexes à traiter, un nombre significatif de récurrence (environ 30% des patients) est observé et la procédure doit alors être répétée. Une cause de récurrence de l'arythmie est la délivrance d'une énergie insuffisante pour assurer un blocage permanent des influx électriques à la source de l'arythmie. L'imagerie par fluoroscopie et les cathéters actuels ne permettent pas de contrôler la formation de la lésion durant l'ablation.

La thermométrie IRM permet de suivre l'évolution de la température du tissu et d'estimer directement l'étendue de la lésion. Si cette technique est déjà utilisée pour guider l'ablation de tumeurs dans différents organes, la thermométrie IRM reste difficile sur le cœur à cause du mouvement de contraction myocardique et de respiration. Dans le cadre de ce travail de thèse, une méthode de thermométrie cardiaque a été développée pour réaliser une cartographie temps réel de la température du myocarde en condition de respiration libre. Les principaux développements réalisés durant cette thèse sont résumés ci-après.

### Chapitre 3 : Thermométrie et dosimétrie temps réel sur le cœur

**Introduction :** Dans cette étude, une nouvelle chaîne de traitement de thermométrie cardiaque a été développée, permettant une cartographie temps réel de la température du cœur à raison de plusieurs coupes par cycle cardiaque avec une taille de pixel de  $1.6 \times 1.6 \times 3 \text{ mm}^3$ . Cette méthode a été validée sur 10 volontaires sains sans chauffage et durant des ablations radiofréquences réalisées sur brebis.

**Matériel et méthode :** Une séquence EPI multi-coupe, synchronisée avec l'électrocardiogramme, a été combinée avec une méthode d'imagerie parallèle, permettant une acquisition rapide en respiration libre. Un algorithme de flot d'optique a été utilisé pour corriger le mouvement dans le plan de coupe. Les artéfacts de susceptibilité induits par le mouvement ont été compensés sur les images de phase par un algorithme basé sur une analyse en composantes principales. Une correction de la dérive temporelle du signal de phase (lié à un échauffement des gradients du scanner IRM) et un filtrage temporel de la température ont également été implémentés. Cette chaîne de traitement a été intégrée à un logiciel open-source de reconstruction des images, le "Gadgetron". Les signaux électrophysiologiques du cœur ont été enregistrés pendant la séquence de thermométrie IRM via les électrodes du cathéter d'ablation compatible IRM.

**Résultats :** Une déviation standard temporelle de la température inférieure à  $2^\circ\text{C}$  a été obtenue sur le ventricule gauche de chaque volontaire. Sur la brebis, le chauffage local à l'extrémité du cathéter a pu être observé sur les cartes de température (élévation maximale de la température de  $38^\circ\text{C}$ ) pendant l'ablation radiofréquence, tout en enregistrant des électrogrammes de qualité acceptable. La dimension des lésions mesurées après dissection du cœur correspondait bien à celle observée sur la carte de dose thermique.

**Discussion et conclusion :** La méthode de thermométrie IRM cardiaque proposée permet de suivre en temps réel la formation de la lésion durant une ablation radiofréquence. La validation de la méthode a cependant été limitée à une brebis, ce qui n'est pas suffisant pour réaliser une corrélation poussée entre la dose thermique et les tailles de lésion. L'orientation des coupes est par ailleurs limitée à la direction principale du mouvement pour minimiser les mouvements hors plan de coupe.

## Chapitre 4 : Compensation de mouvement par flot d'optique combiné avec une analyse en composantes principales

**Introduction :** Durant l'ablation radiofréquence, le chauffage induit une variation des propriétés tissulaires se traduisant par des variations locales d'intensité sur les images de magnitude. La compensation de mouvement par flot d'optique peut être biaisée en attribuant ces variations à un mouvement. Dans cette étude, l'impact de cette perturbation est quantifiée par des données expérimentales et simulées sur fantôme et brebis. Une méthode de flot d'optique Horn & Schunck combinée avec une analyse en composantes principales (ACP) a été récemment proposée par De Senneville et al. et validée sur des chauffages simulés sur des images IRM de foie et de rein de volontaires sains. Le but de cette étude est d'intégrer cet algorithme dans la chaîne de traitement de thermométrie IRM cardiaque présentée dans le précédent chapitre afin d'évaluer sa robustesse aux variations locales d'intensités.

**Matériel et méthode :** L'algorithme de flot d'optique Horn and Schunck est utilisé pour estimer le mouvement des images lors d'une étape de pré-traitement couvrant plusieurs cycles respiratoires. L'ACP est alors utilisée pour analyser les champs de déplacements obtenus et les principales composantes appelées "eigen vectors" sont conservées. Les champs de déplacement des images, suivants cette étape de pré-traitement, sont alors calculés comme une combinaison linéaire des "eigen vectors" précédemment obtenus. De cette manière, l'influence des variations locales d'intensité induite par chauffage est réduite. Cette méthode a été évaluée et comparée à la technique Horn and Schunck conventionnelle sur des données de volontaires sains en respiration libre en terme de qualité de thermométrie IRM. La robustesse des deux algorithmes a été évaluée avec différents niveau de variation d'intensités ajoutés sur des images expérimentales (fantôme, statique et en mouvement, et ventricule gauche de brebis). Ils ont ensuite été testés en condition expérimentale d'ablation radiofréquence sur ces mêmes cibles.

**Résultats :** La méthode de flot d'optique associée à l'ACP permet d'obtenir une qualité de thermométrie IRM similaire à la méthode Horn and Schunck conventionnelle avec une incertitude d'environ  $1^{\circ}\text{C}$  en moyenne sur neuf volontaires (avec filtre temporel présenté dans le chapitre 3). Dans chaque configuration de variation d'intensité simulée, la méthode proposée présentait un biais moins important sur les champs de déplacement que Horn and Schunck. Durant le chauffage RF sur fantôme de gel, l'erreur d'estimation du mouvement s'est répercutée sur la température, avec une erreur allant jusqu'à  $15^{\circ}\text{C}$  avec Horn and Schunck, contre moins de  $1.5^{\circ}\text{C}$  avec la technique proposée. La différence de température obtenue avec les deux méthodes est cependant moins importante lors d'un chauffage in vivo:  $\sim 5^{\circ}\text{C}$  à proximité de la pointe du cathéter, sur le ventricule gauche de la brebis.

**Discussion et conclusion :** La combinaison de Horn and Schunck avec une ACP a permis de diminuer l'influence des variations d'intensité sur l'estimation du mouvement, tout en accélérant le temps de calcul des champs de déplacement. Le biais introduit dans la méthode Horn and Schunck conventionnelle dépend du contenu des images, d'où l'intérêt du protocole de simulation

des variations d'intensité proposé dans cette étude.

## **Chapitre 5 : Faisabilité de la cartographie temps réel de la dose thermique pour estimer la lésion induite par ablation radiofréquence**

**Introduction :** Plusieurs améliorations ont été apportées à la méthode de thermométrie IRM cardiaque précédemment développée (voir Chapitre 3) pour permettre une corrélation entre les tailles de lésion et la dose thermique lors d'une étude pré-clinique plus avancée.

**Matériel et méthode :** Un écho-navigateur est acquis entre deux acquisitions EPI successives, permettant un changement dynamique de la position des coupes en fonction de l'état respiratoire. Cette méthode permet de positionner librement les coupes sans être limité à une direction parallèle au mouvement principal. Une méthode de "zero filling" a également été ajoutée à la reconstruction d'images pour obtenir une taille de pixel reconstruit de  $0.8 \times 0.8 \text{ mm}^2$ . Ce protocole a été validé sur volontaires sains (N=5) et chez la brebis (N=3) pour le suivi de 12 ablations radiofréquences sur le ventricule gauche. Le guidage et la localisation du cathéter ont été facilités par les 4 micro-antennes du cathéter, permettant un suivi dit "actif". Une séquence 3D inversion récupération (long temps d'inversion) a été réalisée après chaque ablation pour visualiser les lésions. Les mesures des lésions ont été effectuées sur la carte de dose thermique, sur les images 3D post-ablation et après dissection du cœur.

**Résultats :** L'orientation libre des coupes a permis d'obtenir une incertitude de la température de  $1.5^\circ\text{C}$  sur les deux ventricules des volontaires en orientation petit axe. L'utilisation de l'écho-navigateur permet donc de compenser efficacement le mouvement hors plan de coupe. La cartographie temps réel de la température a permis de suivre précisément l'évolution de la température du myocarde autour du cathéter durant 12 ablations. La taille des lésions mesurées sur les cartes de dose thermique cumulée correspondait bien avec celles mesurées sur les images 3D acquises après ablation ( $R=0.87$ ). Les tailles de lésions étaient également bien corrélées entre l'imagerie 3D et les observations après dissection du cœur ( $R=0.89$ ).

**Discussion et conclusion :** La mesure temps réel de la dose thermique est possible et permet une estimation directe de l'étendue de la lésion durant l'ablation. Cette mesure pourrait être un indicateur fiable du résultat de l'ablation, permettant une amélioration future de l'efficacité de la procédure.

## Chapitre 6 : Thermométrie IRM et suivi simultané du cathéter

**Introduction :** La qualité du suivi dynamique des coupes basé sur un navigateur est lié au facteur de suivi, qui donne la relation entre le mouvement du foie et du cœur. Ce facteur de suivi, le plus souvent fixé à 0,6 en pratique clinique, dépend de l'anatomie du patient et de sa manière de respirer. Pour cette raison, nous proposons dans cette étude préliminaire de réaliser le suivi dynamique des coupes de thermométrie IRM directement sur la pointe du cathéter, équipé de micro-antennes.

**Matériel et méthode :** La position de la micro-antenne situé à 2 mm de l'extrémité du cathéter est détectée entre deux acquisitions EPI par une méthode de suivi actif. Un gradient linéaire est appliqué dans une direction de l'aimant et le spectre du signal reçu par la micro-antenne présente un pic à une fréquence donnée. Cette fréquence est directement liée à la position de la micro-antenne le long de cet axe. Cette méthode est réalisée dans les 3 directions de l'espace pour obtenir la position (X,Y,Z) du cathéter. Cette position est utilisée pour mettre à jour la position de la coupe EPI suivante. Durant une phase préparatoire couvrant plusieurs cycles du mouvement, la relation entre la variation de l'image de phase et la position du cathéter est analysée. Cette relation est ensuite utilisée pour reconstruire une phase de référence synthétique à soustraire à l'image de phase courante durant le chauffage radiofréquence afin de corriger les artéfacts de susceptibilité causés par le mouvement. Cette technique combinée de thermométrie IRM et de suivi actif du cathéter a été évaluée sur un fantôme de gel en mouvement (translation dans l'axe principal de l'aimant), avec ou sans chauffage RF.

**Résultats :** Une précision de température inférieure à 2°C sans filtrage temporel a été obtenue sur le fantôme en mouvement (amplitude 10 mm, période 6 s), avec différentes orientations de coupes, parallèles ou perpendiculaires au mouvement. L'élévation de température durant un chauffage RF de 4 W pendant 20 s a pu être correctement suivie. Une puissance RF supérieure à 4 W entraînait cependant des interférences avec la détection de la position du cathéter, basée sur un pic de fréquence, malgré l'utilisation de filtre coupe-bande à 64 MHz sur la ligne de transmission entre le générateur et le cathéter.

**Discussion et conclusion :** La technique proposée permet un suivi automatique de la position des coupes en fonction de la position du cathéter. La chaîne de traitement a permis d'obtenir une précision satisfaisante de  $\pm 2^\circ\text{C}$  sur un gel en mouvement indépendamment de l'orientation des coupes et tout en conservant une résolution temporelle de 100 ms par image et une taille de voxel de  $2 \times 2 \times 3 \text{ mm}^3$ . De futurs développements sont nécessaires pour permettre une ablation RF standard ( $> 50 \text{ W}$ ) sans interférences avec le suivi du cathéter, afin d'évaluer cette méthode in vivo chez la brebis.

## Conclusion

L'objectif de cette thèse était de développer une méthodologie de thermométrie IRM cardiaque permettant le guidage et le suivi des ablations radiofréquences sur le cœur en temps réel. Les études récentes, démontrant la faisabilité de la thermométrie IRM cardiaque, présentaient des limitations significatives de résolutions temporelle et spatiale.

Dans le cadre de cette thèse, une chaîne de traitements a été implémentée pour permettre une cartographie de la température et de la dose thermique du cœur avec une résolution temporelle élevée de l'ordre de 100 ms par image, associée à une taille de voxel de  $1.6 \times 1.6 \times 3 \text{ mm}^3$ . Une séquence IRM rapide a été combinée avec une méthode d'imagerie parallèle afin de minimiser les mouvements intra-scans. Plusieurs solutions ont été proposées pour réduire les mouvements hors plan de coupe lors de l'acquisition des images: positionnement des coupes parallèlement à la direction principale du mouvement respiratoire (Chapitre 3), suivi dynamique des coupes en fonction d'un navigateur (Chapitre 5) ou de la position du cathéter (Chapitre 6).

Des développements méthodologiques ont été réalisés sur plusieurs étapes de la chaîne de traitement. Plusieurs méthodes de correction des artefacts de susceptibilité, présentes dans l'état de l'art de la thermométrie IRM, ainsi qu'une nouvelle méthode de correction de la ligne de base ont été évaluées sur le cœur (Chapitre 3). L'intérêt d'une nouvelle méthode de correction de mouvement a été démontré afin d'améliorer la robustesse de l'algorithme de flot d'optique aux variations d'intensité générées par le chauffage radiofréquence (Chapitre 4). Ces développements méthodologiques ont été validés sur fantôme, sur volontaires sains en respiration libre et finalement chez la brebis pendant une procédure d'ablation radiofréquence.

La chaîne de traitement de thermométrie IRM permet d'atteindre une précision de l'ordre de  $2^\circ\text{C}$  sur les ventricules. L'étude pré-clinique, réalisée chez 3 brebis, a permis de corréler l'estimation de la lésion par dose thermique avec les tailles de lésions mesurées par imagerie 3D post-ablation et après dissection du cœur (Chapitre 5). Ces résultats sont très prometteurs quant à la pertinence de cette mesure pour une estimation temps réel de l'étendue de la lésion pendant l'ablation.

**Perspectives :** Les études menées dans le cadre de cette thèse ont principalement été réalisées sur le ventricule gauche. L'arythmie la plus courante étant la fibrillation auriculaire, une cible de la thermométrie IRM est l'oreillette, beaucoup plus fine que le ventricule avec une épaisseur de l'ordre de 1-3 mm. Les premiers résultats de stabilité de la température obtenus sur le ventricule droit (3-5 mm d'épaisseur) de volontaires sains sont prometteurs, mais la résolution spatiale reste limitée pour distinguer les oreillettes. Ainsi, de nouvelles stratégies pour améliorer la résolution spatiale devront être explorées, telle que l'utilisation d'une antenne d'imagerie intra-vasculaire positionnée sur le cathéter. En vue d'une future étude clinique, la méthode de thermométrie IRM actuelle devra être évaluée sur des patients présentant des périodes d'arythmie.

# Publications

## Peer-reviewed journal papers

- Feasibility of real-time MR thermal dose mapping for predicting radiofrequency ablation outcome in the myocardium in vivo  
**Solenn Toupin**, Pierre Bour, Valery Ozenne, Matthieu Lepetit-Coiffé, Baudouin Denis de Senneville, Rainer Schneider, Alexis Vaussy, Arnaud Chaumeil, Hubert Cochet, Frederic Sacher, Pierre Jaïs and Bruno Quesson, accepted in Journal of Cardiovascular Magnetic Resonance (JCMR)
- Combination of Principal Component Analysis and optical-flow motion compensation for improved cardiac MR thermometry  
**Solenn Toupin**, Baudouin Denis de Senneville, Pierre Bour, Valery Ozenne, Matthieu Lepetit-Coiffé, Manuel Boissenin, Pierre Jaïs and Bruno Quesson, accepted in journal of Physics in Medicine and Biology (PMB)
- Improved cardiac magnetic resonance thermometry and dosimetry for monitoring lesion formation during catheter ablation  
Valery Ozenne, **Solenn Toupin**, Pierre Bour, Baudouin Denis de Senneville, Matthieu Lepetit-Coiffé, Manuel Boissenin, Jenny Benois-Pineau, Michael Hansen, Souheil Inati, Pierre Jaïs and Bruno Quesson, Magn. Reson. Med. 2016 Feb 21
- Magnetic Resonance Imaging guided cardiac radiofrequency ablation  
Valery Ozenne, **Solenn Toupin**, Pierre Bour, Aurélie Emilien, Fanny Vaillant, Baudouin Denis de Senneville, Pierre Jaïs, Eric Dumont, Jenny Benois-Pineau, Pierre Desbarats and Bruno Quesson, IRBM, 2015, Volume 36, Issue 2, Pages 86-91

## Peer-reviewed oral presentations

### 11<sup>th</sup> Interventional MRI Symposium, October 2016, Baltimore

- In vivo monitoring of cardiac radiofrequency ablation by real-time MR Thermometry  
**Solenn Toupin\***, Pierre Bour, Valery Ozenne, Matthieu Lepetit-Coiffé, Baudouin Denis de Senneville, Rainer Schneider, Arnaud Chaumeil, Pierre Jaïs and Bruno Quesson
- Online visualization of lesion extent during RF ablation by thermal dose mapping: correlation with post-ablation T1-w imaging and gross-pathology  
**Solenn Toupin\***, Valery Ozenne, Pierre Bour, Matthieu Lepetit-Coiffé, Baudouin Denis de Senneville, Rainer Schneider, Arnaud Chaumeil, Pierre Jaïs and Bruno Quesson
- First clinical evaluation of real-time cardiac MR thermometry  
Valery Ozenne, **Solenn Toupin\***, Pierre Bour, Baudouin Denis de Senneville, Alexis Vaussy, Matthieu Lepetit-Coiffé, Pierre Jaïs, Hubert Cochet and Bruno Quesson

### 24<sup>th</sup> ISMRM, May 2016, Singapore

- In-vivo echo-navigated MR thermometry for real-time monitoring of cardiac radiofrequency ablation  
**Solenn Toupin\***, Matthieu Lepetit-Coiffé, Pierre Bour, Valéry Ozenne, Baudouin Denis de Senneville, Rainer Schneider, Kim Jenkins, Arnaud Chaumeil, Pierre Jaïs and Bruno Quesson
- Non-invasive cardiac stimulation with MR guided HIFU: a rapid, cardiac triggered, MR-ARFI method for direct visualization of stimulation site and assessment of tissue stiffness  
Pierre Bour\*, Fabrice Marquet, Fanny Vaillant, Valery Ozenne, **Solenn Toupin**, Erik Dumont and Bruno Quesson

### 32<sup>nd</sup> ESMRMB, October 2015, Edinburgh

- MR-guided thermometry for cardiac radiofrequency ablation monitoring  
**Solenn Toupin\***, Valéry Ozenne, Pierre Bour, Baudouin Denis de Senneville, Manuel Boissenin, Matthieu Lepetit-Coiffé, Jenny Benois-Pineau, Erik Dumont, Pascal Desbarats, Pierre Jaïs and Bruno Quesson
- A robust PCA-based motion estimation approach for MR Thermometry radiofrequency ablation monitoring  
**Solenn Toupin\***, Valéry Ozenne, Pierre Bour, Bruno Quesson and Baudouin Denis de Senneville

### 23<sup>rd</sup> ISMRM, May 2015, Toronto

- Motion correction strategies for cardiac MR thermometry during RF-ablation  
Valéry Ozenne\*, **Solenn Toupin**, Baudouin Denis de Senneville, Pierre Bour, Fanny Vaillant, Matthieu Lepetit-Coiffé, Pierre Jaïs and Bruno Quesson

## Poster presentations

### 24<sup>th</sup> ISMRM, May 2016, Singapore

- First clinical evaluation of real-time cardiac MR thermometry (e-poster)  
Valéry Ozenne\*, **Solenn Toupin**, Pierre Bour, Baudouin Denis de Senneville, Alexis Vaussy, Matthieu Matthieu Lepetit-Coiffé, Pierre Jaïs, Hubert Cochet, and Bruno Quesson
- Automatic temperature control for radiofrequency ablation using 2D cardiac MR thermometry (e-poster)  
Valery Ozenne\*, Thibaud Troadec, Pierre Bour, **Solenn Toupin**, Erik Dumont and Bruno Quesson

### Congrès de la section 28 du CNRS, June 2016, Bordeaux

- Real-time Magnetic Resonance (MR) Thermometry for cardiac radiofrequency ablation monitoring: a direct visualization of lesion formation.  
**Solenn Toupin**\*, Pierre Bour, Valery Ozenne, Matthieu Lepetit-Coiffé, Baudouin Denis de Senneville, Rainer Schneider, Arnaud Chaumeil, Pierre Jaïs and Bruno Quesson

### Journée de la FR Tecsán, June 2016, Pessac

- Real-time Magnetic Resonance (MR) Thermometry for cardiac radiofrequency ablation monitoring: a direct visualization of lesion formation.  
**Solenn Toupin**\*, Pierre Bour, Valery Ozenne, Matthieu Lepetit-Coiffé, Baudouin Denis de Senneville, Rainer Schneider, Arnaud Chaumeil, Pierre Jaïs and Bruno Quesson

### 37<sup>th</sup> Heart Rhythm Society (HRS), May 2016, San Francisco

- Real-time visualization of temperature distribution in the myocardium during radiofrequency ablation by Magnetic Resonance thermometry  
**Solenn Toupin**, Matthieu Lepetit-Coiffé, Pierre Bour, Valery Ozenne, Baudouin D. De Senneville, Rainer Schneider, Kimble Jenkins, Arnaud Chaumeil, Pierre Jaïs\* and Bruno Quesson

### 33<sup>rd</sup> annual meeting of the European Section of ISHR, July 2015, Bordeaux

- Real-time MR-thermometry for monitoring RF ablation of cardiac arrhythmia: a proof of concept on isolated working heart from pig.  
**Solenn Toupin**\*, Valery Ozenne, Pierre Bour, Fanny Vaillant, Baudouin Denis de Senneville, Aurélie Emilien, Matthieu Lepetit-Coiffé, Jenny Benois-Pineau, Erik Dumont, Pierre Desbarats, Pierre Jaïs and Bruno Quesson

### Journée de la FR Tecsán, May 2015, Pessac

- Real-time MR-thermometry for monitoring RF ablation of cardiac arrhythmia: a proof of concept on isolated working heart from pig.  
**Solenn Toupin**\*, Valery Ozenne, Pierre Bour, Fanny Vaillant, Baudouin Denis de Senneville, Aurélie Emilien, Matthieu Lepetit-Coiffé, Jenny Benois-Pineau, Erik Dumont, Pierre Desbarats, Pierre Jaïs and Bruno Quesson